Nonsmooth Modal Analysis via the Nodal Boundary Method

David Urman

A thesis submitted to McGill University in
partial fulfilment of the requirement of the degree of
Doctor of Philosophy

Department of Mechanical Engineering
McGill University, Montreal
August, 2023

This thesis is dedicated to Alexander Urman and Ludmila Veremeitchik

Your sacrifice for the betterment of your children's lives cannot be summarized in a finite amount of words. You have always sought for advancing us and have put us always first. Your selflessness and dedication are my inspiration. I thank you for always believing in me and for guiding me to be the person I am today.

Спасибо, я радюсь и горжусь быть вашим сыном

Acknowledgements

I would like to primarily thank Prof. Mathias Legrand for supporting me in all the works that were required for this thesis. I have known Prof. Legrand since my bachelor's thesis, when I approached him to work on what seems to me the most interesting topic in mathematics: nonlinear dynamics. As a researcher, I learned from Prof. Legrand to appreciate the beauty that the field of nonlinear dynamics has to offer. As a supervisor, prof. Mathias Legrand has always provided guidance and was involved immensely in this research. Nevertheless, prof. Legrand allowed me the freedom to explore and has taught me the responsibility of a researcher: rigour and creativity. I am thankful for the research environment that allowed me to express my creativity and for the dedication that prof. Legrand had for revising and providing the fundamentals on which my research stands.

I thank also Dr. Stéphane Junca for helping me in writing my first article *D'Alembert function for exact non-smooth modal analysis of the bar in unilateral contact*. Your comments have helped to improve the paper quality and also contributed to my learning experience. Thank you for your part in making the writing of this paper a pleasant experience!

I would also like to thank Dr. Carlos Yoong and Tianzheng Lu for their support and for the discussions on nonsmooth modal analysis and structural dynamics. I am very glad to have passed my time with them as colleagues and hope our paths will cross again in the future.

I thank especially Dr. Anders Thorin for being a mentor and a guide in this field of nonsmooth dynamics. I was happy to work with Anders and to consult with him on a variety of topics in mathematics. Nevertheless, Dr. Anders Thorin was always a good friend and a model researcher. I thank him for his persistent support at the beginning of my dissertation.

Special thanks are also due to Vassily Korotkine and Grace Genszler for their work as undergraduates in the Laboratory of Structural Dynamics. Your commitment and dedication to explore and learn new topics, and your courage to handle projects independently has been a pleasure to witness. I have learned a lot from my experience with you and I only wish you nothing less than the best in your future careers.

Nevertheless, I would like to thank my family: my parents, Alexander Urman and Ludmila Urman; my brother and his wife, Timor Urman and Oryan Vashdy; and my nieces: Mia, Lianne, and Adele Urman. I thank them for providing the warmth and support throughout my dissertation.

At last, I would like to thank my wife: Dr. Anne-Julie Lafrenaye-Dugas. I have met her during my PhD studies, and I am very lucky she has accepted being my wife. As a former PhD student herself, she was always my rock, and in all the porous oscillations that occur in my life, she was the viscous damper that smooths my trajectory. Borrowing from Nassim Taleb's theory on dynamics of chaotic systems, she is my black swan, and I am glad for her impact on my life.

Abstract

The prediction of resonance in vibrating structures is a subject of importance in the field of mechanical engineering and is useful for structural health as well as for estimating the capabilities of vibrating structures. Modal analysis allows prediction of resonance by depicting of dynamics in the frequency domain in the form of modes of vibration. While in linear systems, the notion of modes of vibration is directly related to the principle of superposition, nonlinear dynamical systems lack superposition and the notion of modes of vibration has been extended to nonlinear normal modes: families of periodic motions of the dynamical system. Indeed, nonlinear normal modes correspond to resonant frequencies and energies of the dynamical system similarly to mode-shapes and natural frequencies in linear dynamics. This thesis focuses on the detection of nonlinear normal modes in structures that are prone to unilateral contact.

Here, unilateral contact is described via the Signorini complementarity conditions which exhibit a set of nonsmooth equations involving the displacement and stress of the structure at the contact boundary. While numerical tools for nonlinear modal analysis are widely applied for smooth nonlinear systems, determination of nonlinear modes in nonsmooth systems, such as systems involving unilateral contact, is a challenging topic. Determination of periodic solutions in nonsmooth systems requires both accurate numerical schemes to describe the motion of the system and schemes to solve for periodic motions. In turn, detection of multiple periodic motions that form a nonsmooth mode is done by continuation methods. This thesis describes both analytical and numerical nonsmooth modal analysis of structures in unilateral contact. Analytical modal analysis is performed for the cantilever bar of uniform area (internally resonant bar) prone to unilateral contact. The nonsmooth modes are found by formulating the conditions for periodic motions using the d'Alembert travelling-wave function. Analytical modal analysis in this approach results in the discovery of nonsmooth modes composed of piecewise-smooth motions yet observed in literature. Other than analytical nonsmooth modal analysis, numerical nonsmooth modal analysis constitutes the dominant portion of this thesis. Since closed-form solutions are rarely available for either one-dimensional or two-dimensional structures prone to contact, numerical methods for nonsmooth modal analysis must be used. Existing numerical schemes to treat the unilateral contact boundary conditions exhibit deficiencies such as: numerical chattering, energy dissipation,

or non-physical penetration of the obstacle. For purposes of nonsmooth modal analysis, periodic motions of structures in unilateral contact without numerical chattering or penetration of the obstacle are sought. To this end, the nodal boundary method is conceived in this thesis. The nodal boundary method treats the Signorini conditions by approximating the structure's displacement using shape functions that satisfy the Signorini complementarity conditions in a strong manner. Specifically, different shape functions are used to describe the structure away from the obstacle (inactive contact phase) and in contact with the obstacle (active contact phase). The switching method is then used to determine the shape functions used and the contact phase(s) in any given instant of the motion. The nodal boundary method results in motions that exhibit continuous contact phases (elimination of numerical chattering) and allows for existence of periodic motions. The nodal boundary method is applied to find periodic solutions of both the bar and the plate in unilateral contact. Specifically, this thesis brings forth novel results such as the nonsmooth modal analysis of the varying-area bar and nonsmooth two-dimensional plate.

Abrégé

La détection d'instances de résonance dans des structures en vibration est un sujet d'importance en génie mécanique. Elle est utile pour la santé structurelle des structures ainsi que pour prédire les performances des structures sujettes aux vibrations. L'analyse modale permet de déterminer les instances de résonance par investigation de la dynamique dans le domaine fréquentiel et des modes de vibration. En dynamique linéaire, la notion des modes de vibration repose sur le principe de superposition lequel ne tient pas pour les dynamiques non-linéaires. Pour les systèmes dynamiques non-linéaires, la notion de modes de vibration est étendue aux modes de vibration non-linéaires: familles de mouvements périodiques du système dynamique. En effet, ces variétés dans l'espace de phase correspondent aux fréquences et aux énergies de résonance du système dynamique, de même que les modes de vibration en dynamique linéaire. Cette thèse porte sur la détection des modes de vibration non-linéaires dans les structures sujettes au contact unilatéral.

Ici, le contact unilatéral est décrit via les conditions de complémentarité de Signorini qui sont composées des équations non-lisses entre le déplacement et la contrainte de la structure à la frontière de contact. Alors que les outils numériques pour l'analyse modale non-linéaire ont été principalement développés pour les systèmes non-linéaires lisses, la résolution des modes non-linéaires dans les systèmes non-lisses, en particulier dans les systèmes impliquant un contact unilatéral, est un défi académique. Le défi de l'analyse modale non-lisse (l'analyse modale non-linéaire des systèmes non-lisse) des structures en contact unilatéral est double : (1) résolution des mouvements périodiques et (2) continuation des modes non-lisses. La résolution de mouvements périodiques dans des systèmes non-lisses nécessite des schémas numériques précis pour décrire le mouvement du système et des schémas pour résoudre des mouvements périodiques entre tous les mouvements possibles. Ensuite, les méthodes de continuation servent à la détection de plusieurs mouvements périodiques qui forment un mode non-lisse.

Cette thèse décrit à la fois l'analyse modale non-lisse analytique et l'analyse modale numérique des structures en contact unilatéral. Une analyse modale analytique est effectuée pour la barre en porte-à-faux de section transversale uniforme (la barre avec résonance interne) en contact unilatéral et mène à de nouveaux modes non-lisses non obtenus dans la littérature existante.

Outre l'analyse modale non-lisse analytique, l'analyse modale non-lisse numérique constitue

la partie principale de cette thèse. Étant donné que les solutions de forme fermée sont rarement disponibles pour les structures unidimensionnelles ou bidimensionnelles, des méthodes numériques pour l'analyse modale non-lisse doivent être utilisées. Les schémas numériques existants pour traiter les conditions aux limites de contact unilatéral présentent des lacunes telles que: le rebond de contact numérique, la dissipation d'énergie ou la pénétration non physique de l'obstacle. Afin de réaliser l'analyse modale non-lisse, les mouvements périodiques des structures en contact unilatéral sans rebond de contact numérique ni pénétration de l'obstacle sont recherchés. À cette fin, la *méthode de la frontière nodale* est développée dans cette thèse. La méthode de la frontière nodale traite les conditions de Signorini en approximant les mouvements à l'aide de fonctions qui satisfont fortement les conditions de complémentarité de Signorini. Plus précisément, différentes fonctions de forme sont utilisées pour décrire la structure éloignée de l'obstacle (phase de contact inactif) et en contact avec l'obstacle (phase de contact actif). La méthode de commutation est ensuite utilisée pour déterminer la (les) phase(s) de contact à un instant donné du mouvement. La méthode de la frontière nodale génère des mouvements qui présentent des phases de contact continues (élimination du rebond de contact numérique), et des mouvements périodiques peuvent être trouvés. La méthode des limites nodales a été appliquée pour trouver des solutions périodiques de la barre et de la plaque en contact unilatéral. Plus précisément, cette thèse apporte de nouveaux résultats tels que l'analyse modale non-lisse de la barre à surface variable et de la plaque bidimensionnelle.

Claims of Originality

This thesis explores the nonsmooth modal analysis of deformable structures that are prone to unilateral contact with a rigid obstacle. Specifically, analytical nonsmooth modal analysis of the internally resonant bar is done together with numerical nonsmooth modal analysis of various models of the bar and the two-dimensional plate. In this context, the original contributions to knowledge of nonsmooth modal analysis are as follows:

1. Analytical modal analysis of the bar is done via application of the method of steps and switching on the d'Alembert solutions to the wave equation. Specifically, the cantilever bar prone to unilateral contact is studied. The cantilever bar is a one dimensional deformable structure of which internal motion is governed by the wave equation, Signorini complementarity conditions on the contacting end and homogeneous Dirichlet conditions on the non-contacting end. The motion of the bar away from contact can be described by the d'Alembert travelling wave function which is used in this thesis to constitute a solution to the bar prone to contact. A closed-form solution of the bar experiencing a single contact phase is obtained via the method of steps together with switching method.
2. The formulation of the cantilever bar's motion via d'Alembert functions and the method of switching are used to form the equations for determining nonsmooth modes of the bar. Solution of these equations then allows for defining novel nonsmooth modes of the bar. Specifically, new nonsmooth modes consisting of piecewise-smooth displacement field are discovered. The results presented in this context complement current knowledge of the nonsmooth modal space of the cantilever bar. Moreover, original conjectures on the nonsmooth modal space of the cantilever bar are presented in this thesis.
3. A novel numerical method, the nodal boundary method, is presented in this thesis for the nonsmooth modal analysis of structures under the framework of the finite element method. The nodal boundary method is based on the method of basis recombination and switching method to treat the unilateral conditions in a strong manner. The basis recombination method is used to define shape functions, based on the finite element Lagrangian shape functions, that answer the boundary conditions in free motion (inactive contact) and during contact (active contact) to form an approximation of the deformable structure's displacement field. The

switching method is then used to determine the shape functions and the contact phase (either active or inactive) in any given instant of the motion. The nodal boundary method applies to both the bar and the plate in unilateral contact and is compared to other methods in FEM for the treatment of Signorini complementarity conditions. Compared to other methods, the nodal boundary method allows for the existence of periodic solutions together with elimination of chattering and can be readily used for numerical modal analysis.

4. Nonsmooth modal analysis of the bar of varying area is performed in this thesis via the nodal boundary method and shooting method. These nonsmooth modes are detected for different models of the bar of varying area. The discovered nonsmooth modes fit closely to resonance peaks in the forced response diagrams. Furthermore, nonsmooth modal analysis using the nodal boundary method of the bar is performed for the internally resonant bar and bar with soft support for comparisons with existing literature.
5. Nonsmooth modal analysis of the plate is performed via the nodal boundary method and harmonic balance. New nonsmooth modes of the plate are presented including a dominantly longitudinal mode involving mainly collision in the normal direction to the obstacle and a transverse mode where the plate is vibrating mainly in the tangential direction to the rigid obstacle.

Nomenclature

Abbreviations

kCPP	k (number) Contact Phases per Period (ie, 1CPP)
kD	k (number) Dimensions
CN	Crank-Nicolson (time marching scheme)
CPS	Conditions for Periodic Solution (defined in Section 3.2.1)
DGM	Discontinuous Galerkin Method
FD-BEM	Frequency Domain Boundary Element Method
FE	Finite Element
FEM	Finite Element Method
FEP	Frequency Energy Plot
FVM	Finite Volume Method
HBM	Harmonic Balance Method
LCP	Linear Complementarity Problem
MRM	Mass Redistribution Method
NBM	Nodal Boundary Method
NNM	Nonlinear Normal Mode
NSM	Nonsmooth Mode
ODE	Ordinary Differential Equation
PDE	Partial Differential Equation
SCC	Sequential Continuation with Correction
TD-BEM	Time Domain Boundary Element Method
WFEM	Wave-Finite Element Method

Operators

∂_x	First partial derivative in x
∂_{xx}	Second partial derivative in x
$\dot{\circ}$	First definite derivative with respect to time
$\ddot{\circ}$	Second definite derivative with respect to time
$\circ'$	Definite derivative of mono-variable functions
∇	Del operator
$\circ^\top$	Transpose of a matrix
$\min(\circ, \circ)$	Minimum operator
$\max(\circ, \circ)$	Maximum operator
:	Frobenius inner product between two tensors

Symbols

$\mathbf{A}^*, \mathbf{d}^*$	Linear operator and non-homogeneous Dirichlet contribution for 2D-NBM approximation
$\mathbf{A}^N, \mathbf{A}^D, \mathbf{d}$	Linear operator for 1D-NBM approximation of inactive and active contact phases and non-homogeneous Dirichlet contribution
$A, A(x)$	Cross-sectional area
$E, E(t)$	Energy
e	Coefficient of restitution (Newton's impact law)
$f(s), f_0(s), f_p(s)$	D'Alembert function, initial guess in d'Alembert form, and final state in period in d'Alembert form
g_0	Initial gap distance
$\mathbf{H}$	Coefficients of harmonics in HBM
k	Spring constant
L	Length of bar
$\mathbf{M}_N, \mathbf{K}_N$	Mass and Stiffness matrices for active contact phase in 1D-NBM
$\mathbf{M}_D, \mathbf{K}_D, \mathbf{f}_D$	Mass, Stiffness and Force matrices for active contact phase in 1D-NBM
$\mathbf{M}^*, \mathbf{K}^*, \mathbf{f}^*$	Mass, Stiffness and Force matrices for 2D-NBM approximation
N	Number of discrete displacement variables
N_h	Number of harmonics in HBM
N_O	Number of internal nodes
N_C	Number of contact nodes
$\mathbf{P}(x), \mathbf{P}(\mathbf{x})$	Array of FE Lagrangian shape functions
$\mathbf{p}$	Contact configuration
$\mathbf{R}(\circ)$	Residual error function (in Chapter 3, denotes a linear operator)

$S(\circ)$	Switching Function (defined in Equation (4.33))
s	Parameter distinguishing periodic solutions (in Chapter 2), argument of d'Alembert function (in Chapter 3)
T	Period of motion
t	Time coordinate
t_s	Time of switch (NBM)
$\mathbf{u}(t)$	Displacement of nodal quantities
$\mathbf{u}^o(t)$	Displacement of internal nodes
$\mathbf{u}^c(t)$	Displacement of contact nodes
$u(x,t), \mathbf{u}(\mathbf{x},t)$	Displacement field, one- and multi- dimensional
$v(x,t), \mathbf{v}(\mathbf{x},t)$	Velocity field, one- and multi- dimensional
$\mathbf{v}(t)$	Velocity of nodal quantities, $\dot{\mathbf{u}}(t)$
$w, \mathbf{w}$	Weight/test function(s)
$x, \mathbf{x}$	Position coordinate(s)
Y	Young's Modulus
$\Gamma_\mathrm{D}, \Gamma_\mathrm{N}, \Gamma_\mathrm{R}, \Gamma_\mathrm{C}$	Dirichlet, Neumann, Robin and Unilateral contact boundaries
γ	Nitsche parameter
Δt	Constant step in variable t
δ_{ij}	Kronecker delta
$\epsilon(\circ), \boldsymbol{\epsilon}(\circ)$	Strain function (scalar, tensor)
$\boldsymbol{\Theta}$	Heaviside function
θ	Phase variable
ν	Poisson's Ratio
ξ	Damping coefficient
ρ	Density
$\sigma(\circ), \boldsymbol{\sigma}(\circ)$	Stress function (scalar, tensor)
σ_n	Magnitude of normal component of stress or contact pressure
$\boldsymbol{\sigma}_t$	Tangential component of boundary stress
τ	Duration of inactive contact
$\phi_i(x)$	FE Lagrangian shape functions
$\boldsymbol{\Omega}, \Gamma, \mathbf{n}$	Domain, domain boundary, and normal to domain boundary
ω	Radial Frequency
C^n	Space of continuous n differentiable functions
$\hat{C}^n$	Space of piecewise n differentiable functions
$\mathbb{Q}$	Space of rational numbers
$\mathbb{R}, \mathbb{R}^+$	Space of real and positive real numbers

$\mathcal{T}(\mathbf{p})$	Configuration phase of configuration $\mathbf{p}$

Contents

List of Figures

List of Tables

Chapter 1

Introduction

In the field of structural dynamics, modal analysis is a tool that allows to predict incidences of resonance in structures subject to oscillatory forces. Modal analysis techniques depend on the governing equations describing the structure. For example, eigen-decomposition or Fourier transform can be used for modal analysis in structures governed by linear differential equations. However, most of the mechanical systems in the field of engineering, particularly in structural dynamics, are governed by nonlinear laws and cannot be analyzed via linear modal analysis unless their governing equations are linearized. Although, linearization of nonlinear systems is often not preferred since it annihilates important phenomena existing strictly in nonlinear settings such as: subharmonics, hysteresis, and dependence of resonant frequencies on energy [29, 39, 45, 58, 61]. For nonlinear system, the notion of modes of vibration has been extended in the form of nonlinear normal modes (NNMs) [70, 75, 76]. These NNMs consist of families of periodic solutions to the autonomous system, and they were shown to correspond to occurrences of resonance [38, 39, 45, 84]. Similarly to eigen-modes in linear modal analysis, NNMs of a system exhibit similar behaviours to the forced and damped system during resonance and, more importantly, the energies and frequencies of nonlinear modes correspond closely to frequencies of and energies at resonance. Thus, nonlinear modal analysis entails the detection of NNMs and periodic solutions composing them.

In this thesis, the nonlinear modal analysis of deformable structures prone to unilateral contact is of interest. Modeling unilateral contact mathematically requires implementation of nonsmooth complementarity conditions on the displacement and stress at the contacting boundary of the structure [16, 46, 95, 96]. Thus, the nonlinearity exhibited by structures in unilateral contact is nonsmooth. In this manuscript, modal analysis on nonsmooth systems is referred to as nonsmooth modal analysis as opposed to conventional nonlinear modal analysis which prevalently deals with smooth nonlinearities [84]. Nonsmooth modal analysis is useful for systems where vibrations and contact mechanics are detrimental to structural health and performance. For example, vibrations prone to unilateral contact are common in drilling systems and different applications in mining

engineering [36, 62], or vibrating structures in loose supports [63, 94]. Another prominent example is the blades of jet engines which are prone to vibration and to contact with casing due to small clearances [9, 99].

Thus, the primary objective of this thesis is to accurately depict periodic solutions of systems prone to unilateral contact in order to detect nonsmooth modes (NSMs). The main challenge in determining periodic solutions to such systems lies in resolving the nonsmooth contact dynamics in an accurate manner. Specifically, solutions to governing equations involving unilateral contact require application of numerical schemes since closed-form solutions exist only for selected cases [46, 84, 97]. The solution of structural dynamics involving unilateral contact conditions presents two tasks: the solution of the PDEs governing the elastodynamics and the nonsmooth problem of contact involving the displacements and forces at the contact boundary. While methods for the solution of PDEs in elastodynamics are common, the solution to the nonsmooth contact conditions sets a significant academic challenge. To solve for the unilateral contact boundary condition, there exist various methodologies. However, most are not fitted for nonsmooth modal analysis and each methodology exhibits different drawbacks in determining accurate periodic solutions of the nonsmooth system. Main drawbacks of these methodologies include: energy dissipation annihilating periodic solutions, non-physical chattering, and non-physical penetration of obstacles [19, 24, 97]. These drawbacks are not attractive for nonsmooth modal analysis schemes since they do not allow detection of accurate periodic solution. Hence, the main subject of this thesis lies in constructing a numerical treatment for unilateral contact conditions that is suitable for nonsmooth modal analysis.

A novel numerical treatment of unilateral contact suitable for nonsmooth modal analysis is proposed in this thesis and is named the *nodal boundary method* (NBM). The NBM is developed under the framework of finite elements (FEs) and by adapting the method of basis recombination [14, 58] to the Signorini problem. Specifically, the nodal boundary method uses sets of basis functions that are tailored to answer the unilateral boundary conditions. The NBM has been conceived primarily to allow for determination of periodic solutions that do not exhibit non-physical chattering nor penetrability of the obstacle. In this thesis, it will be shown that the NBM allows for numerical nonsmooth nodal analysis of a variety of deformable structures prone to unilateral contact.

1.1 Scope of research

In this thesis, nonsmooth modal analysis will be performed on an elastic solid prone to frictionless contact with a rigid obstacle. The problem of frictionless contact between two solids is conventionally named the *Signorini problem* [96]. The investigated structures will be limited to one and two spatial dimensions. Nevertheless, the developed techniques for the nonsmooth modal analysis of the two-dimensional structure can be extended to three dimensional models (this will be discussed

further in this thesis). The Signorini problem does not include any nonlinearities in the internal displacements (only displacements on the contact boundary are governed by nonsmooth laws) and the deformable structure abides linear elasticity.

The objective of this manuscript is to perform nonsmooth modal analysis of one and two-dimensional deformable structures. To perform this task, multiple achievements and breakthroughs were obtained. These are described here to provide further context to the main objective of this thesis: nonsmooth modal analysis of multi-dimensional deformable structures.

Analytical (exact) nonsmooth modal analysis of the cantilever bar The motion of the cantilever bar enjoys closed-form solution in the form of d'Alembert function. In this thesis, the method of steps is applied on the d'Alembert functions to obtain periodic solutions to the Signorini problem. The solutions obtained here extend the known nonsmooth modal space of the bar beyond current literature. In turn, the nonsmooth modal space of the bar is revealed to exhibit interesting phenomena such as modal families of the same period and energy, and a highly dense modal space. These findings shed a new light on previous numerical findings and allow to foresee difficulties in numerical approaches to nonsmooth modal analysis. Specifically, the results of exact nonsmooth modal analysis of the bar influence the choice of numerical techniques used for nonsmooth modal analysis in this thesis.

Nodal Boundary Method The NBM is developed for finding periodic solutions of the Signorini problem. A complete derivation of the method will be presented together with accompanying theorems and convergence tests.

Nonsmooth Modal Analysis The NBM will be used to determine the non-smooth modes in various cases of the Signorini problem. Furthermore, vibration profiles and resonant behaviours of the structure will be presented and discussed. Specifically, novel results in this thesis include the nonsmooth modal analysis of the varying area bar and the two-dimensional plate.

1.2 Organization of thesis

The thesis is divided into six chapters, including the current introduction chapter. In Chapter 2, a literature review for existing methodologies and recent publications on the topic of the thesis will take place. For example, the mathematical models of linear elasticity and unilateral contact will be presented together with known methods for linear, nonlinear, and nonsmooth modal analysis. At last, several numerical schemes for solution of the Signorini problem are presented together with their limitations with respect to nonsmooth modal analysis.

Chapter 3 consists of exact nonsmooth modal analysis of the bar. Here, the d'Alembert method together with the method of steps were used to determine the conditions for periodic solutions consisting of one contact phase per period. These conditions were solved to obtain new NSMs of

the cantilever bar.

Chapter 4 consists of application of the NBM on the one-dimensional bar. The NBM is developed in the framework of continuous FE and consists of a novel treatment for the contact boundary conditions. In this chapter, the NBM will be applied on the one-dimensional Signorini problem - the bar in unilateral contact. The NBM is then used for nonsmooth modal analysis for the cantilever bar, bar with soft support and varying area bar (all prone to unilateral contact).

Chapter 5 details the extension of the NBM to multidimensional Signorini problems. Furthermore, nonsmooth modal analysis on the rectangular plate will be performed.

Chapter 6 includes then conclusions and discussions in regard to nonsmooth modal analysis via NBM. In this chapter, future avenues for future research are proposed as well.

Chapter 2

Literature Review

2.1 Nonlinear modal analysis

Nonlinear modal analysis is the extension of linear modal analysis to dynamical systems governed by nonlinear governing equations. Similarly to its linear counterpart, nonlinear modal analysis allows for the prediction of resonance behaviours and frequencies in dynamical systems. In this section, the preliminary definition of NNMs is first presented. This definition provides the context for nonlinear modal analysis via detection of periodic solutions. Next, numerical techniques for nonlinear modal analysis will be presented. At last, phenomena and behaviours specific to nonlinear dynamical systems will be discussed to emphasize the importance of nonlinear modal analysis.

It is important to note that nonlinear modal analysis and nonsmooth modal analysis are treated as different types of analysis in this thesis. The reason to this terminology involves mainly the extension of the numerical techniques used for nonlinear smooth systems to nonsmooth systems as it will be further elaborated in Section 2.2.

2.1.1 Nonlinear normal modes

For nonlinear dynamical systems, linear modal analysis techniques involving eigen-decomposition fail due to the lacking of the principle of superposition. Instead, in the domain of nonlinear modal analysis, NNMs are used. NNMs are constructs that allow identification of resonance behaviour and frequencies similar to linear modes. Building from properties of linear normal modes, Rosenberg defined NNMs as synchronized periodic motions of the system [70]. Later research by Shaw and Pierre have extended Rosenberg's definition to autonomous motion taking place on a two-dimensional invariant manifold in the system's phase space tangent to the space of linearized motions at the equilibrium point of the system [75, p. 3]. For autonomous motions, this two-dimensional manifold consists of periodic solutions that are coincident to the plane of motions

of the linearized system at its equilibrium point [39, 45, 75].

There exist analytical and numerical techniques to determine the NNMs. Analytical methods rely on finding expressions to describe the motion of a system that depend on a single degree of freedom [70, 75]. These analytical methods are generally applied to systems of low nonlinearity [70, 75]. On the other hand, a prominent approach to nonlinear modal analysis which has been widely used in recent years is to trace NNMs via detection of periodic solutions numerically [39, 45, 64, 84]. To describe this numerical approach for nonlinear modal analysis, a system consisting of two point masses of displacements $\mathbf{u}(t) : \mathbb{R} \to \mathbb{R}^2$ will be analyzed. The governing equations of the system consist of inertial and potential forces where the potential forces may consist of linear and nonlinear terms in the displacement only (where $\dot{\circ}$ and $\ddot{\circ}$ represent the derivative and double derivative of $\circ$ in time, respectively)

$$\mathbf{M}\ddot{\mathbf{u}}(t) + \mathbf{K}\mathbf{u}(t) + \mathbf{f}_{\text{nl}}(\mathbf{u}(t)) = \mathbf{0}, \tag{2.1}$$

where $\mathbf{M}$ and $\mathbf{K}$ are square 2×2 mass and stiffness matrices, respectively, and consist of constant entries. The vector function $\mathbf{f}_{\text{nl}}(\mathbf{u}(t)) : \mathbb{R} \to \mathbb{R}^2$ describes the nonlinear contributions of the potential forces. Specifically, the system is described by the following quantities

$$\mathbf{M} = \begin{bmatrix} 1 & 0 \\ 0 & 1 \end{bmatrix}, \quad \mathbf{K} = \begin{bmatrix} 2 & -1 \\ -1 & 1 \end{bmatrix}, \quad \mathbf{f}_{\text{nl}}(\mathbf{u}(t)) = \begin{pmatrix} 0.1(u_1 - u_2)^3 \\ 0.1(u_2 - u_1)^3 \end{pmatrix} \tag{2.2}$$

and is illustrated in Figure 2.1.

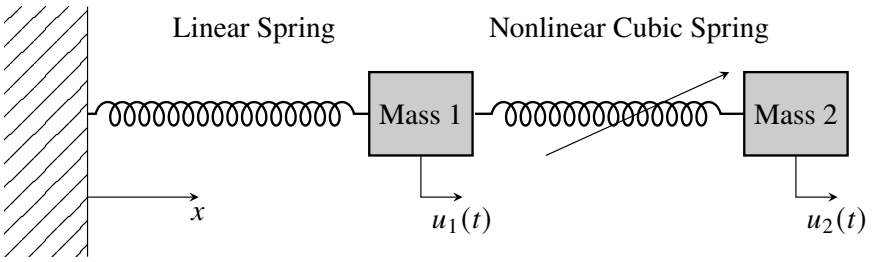

Figure 2.1: Nonlinear mass-spring system identified by Equations (2.1) and (2.2).

Finding periodic solutions to the nonlinear systems of ODEs (2.1) (and by extension, its NNMs) requires to solve for the initial conditions $\mathbf{u}^0$ and $\mathbf{v}^0$ and period T such that

$$\begin{aligned} \mathbf{u}(0) - \mathbf{u}(T) &= \mathbf{0}, \quad \mathbf{u}(0) = \mathbf{u}^0, \\ \dot{\mathbf{u}}(0) - \dot{\mathbf{u}}(T) &= \mathbf{0}, \quad \dot{\mathbf{u}}(0) = \mathbf{v}^0. \end{aligned} \tag{2.3}$$

Since closed-form solutions of Equation (2.1) to formulate the quantities $\mathbf{u}(T)$ and $\dot{\mathbf{u}}(T)$ are not easily found, numerical methods are used to approximate these quantities. In fact, the method for numerical nonlinear modal analysis presented in this chapter rely on numerical approximations to Equation (2.1) that satisfy the periodicity conditions (2.3).

The solution to Equations (2.1) and (2.3) consists of several two-dimensional manifolds. These two-dimensional manifolds constitute the nonlinear normal modes of the system [39, 75]. In what follows, a specific solution manifold of Equations (2.1) and (2.3) will be analyzed in order to illustrate different notions in nonlinear modal analysis.

A solution manifold of Equations (2.1) and (2.3) can be parametrized as follows: $\mathbf{u}^0(\theta, s)$, $\mathbf{v}^0(\theta, s)$, $T(\theta, s)$ where θ denotes the *phase* variable of a given periodic motion while s is a dummy parameter distinguishing periodic solutions in the phase space. A space of solutions to the ODE (2.1) (subject to Equation (2.2)) and periodicity equations (2.3) are presented in Figure 2.2.

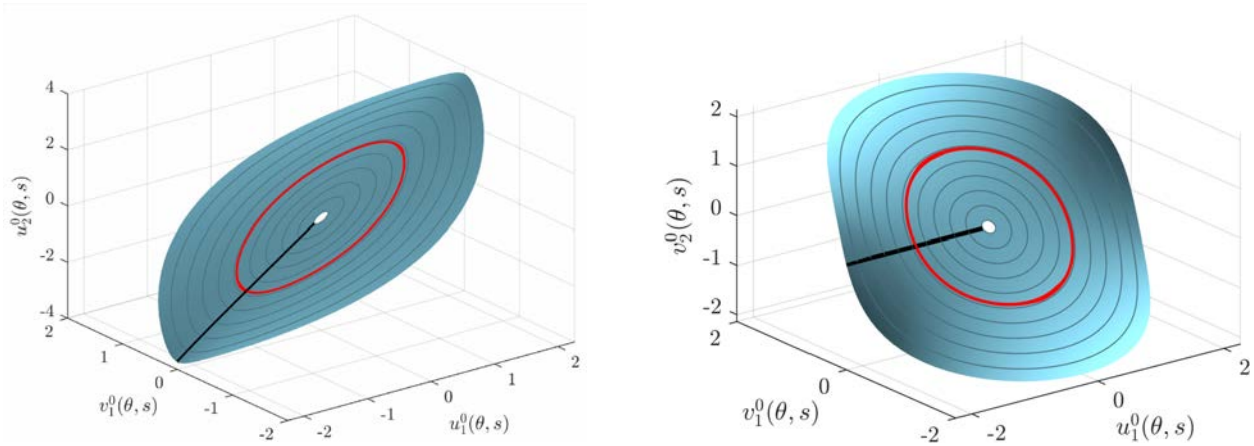

(a) Invariant manifold in u_1, v_1 and u_2

(b) Invariant manifold in u_1, v_1 and v_2

Figure 2.2: Portion of NNMs of the system identified by (2.1) and (2.2). The surfaces represent the space of solution to (2.3). The black curves represent solution curves for varying s and constant phase $\theta = 0$ ($\mathbf{u}^0(0, s)$ and $\mathbf{v}^0(0, s)$). The red curves represent solution curves for varying θ and constant dummy variable $s = s^0$ ($\mathbf{u}^0(\theta, s^0)$ and $\mathbf{v}^0(\theta, s^0)$). Every set of initial conditions on the black curve represents a distinct periodic solution, and initial conditions on the red curve depict different phases of the same periodic solution. In nonlinear modal analysis, it is of interest to detect *distinct* periodic solution within the two-dimensional manifold. This is equivalent to detecting the black curve in this figure.

In fact, Figure 2.2 shows a couple of three-dimensional perspectives of the two-dimensional manifold that constitutes the NNM. In this manifold, the phase variable $\theta \in [0, 2\pi]$ depicts different states of $\mathbf{u}(t)$ and $\mathbf{v}(t)$ within a period ($t \in [0, T]$) of the periodic solution. Otherwise put, fixing the parameter s to some constant s^0 (this corresponds to the red curve in Figure 2.2), $\mathbf{u}^0(\theta, s^0)$ depicts different phases of $\mathbf{u}(t = \theta T/2\pi)$ given a specific initial condition $\mathbf{u}^0(0, s^0)$ and $\mathbf{v}^0(0, s^0)$. In contrast, varying the variable s while fixing θ corresponds to depiction of a given phase of different periodic solutions of the NNM (this corresponds to the black curve in Figure 2.2). To determine a NNM, it is of interest to determine distinct periodic solutions in the phase-space. Therefore, the phase θ is often fixed in numerical nonlinear modal analysis and the resulting curve of initial conditions is of interest. In practice, detection of a curve consisting of initial conditions in the same phase is accomplished by imposing a phase condition on the system of equations (2.3) [13, p. 156].

The phase condition is a set of equations $\mathbf{F}(\mathbf{u}(t), \mathbf{v}(t)) = \mathbf{0}$ of which root depicts a single phase in any periodic solution. A common phase condition requires that all initial velocities are set to zero [6, 29, 64]

$$\dot{\mathbf{u}}(0) = 0. \tag{2.4}$$

Since this phase condition is widely used [29, 39, 64] for numerical nonlinear modal analysis, it is found suitable for numerical modal analysis in this manuscript. A different phase condition is used in the analytical modal analysis portion of this work in Chapter 3. There, the phase condition restricts the initial state of a motion to occur at the transition from active to inactive contact phase of motion (see Section 3.1.1). Other examples of phase conditions include: setting one of the motion's Fourier coefficients to zero [65, p. 797], or orthogonality of the motion with a known periodic motion using a Poincaré orthogonality condition [13, p. 156]. Nevertheless, the phase condition (2.4) is proven successful for the detection of periodic solutions in this thesis (as evident in Chapters 4 and 5). It is important to note that the phase condition depicts only a certain state of the motion. Therefore, it is possible that the chosen phase condition may lead to ignorance of other solutions. Although, the manuscript is focused on techniques for nonsmooth modal analysis whereas the all presented methodologies can accommodate other phase conditions. The numerical methods presented involve two types of algorithms necessary for the detection of NNMs: approximation of the nonlinear Equations (2.1), (2.3) and (2.4) (discussed in Section 2.1.2), and continuation of the space of solutions (discussed in Section 2.1.3).

2.1.2 Approximation of periodic solutions to nonlinear ODEs

In this section, two methods to approximate the solution to the Equations (2.1), (2.3) and (2.4) will be presented: the harmonic balance method and the shooting method.

Harmonic balance method

The harmonic balance method (HBM) assumes the approximation of the motion as a series of periodic sine and cosine functions [37, 39, 41, 93]. Since solutions with zero initial-velocity (see phase condition in Equation (2.4)) are targeted, it is sufficient to approximate the motion as a series of N_h cosine functions

$$u_i(t) \approx \sum_{j=1}^{N_h} \mathrm{H}_{ij} \cos((j-1)\omega t) \equiv u_i^{N_h}(\mathbf{H}, \omega, t), \quad i = 1, \ldots, N \tag{2.5}$$

where the unknown frequency is denoted $\omega \in \mathbb{R}$, the unknown harmonic coefficients are gathered in $\mathbf{H} \in \mathbb{R}^{N \times N_h}$, and $\mathbf{u}^{N_h}(\mathbf{H}, \omega, t)$ denotes the HBM approximation of $\mathbf{u}(t)$. Furthermore, it is noted that the periodicity conditions (2.3) are satisfied for any choice of ω, $\mathbf{H}$ and $N_h > 0$ since the motion

is always periodic with $T = 2\pi/\omega$. In the HBM, the approximation (2.5) is then plugged into the ODE (2.1) to form a residual

$$\mathbf{R}(\mathbf{H}, \omega, t) = \mathbf{M}\ddot{\mathbf{u}}^{N_h}(\mathbf{H}, \omega, t) + \mathbf{K}\mathbf{u}^{N_h}(\mathbf{H}, \omega, t) + \mathbf{f}_{\text{nl}}\left(\mathbf{u}^{N_h}(\mathbf{H}, \omega, t)\right). \tag{2.6}$$

To determine the appropriate ω and $\mathbf{H}$ for the solution to the ODE, the Galerkin method is used [68]. By the Galerkin method, the appropriate ω and $\mathbf{H}$ are chosen such that the residual (2.6) is orthogonal to the series of cosine functions used in the approximation. Otherwise put, the appropriate ω and $\mathbf{H}$ are found by solving the system of equations

$$F_i(\mathbf{H}, \omega) = \int_0^{2\pi/\omega} \cos((i-1)\omega t)\mathbf{R}(\mathbf{H}, \omega, t)\mathrm{d}t = \mathbf{0}, \quad i = 1, \ldots, N_h. \tag{2.7}$$

System (2.7) is ill-defined with $N \times N_h$ equations and $N \times N_h + 1$ variables. The solution set is a curve ($\mathbf{H}(s)$ and $\omega(s)$) similar to the expectations from nonlinear modal analysis. In the Galerkin method, convergence to the true solution (and true modal space) of the ODE (2.1) is expected as $N_h \to \infty$ [41, 68, 93].

Shooting method

The shooting method [7, 69] assumes that the states $\mathbf{u}(T)$ and $\dot{\mathbf{u}}(T)$, solutions to the ODE (2.1), can be approximated as a function of the period and initial conditions

$$\mathbf{u}(T) \approx \mathbf{U}(\mathbf{u}^0, \mathbf{v}^0, T), \qquad \dot{\mathbf{u}}(T) \approx \mathbf{V}(\mathbf{u}^0, \mathbf{v}^0, T) \tag{2.8}$$

where $\mathbf{U}$ and $\mathbf{V}$ represent the approximation resulting from a numerical solver. For example, $\mathbf{U}$ and $\mathbf{V}$ may stand for the result after a finite number of iterations in a given time-marching technique [7, 69, 78]. Then, plugging the approximation (2.8) into the periodicity conditions (2.3) admits

$$\mathbf{u}^0 - \mathbf{U}(\mathbf{u}^0, \mathbf{v}^0, T) = \mathbf{0} \tag{2.9}$$

$$\mathbf{v}^0 - \mathbf{V}(\mathbf{u}^0, \mathbf{v}^0, T) = \mathbf{0}. \tag{2.10}$$

Next, the phase condition (2.4) implies $\mathbf{v}^0 = \mathbf{0}$ and is added to Equation (2.10) to admit the numerical nonlinear modal analysis problem

$$\mathbf{F}(\mathbf{u}^0, T) = \begin{pmatrix} \mathbf{u}^0 - \mathbf{U}(\mathbf{u}^0, \mathbf{0}, T) \\ \mathbf{V}(\mathbf{u}^0, \mathbf{0}, T) \end{pmatrix} = \mathbf{0} \tag{2.11}$$

consisting of $N + 1$ variables and $2 \times N$ equations. In practice, N is greater than 1 which renders the system of equations over-determined. Nevertheless, since NNMs are expected, the solution to the system of equations (2.11) is expected to be a curve $(\mathbf{u}^0(s), T(s))$ [13, 64].

Lastly, the accuracy of the shooting method depends on the accuracy of $\mathbf{U}(\mathbf{u}^0, \mathbf{0}, T)$ and

$\mathbf{V}(\mathbf{u}^0, \mathbf{0}, T)$ in approximating the ODE (2.1). Specifically, the accuracy of the shooting method depends on the size of the time-step used in generating $\mathbf{U}(\mathbf{u}^0, \mathbf{0}, T)$ and $\mathbf{V}(\mathbf{u}^0, \mathbf{0}, T)$ [78].

2.1.3 Continuation methods

Both the HBM and shooting methods result in a system of equations of the type $\mathbf{F}(\mathbf{q}, T) = \mathbf{0}$ where $\mathbf{q}$ denotes all variables describing the state's configuration and is introduced to simplify the notation. For example, in the HBM (see Equation (2.7)), $\mathbf{q}$ denotes the harmonic coefficients $\mathbf{H}$, and T is related to ω as follows: $T = 2\pi/\omega$. In the shooting method (see Equation (2.11)), $\mathbf{q}$ denotes the set of initial conditions $\mathbf{u}^o$. In turn, the solution to $\mathbf{F}(\mathbf{q}, T) = \mathbf{0}$ is expected to constitute a hyper-curve $\mathbf{q}(s)$ and $T(s)$ depicting different periodic solutions of the expected NNM.

To determine the curve $\mathbf{F}(\mathbf{q}(s), T(s)) = \mathbf{0}$, continuation methods are used. Continuation methods determine the solution curve $(\mathbf{q}(s), T(s))$ by finding distinct solutions of the curve $\mathbf{F}(\mathbf{q}^i, T^i) = \mathbf{0}$ where the superscript i enumerates the solutions detected in the NNM. To do so, continuation methods often require an initial guess close to the curve, e.g. a known solution $(\mathbf{q}^0, T^0)$. Then, it is assumed that the solution curve is continuous and that the next solution on curve $(\mathbf{q}^1, T^1)$ is found in some proximity to the point $(\mathbf{q}^0, T^0)$. It is used iteratively to find the remainder of the $(\mathbf{q}^i, T^i)$ solutions in the NNM.

For nonlinear modal analysis, a sufficient initial guess is generally taken to be the linearized periodic motion at low energies. The continuation method determines a sequence of distinct solutions along this curve which, in turn, represent the NNM. Mathematically, the continuation methods consist of complementing the system of equations $\mathbf{F}(\mathbf{q}, T) = \mathbf{0}$ with an additional *continuation* equation $\mathrm{F}^*(\mathbf{q}, T, \mathbf{q}^0, T^0) = 0$. The continuation equation is expected to restrict the space of solutions of $F(\mathbf{q}, T)$ from a curve $(\mathbf{q}(s), T(s))$ to a unique point: $(\mathbf{q}^1, T^1)$.

Sequential continuation

Given a solution $(\mathbf{q}^0, T^0)$, sequential continuation assumes that the next solution $(\mathbf{q}^1, T^1)$ is found by tuning of a single variable [13, 64]. For our purposes, it is commonly assumed that there exist a solution of a distinct period $T^1 = \Delta T + T^0$ such that the continuation equation reads

$$\mathrm{F}^*(T, T^0) = T - \Delta T - T^0 = 0 \tag{2.12}$$

where ΔT is controlled by the user. The main weakness of sequential continuation is its ability to detect solution curves parametrized in T explicitly, i.e., $\mathbf{q}(T)$ is described via an explicit function in T. However, as will be seen later in this section, this assumption does not hold when $(\mathbf{q}(s), T(s))$ consists of an implicit curve. For such curves, the pseudo-arclength continuation is commonly used.

Pseudo-arclength continuation

Pseudo-arclength continuation [4] assumes that the curve is at least once-differentiable (C^1) such and that a tangent to the curve at the initial point, denoted[1] $\begin{pmatrix}\dot{\mathbf{q}}^0 & \dot{T}^0\end{pmatrix}$, is known [4, p. 9]. In practice, the tangent to the curve can be estimated using educated guesses. In pseudo-arclength continuation, the next solution to the curve is found along the perpendicular to the tangent at some fixed distance Δs, as shown in Figure 2.3. This is accomplished through the equation

$$\mathrm{F}^*(\mathbf{q}, T, \mathbf{q}^0, T^0) = (\dot{\mathbf{q}}^0)^\top(\mathbf{q} - \mathbf{q}^0) + \dot{T}^0(T - T^0) + \Delta s = 0. \tag{2.13}$$

Then, $(\mathbf{q}^1, T^1)$ constitutes the solution to $\mathbf{F}(\mathbf{q}, T)$ and Equation (2.13). Once $(\mathbf{q}^1, T^1)$ is found, the new tangent $(\dot{\mathbf{q}}^1, \dot{T}^1)$ is determined by solving for the tangent to all hyper-surfaces $\mathbf{F}(\mathbf{q}, T)$ and $\mathrm{F}^*(\mathbf{q}, T, \mathbf{q}^0, T^0)$ at the point $(\mathbf{q}^1, T^1)$ [4, 93] ($\partial_\circ$ denotes the partial derivative with respect to $\circ$)

$$\begin{bmatrix}\partial_{\mathbf{q}}\mathbf{F}(\mathbf{q}^1, T^1) & \partial_T\mathbf{F}(\mathbf{q}^1, T^1) \\ (\dot{\mathbf{q}}^0)^\top & \dot{T}^0\end{bmatrix}\begin{pmatrix}\dot{\mathbf{q}}^1 \\ \dot{\mathbf{T}}^1\end{pmatrix} = \begin{pmatrix}\mathbf{0} \\ 1\end{pmatrix}. \tag{2.14}$$

Indeed, pseudo-arclength continuation assumes the parametrization of the curve using the arclength s which participates implicitly in the formulation, and the quantity Δs in Equation (2.13) controls the step-size along the arclength of the curve. It is important to note that the pseudo-arclength continuation is considered practical in continuing at turning points [4, 39, 72, 93]. Accordingly, the pseudo-arclength continuation is successful in tracing implicit solution curves, see Figure 2.3.

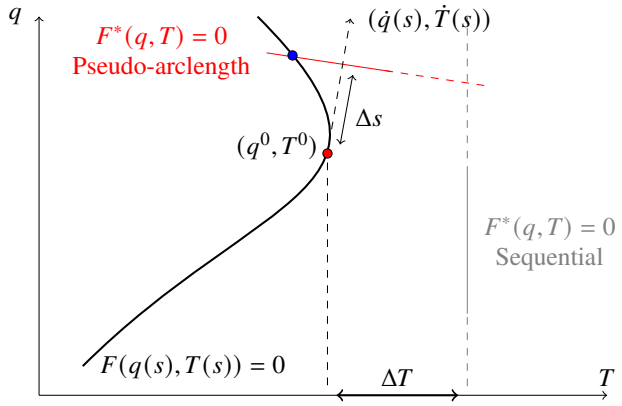

Figure 2.3: Comparison of sequential and pseudo-arclength continuations. The line traced by pseudo-arclength equation crosses the curve at the blue point while the line traced by the sequential continuation equation does not. The pseudo-arclength continuation equation depends on the tangent to the curve and allows for the continuation of implicit curves. In contrast, sequential continuation assumes a fixed direction for the curve and therefore fails at turning points.

In nonlinear modal analysis, the solution curves are often expected to constitute implicit curves

[1] While the dot notation $\dot{\circ}$ is reserved for differentiation in time, it is also used to denote a tangent to a curve for consistency with the notation presented in [13, 93]

and the pseudo-arclength method is commonly used for the detection of NNMs. This is discussed in depth in Section 2.1.5.

2.1.4 Root solvers

Application of nonlinear modal analysis, in this manuscript, reduces to solving a system of equations iteratively to determine periodic solutions to nonlinear ODEs. Specifically, detection of either nonlinear or nonsmooth modes requires solving

$$\begin{pmatrix} \mathbf{F}(\mathbf{q}, T) \\ \mathrm{F}^*(\mathbf{q}, T, \mathbf{q}^i, T^i) \end{pmatrix} = \mathbf{0} \tag{2.15}$$

where $\mathbf{F}(\mathbf{q}, T)$ represents the numerical scheme for obtaining a periodic solution, and $\mathrm{F}^*(\mathbf{q}, T, \mathbf{q}^i, T^i)$ represents the continuation equation at step i. At each step i, it is assumed that the system of equations (2.15) exhibits a unique solution [39, 64, 93]. To solve for the system of equations numerically, MATLAB's `fsolve` is used [55]. The `fsolve` algorithm consists of multiple gradient-based root solvers. In this manuscript, two numerical schemes are used depending on whether the system of equations is well-determined, such as the HBM equations, or over-determined such as the shooting equations: (1) for the solution of well-determined systems of equations, `fsolve` uses a trust-region-dogleg gradient-based optimization [66] (2) for over-determined systems of equations, `fsolve` uses the Levenberg-Marquardt scheme which solves via the set of equations as a nonlinear least squares problem [59]. The Jacobian for both methods can be either supplied by the user or calculated by MATLAB via finite differences [55].

The Jacobian matrix can be derived via analytical procedures or other numerical methods by finding the derivatives belonging to the equations approximating the ODE, $\partial_{\mathbf{q}}\mathbf{F}(\mathbf{q}, T)$ and $\partial_T\mathbf{F}(\mathbf{q}, T)$, and the continuation equation $\partial_{\mathbf{q}}\mathrm{F}^*(\mathbf{q}, T, \mathbf{q}^0, T^0)$ and $\partial_T\mathrm{F}^*(\mathbf{q}, T, \mathbf{q}^0, T^0)$. While some of these derivatives can be trivially found, some require additional work. For example, in the shooting method, the value of $\partial_{\mathbf{q}}\mathbf{F}(\mathbf{q}, T)$ is obtained via a time-marching approximation [64]. Meanwhile, calculation of $\partial_{\mathbf{q}}\mathbf{F}(\mathbf{q}, T)$ in the HBM requires knowledge of $\partial_{\mathbf{u}(t)}\mathbf{f}_{\mathrm{nl}}(\mathbf{u}(t))$, as can be seen from Equations (2.6) and (2.7). Along the same line, definition of the Jacobian to either sequential or pseudo-arclength continuation F^* is a trivial task. For the sake of conciseness, no further explanation on the derivation of these Jacobians will be given in this manuscript.

2.1.5 Characteristics of nonlinear modal space

In this section, the nonlinear mass-spring system identified by (2.2) is used to demonstrate particular properties of NNMs with respect to linear modes. The results and figures shown in this section were obtained via the shooting method and pseudo-arclength continuation.

Figure 2.4 shows the linear and NNMs on an energy-frequency plot (FEP). In the FEP, the nonlinear (or linear) normal mode is represented as a continuum of frequencies and energies. These frequencies and energies are those exhibited by the periodic motions composing the NNM. Each point in this plot represents a periodic solution of specific mechanical energy (sum of potential and kinetic energies) and period of motion. Moreover, Figure 2.4 allows comparison between linear and NNMs. While linear modes of vibration exhibit the same frequency for any energy level, the nonlinear modes of vibration exhibit a dependency between energy of oscillation and frequency of oscillation. Indeed, this characteristic is specific to nonlinear systems and does not exist in linear systems. Another difference between nonlinear and linear normal modes is the existence of internal resonance. Internal resonance occurs in the proximity of ω_1 and can be seen in a form of "tongue" in Figure 2.4. The internal resonance in a nonlinear systems can be described as the coincidence of different NNMs. In Figure 2.4, the first mode of the nonlinear system (denoted backbone ω_1) coincides with the third subharmonic of the second mode of the system (starting from $\omega_2/3$). To clarify, the two modes share an identical periodic motion that can be seen as both belonging to the first nonlinear mode and to the third subharmonic of the second nonlinear mode. In contrast, linear modes do not generally interact with one another and therefore internal resonances occur for nonlinear systems exclusively. Numerically, internal resonances can be discovered via the pseudo-arclength method which is, therefore, the more commonly used continuation method for nonlinear modal analysis [39, 64, 72, 93].

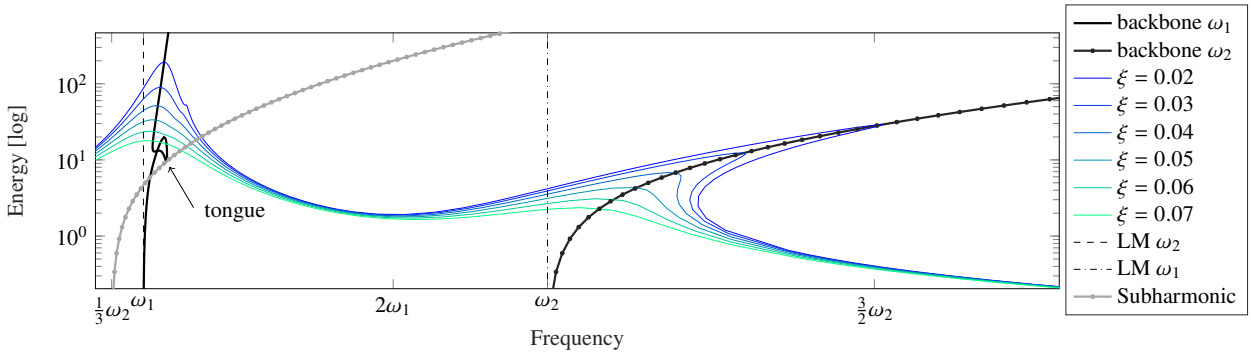

Figure 2.4: Backbone, and forced-response, and subharmonic curves of the system investigated in Figure 2.1. Forced response curves are formed by performing shooting and continuation to find periodic solutions of the system in expression (2.16). LM stands for linear modes of vibration and and the values $\omega_1 \approx 0.618$ and $\omega_2 \approx 1.618$ where obtained from linear modal analysis of the linearized investigated system.

To demonstrate the relationship between the nonlinear modes and the forced response behaviour, the forced response curves are sought. The forced response curves consist of periodic solutions of

the forced and damped ODE corresponding to the investigated system identified by (2.2)

$$\begin{aligned} \ddot{u}_1(t) + \xi(C_{11}\dot{u}_1(t) + C_{12}\dot{u}_2(t)) + 2u_1(t) - u_2(t) + 0.1(u_1(t) - u_2(t))^3 = 0 \\ \ddot{u}_2(t) + \xi(C_{12}\dot{u}_1(t) + C_{22}\dot{u}_2(t)) + \dot{u}_2(t) - u_1(t) + 0.1(u_2(t) - u_1(t))^3 = 2\cos(\omega t) \end{aligned} \tag{2.16}$$

where ξ denotes the damping coefficient and ω the forcing frequency. Furthermore, the values $C_{11} = 6.75$, $C_{12} = -1.80$ and $C_{22} = 4.95$ were implemented in the explored results (these values were chosen from aesthetic considerations only). The results for varying values of ξ are presented in Figure 2.4 in comparison to the backbone curves. In Figure 2.4, it can be seen that the curves corresponding to normal modes lay directly at resonance peaks of the forced-response diagram, similarly to linear modes of vibration. As such, the curves describing NNMs are often referred to as *backbone* curves, and they entail the importance of nonlinear modal analysis. It is important to note that the backbone curves were shown to intersect resonance points both analytically and numerically for a large group of nonlinear systems [39, 45, 64, 70, 75, 93]. Moreover, the internal resonances also affect the shape of resonance curves as seen in the formation of a second peak in the proximity of $\xi = 0.02$ in the proximity of ω_1. It is important to note that intricate behaviours of NNMs such as energy-frequency dependence and internal resonances are detrimental in vibration analysis of nonlinear systems as the latter might feature vibratory resonances far from the natural frequencies of the linearized system, and those vibratory resonances cannot be detected via linear modal analysis [64, 75, 93].

2.2 Nonsmooth modal analysis

In this manuscript, the term nonsmooth modal analysis will be used to distinguish between the modal analysis of smooth nonlinear systems and this of nonsmooth systems, such as those described by the Signorini problem. It is noted the numerical methods investigated in Sections 2.1.2 and 2.1.3 for nonlinear modal analysis rely on the continuity and smoothness of the solutions to ODEs. Meanwhile, nonsmooth modal analysis presents an academic challenge since methods for nonlinear modal analysis do not readily apply for the detection of nonsmooth solutions. For example, the model of mass-spring systems in unilateral contact treated via a fully elastic Newton impact law requires multiple shooting for the detection of NSMs [83, 84]. Furthermore, the HBM method cannot be applied in schemes involving Newton's impact law due to the existence of impulse forces [84]. However, the HBM can be used in other numerical treatments of the contact boundary conditions [41, 74]. Although, the HBM assumes a smooth transient behaviour, contrary to the actual nonsmooth motion, and is therefore often accompanied by the Gibbs phenomenon [41, 51, 74]. The detection of nonsmooth solutions is not the only challenge in nonsmooth modal analysis, but the continuation of NSMs as well. For example, [5, 35, 84] depict NSMs that exist as piecewise-smooth

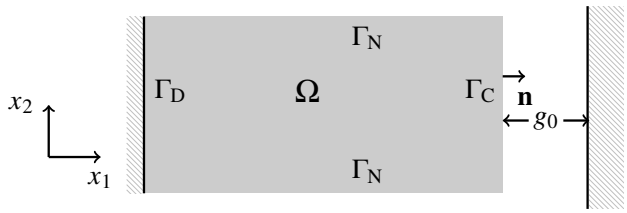

Figure 2.5: Plate prone to unilateral contact with a rigid obstacle. This is the two-dimensional structure explored in this thesis. The structure is always prone to unilateral contact with a rigid foundation situated a distance g_0 from the non-deformed boundary.

continuous curves on the FEP. Thus, methods which rely on the differentiability of the solution curve, such as pseudo-arclength continuation, do not apply straightforwardly to nonsmooth systems. On another note, in the case of mass spring systems involving an inelastic impact law, periodic solutions were found to be isolated rather than to exist on continua [82]. Nevertheless, several research works showed that the nonsmooth modal space coincides with resonance peaks in the forced response diagram, similarly to modes in nonlinear smooth modes [84, 97]. Still, there exist successful techniques for nonsmooth modal analysis. For example, in [97, 98], a brute-force approach was taken to solve the shooting equations in order to detect periodic solutions, without the use of continuation techniques. In [84], the shooting equations for the periodic solutions of discrete mass-spring systems with elastic Newton's impact law were solved by applying pseudo-arclength continuation on smooth sections of the backbone curve. A similar detection of smooth continuous sections of the NSMs is found in [35]. Furthermore, sequential continuation was proven successful for the continuation of nonsmooth system in [51].

Thus, a significant portion of this thesis deals in adapting nonlinear modal analysis techniques (Section 2.1) to nonsmooth modal analysis.

2.3 Model description

For nonsmooth modal analysis of the Signorini problem, both one- and two-dimensional ($d = 1, 2$) structures will be considered. The domain $\Omega \in \mathbb{R}^d$ describes the spatial configuration of the deformable structure. The position coordinates within the structure are denoted $\mathbf{x} \in \Omega$, and $t \in \mathbb{R}^+$ is used to denote time. A displacement field denoted $\mathbf{u}(\mathbf{x}, t) : \Omega \times \mathbb{R}^+ \to \mathbb{R}^d$ characterizes the deformations within the structure. The structures in this thesis are made of isotropic materials and the two-dimensional structure consists of a thin-plate such that a plane-stress formulation can be considered. An example of the plate in unilateral contact is presented in Figure 2.5.

In this manuscript, the rigid obstacle is described by a constant plane in x_1 set at a distance g_0 from the structure initially. Curved obstacles in the Cartesian space (i.e., a gap g_0 variable in space) are not explored in this thesis since it requires the implementation of contact detection

algorithms [95, 96]. Indeed, these are beyond the scope of this research since the problem of non-smooth modal analysis is proven to be of sufficient academic challenge.

The boundary Γ of the structure is subject to four kinds of boundary conditions. In what follows, the vector quantity $\mathbf{n}$ denotes the unit outward normal to the boundary Γ. The boundary conditions considered in this thesis are as follows:

Dirichlet (essential) boundary conditions on $\Gamma_\mathbf{D}$ The displacement along this boundary is prescribed.

Neumann (natural) boundary conditions on $\Gamma_\mathbf{N}$ The stresses normal to this boundary $\boldsymbol{\sigma}(\mathbf{u}(\mathbf{x}, t))\mathbf{n}$ are prescribed.

Robin boundary conditions on $\Gamma_\mathbf{R}$ in elastodynamics, the Robin conditions enforce a relationship between the stress and displacement at the boundary and can be illustrated as a spring foundation or soft support at the boundary.

Unilateral contact boundary conditions on $\Gamma_\mathbf{C}$ These boundary conditions describe the unilateral contact conditions and will be explained in Section 2.3.2.

Accordingly, these boundary conditions must define the whole boundary such that $\Gamma = \Gamma_\mathrm{D} \cup \Gamma_\mathrm{N} \cup \Gamma_\mathrm{R} \cup \Gamma_\mathrm{C}$ and the intersection between all types of boundaries is empty. In the next sections, the set of governing equations is developed considering a linear elasticity approximation of the strains and Signorini conditions for the unilateral boundary conditions.

2.3.1 Linear elasticity

The motion of the deformable structures is described via the theory of linear elasticity. Although this theory is limited for small amplitude deformations, it is found sufficient to describe the mechanics and dynamics of a large variety of mechanical systems involving unilateral contact [19,24,65,84,95,96,98]. To conform with this limitation on small amplitudes, relatively small gaps between the structure and the rigid obstacle are considered in this study.

In this thesis, either the one- or two-dimensional formulations of linear elasticity are considered. Primarily, the equations governing the dynamics of the structure are the stress equilibrium equations

$$\rho \partial_{tt} \mathbf{u}(\mathbf{x}, t) - \nabla \cdot \boldsymbol{\sigma}(\mathbf{u}(\mathbf{x}, t)) = \mathbf{0} \tag{2.17}$$

where ρ stands for density, ∇ denotes the gradient operator in the spatial coordinates $\mathbf{x}$. Next, the stress within the deformable solid is denoted $\boldsymbol{\sigma}(\mathbf{u}(\mathbf{x}, t))$. At last, ∂_{tt} denotes partial differentiation twice in time. In this manuscript, the symbol ∂_t corresponds to partial differentiation in Leibniz notation: $\partial/\partial t$.

The definition of the stress function changes according to the number of dimensions and model of linear elasticity used. For the one-dimensional case $d = 1$, the displacement field is a scalar

function the stress in the bar reads

$$\sigma(u(x,t)) = YA(x)\partial_x u(x,t) \tag{2.18}$$

where Y denotes Young's modulus, and $A(x) > 0$ denotes the cross-sectional area of the bar.

For the two-dimensional case $d = 2$, the plane-stress formulation in linear elasticity are used to define the internal stress and strains. Small deformations ($||\nabla \mathbf{u}(\mathbf{x},t)||_2 \ll 1$) are assumed and, in turn, the strain tensor for such displacement is represented as a linear operation on $\mathbf{u}$, that is

$$\boldsymbol{\epsilon}(\mathbf{u}(\mathbf{x},t)) = \frac{1}{2}(\nabla \mathbf{u}(\mathbf{x},t)^\top + \nabla \mathbf{u}(\mathbf{x},t)). \tag{2.19}$$

To simplify the formulation of the problem, isotropic materials are considered. Next, for the two-dimensional case, the stress-strain relationship is presented via Voigt notation [34]. Specifically, the plate-stress assumption of the stress-strain relationship

$$\begin{pmatrix} \sigma_{11}(\mathbf{u}(\mathbf{x},t)) \\ \sigma_{22}(\mathbf{u}(\mathbf{x},t)) \\ \sigma_{12}(\mathbf{u}(\mathbf{x},t)) \end{pmatrix} = \frac{Y}{1-\nu^2} \begin{bmatrix} 1 & \nu & 0 \\ \nu & 1 & 0 \\ 0 & 0 & \frac{1-\nu}{2} \end{bmatrix} \begin{pmatrix} \epsilon_{11}(\mathbf{u}(\mathbf{x},t)) \\ \epsilon_{22}(\mathbf{u}(\mathbf{x},t)) \\ \epsilon_{12}(\mathbf{u}(\mathbf{x},t)) \end{pmatrix}. \tag{2.20}$$

is used, where $\sigma_{12}(\mathbf{u}(\mathbf{x},t)) = \sigma_{21}(\mathbf{u}(\mathbf{x},t))$ and $\epsilon_{12}(\mathbf{u}(\mathbf{x},t)) = \epsilon_{21}(\mathbf{u}(\mathbf{x},t))$; ν denotes Poisson's ratio.

2.3.2 Unilateral contact

The problem of frictionless unilateral contact is treated using the Signorini conditions [96]. For the remainder of this section, the Signorini conditions are presented under the framework of multidimensional deformable mechanics except at points where the one-dimensional formulation is significantly different.

To describe unilateral contact, a gap function $g(\mathbf{x},t)$ is introduced to describe the distance of the deformable structure from the obstacle

$$g(\mathbf{x},t) = g_0 - \mathbf{u}(\mathbf{x},t)\cdot\mathbf{n} \qquad \forall \mathbf{x} \in \Gamma_C \tag{2.21}$$

where g_0 represents the distance between the rigid obstacle when the deformable structure is not deformed. Next, the contact pressure σ_n quantifies the repulsion the deformable structure experiences at contact with the rigid obstacle. Mathematically, $\sigma_n(\mathbf{u}(\mathbf{x},t))$ is defined as the magnitude of the normal component to the boundary stress $\boldsymbol{\sigma}(\mathbf{u}(\mathbf{x},t))\mathbf{n}$

$$\boldsymbol{\sigma}(\mathbf{u}(\mathbf{x},t))\mathbf{n} = \sigma_n(\mathbf{u}(\mathbf{x},t))\mathbf{n} + \boldsymbol{\sigma}_t, \quad \sigma_n(\mathbf{x},t) = \mathbf{n}^\top \boldsymbol{\sigma}(\mathbf{u}(\mathbf{x},t))\mathbf{n} \qquad \forall \mathbf{x} \in \Gamma \tag{2.22}$$

where $\boldsymbol{\sigma}_t$ denotes the tangential component of the boundary stress. For frictionless unilateral contact, the tangential component must vanish at all times $\boldsymbol{\sigma}_t = \mathbf{0}$. The one-dimensional contact pressure is

defined as

$$\sigma_n(u(x,t)) = nYA(x)\partial_x u(x,t), \qquad x \in \Gamma_C \tag{2.23}$$

where scalar $n = 1, -1$ represents the direction of the outward pointing normal along x. Using the gap function and the contact pressure, the Signorini conditions are presented as a set of complementarity conditions

$$0 \leq g(\mathbf{x},t) \perp \sigma_n(\mathbf{u}(\mathbf{x},t)) \leq 0, \quad \boldsymbol{\sigma}_t = \mathbf{0} \qquad \forall \mathbf{x} \in \Gamma_C. \tag{2.24}$$

The Signorini conditions (2.24) assume the existence of two phases of motion for each stencil $\mathbf{x}$ on the boundary Γ_C (also illustrated in Figure 2.6)

Inactive contact phase the structure is allowed to move freely as long as there is no contact with the rigid obstacle. At this phase, homogeneous Neumann conditions $\boldsymbol{\sigma}(\mathbf{u}(\mathbf{x},t))\mathbf{n} = \mathbf{0}$ hold while $0 \leq g(\mathbf{x},t)$.

Active contact phase the structure must remain in contact with the obstacle as long as a repulsion is exerted by obstacle on the moving structure such that $\sigma_n(\mathbf{u}(\mathbf{x},t)) \leq 0$. During this phase, $\mathbf{u}(\mathbf{x},t) \cdot \mathbf{n} = g_0$ and $\boldsymbol{\sigma}_t = \mathbf{0}$ hold to allow sliding in the tangential direction to the boundary Γ_C while contact with the obstacle is kept. In the one-dimensional case $d = 1$, the active contact phase is described by a non-homogeneous boundary condition of the type $u(x,t) = g_0$. Throughout this phase, the structure must be repulsed such that $\sigma_n(\mathbf{u}(\mathbf{x},t)) \leq 0$.

For each stencil on the contact boundary $\mathbf{x} \in \Gamma_C$, these phases are mutually exclusive.

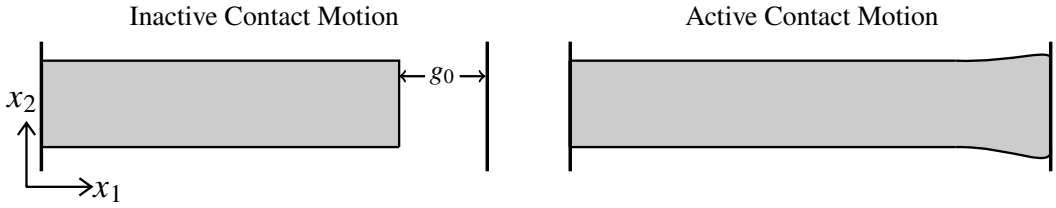

Figure 2.6: Active and inactive contact phases of the Signorini condition.

Next, the term *admissibility* is introduced to denote a motion abiding the Signorini conditions.

Definition 2.1 (Admissibility)**.** *A motion or a state is said to be admissible if and only if it satisfies the Signorini conditions* (2.24)*. During inactive contact motion, the structure is allowed to move freely in space and no force is applied on the boundary. During active contact motion, the structure can move tangentially to the obstacle and is repulsed by the obstacle.*

In this thesis, the standard Signorini problem consists then of a set of hyperbolic PDEs

complemented with boundary conditions

$$\begin{aligned}
&\rho\partial_{tt}\mathbf{u}(\mathbf{x},t) - \nabla\cdot\boldsymbol{\sigma}(\mathbf{u}(\mathbf{x},t)) = \mathbf{0} && && \mathbf{x}\in\Omega, t\in\mathbb{R}^+ \\
&0 \le g(\mathbf{x},t) \perp \sigma_n(\mathbf{u}(\mathbf{x},t)) \le 0, && \boldsymbol{\sigma}_t = \mathbf{0} && \mathbf{x}\in\Gamma_{\mathrm{C}}, t\in\mathbb{R}^+, \quad \Gamma_{\mathrm{C}}\neq\emptyset \\
&\mathbf{u}(\mathbf{x},t) = \mathbf{0} && && \mathbf{x}\in\Gamma_{\mathrm{D}}, t\in\mathbb{R}^+ \\
&\boldsymbol{\sigma}(\mathbf{u}(\mathbf{x},t))\mathbf{n} = \mathbf{0} && && \mathbf{x}\in\Gamma_{\mathrm{N}}, t\in\mathbb{R}^+ \\
&k\mathbf{u}(\mathbf{x},t) + \boldsymbol{\sigma}(\mathbf{u}(\mathbf{x},t))\mathbf{n} = \mathbf{0}, && k\neq 0 && \mathbf{x}\in\Gamma_{\mathrm{R}}, t\in\mathbb{R}^+
\end{aligned} \tag{2.25}$$

where k denotes the spring coefficient of the elastic foundation in the Robin boundary. Solutions to this system of equations exhibit two specific properties that are of interest for nonsmooth modal analysis: propagation of discontinuities and energy conservation. Both propagation of discontinuities and energy conservation constitute academic challenges in numerical modal analysis of the Signorini problem.

2.3.3 Discontinuities in expected solutions

At the moment of contact, the Signorini boundary conditions require an instantaneous change in boundary conditions between inactive and active phases at a given stencil $\mathbf{x}\in\Gamma_C$. This immediate change in boundary conditions is often followed by a propagation of a discontinuous wave in the internal velocity- and stress-fields of the elastic structure [24, 47]. Furthermore, the PDE (2.17) defining the dynamic linear elasticity problem is hyperbolic [49] and any propagating discontinuities in hyperbolic PDEs are preserved [26]. Thus, it is expected that solutions involving a unilateral contact will induce and preserve discontinuities within the stress $\boldsymbol{\sigma}(\mathbf{u}(\mathbf{x},t))$ and velocity $\partial_t\mathbf{u}(\mathbf{x},t)$ fields. In turn, the space of solutions considered for this problem must allow for such discontinuities to exist. In what follows, we shall presume that the quantities embedded in $\nabla\mathbf{u}(\mathbf{x},t)$ and $\partial_t\mathbf{u}(\mathbf{x},t)$ anywhere in $(\mathbf{x},t)\in\Omega\times\mathbb{R}^+$ and are finite and integrable. Furthermore, it is assumed that the desired periodic solutions of $\mathbf{u}(\mathbf{x},t)$ are continuous in any possible direction in $(\mathbf{x},t)\in\Omega\times\mathbb{R}^+$.

In theory of PDEs, the concept of characteristics is often helpful in understanding the behaviour of a system. Characteristics are paths, defined in the domains of interest (i.e., space and time), along which information propagates [92]. Discontinuities follow those characteristics as well. For one-dimensional linearly elastic solids with constant (in time and space) physical properties, the characteristics follow straight lines in space-time [22] and propagate either backwards or forwards along the space axis [26, 49]. For two- and three-dimensional problems, the notion of characteristic lines must be extended. Rather, information propagates along characteristic surfaces and in infinitely many directions [57, 92]. This sets a difficulty for numerous numerical schemes that attempt to preserve information in multiple dimensions since the discretized grids cannot capture characteristic surfaces properly [49]. Thus, numerical schemes often exhibit dissipation or spurious oscillations

along discontinuities [22, 49, 52]. The propagation of discontinuities and theory of characteristics are useful in the analysis and interpretation of numerical methods for the Signorini problem.

2.3.4 Conservation of energy

The total energy of the structure (expressed for the two-dimensional case) prone to unilateral contact ($\Gamma_R \neq \emptyset$) is given as follows:

$$E(t) = \frac{1}{2}\int_{\Omega}\Big(\rho\partial_t\mathbf{u}^{\top}(\mathbf{x},t)\partial_t\mathbf{u}(\mathbf{x},t)+\boldsymbol{\sigma}(\mathbf{u}(\mathbf{x},t)) : \boldsymbol{\epsilon}(\mathbf{u}(\mathbf{x},t))\Big)\mathrm{d}\mathbf{x}+\frac{k}{2}\int_{\Gamma_R}\mathbf{u}(\mathbf{x},t)\cdot\mathbf{u}(\mathbf{x},t)\mathrm{d}\mathbf{x}. \quad (2.26)$$

where ":" denotes the Frobenius inner product operation. In the investigated Signorini problems, friction mechanisms are ignored and it is suggested that the total energy should be conserved during inactive and active contact phases (as well as in the transition between them). Thus, all solutions are considered to be *energy conservative* such that $\dot{E}(t) = 0$ for all t [24, 40, 98]. The conservation of energy is a desired feature for schemes in structural dynamics as it allows better approximation of the dynamics [24, 40, 43, 98]. These energy conserving methods focus on the conservation of the numerical discrete approximation of the energy at different instances of time, i.e., $E_i \approx E(t_i)$ with $E_{i+1} = E_i$ for any i.

2.4 Enforcement of Signorini conditions

The Signorini problem does not generally admit closed-form solutions except for specific cases (such as this presented in Chapter 3). Instead, solutions of the Signorini problem are mostly obtained via numerical techniques [16, 84, 96]. While numerical PDE solvers for the dynamics described by linear elasticity are abundant, the Signorini boundary conditions set an additional difficulty due to the nonsmoothness of the boundary condition. The implementation of such boundary conditions numerically, most often, is not evident. For example, while the FEM has specific guidelines on treatment of Robin, Dirichlet or Neumann boundary conditions, the implementation of Signorini boundary conditions leads to an ill-posed problem [16, 24, 84]. In turn, this ill-posedness can be resolved in various manners leading to varying schemes for the solution of the Signorini problem in the FE framework which allow different treatment of the Signorini boundary conditions.

In this section, three main strategies for the implementation of the Signorini boundary conditions will be discussed: penalty, weak treatment, and switching.

2.4.1 Penalty methods

Penalty methods seek to regularize and "smoothen" the behaviour of the displacement at the contact boundary. Regularization of the Signorini conditions consists of assigning a force $\mathbf{f}_\mu(\mathbf{u}(\mathbf{x},t),\mu)$ characterized by a penalty parameter μ. This force is often constructed such that the structure is repulsed by a force proportional to the penetration of the obstacle [24, 58, 96]. To illustrate this penalty force, the Signorini problem in the one-dimensional case - the unforced cantilever bar of $\rho = Y = A(x) = 1$ with unilateral contact conditions at $x = 1$ with a rigid obstacle at $g_0 > 0$ - is considered

$$\partial_{tt}u(x,t) - \partial_{xx}u(x,t) = 0 \qquad (x,t) \in (0,1) \times \mathbb{R}^+ \tag{2.27}$$

$$u(0,t) = 0 \tag{2.28}$$

$$0 \leq g_0 - u(1,t) \perp \partial_x u(1,t) \leq 0 \tag{2.29}$$

The Signorini boundary conditions (2.29) describe an implicit relationship between $\partial_x u(1,t)$ and $u(1,t)$. The resulting $u(1,t)$ and $\partial_x u(1,t)$ then behaves in a nonsmooth fashion. However, penalty methods to this problem are aimed to approximate the Signorini conditions via a relatively smoother condition on $\partial_x u(1,t)$. A common penalization approach is to substitute Equation (2.29) with a Robin condition consisting of an explicit relationship between $\partial_x u(1,t)$ and $u(1,t)$ which is more suited for classical numerical PDE solvers [24, 96]. For example, a possible approximation of the Signorini conditions (2.29) is the Robin condition

$$\partial_x u(1,t) = \mathrm{f}_\mu(u(1,t)) = \min(0, \mu(g_0 - u(1,t))), \quad \mu > 0. \tag{2.30}$$

This Robin condition is equivalent to a soft support with a spring coefficient μ replacing the rigid obstacle. A comparison of the penalty function with the Signorini conditions is presented in Figure 2.7. In penalty methods, it is often considered that when the penalty parameter reaches a

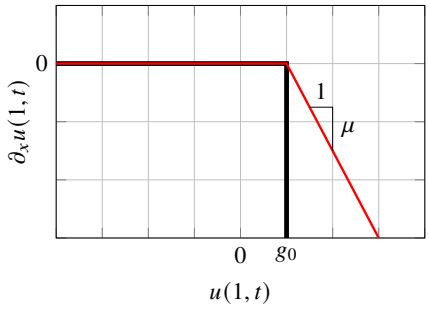

(a) Relation between stress and displacement at $x = 1$ for the Signorini conditions (2.31) [——] and the penalized model (2.30) [——]

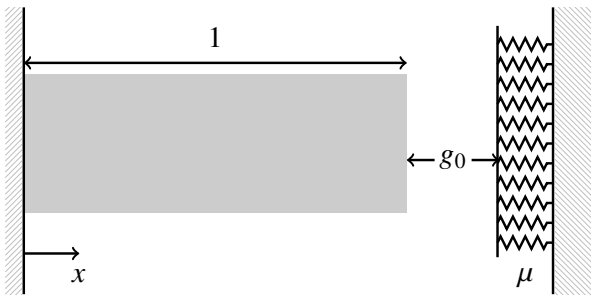

(b) Physical illustration of the penalized one-dimensional bar described by Equations (2.27) and (2.29)

Figure 2.7: penalty force: plot and physical illustration.

magnitude of infinity (i.e., $\mu \to \infty$ in Equation (2.30)), a more accurate depiction of the Signorini solution will be achieved. In the context of numerical methods, a high value of μ inevitably leads to stiff PDEs which, in turn, poses a difficulty on the convergence of numerical solvers [71]. Another disadvantage of the penalty method is that the penalty force, at relatively high values of μ, adds significant energy to the system which is not reflective of the system in unilateral contact [19, 30]. Thus, penalty methods are not discussed in this thesis.

2.4.2 Weak Signorini boundary conditions

Besides the penalty method, there exist schemes where the Signorini boundary conditions are treated in a weak manner. In these schemes, the Signorini boundary conditions are not regularized. Rather, approximations of the displacement at the contact boundary and contact pressures are inserted into the Signorini conditions and introduce a residual error in the Signorini conditions. This residual error is then projected onto the space of approximating functions to form a system of equations to be solved. To better illustrate the weak Signorini boundary conditions, the "min" operator representation of the Signorini boundary conditions (2.29) will be used

$$\partial_x u(1,t) = \min(0, \gamma(g_0 - u(1,t)) + \partial_x u(1,t)), \quad \gamma > 0. \tag{2.31}$$

where γ is referred to as the Nitsche parameter in this manuscript (even though its use does not always correspond to the Nitsche method [51]). The Nitsche parameter is a dummy parameter in Equation (2.31) and the equivalence between Equation (2.29) and Equation (2.31) is valid for all $\gamma > 0$.

Weakening of the boundary condition (2.31) implies that the weak form of (2.31) is solved instead of the form presented in (2.31). Thus, it is assumed that as the order of approximation increases, the weak Signorini boundary conditions will be better satisfied [19, 51].

For example, the FD-BEM treatment of the Signorini boundary conditions consists of using harmonic functions that are solutions of the governing PDE to approximate the displacement $u(1,t)$ and stress $\partial_x u(1,t)$. A Galerkin projection is then used on Equation (2.31) to solve for the appropriate coefficients of the harmonic functions [51]. Thus, the Signorini condition (2.31) is not answered exactly, and it is assumed that as the number of participating harmonics increases, the approximated solution will satisfy better the Signorini conditions. The weak treatment of the Signorini conditions in Nitsche's method will be discussed in Section 2.5.3.

It is important to note that the Nitsche parameter, γ, introduced in (2.31) may affect the penetration of the obstacle in FD-BEM and Nitsche in numerical solutions. However, in contrast to penalty methods, γ does not need to be infinite in order to ensure the Signorini conditions are satisfied. To clarify, given a fixed value $\gamma = \gamma_0$, the accuracy of methods that use the weak Signorini boundary conditions depends solely on the order of approximation. For example, in FD-BEM more

accurate satisfaction of the Signorini conditions is achieved with more harmonics, while in Nitsche's method it is achieved by using a more elements or higher order shape functions [19].

2.4.3 Switching

The switching algorithm satisfies the Signorini by changing the boundary conditions on the system rather than approximating the Signorini force [3]. Compared to the weak enforcement of the Signorini conditions, the switching algorithm requires a strong implementation of the Signorini conditions in the time domain. This is done by solving the approximated governing equations while switching between two boundary conditions: the active and inactive contact phases. Application of the switching method on the problem of the one-dimensional bar (2.27)-(2.29) can be described as follows:

- For all times where inactive contact is assumed, the PDE (2.27) is solved with Neumann boundary conditions $\partial_x u(1,t) = 0$. During inactive contact, the motion must abide $g_0 - u(1,t) \geq 0$.
- For all times where active contact motion is assumed, the PDE (2.27) is solved with Dirichlet conditions $u(1,t) = g_0$. During active contact, the motion must abide $\partial_x u(1,t) \leq 0$

It is noted that the accuracy of the switching method relies on the accuracy of the PDE solver and on finding the appropriate time of switch. An example of a PDE solver applying the switching method is the finite volume method complemented with ghost cell method for the treatment of boundary conditions. The switching method is referred to as "floating-boundary" methods [77, 98]. Another example is the mass redistribution method [40] which also employs a switching mechanism.

2.5 Numerical methods for the Signorini problem

To solve the Signorini problem numerically, a PDE solver must be chosen. In this manuscript, three general frameworks are discussed: finite volume methods, boundary elements methods, and finite element methods.

2.5.1 Finite volume strategies

In this thesis, finite volume strategies refer to methods solving the weak form of a PDE via the discretization of quantities of interest using discontinuous shape functions. Namely, two families of numerical methods are considered: finite volume methods (FVM) and discontinuous Galerkin methods (DGM). While the discontinuous Galerkin is generally considered as combination of FEMs and finite volume methods [33, p. 7]. The DGM can also be seen as the extension of FVM via

discontinuous piecewise-polynomial shape functions [81]. In fact, the DGM and FVM share some important features such as approximation of solutions via discontinuous functions and the usage of fluxes in numerical schemes. Since either FVM or DGM are not explored in depth in this section, the description of finite volume strategies will be done in terms of DGM for the sake of conciseness. Most properties and formulation of DGM presented in this section are also shared by the FVM (in this context, the FVM is equivalent to application of DGM with piecewise constant shape functions).

In DGM, the domain is discretized into elements, and the quantities of interest in the PDE are approximated using discontinuous functions. The discontinuous functions are assumed to be smooth within the elements and discontinuous on element boundaries. Then, the elements are coupled using fluxes on the boundaries. Since the displacement field in the Signorini problem is assumed to be continuous, the DGM (and FVM) has been largely applied on the velocity-stress formulation of the PDE which indeed consist of discontinuities [49, 84, 98]. To illustrate the DGM and finite volume strategies, the velocity-stress formulation of the bar in Equation (2.27) is introduced

$$\begin{aligned} \partial_t v(x,t) &= \partial_x \sigma(x,t) \\ \partial_t \sigma(x,t) &= \partial_x v(x,t) \end{aligned} \tag{2.32}$$

where $v(\mathbf{x},t) \equiv \partial_t u(\mathbf{x},t)$ represents the velocity field of the structure in question. In the DGM, a given element of domain R_i and boundary ∂R_i in Ω abides the following weak form of Equation (2.32) evaluated against test function $\omega(x)$

$$\int_{R_i} w(x)^\top \partial_t \bar{v}(x,t)\mathrm{d}x = -\int_{R_i} \partial_x w(x)\sigma(x,t)\mathrm{d}x + \underbrace{\oint_{\partial R_i} w(x)\sigma(x,t)\mathrm{d}x}_{\text{Boundary Integral = Flux Term}} \tag{2.33a}$$

and

$$\int_{R_i} w(x)^\top \partial_t \sigma(x,t)\mathrm{d}x = -\int_{R_i} \partial_x w(x)v(x,t)\mathrm{d}\mathbf{x} + \underbrace{\oint_{\partial R_i} w(x)v(x,t)\mathrm{d}\mathbf{x}}_{\text{Boundary Integral = Flux Term}} . \tag{2.33b}$$

Since approximations to v and σ consist of discontinuities on ∂R_i, the boundary integral are rather treated as fluxes [33]. These fluxes consist of terms from neighbouring cells R_{i+1}, R_{i-1}, etc. and are in fact integral to finite volume strategies. In both DGM and FVM, the fluxes will affect and determine the behaviour exhibited by the numerical solutions [33, 49, 52].

The boundary conditions in finite volume strategies are generally treated using the ghost cell method. By the ghost cell method, boundary conditions are applied by assuming specific values of outside the boundary (via ghost elements/cells) such that the mean the ghost and interior elements satisfy the boundary conditions [33, 49, 97]. The ghost cell method readily allows for the switching method by simply modifying the boundary fluxes according to the perceived contact phase of the structure. In fact, the switching method has been proven successful in nonsmooth modal analysis of

the bar under the framework of the Wave-FEM (WFEM, the proposed implementation is in essence FVM with an up-wind flux) [97]. However, the WFEM was not proven successful for the case of the bar with varying area or the two-dimensional case. In these cases, dissipation of energy was reported and periodic solution involving unilateral contact could not be found [97]. Similarly, other FVM schemes have reported significant dissipation of energy [47, 52] which also impedes the detection of periodic solutions. Thus, finite volume strategies are not further considered in this manuscript.

2.5.2 Boundary elements methods

BEMs solve a PDE using its fundamental solution as the trial function [17]. In this formulation, the states within the structure are related to the state of structure along the boundaries of $\Omega \times \mathbb{R}^+$ via fundamental solutions (or approximations of fundamental solutions). For example, a time-domain BEM (TD-BEM) formulation of the wave equation describing the cantilever bar

$$\partial_{tt} u(x,t) + \partial_{xx} u(x,t) = 0, \qquad (x,t) \in [0,1] \times \mathbb{R}^+ \tag{2.34}$$

admits a solution involving boundary integrals and fundamental solutions to the wave equation

$$\begin{aligned} u(x,t) = &\int_0^t p^*(x,t,0,r)u(0,r)\mathrm{d}r + \int_0^t p^*(x,t,1,r)u(1,r)\mathrm{d}r + \dots \\ &\int_0^t u^*(x,t,0,r)\partial_x u(0,r)\mathrm{d}r + \int_0^t u^*(x,t,1,r)\partial_x u(1,r)\mathrm{d}r + \dots \\ &\int_0^1 u^*(x,t,s,0)\partial_t u(s,0)\mathrm{d}s + \int_0^1 \partial_r u^*(x,t,s,0)u(s,0)\mathrm{d}s. \end{aligned} \tag{2.35}$$

Here, $u^*(x,t,s,r)$ and $p^*(x,t,s,r)$ represent the fundamental solutions to displacement and stress, respectively [50, 91]. Equation (2.35) is then discretized in both space, x_i, and time, t_j, to form an iterative algorithm calculating the state $u(x_i, t_j)$ given initial state and boundary conditions [50, 91]. Moreover, the TD-BEM formulation allows for the application of the switching method in obtaining the solution of the Signorini problem [91]. In fact, nonsmooth modal analysis of the bar in unilateral contact was proven successful [50, 91]. Although, since TD-BEM requires knowledge of the fundamental solution, it cannot be readily applied to a wide variety of systems since they are not readily equipped with a fundamental solution. For example, the application of TD-BEM to the bar with varying-area or the two-dimensional Signorini problem where the fundamental solution is not available, requires additional approximation of the fundamental solution [50, 51]. Although, investigation of the problem of nonsmooth modal analysis using TD-BEM and frequency-domain BEM (FD-BEM) has recently proven fruitful, and research on the topic is currently ongoing in the structural dynamics laboratory of McGill University [51]. Since application of BEM on nonsmooth modal analysis is ongoing, BEM methods will not be explored in this thesis.

2.5.3 Finite elements methods

In what follows, the Signorini problem in the FEM will be presented together with review of existing treatments of the Signorini boundary conditions. For the sake of conciseness, derivation of elementary terms in FEM will not be presented in this section.

In the FEM, the domain of the structure is discretized into elements and quantities of interest in the PDE are approximated using piecewise-smooth continuous functions. FEMs are widely used in the domain of structural dynamics and modal analysis. In general, FEMs are considered adaptable to complex geometries, nonlinear material properties and heterogeneous materials [34].

In classical FEM, shape functions within each element consist of Lagrangian polynomials and nodal quantities. The Lagrangian polynomials of the FE model are collectively gathered in $\mathbf{P}(x)$. The nodal quantities $u(x_i, t)$ where x_i are the nodal loci $i = 1, 2, \ldots, N$ with N being the number of nodes are denoted $u_i(t)$ (i.e., $u(x_i, t) \approx u_i(t)$). Both nodal quantities and the Lagrange polynomials are used to approximate the displacement field

$$u(x, t) \approx \mathbf{P}(x)\mathbf{u}(t). \tag{2.36}$$

Using this approximation, the PDE is discretized to form an ODE in the nodal quantities $\mathbf{u}(t)$. To illustrate the FEM, the Signorini problem of the one-dimensional cantilever bar in Equations (2.27)-(2.29) is used. The FEM approximation of this problem can be represented as follows:

$$\begin{aligned} &\mathbf{M}\ddot{\mathbf{u}}(t) + \mathbf{K}\mathbf{u}(t) = \mathbf{G}^{\mathrm{T}}\lambda(t) \\ &u_0 = 0 \\ &0 \leq g_0 - u_N(t) \perp \lambda(t) \leq 0 \end{aligned} \tag{2.37}$$

where $\lambda(t)$ defines the contact pressure at the tip of the bar, i.e., $\partial_x u(1, t) = \lambda(t)$, and $\mathbf{G}$ is a vector satisfying $G_i = 0$ for $i = 1, 2, \ldots, N-1$ with $G_N \neq 0$ relating the stress at the boundary to the internal quantities. The problem presented in (2.37), is in fact ill-posed and does not have a unique solution [16, 19, 24, 84]. However, there exist multiple techniques to render formulation (2.37) solvable. Each of these techniques entails a different enforcement of the unilateral conditions in the FEM. A selected few will be explored in this section.

Newton's impact law

One commonly used method in applications is the addition of a Newtonian impact law to expression (2.37). The Newtonian impact law imposes a relationship between the incoming and outgoing velocities at the contact boundary at the moment of impact

$$\text{if } u_N(t) = g_0 \text{ then } \dot{u}_N(t^+) = -e\dot{u}_N(t^-) \tag{2.38}$$

where $1 \geq e \geq 0$ denotes the coefficient of restitution. In continuous time, this impact law does not allow penetration of the obstacle. However, nonsmooth modal analysis of the Signorini problem via FEM with Newton's impact law is not an evident task. To find periodic solutions, the ODE must allow energy conservation necessitating a fully elastic Newton impact law $e = 1$. Application of $e = 1$ leads to chattering which is not exhibited in the true solution to the Signorini problem [24]. In contrast, a Newton impact law $e = 0$ eliminates chattering but dissipates energy for non-zero pre-impact velocities. Thus, periodic solutions with non-zero pre-impact velocities cannot be found although these exist in the true modal space of the solution to the Signorini problem [84, 98]. Furthermore, application of these methods for nonsmooth modal analysis of the continuous problem (i.e., for high N) was found computationally expensive and infeasible as reported in [84, p. 23].

Mass redistribution method

The outlining principle of mass redistribution methods (MRMs) [40] is to render the system of equations (2.37)solvable by eliminating the inertia of the contact node(s).

To present the mass redistribution formulation, equations involving the contact node u_N are specified in Equation (2.37)

$$\begin{aligned} &\begin{bmatrix} \mathbf{M}_{OO} & \mathbf{M}_{OC} \\ \mathbf{M}_{OC}^\top & \mathrm{M}_{CC} \end{bmatrix} \begin{pmatrix} \ddot{\mathbf{u}}_O(t) \\ \ddot{u}_N(t) \end{pmatrix} + \begin{bmatrix} \mathbf{K}_{OO} & \mathbf{K}_{OC} \\ \mathbf{K}_{OC}^\top & \mathrm{K}_{CC} \end{bmatrix} \begin{pmatrix} \mathbf{u}^o(t) \\ u_N(t) \end{pmatrix} = \begin{pmatrix} \mathbf{0} \\ \mathrm{G}_N \lambda(t) \end{pmatrix} \\ &0 \leq g_0 - u_N(t) \perp \lambda(t) \leq 0. \end{aligned} \tag{2.39}$$

where $\mathbf{u}^o(t)$ gathers all internal nodes that are not prone to contact. The MRM then seeks to eliminate the inertia of contact nodes. This is done by elimination of $\mathbf{M}_{OC}$, M_{CC} in $\mathbf{M}$ and substitution of a redistributed mass matrix $\mathbf{M}_{\mathrm{MRM}}$ instead of the matrix $\mathbf{M}_{\mathrm{OO}}$. With these substitutions, expression (2.39) reads

$$\begin{aligned} &\begin{bmatrix} \mathbf{M}_{\mathrm{MRM}} & \mathbf{0} \\ \mathbf{0} & 0 \end{bmatrix} \begin{pmatrix} \ddot{\mathbf{u}}_O(t) \\ \ddot{u}_N(t) \end{pmatrix} + \begin{bmatrix} \mathbf{K}_{OO} & \mathbf{K}_{OC} \\ \mathbf{K}_{OC}^\top & \mathrm{K}_{CC} \end{bmatrix} \begin{pmatrix} \mathbf{u}_O(t) \\ u_N(t) \end{pmatrix} = \begin{pmatrix} \mathbf{0} \\ \mathrm{G}_N \lambda(t) \end{pmatrix} \\ &0 \leq g_0 - u_N(t) \perp \lambda(t) \leq 0. \end{aligned} \tag{2.40}$$

The last row of Equation (2.40) then allows to construct a function of λ in terms of $\mathbf{u}(t)$

$$\lambda(\mathbf{u}(t)) = \frac{1}{G_N}(\mathbf{K}_{OC}^\top \mathbf{u}_O(t) + K_{CC} u_N(t)) \tag{2.41}$$

which then allows for a reduced ODE formulation of the Signorini problem in FEM:

$$\begin{aligned} &\mathbf{M}_{\mathrm{MRM}} \ddot{\mathbf{u}}_O(t) + \mathbf{K}_{OO} \mathbf{u}_O(t) = -\mathbf{K}_{OC} u_N(t) \\ &0 \leq g_0 - u_N(t) \perp \frac{1}{G_N}(\mathbf{K}_{OC}^\top \mathbf{u}_O(t) + K_{CC} u_N(t)) \leq 0. \end{aligned} \tag{2.42}$$

The formulation of the matrix $\mathbf{M}_{\mathrm{MRM}}$ is a key component in the MRM since it allows to define λ

in terms of $\mathbf{u}(t)$ (see Equation (2.41)). The formulation $\mathbf{M}_{\text{MRM}}$ consists of redistributing the mass of the contact node(s) via solution of a constrained optimization problem [40]. The constraints include preservation of the center of mass, inertia and the total mass of the original structure [40]. The ODE (2.42) exhibits a unique solution, and the MRM converges to the true solution of the Signorini problem with higher number of elements or order of shape functions [24, 32, 40]. However, a disadvantage of this method is that it requires either a construction of a new mass matrix (or usage of specific quadrature rules as shown in [31]).

It is noted that in [24, 65] apply the MRM by ignoring the mass of contact nodes (i.e., by setting $\mathbf{M}_{\text{MRM}} = \mathbf{M}_{\text{OO}}$) and can be applied readily to existing FE models. Furthermore, it has been shown that ignoring the mass on the contact boundary is suitable for nonsmooth modal analysis [65], However, in this approach the original eigen-frequencies and mode shapes are modified and the modified mass matrix is not representative of the original mass matrix [65, 84]. Therefore, in the following chapters, this approach to mass redistribution will not be addressed. Furthermore, it will be shown that the NBM eliminates the contact node from the system of equations without requiring a construction of a new mass matrix.

Nitsche's method

In unilateral contact mechanics, the Nitsche method solves the ill-definition of the FEM formulation by introducing a relationship between the contact pressure $\lambda(t)$ and the displacement $u_N(t)$. In [19], a general θ-formulation of the Nitsche method is presented where different values of θ are used to admit ODEs of different properties. For example, $\theta = 1$ allows for a symmetric formulation of the resulting FEM-ODE. Only the Nitsche method with $\theta = 0$ (which constitutes the simplest implementation) is explored in this manuscript for the sake of conciseness.

The formulation of the contact pressure in Nitsche's method is done via the introduction of the FE approximation of the stress at the contact boundary into the "min" formulation of the Signorini contact conditions (2.31):

$$\lambda(\mathbf{u}(t)) = \min(0, \gamma(g_0 - u(1,t)) + \partial_x u(1,t)) \approx \min(0, \gamma(g_0 - u_N(t)) + \mathbf{P}'(1)^{\mathrm{T}}\mathbf{u}(t)). \quad (2.43)$$

The FEM-ODE (2.37) with the Nitsche stress approximation then reads (in this manuscript, $\circ'$ denotes differentiation of a mono-variable function $\circ$ with respect to its argument)

$$\mathbf{M}\ddot{\mathbf{u}}(t) + \mathbf{K}\mathbf{u}(t) = \mathbf{G}^{\mathrm{T}} \min(0, \gamma(g_0 - u_N(t)) + \mathbf{P}'(1)^{\mathrm{T}}\mathbf{u}(t)), \quad \gamma > 0. \quad (2.44)$$

The Nitsche formulation treats the Signorini boundary conditions weakly and penetration of the obstacle is effectively allowed for finite N [20]. It is expected that, as the number of nodes or order of shape functions increases, we will have $u_N(t) \to u(1,t)$, $\lambda(\mathbf{u}(t)) \to \partial_x u(1,t)$ and $\mathbf{P}'(1)^{\mathrm{T}}\mathbf{u}(t) \to \partial_x u(1,t)$ such that expression (2.43) is equivalent to the Signorini conditions (2.31).

However, since the Nitsche method allows for penetration of the obstacle at finite N, it is not considered for nonsmooth modal analysis.

2.5.4 Basis Recombination

The method of basis recombination [14, p. 112] assumes that the shape functions used in the approximation of the PDE satisfy the boundary conditions. The methodology is commonly used in Galerkin approaches for the solution of nonlinear PDEs [44, 58]; [61, p. 300]. In comparison with FEM, WFEM or FVM, basis recombination assumes that any type of boundary conditions is always answered in a strong manner. However, application of basis recombination to problems involving contact conditions has yet been attempted to the knowledge of the author. Thus, the dominant portion (Chapters 4 and 5) of this manuscript focuses on numerical modal analysis using basis recombination techniques, otherwise referred to as the nodal boundary method (NBM). Specifically, the NBM consists of two innovative approaches: (1) the NBM modifies the Lagrangian shape functions to answer the Neumann conditions strongly (which is not done in classical finite element) (2) the NBM solves the Signorini problem by switching between two families of shape functions describing both active and inactive contact. The method is explained in length for both the one-dimensional case (Chapter 4) and the two-dimensional case (Chapter 5). While the NBM is used to solve the problem of nonsmooth modal analysis, FEM with Nitsche or Newton's impact law are used to validate the obtained results and for comparative analysis.

Chapter 3

Exact Nonsmooth Modal Analysis of an Internally Resonant Bar

This chapter entails the exact nonsmooth modal analysis of the cantilever bar of uniform area in unilateral contact. The uniform area bar is referred to as the *internally resonant* bar due its commensurate fundamental frequencies, i.e., the fundamental frequencies of the bar are integer multiples of its first fundamental frequency $\omega_n = 2\pi n/c$ where c is the speed of sound in the bar and $n = 1, 2, 3, \ldots$ [84,97,98]. The nonsmooth modal analysis of the internally resonant bar has attracted experimental interest [65] and was investigated analytically and numerically in semi-discrete and continuous settings in space [12, 48, 60, 74, 80, 84, 85, 98]. The bar of uniform area enjoys the well-known d'Alembert travelling-wave solution [26, 84], and, in this chapter, this d'Alembert travelling-wave solution of the bar is used to formulate a closed-form solution of the bar's motion prone to contact via the switching method. The formulation of the bar prone to contact presented in this chapter is used to find new NSMs of the bar. Also, existing theory on the nonsmooth bar will be revisited and extended through new theorems developed in this chapter. At last, the results presented here have implications on numerical techniques for nonsmooth modal analysis and influence the choice of continuation techniques later in the thesis.

The outline of this chapter is given as follows: the formulation of the bar in unilateral contact is briefly recalled in Section 3.1. Preliminaries to nonsmooth modal analysis, such as the d'Alembert solution to the contact problem, formulation of the periodicity condition, and lemmas on the existence of solutions are exposed in Section 3.2. Then, nonsmooth modal analysis is performed and compared with existing literature in Section 3.3. At last, discussion and implications of the findings in this chapter on the remainder of the thesis are presented in Section 3.4.

The findings in this thesis were published in [85] and [89]. Large part of this chapter replicates the article [89]. Although, novel results based on the methodology presented in [89] are presented in Section 3.3.3. These results affirm conjectures that were presented in [89] and were developed

more recently. Also, Section 3.1.1 is added to this chapter (and does not appear in [89]) in order to provide context on the choice of phase condition in reference to earlier discussion on the phase condition in Section 2.1.1.

Furthermore, it is important to note the contribution of Dr. Stéphane Junca in the writing of this chapter, specifically in establishing a robust mathematical terminology (prominently in Section 3.1.2) and for advising on the validity of the propositions and theorems presented in this chapter.

3.1 Problem statement

As depicted in Figure 3.1, we consider the displacement field $u(\bar{x}, \bar{t})$ inside a bar of length L, where $\bar{x}$ and $\bar{t}$ denote *physical* position and time, respectively. Assuming linear elasticity, the displacement

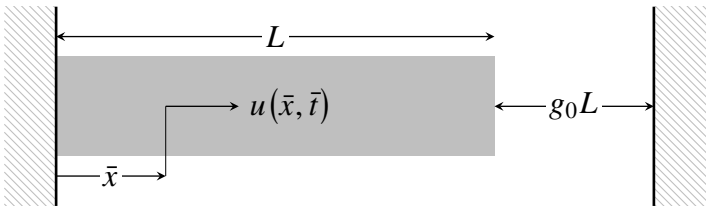

Figure 3.1: Unilaterally constrained cantilever bar.

of the bar with area $A(x) = A$ satisfies the non-dimensional wave equation

$$\partial_{tt} u(x,t) = \partial_{xx} u(x,t), \quad x = \bar{x}/L, \quad t = \alpha \bar{t}/L, \tag{3.1}$$

where $\alpha = \sqrt{\rho/AY} > 0$. To simplify further the notations, the dimensionless coordinates x and t are introduced and, for the remainder of the article, the displacement is expressed exclusively in these coordinates, i.e., $u(x,t)$. As non-smooth modal analysis requires obtaining periodic solutions of the autonomous system [38, 76, 84], the analysis will be performed on a single period of motion, of normalized period T such that the domains $t \in [0,T]$ and $x \in [0,1]$ are considered.

On the boundary $x = 1$, the bar is prone to unilateral contact with a rigid wall initially at a normalized distance $g_0 > 0$. For the sake of simplicity, non-smooth modes consisting of a single active contact per period are sought; these are referred to as 1CPP (one active Contact Phase per Period) modes [84, 97].

Definition 3.1 (1CPP motion)**.** *A periodic motion of the bar with period T is said to be a 1CPP motion if there exist an instance in time t_0 and a duration τ such that the bar is in inactive contact for $t \in [t_0, t_0 + \tau]$ and in active contact for $t \in [t_0 + \tau, t_0 + T]$.*

Without loss of generality, we can pick $t_0 = 0$. A 1CPP motion at $x = 1$ with $t_0 = 0$ is illustrated in Figure 3.2.

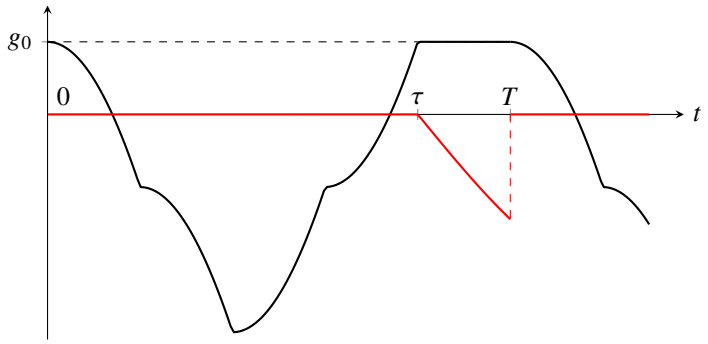

Figure 3.2: Example of a 1CPP motion: $u(1,t)$ [—] and $\partial_x u(1,t)$ [—]. Note the cusps in $u(1,t)$ (indicating discontinuities in $\partial_t u(1,t)$) away from the instance of contact. Indeed, these cusps are expected in motions prone to unilateral contact [24, 50, 57, 84, 97]. The noted cusps emanate from contact discontinuities which are preserved in hyperbolic PDEs [49]. As a consequence, it assumed that displacement of 1CPP motions are continuous and piecewise-C^1. This is discussed further in Section 3.2

A 1CPP motion should satisfy the boundary conditions

$$\text{Cantilever bar} \quad u(0,t) = 0 \quad \forall t \in [0,T] \tag{3.2}$$

$$\text{Inactive contact} \quad u(1,t) \leq g_0 \quad \forall t \in [0,T] \quad \text{and} \quad \partial_x u(1,t) = 0 \quad t \in [0,\tau] \text{ a.e.} \tag{3.3}$$

$$\text{Active contact} \quad u(1,t) = g_0 \quad \forall t \in [0,T] \quad \text{and} \quad \partial_x u(1,t) \leq 0 \quad t \in [\tau,T] \text{ a.e.} \tag{3.4}$$

together with the periodicity conditions

$$u(x,0) = u(x,T) \quad \forall x \in [0,1] \tag{3.5}$$

$$\partial_t u(x,0) = \partial_t u(x,T) \quad x \in [0,1] \text{ a.e.} \tag{3.6}$$

where a.e. denotes *almost-everywhere in* the prescribed domain and is used for piecewise-continuous functions not defined on specific loci. Specifically, the indication a.e. shall apply to constraints involving the derivatives of the displacement field (stress and velocity) due to the choice of solution space, as discussed in Section 2.3.3.

Note that solutions where the bar enters into contact with the wall with zero incoming velocity at the contact boundary, known as grazing motion [16], are valid solutions to (3.1)-(3.4). However, such solutions are intentionally omitted in the discussion for the sake of conciseness. Accordingly, the restriction where the tip of the bar must approach the wall with positive incoming velocity just before contact is considered:

$$\lim_{t \to \tau^-} \partial_t u(1,t) > 0. \tag{3.7}$$

3.1.1 Phase condition

As mentioned previously in Section 2.1.1, a phase condition must be added to the periodicity conditions (periodicity conditions in Equations (3.5) and (3.6)) in order to depict solutions that do not belong to the same phase-space (i.e., there exist no continuum of initial conditions that answers the phase conditions and pertains to the same periodic solution in the phase-space). The phase condition is implemented by Definition 3.1 and Equation (3.7). In Definition 3.1, the motion is constrained to start at inactive contact and to end at active contact with a single contact phase per period. Given that periodic solutions are sought, the initial condition used for a motion of the type Definition 3.1 must lie at the intersection between inactive and active contact phases. Furthermore, Definition 3.1 requires that the solution to the phase condition be an isolated point. For grazing motions, there may exist a continuous interval in time where $\partial_x u(1,t) = 0$ and $u(1,t) = g_0$ and, for such motions, there is no single point in time that separates active contact phase from the inactive contact phase. For example, a grazing motion may exhibit an interval where it is possible to have $\partial_x u(1,t^+) = 0$ and $u(1,t^+) = g_0$ for $t \in [\tau, t_g)$ where $t_g < T$ and $t_g - \tau$ denotes the duration of grazing [82]. However, for non-grazing motion, the switching instance between inactive and active contact phases can be defined by an isolated instance in time (for the investigated 1CPP motion, this is $t = 0$ and $t = \tau$). Here, non-grazing motions are sought and are restricted by Equation (3.7). In sum, since non-grazing motions of the type in Definition 3.1 are sought, the initial conditions must lie on the point of intersection at the *beginning* of inactive contact phase and at the *end* of active contact phase which constitutes the phase condition for this problem. Furthermore, any distinct set of initial conditions answering the periodicity conditions in Equations (3.5) and (3.6) and producing a 1CPP motion constitutes a distinct periodic motion in the phase-space.

3.1.2 Important terminology

We define non-smooth modes as families of motions defined by non-smooth d'Alembert functions. Piecewise-*linear* modes consist of piecewise-linear d'Alembert solutions, as depicted in Figure 3.3 and piecewise-*smooth* modes consist of piecewise-smooth d'Alembert functions, which include piecewise-linear d'Alembert functions. This distinction will be used to further emphasize the novelty presented in this manuscript. To clarify, an example of a piecewise-smooth yet not piecewise-linear d'Alembert function is illustrated later in the manuscript, in Figure 3.7, where the newly detected piecewise-smooth modes are discussed. Still, it should be understood that both families (piecewise-smooth and piecewise-linear) pertain to the family of non-smooth modes.

3.2 D'Alembert solution to the Signorini problem

The d'Alembert solution satisfying Equations (3.1) and (3.2) reads [26, p. 69]

$$u(x,t) = f(t+x) - f(t-x), \quad \forall (x,t) \in [0,1] \times [0,T] \tag{3.8}$$

where the function f, referred to as the *d'Alembert function*, can be defined up to a constant. In the sequel, the convention

$$f(-1) = 0 \tag{3.9}$$

is chosen and does not affect the displacement, velocity or stress solutions derived. With $t = 0$ and $x = 1$ in (3.8), this convention yields $f(1) = u(1,0)$. Moreover, for $(x,t) \in [0,1] \times [0,T]$, f has to be defined on the interval $[-1, 1+T]$. Defining f is, therefore, equivalent to determining a cantilever motion of the bar. Section 3.2 shows how the boundary conditions (3.3)-(3.6) are translated into conditions on the d'Alembert function.

According to the assumptions of continuous displacement field solution established in Section 2.3.3, f is chosen as a continuous and piecewise-C^1 function on its domain of definition, that is $f \in C^0([-1,1+T]) \cap \hat{C}^1([-1,1+T])$. This means that the classical derivative of f is defined everywhere except over a finite number of points on any bounded set. Also, at a point[1] s where f' is not defined, the right limit $f'(s^+)$ and the left limit $f'(s^-)$ still exist. An equality involving f' is thus satisfied at all points of the considered interval except at the finite number of points where f is not differentiable.

In previous research on the topic of interest [84,97,98], nonsmooth modal analysis was formulated using the displacement, stress and velocity fields and was performed by computing initial conditions that generate admissible periodic solutions. Instead, in this manuscript, the d'Alembert function is exploited exclusively, which leads to new insights. To illustrate the idea, a known admissible periodic solution and its associated d'Alembert function are plotted in Figure 3.3.

Before solving Equations (3.1)-(3.6) using the d'Alembert function, the considered solution space is characterized.

3.2.1 Solution via the method of steps

Consider the Cauchy problem consisting of the governing PDE (3.1) with boundary conditions (3.2)-(3.4) and initial conditions $u(x,0) = u_0(x)$ and $\partial_t u(x,0) = v_0(x)$. The periodicity conditions (3.5)-(3.6) will be considered later in Section 3.2.1. The d'Alembert function is defined on $[-1,1]$

[1]The variable s is used both in this chapter and in Appendix A to denote the argument of the d'Alembert function, i.e., $f(s)$, in contrast to the use of s in Chapter 2 where it is used to distinguish between periodic solution in the two-dimensional manifold.

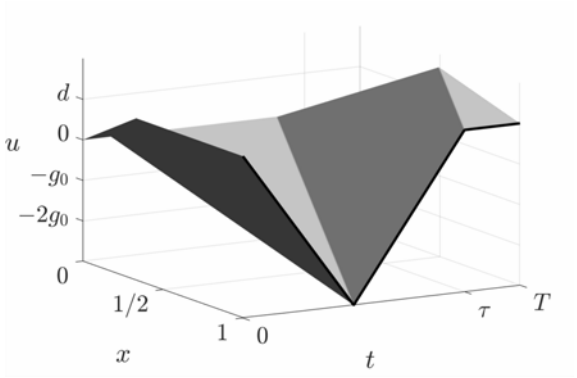

(a) Displacement field $u(x,t) = f(t+x) - f(t-x)$ [ ] with motion of tip of the bar $u(1,t)$ [—]

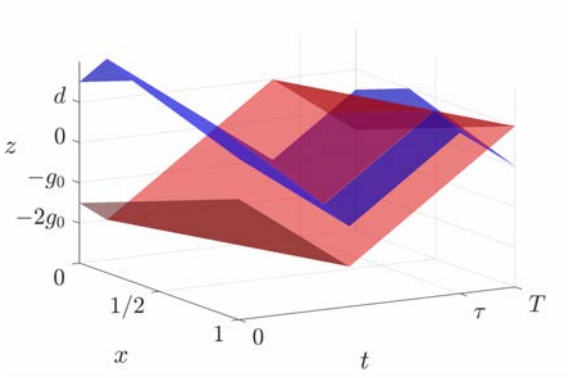

(b) d'Alembert functions from Figure 3.3(a) seen as surfaces: $z(x,t) = f(t+x)$ [ ] and $z(x,t) = f(t-x)$ [ ]

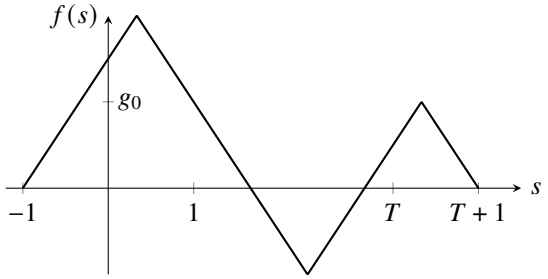

(c) (Piecewise-linear) d'Alembert function $f(s)$ corresponding to Figure 3.3(a)

Figure 3.3: A 1CPP motion from [98] and corresponding d'Alembert function.

as [26, p. 69]

$$2f_0(s) \equiv 2f(s) = \begin{cases} u_0(s) + C_0 + \int_0^s v_0(\zeta)\,\mathrm{d}\zeta & s \in [0,1], \\ -u_0(-s) + C_0 + \int_0^{-s} v_0(\zeta)\,\mathrm{d}\zeta & s \in [-1,0]. \end{cases} \tag{3.10}$$

Our convention (3.9) implies

$$C_0 = u_0(1) - \int_0^1 v_0(\zeta)\,\mathrm{d}\zeta. \tag{3.11}$$

Note that imposing a value on the constant C_0 does not affect any of the fields of interest: displacement $u(x,t)$, velocity $\partial_t u(x,t)$ or stress $\partial_x u(x,t)$. Additionally, the notation f_0 is introduced to describe the part of f depending *exclusively* on initial conditions, i.e., $f_0(s) \equiv f(s)\ \forall s \in [-1,1]$ (as discussed later, the d'Alembert function beyond $s > 1$ depends on both boundary and initial conditions). Therefore, to simplify the terminology used in the remainder of this chapter, f_0 will be referred to as *initial conditions*. Moreover, as the d'Alembert function is assumed to be continuous for $s \in [-1,1]$, the space of initial conditions u_0 and v_0 consists of those generating piecewise-C^1 continuous functions f_0.

As mentioned previously, the d'Alembert function in (3.8) is a solution to (3.1) and (3.2).

However, the boundary condition at $x = 1$ remains unsatisfied. To satisfy boundary conditions at both $x = 1$ and $x = -1$, the d'Alembert function is generally extended from $[-1, 1]$ to $[-1, T + 1]$ via initial conditions using reflections at $s = 1$ and $s = -1$ [26, 67]. In the present article, this extension will be derived by *solving* the boundary conditions Equations (3.3) and (3.4) in terms of the d'Alembert function (omitting inequality constraints)

$$\text{Inactive contact} \quad f'(t+1) + f'(t-1) = 0, \quad t \in [0, \tau] \text{ a.e.} \tag{3.12}$$

$$\text{Active contact} \quad f(t+1) - f(t-1) = g_0, \quad t \in [\tau, T]. \tag{3.13}$$

Collectively, Equations (3.12) and (3.13) represent a degenerate Neutral Delay Differential Equation (NDDE) which requires knowledge of an initial condition on f spanning a domain of length equal to the delay [25]. Namely, to solve (3.12), the d'Alembert function must be known for any $s \in [-1, 1]$. Here, the values of $f(s)$ for $s \in [-1, 1]$ are given by the initial conditions (3.10). Thus, given f_0, Equation (3.12) determines f on $[1, \tau + 1]$ and, consecutively, Equation (3.13) determines f on $[\tau + 1, T + 1]$.

In what follows, we derive the conditions on f_0, τ and T in order to find 1CPP solutions of the cantilever bar. To this end, we use the method of steps to construct solutions to the inactive contact motion (3.12) and active contact motion (3.13), separately, using linear arguments. The nonlinearity of the problem at hand arises when the inequalities in (3.3) and (3.4) together with periodicity conditions (3.5) to (3.6) are enforced on the d'Alembert function.

Inactive Contact Motion

This section details the extension of the d'Alembert function to the domain $s \in [-1, 1 + \tau]$ via boundary condition (3.12). Beforehand, since (a) the tip of the bar is in contact with the wall at the end of the period, see (3.4), (b) the motion must be periodic, see (3.5), and (c) the tip of the bar must be initially in contact with the obstacle to preserve continuity in time from (3.8), the tip of the bar must contact the obstacle at the beginning of the period

$$u(1, 0) = f(1) - f(-1) = f_0(1) - f_0(-1) = f_0(1) = g_0. \tag{3.14}$$

Next, the inactive contact condition (3.12) leads to

$$f'(s) = -f'(s - 2), \quad s \in [1, \tau + 1] \text{ a.e.} \tag{3.15}$$

Integration of (3.15) reads

$$f(s) = g_0 - f(s - 2), \quad \forall s \in [1, \tau + 1]. \tag{3.16}$$

By the method of steps, given $f(s) = f_0(s)$ for $s \in [-1, 1]$, the solution to (3.16) is

$$f(s) = \begin{cases} f_0(s) & s \in [-1, 1] \\ g_0 - f_0(s-2) & s \in [1, \tau+1] \end{cases}, \quad 0 \le \tau \le 2 \tag{3.17}$$

this definition applies strictly to the case of $\tau \le 2$ since the domain of definition of initial conditions is of length 2. Instead, for $2 < \tau \le 4$, we obtain

$$f(s) = \begin{cases} f_0(s) & s \in [-1, 1] \\ g_0 - f_0(s-2) & s \in [1, 3] \\ g_0 - f(s-2) & s \in [3, \tau+1] \end{cases} \tag{3.18}$$

Here, the last component, $f(s) = g_0 - f(s-2)\ s \in [3, \tau+1]$, is determined by substituting the previous step, $f(s) = d - f_0(s-2)\ s \in [1, 3]$, in $f(s-2)$, admitting

$$f(s) = \begin{cases} f_0(s) & s \in [-1, 1] \\ g_0 - f_0(s-2) & s \in [1, 3] \\ f_0(s-4) & s \in [3, \tau+1] \end{cases}, \quad 2 < \tau \le 4. \tag{3.19}$$

A solution of the type (3.19) is illustrated in Figure 3.4. Further extension of the d'Alembert function for $\tau > 4$ is not illustrated because the d'Alembert function subject to (3.15) is 4-periodic

$$f(s) = f(s-4), \quad \forall s \in [3, \tau+1], \quad \tau > 2. \tag{3.20}$$

In fact, an inactive contact motion sets an upper bound on the value of τ for a 1CPP.

Proposition 3.2 (Maximal duration of an inactive contact for a 1CPP)**.** *For 1CPP motions, the duration of inactive contact motion must satisfy*

$$\tau < 4. \tag{3.21}$$

As well, initial conditions must satisfy

$$f_0(s) \ge 0 \quad \forall s \in [-1, \min(1, \tau - 1)], \tag{3.22}$$

$$f_0(s) \le g_0 \quad \forall s \in [-1, \tau - 3] \text{ if } 2 < \tau < 4. \tag{3.23}$$

Proof. Proof for this proposition is provided in section Appendix A.1 □

In turn, the inactive contact phase must end with the bar contacting the obstacle

$$u(1, \tau) = f(\tau + 1) - f(\tau - 1) = g_0 \tag{3.24}$$

and the velocity of the tip at this instant τ must be strictly positive, due to (3.7), such that

$$\partial_t u(1, \tau^-) = f'(\tau^- + 1) - f'(\tau^- - 1) > 0. \tag{3.25}$$

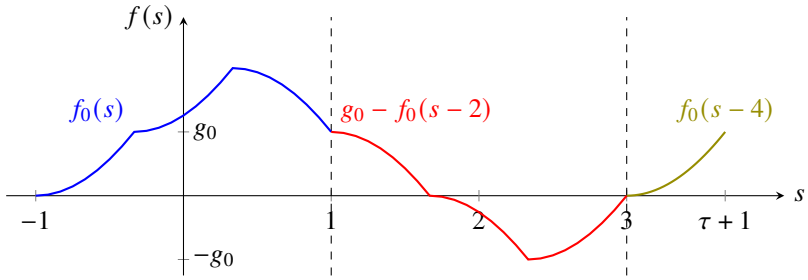

(a) D'Alembert function as defined for $t \in [-1, 3]$. Red and Olive functions represent the extension beyond $t = 1$, via (3.19) and depend on the function in blue

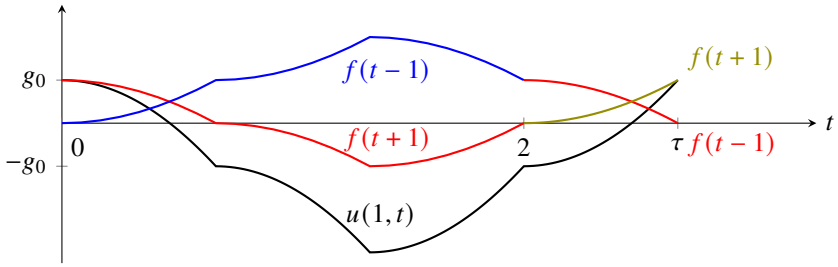

(b) Displacement at tip and d'Alembert function components, $u(1, t) = f(t + 1) - f(t - 1)$ for $t \in [0, 2]$. Colours correspond to plot 3.4(a)

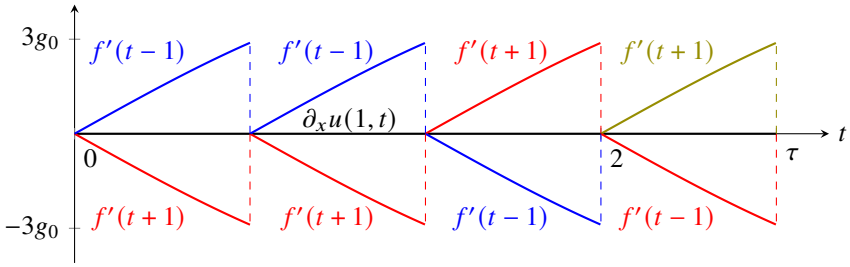

(c) Stress at tip and d'Alembert function components, $\partial_x u(1, t) = f'(t + 1) + f'(t - 1) = 0$ (due to inactive contact), for $t \in [0, 2]$. Colours correspond to plot 3.4(a)

Figure 3.4: Extension of d'Alembert function due to inactive contact conditions (3.15) given specific initial conditions f_0 (here, piecewise-cubic polynomials for the sake of illustration) and $\tau = 7/3 \geq 2$, and resulting motion.

Active contact motion

Similarly to the procedure presented in Section 3.2.1, the d'Alembert function is extended for $s > \tau + 1$ via condition (3.13), which equivalently reads

$$f(s) = g_0 + f(s - 2), \quad \forall s \in [\tau + 1, T + 1]. \tag{3.26}$$

Note that $f(s - 2)$ is assumed to be known for $s \in [\tau + 1, T + 1]$, by virtue of (3.17) or (3.19). An illustration of extension (3.26) is provided in Figure 3.5. Moreover, we note that $u_x(1, t)$ is 2-periodic during active contact since

$$u_x(1, t + 2) = f'(t + 3) + f'(t + 1) = f'(t + 1) + f'(t - 1) = u_x(1, t), \quad t \in [\tau, T] \text{ a.e.} \tag{3.27}$$

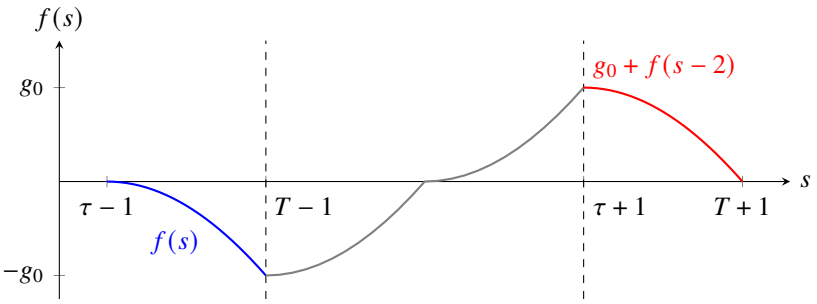

(a) D'Alembert function for $t \in [\tau - 1, T + 1]$. Extension beyond $t = \tau + 1$ via (3.26) [——] dependent on the blue plot

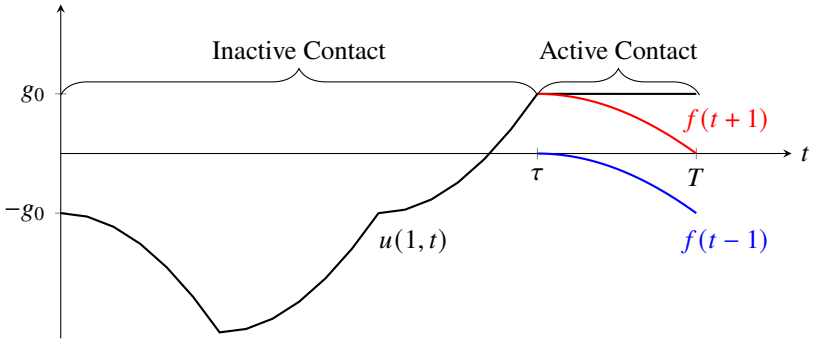

(b) Displacement at tip and d'Alembert function components

Figure 3.5: Extension of the d'Alembert function due to active contact conditions (3.15) given specific initial conditions f_0 and f in inactive contact motion (shown in Figure 3.4) from (3.17) and (3.19), and resulting motion.

holds true. This imposes a bound on the duration $T - \tau$ of active contact.

Proposition 3.3 (Maximal duration of an active contact for a 1CPP)**.** *For 1CPP motions, the duration of active contact motion, $T - \tau$ where $T > \tau$, must satisfy*

$$T - \tau < 2, \tag{3.28}$$

and the d'Alembert function must satisfy

$$f'(t-1) \leq 0 \quad t \in [\tau, T] \text{ a.e.} \tag{3.29}$$

Proof. Proof for this proposition is provided in section Appendix A.2 □

Periodicity and admissibility conditions

The periodicity of the solution is now determined by a difference equation involving the d'Alembert function.

Proposition 3.4. *The displacement u is T-periodic if its associated d'Alembert function satisfies*

$$f'(s+T) = f_0'(s) \quad \forall s \in [-1, 1] \text{ a.e.} \tag{3.30}$$

and f' is T-periodic. Conversely, if (3.30) is fulfilled, then $u(x,t) = f(t+x) - f(t-x)$ consists of a periodic motion. Thus, (3.30) is true if and only if $u(x,t)$ is periodic in time with period T.

Proof. Proof for this proposition is provided in section Appendix A.3 □

Summary of necessary conditions for periodic solutions

Via the d'Alembert travelling wave solutions, the conditions for finding a periodic solution consist of functional equations and inequalities summarized below.

Conditions for Periodic Solutions of the Bar in Unilateral Contact (CPS) *For $g_0 > 0$, a 1CPP motion subject to (3.1)-(3.6) and described by $u(x,t) = f(t+x) - f(t-x)$ requires finding $\tau < 4$, $T < \tau + 2$ and $f_0(s)$ continuous and piecewise C^1 on $[-1,1]$ such that (equation tags are recalled)*

$$f_0(-1) = 0 \tag{3.9}$$

$$f_0(1) = g_0 \tag{3.14}$$

No penetration conditions for** $t \in [0,\tau]$ **($u(1,t) < g_0$):

$$f_0(s) \geq 0 \quad \forall s \in [-1, \min(1, \tau - 1)] \tag{3.22}$$

$$f_0(s) \leq g_0 \quad \forall s \in [-1, \tau - 3] \text{ if } 2 < \tau < 4 \tag{3.23}$$

Positive incoming velocity and contact at** $t = \tau$ **($u(1,\tau) = g_0$, $\partial_t u(1,\tau^-) > 0$):

$$f(\tau + 1) - f(\tau - 1) = g_0 \tag{3.24}$$

$$f'(\tau^- + 1) - f'(\tau^- - 1) > 0 \tag{3.25}$$

Repulsion by obstacle for** $t \in [\tau, T]$ **($\partial_x u(1,t) < 0$):

$$f'(s) \leq 0 \quad s \in [\tau - 1, T - 1] \text{ a.e.} \tag{3.29}$$

Periodicity condition:

$$f'(s + T) - f_0'(s) = 0 \quad \forall s \in [-1, 1] \tag{3.30}$$

where f' is defined by combining (3.17) and (3.26) and then differentiating as

$$\tau \leq 2: \quad f'(s) = \begin{cases} f_0'(s) & s \in [-1, 1] \\ -f_0'(s-2) & s \in [1, \tau + 1] \\ f'(s-2) & s \in [\tau + 1, T + 1] \end{cases} \tag{3.31}$$

or

$$2 \le \tau < 4: \quad f'(s) = \begin{cases} f_0'(s) & s \in [-1, 1] \\ -f_0'(s-2) & s \in [1, 3] \\ f_0'(s-4) & s \in [3, \tau+1] \\ f'(s-2) & s \in [\tau+1, T+1] \end{cases} \tag{3.32}$$

While a complete closed-form solution to the CPS could not be found, it will be shown that the CPS can be solved for some cases.

3.3 Non-smooth modal analysis

3.3.1 Piecewise-linear mode

In this section, the CPS are solved to find the NSM in [12, 97] where it was proven that NSMs parametrized by the period must be piecewise-linear. Such mode is known to exist for $T \in (3, 4)$ and $\tau \in (2, 4)$ [97], see Figure 3.6 for the initial conditions

$$u_0(x) = \frac{g_0 x}{3 - T}, \quad v_0(x) = 0 \quad \forall x \in [0, 1]. \tag{3.33}$$

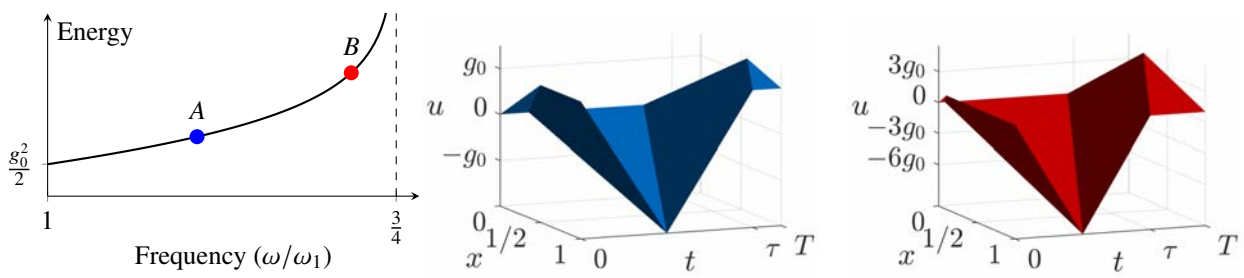

(a) Frequency energy plot (b) Motion at point A (c) Motion at point B

Figure 3.6: NSM found in [12, 97]. In plot (a): $\omega = 2\pi/T$ and $\omega_1 = 2\pi/4$.

To find this piecewise-linear mode via the CPS, periods $T \in (3, 4)$ and inactive contact durations $\tau \in (2, 4)$, with $2 > T - \tau > 0$. For $\tau \in (2, 4)$, the d'Alembert function is described by (3.32) and its last component, $f'(s) \in [\tau + 1, T + 1]$, is defined implicitly by previous components. Here, we will define the last component *explicitly* in $f_0'(s)$ using the requirement $T \in (3, 4)$. We first note that for $T \in (3, 4)$ and $\tau \in (2, 4)$ the argument of the last component in (3.32), $s - 2 \in [\tau + 1, T + 1]$, must span $s - 2 \in [3, 5]$ (or $s \in [1, 3]$). Therefore, the last component of f is determined exclusively

by $f(s)$ for $s \in [1,3]$. Namely, for $\tau \in (2,4)$ and $T \in (3,4)$, we obtain

$$f'(s) = \begin{cases} f_0'(s) & s \in [-1,1] \\ -f_0'(s-2) & s \in [1,3] \\ f_0'(s-4) & s \in [3,\tau+1] \\ f'(s-2) & s \in [\tau+1, T+1] \end{cases} = \begin{cases} f_0'(s) & s \in [-1,1] \\ -f_0'(s-2) & s \in [1,3] \\ f_0'(s-4) & s \in [3,\tau+1] \\ -f_0'(s-4) & s \in [\tau+1, T+1] \end{cases} \tag{3.34}$$

without loss of generality. Before plugging Expression (3.34) into the CPS, we determine the appropriate space of functions for f_0. Here, since the sought NSM consists of piecewise linear displacements, it is assumed that f_0 consists of piecewise-linear functions. Next, the loci of non-smoothness in f_0 are determined. This is done by noting the CPS conditions (3.23) and (3.29) apply for two adjacent non-overlapping domains: $[-1, \tau-3]$ and $[\tau-3, T-3]$. Thus, it is trivial to assume that loci of non-smoothness are $\tau-3$ and $T-3$. Accordingly, we dissect f_0 into three parts spanning $[-1,\tau-3]$, $[\tau-3, T-3]$, and $[T-3, 1]$ to obtain a piecewise-linear and continuous function

$$f_0(s) = \begin{cases} a_0 + b_0 s & s \in [-1, \tau-3] \\ a_0 + b_0(\tau-3) + b_1(s-\tau+3) & s \in [\tau-3, T-3] \\ a_0 + b_0(\tau-3) + b_1(T-\tau) + b_2(s-T+3) & s \in [T-3, 1]. \end{cases} \tag{3.35}$$

Then, the piecewise-linear f_0 (3.35) is plugged into the CPS conditions such that

$$\text{Eq.}(3.9) \quad \Rightarrow \quad a_0 = b_0 \tag{3.36}$$

$$\text{Eq.}(3.22, 3.23, 3.24) \quad \Rightarrow \quad b_0 = g_0/(\tau-2) \tag{3.37}$$

$$\text{Eq.}(3.14, 3.36, 3.38) \quad \Rightarrow \quad b_2 = -b_1(T-\tau)/(4-T) \tag{3.38}$$

$$\text{Eq.}(3.24, 3.25, 3.29) \quad \Rightarrow \quad b_1 > 0. \tag{3.39}$$

Expressions (3.36)-(3.38) are plugged back into (3.35), itself inserted in (3.34), to form an expression

of f dependent on b_1, τ and T only

$$f(s) = \begin{cases} \frac{g_0}{\tau-2}(s+1) & s \in [-1, \tau-3] \\ g_0 + b_1(s-\tau+3) & s \in [\tau-3, T-3] \\ g_0 + b_1\frac{(T-\tau)}{4-T}(1-s) & s \in [T-3, 1] \\ g_0 - \frac{g_0}{\tau-2}(s-1) & s \in [1, \tau-1] \\ -b_1(s-\tau+1) & s \in [\tau-1, T-1] \\ -b_1\frac{(T-\tau)}{4-T}(3-s) & s \in [T-1, 3] \\ \frac{g_0}{\tau-2}(s-3) & s \in [3, \tau+1] \\ g_0 - b_1(s-\tau-1) & s \in [\tau+1, T+1]. \end{cases} \tag{3.40}$$

It is noted that the first component of f does not depend on b_1 since Equations (3.9) (which defines the reference point for f) and (3.24) (which establishes contact with the rigid wall at the beginning of the active contact motion) are sufficient to determine the constants a_0 and b_0.

Next, we will show that the free parameter b_1 becomes a mono-valued function of τ as soon as periodicity is enforced. For the d'Alembert function, periodicity (3.30) reads

$$f_p'(s) \equiv f'(s+T) = f_0'(s) \quad \forall s \in [-1, 1] \tag{3.41}$$

where f_p denotes the section of the d'Alembert function defining the motion at the end of the period. Based on the d'Alembert function (3.40), f_p' reads

$$f_p'(s) = \begin{cases} b_1 & s \in [-1, 3-T] \\ \frac{g_0}{\tau-2} & s \in [3-T, \tau-T+1] \\ -b_1 & s \in [\tau-T+1, 1] \end{cases} \tag{3.42}$$

and, accordingly, f_0 reads

$$f_0'(s) = \begin{cases} \frac{g_0}{\tau-2} & s \in [-1, \tau-3] \\ b_1 & s \in [\tau-3, T-3] \\ -b_1 & s \in [T-3, 1]. \end{cases} \tag{3.43}$$

Naturally, the first requirement for equality of f_p and f_0 is that their loci of non-smoothness will be congruent. Currently, the components in (3.42) and (3.43) do not span identical domains. It is chosen to establish a relationship between τ and T such that the loci of non-smoothness align. Here, equality between f_p and f_0 can be enforced as soon as the domains of definition (or support) of the last component of each function are identical, i.e., $T-3 = \tau - T + 1$ or

$$2T(\tau) = \tau + 4. \tag{3.44}$$

This relationship also agrees with the piecewise-linear mode in [97] reproduced in this section. Furthermore, it can be easily noted that at $s = -1$, a periodic solution requires $f_p'(-1^+) = f_0'(-1^+)$

$$f_0'(-1^+) = b_1(\tau) = \frac{g_0}{\tau - 2} = f_p'(-1^+) \tag{3.45}$$

Plugging Equations (3.44) and (3.45) into (3.42) and (3.43), we note that the periodicity conditions are indeed satisfied

$$f_0'(s) = f_p'(s) = \frac{g_0}{2T(\tau) - 6} \begin{cases} 1 & s \in [-1, T(\tau) - 3] \\ -1 & s \in [T(\tau) - 3, 1] \end{cases} \tag{3.46}$$

for arbitrary $T \in (3, 4)$. The necessary initial conditions for the NSM are obtained by integrating Equation (3.46)

$$f_0(s) = \frac{g_0}{2T(\tau) - 6} \begin{cases} s + 1 & s \in [-1, T(\tau) - 3] \\ 2T(\tau) - 5 - s & s \in [T(\tau) - 3, 1] \end{cases} \tag{3.47}$$

Thus, any initial condition (3.47), for the aforementioned T and τ, generates a periodic motion. This piecewise-linear mode is now properly defined.

NSM1: Piecewise-Linear Mode of the Cantilever Bar in Unilateral Contact *Given $g_0 > 0$, $u(x,t) = f(t+x) - f(t-x)$ with f such that*

$$f(s) = \frac{d}{2T - 6} \begin{cases} s + 1 & s \in [-1, T - 3] \\ 2T - 5 - s & s \in [T - 3, T - 1] \\ s - 3 & s \in [T - 1, 2T - 3] \\ 4T - 9 - s & s \in [2T - 3, T + 1] \end{cases} \tag{3.48}$$

represents a non-smooth nonlinear mode for all $T \in (3, 4)$[2].

To show NSM1 is equivalent to the piecewise-linear mode introduced in [97], it is noted that NSM1 at $t = T - 2$ generates the displacement and velocity fields

$$\begin{aligned} u(x, T-2) &= f(T - 2 + x) - f(T - 2 - x) \\ &= \frac{g_0}{2T - 6}(T - 3 - x) - \frac{g_0}{2T - 6}(2T - 3 + x) = -\frac{g_0 x}{T - 3}, \ \forall x \in [0, 1] \end{aligned} \tag{3.49}$$

$$\begin{aligned} \partial_t u(x, T-2) &= f'(T - 2 + x) - f'(T - 2 - x) \\ &= -\frac{g_0}{2T - 6} + \frac{g_0}{2T - 6} = 0, \ \forall x \in [0, 1] \end{aligned} \tag{3.50}$$

which agree with (3.33). Since the solution is unique with respect to initial condition [73], NSM1 is

[2]Note that any reference to τ has been omitted as it is not critical for illustrating the mode NSM1.

indeed equivalent to the piecewise-linear mode presented in [97]. Furthermore, we note that NSM1 exists for both rational and irrational periods in $(3, 4)$. This fact has been also established in [12] where it is stated that a continua of periodic solutions spanning different periods must consist of piecewise-linear displacements. However, it has been speculated that for the case of rational T, families of periodic solutions that are not piecewise-linear may exist. Here, using the d'Alembert formulation and the CPS, we have found these families of periodic solutions.

3.3.2 Piecewise-smooth mode(s) of the same period

For $T \in \mathbb{Q}$, previous works have only reported piecewise-linear modes [12, 97]. Here, it is shown that piecewise-smooth solutions exist as well. In fact, these solution play a big role in identifying the modal space of the cantilever in unilateral contact and exhibit some of the difficulties expected in numerical approaches to nonsmooth modal analysis. This section details a methodology for determining analytically these piecewise-smooth modes. An illustrative example is provided.

Assume that both T and τ belong to $\mathbb{Q}$ such that T and τ can be described by n, $p < n$, and m belonging to $\mathbb{N}$, namely,

$$T = n/m, \quad \tau = p/m. \tag{3.51}$$

To accommodate for the CPS conditions spanning non-uniform domains, such that no penetration conditions (3.22)-(3.23) and negative repulsion force condition (3.29) are satisfied, it was found useful to dissect f_0 into $2m$ equal components, each consisting of a smooth function $a_i(s)$

$$f_0(s) = \begin{cases} a_0(s+1) & s \in [-1, -1+1/m] \\ a_1(s+1-1/m) & s \in [-1+1/m, -1+2/m] \\ \vdots & \\ a_i(s+1-i/m) & s \in [-1+i/m, -1+(i+1)/m] \\ \vdots & \\ a_{2m-1}(s-1+1/m) & s \in [1-1/m, 1] \end{cases} \tag{3.52}$$

where the functions a_i have the following features:

$$a_i : [0, 1/m] \mapsto [0, g_0], \quad i = 0, 1, \ldots, p-2m-1 \tag{3.53}$$

$$a_i : [0, 1/m] \mapsto [0, \infty) \quad i = p-2m, p-2m+1, \ldots, 2m-1. \tag{3.54}$$

These functions can be nonlinear in s in contrast with (3.35) where a_0 stands for a constant. The condition $a_i(s) \geq 0$ is a consequence of (3.22). In this manuscript, only 1CPP with $\tau > 2$ are considered so $a_i(s) \leq g_0$ from (3.23). Moreover, to preserve the continuity of f_0, the following must hold: $a_{i-1}(1/m) = a_i(0)$ for all $i = 1, 2, \ldots, 2m-2$. This dissection of f_0 allows then for an

easy depiction of the solution space of the CPS for $T \in \mathbb{Q}$.

As an example, a solution for $n = 10$, $p = 8$ and $m = 3$, i.e., inactive motion duration $\tau = 8/3$ and period $T = 10/3$, is derived in the remainder of this section (for other choice of parameters p, n and m this method may fail as further discussed in Section 3.3.4).

First, the periodicity condition (3.30) of the CPS is solved. For $\tau = 8/3$ and $T = 10/3$, $f'(s+T)$ is derived via Equation (3.32) and reads (derivation has been omitted for the sake of conciseness)

$$f'(s+T) = \begin{cases} -a_4'(s+1) & s \in [-1, -2/3] \\ -a_5'(s+1) & s \in [-2/3, -1/3] \\ a_0'(s+1/3) & s \in [-1/3, 0] \\ a_1'(s) & s \in [0, 1/3] \\ -a_2'(s-1/3) & s \in [1/3, 2/3] \\ -a_3'(s-2/3) & s \in [2/3, 1] \end{cases} \tag{3.55}$$

while the initial condition reads

$$f_0'(s) = \begin{cases} a_0'(s+1) & s \in [-1, -2/3] \\ a_1'(s+2/3) & s \in [-2/3, -1/3] \\ a_2'(s+1/3) & s \in [-1/3, 0] \\ a_3'(s) & s \in [0, 1/3] \\ a_4'(s-1/3) & s \in [1/3, 2/3] \\ a_5'(s-2/3) & s \in [2/3, 1]. \end{cases} \tag{3.56}$$

Then, Equation (3.30) can be easily solved by equating each of the components in $f_0(s)$ to their corresponding components in $f(s+T)$ admitting

$$a_0'(s) = -a_4'(s) = a_2'(s), \quad \forall s \in [0, 1/3] \tag{3.57}$$

$$a_1'(s) = -a_5'(s) = a_3'(s), \quad \forall s \in [0, 1/3]. \tag{3.58}$$

From conditions (3.57) and (3.58), it is gathered that f_0 such that a periodic solution ensues depends solely on the choice of $a_0(s)$ and $a_1(s)$. Thus, applying all other conditions in the CPS (besides the already solved periodicity condition), a non-smooth mode is obtained as described below.

NSM2: Piecewise-Smooth Mode of the Cantilever Bar in Unilateral Contact *For an inactive contact duration $\tau = 8/3$ and period $T = 10/3$, the arbitrary piecewise-smooth functions $a_0(s)$ and*

$a_1(s)$ *in the domain* $s \in [0, 1/3]$*, with the constraints*

$$\textit{Continuity of } f_0\text{:} \quad a_0(1/3) = a_1(0) \tag{3.59}$$

$$\textit{Eq.}(3.9, 3.24): \quad a_0(0) = 0 \tag{3.60}$$

$$\textit{Eq.}(3.14): \quad a_1(1/3) = g_0 \tag{3.61}$$

and, recalling the remaining CPS conditions,

$$\textit{Eq.}(3.25) \quad \Rightarrow \quad a_0'(0) > 0 \tag{3.62}$$

$$\textit{Eq.}(3.22, 3.23, 3.29) \quad \Rightarrow \quad 0 < a_0(s) \leq g_0, \quad \forall s \in [0, 1/3] \tag{3.63}$$

$$\textit{Eq.}(3.22, 3.23, 3.29) \quad \Rightarrow \quad 0 \leq a_1(s) \leq g_0, \quad \forall s \in [0, 1/3] \tag{3.64}$$

define a non-smooth mode with $u(x,t) = f(t+x) - f(t-x)$ *where* f *is defined in* (3.32) *with initial condition*

$$f_0(s) = \begin{cases} a_0(s+1) & s \in [-1, -2/3] \\ a_1(s+2/3) & s \in [-2/3, -1/3] \\ g_0 + a_0(s+1/3) & s \in [-1/3, 0] \\ g_0 + a_1(s) & s \in [0, 1/3] \\ 2g_0 - a_0(s-1/3) & s \in [1/3, 2/3] \\ 2g_0 - a_1(s) & s \in [2/3, 1]. \end{cases} \tag{3.65}$$

NSM2 consists of periodic motions existing exclusively for $T = 10/3$. Two distinct NSM2 motions are shown in Figure 3.7. From conditions (3.59)-(3.64) on functions a_0 and a_1, we understand that NSM2 exists in a convex (because of inequalities) subspace of $(C^1[0, 1/3])^2$. In turn, using the procedure presented in this section with different m, n and p, similar mode can be derived for any period of the type $T \in \mathbb{Q}$ and $\tau \in \mathbb{Q}$. However, for some values of m, n and p, the proposed methodology could not generate periodic solutions.

3.3.3 Piecewise-monotonic mode

While most of this chapter consists of findings published in [89], this section provides original content and complements the findings of the author in [89].

It has been found that by restricting the definition of the $a_i(s)$ functions in (3.52) to a single differentiable monotonic function $\eta(s) \in C^1[0; 1/m]$ and coefficients c_i allows derivation of a piecewise-monotonic mode existing on each rational period $T \in (3, 4)$. The main importance of this section is to provide a concrete example of a piecewise-smooth mode and to also show that piece-monotonic mode exist for the dense group $T \in \mathbb{Q}(3, 4)$.

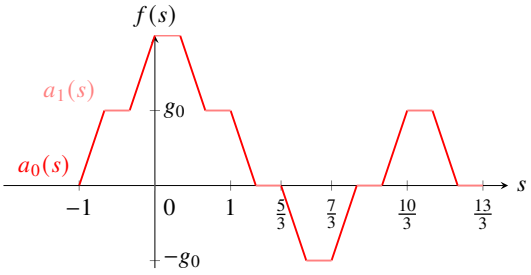

(a) D'Alembert function for $a_0(s) = 3g_0 s$ and $a_1(s) = g_0$

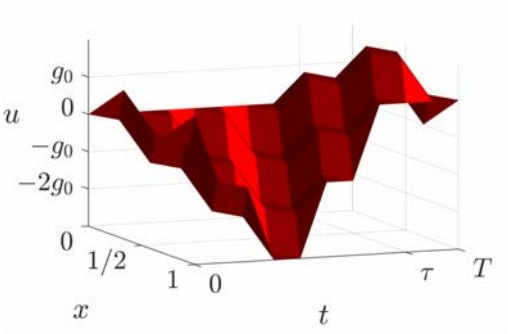

(b) Displacement field

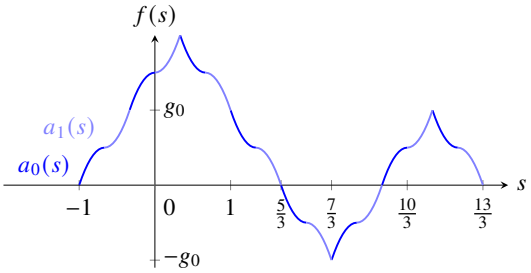

(c) d'Alembert function for $a_0(s) = -4.5g_0((s-1/3)^2 - (1/3)^2)$ and $a_1(s) = 4.5g_0 s^2 + 0.5g_0$

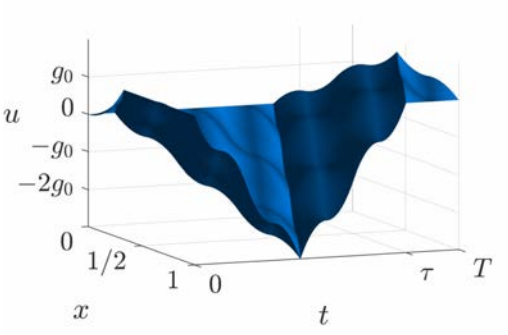

(d) Displacement field

Figure 3.7: Periodic motions belonging to NSM2. The location of these motions in the FEP will be presented later in Figure 3.8.

The derivation of the piecewise monotonic mode starts by restricting the set of variables $a_i(s)$. Here, $a_i(s) = c_i\eta(s)$ for $i = 0, 1, \ldots, 2m-1$ are plugged into the space of initial condition in (3.52) to admit

$$\eta(0) = 0, \quad \eta(s) \in C^1[0; 1/m] \tag{3.66}$$

$$f_0(s) = \begin{cases} c_0\eta(s+1) & s \in [-1, -1+1/m] \\ c_0\eta(1/m) + c_1\eta(s+1-1/m) & s \in [-1+1/m, -1+2/m] \\ \eta(1/m)\displaystyle\sum_{i=0}^{1} c_i + c_2\eta(s+1-2/m) & s \in [-1+2/m, -1+2/m] \\ \vdots & \\ \eta(1/m)\displaystyle\sum_{i=0}^{j-1} c_i + c_j\eta(s+1-j/m) & s \in [-1+j/m, -1+(j+1)/m] \\ \vdots & \\ \eta(1/m)\displaystyle\sum_{i=0}^{2m-2} c_i + c_{2m-1}\eta(s-1+1/m) & s \in [1-1/m, 1] \end{cases} \tag{3.67}$$

Here, the restriction in Equation (3.66) is introduced to answer the CPS condition (3.9): $f(-1) = 0$. Note that the formulation of $f_0(s)$ suggested in Equation (3.67) does not constitute an approximation and does not affect the accuracy of the solution. In fact, all the solutions developed here are exact and admissible 1CPP solutions of the cantilever bar.

In what follows, the CPS problem conditions will be formulated in terms of and solved for c_i and $\eta(s)$ such that a NSM can be concisely defined. Furthermore, it will be shown that the solutions to the CPS problem largely depend on c_i, and $\eta(s)$ can exist in a subspace of monotonic smooth functions. At last, to simplify the following derivation, the piecewise smooth modes consist of motions with $\tau \in (2, 4)$ and $T \in (3, 4)$ (or $2m < p < 4m$ and $3m < n < 4m$) such that the formulation of the d'Alembert function in Equation (3.34) applies (other ranges of τ and T were not explored).

In order to formulate the CPS conditions, the d'Alembert function $f(s)$ is generated by the initial conditions (3.67) via expression (3.34), applicable for $\tau \in [2, 4]$ (the derivation has been omitted for the sake of conciseness)

$$f(s) = \begin{cases} c_0\eta(s+1) & s \in [-1, -1+1/m] \\ c_0\eta(1/m) + c_1\eta(s+1-1/m) & s \in [-1+1/m, -1+2/m] \\ \eta(1/m)\displaystyle\sum_{i=0}^{1} c_i + c_2\eta(s+1-2/m) & s \in [-1+2/m, -1+2/m] \\ \vdots & \\ \eta(1/m)\displaystyle\sum_{i=0}^{2m-2} c_i + c_{2m-1}\eta(s-1+1/m) & s \in [1-1/m, 1] \\ \eta(1/m)\displaystyle\sum_{i=0}^{2m-1} c_i + b_0\eta(s-1) & s \in [1, 1+1/m] \\ \eta(1/m)\left(\displaystyle\sum_{i=0}^{2m-1} c_i + b_0\right) + b_1\eta(s-1-1/m) & s \in [1+1/m, 1+2/m] \\ \vdots & \\ \eta(1/m)\left(\displaystyle\sum_{i=0}^{2m-1} c_i + \sum_{i=0}^{n-2} b_i\right) + b_{n-1}\eta(s-T-1+1/m) & s \in [T+1-1/m, T+1] \end{cases} \tag{3.68}$$

where the variables b_i are introduced to simplify the notation and are described by the scheme

$$b_i = \begin{cases} -c_i & i = 0, 1, \ldots, 2m-1 \\ -b_{i-2m} & i = 2m, 2m+1, \ldots, p-1 \\ b_{i-2m} & i = p, p+1, \ldots, n-1. \end{cases} \tag{3.69}$$

It is noted that b_i are always fully defined if the coefficients c_i are defined. In this section, the matrix presentation of the scheme (3.69) will be useful to derive the NSMs

$$\mathbf{b} = \mathbf{R}(m, n, p)\mathbf{c} \tag{3.70}$$

where $\mathbf{R}(m, n, p)$ is a rectangular $n \times 2m$ matrix.

Next, using the $f(s)$ defined in (3.68) and (3.70), the periodicity conditions (3.30) can be expressed as follows:

$$b_{i+n-2m-1}\eta'(s) = c_i\eta'(s), \quad i = 0, 1, \ldots, 2m-1, \quad s \in [0, 1/m] \tag{3.71}$$

where the term $\eta'(s)$ can be omitted without loss of generality

$$b_{i+n-2m-1} = c_i \quad i = 0, 1, \ldots, 2m-1. \tag{3.72}$$

Next, Equation (3.70) is plugged into (3.72) to formulate the periodicity conditions in c_i exclusively

$$\sum_{j=0}^{2m-1} \mathrm{R}_{i+n-2m,j}(m, n, p)c_j = c_i \quad i = 0, 1, \ldots, 2m-1. \tag{3.73}$$

The remainder of the CPS conditions are constructed in terms of c_i, b_i and $\eta(s)$ where all functional inequalities apply for $s \in (0, 1/m)$

$$Eq.(3.14): \quad \eta(1/m)\left(\sum_{i=0}^{2m-1} c_i\right) = g_0 \tag{3.74}$$

$$Eq.(3.24): \quad \eta(1/m)\sum_{i=p-2m}^{p-1} b_i = g_0 \tag{3.75}$$

$$Eq.(3.22): \quad c_j\eta(s) \geq -\eta(1/m)\sum_{i=0}^{j-1} c_i, \quad j = 0, 1, \ldots, 2m-1 \tag{3.76}$$

$$Eq.(3.23): \quad c_j\eta(s) + \eta(1/m)\sum_{i=0}^{j-1} c_i \leq g_0, \quad j = 0, \ldots, p-3m-1 \tag{3.77}$$

$$Eq.(3.25): \quad \eta'(1/m)b_{p-2m-1} < \eta'(1/m)b_{p-1} \tag{3.78}$$

$$Eq.(3.29): \quad b_{i-2m-1}\eta'(s) \leq 0, \quad i = p+1, p+2, \ldots, n \tag{3.79}$$

Here, conditions (3.74) to (3.79) can be simplified into expressions exclusively in $\mathbf{c}$ by restricting the choice of functions $\eta(s)$ to monotonically increasing functions such that

$$\eta(0) = 0, \quad \eta(1/m) = 1, \quad \eta'(s) > 0 \quad \forall s \in (0, 1/m). \tag{3.80}$$

Plugging restrictions (3.80) and the relation (3.70) into conditions (3.74) to (3.79) admits

$$Eq.(3.14): \quad \sum_{i=0}^{2m-1} c_i = g_0 \tag{3.81}$$

$$Eq.(3.24): \quad \sum_{i=p-2m}^{p-1} \sum_{j=0}^{2m-1} R_{ij} c_j = g_0 \tag{3.82}$$

$$Eq.(3.22): \quad \sum_{i=0}^{j} c_i \geq 0, \quad j = 0, 1, \ldots, 2m-1 \tag{3.83}$$

$$Eq.(3.23): \quad \sum_{i=0}^{j} c_i \leq g_0, \quad j = 0, 1, \ldots, p-3m-1 \tag{3.84}$$

$$Eq.(3.25): \quad \sum_{j=0}^{2m-1} R_{p-2m-1,j} c_j < \sum_{j=0}^{2m-1} R_{p-1,j} c_j \tag{3.85}$$

$$Eq.(3.29): \quad \sum_{j=0}^{2m-1} R_{ij} c_j \leq 0, \quad i = p+1, p+2, \ldots, n. \tag{3.86}$$

To simplify the notation, the CPS conditions in $\mathbf{c}$ (Equation (3.73) and Equations (3.81) to (3.86)) are collectively presented using the matrix notation

$$Eq.(3.73, 3.81, 3.82): \quad \mathbf{G}_1(m,n,p)\mathbf{c} = g_0 \mathbf{g}_1 \tag{3.87}$$

$$Eq.(3.83, 3.84, 3.86): \quad \mathbf{G}_2(m,n,p)\mathbf{c} \geq g_0 \mathbf{g}_2 \tag{3.88}$$

$$Eq.(3.85): \quad \mathbf{G}_3(m,n,p)\mathbf{c} > \mathbf{0} \tag{3.89}$$

where $\mathbf{G}_1$ is a rectangular matrix $(2m+2) \times 2m$ and $\mathbf{g}_1$ is a vector of size $2m+2$. In turn, $\mathbf{G}_2$ is a rectangular matrix of size $(n-m+1) \times 2m$, $\mathbf{g}_2$ is a vector of size $n-m+1$, and $\mathbf{G}_3$ is a vector of size $1 \times 2m$.

It is noted that since $\eta(s)$ does not participate in the CPS conditions (3.87) to (3.89), any $\eta(s)$ such that (3.80) holds generates a valid 1CPP solution given that $\mathbf{c}$ answers (3.87) to (3.89). In fact, since there exist infinitely many functions $\eta(s)$ satisfying (3.80) (e.g., $\eta(s) = (ms)^{\zeta}$ with $\zeta \in (0, \infty)$), determining $\mathbf{c}$ such that expressions (3.87) to (3.89) hold true is equivalent to determining a piecewise-monotone mode.

NSM3: Piecewise-Monotonic Mode of the Cantilever Bar in Unilateral Contact *Consider m, n and p belonging to $\mathbb{N}$ and defining the inactive contact duration $\tau = p/m \in \mathbb{Q}(2,4)$ and period $T = n/m \in \mathbb{Q}(3,4)$. If there exists $\mathbf{c} \in \mathbb{R}^{2m}$ such that expressions (3.87) to (3.89) hold, then any $\eta(s)$ subject to restriction (3.80) generates a NSM via the initial conditions (3.67). The corresponding motions on NSM3 are then described via $u(x,t) = f(t+x) - f(t-x)$ where f is*

defined in Equation (3.32).

The restrictions applied here on the space of initial conditions (3.67) has allowed to transform the CPS from a set of conditions including functional equations into a linear system of equalities and inequalities (3.87) to (3.89). The system can be indeed solved for some choices of m, $3m < n < 4m$ and $2m < p < 4m$. In this manuscript, the problem described by (3.87) to (3.89) is not solved directly, but a subgroup of its solutions is explored. Nevertheless, it is possible to solve the problem in (3.87) to (3.89) using analytical tools.

For example, the system of linear equations (3.87) can be first solved via the reduced row echelon form. For different m, n and p, Equation (3.87) can exhibit no solutions, unique solutions or infinitely many solutions (characterized by one or more free variables in $\mathbf{c}$). In the case of unique solutions, it is important to verify whether inequalities (3.88) and (3.89) are satisfied. If not, the solution is rejected. Otherwise, in the case of infinitely many solutions, the free variables can be adjusted such that inequalities (3.88) and (3.89) are satisfied.

Next, instead of solving the CPS conditions (3.87) to (3.89), a subgroup of NSM3 is derived using NSM1 (which is available in its closed-form in Equation (3.50)).

Notable NSM3 solutions

In what follows, a subspace of NSM3 will be built by analysis of motions from NSM1. To clarify, it is possible to show that motions on NSM1 (particularly those exhibiting $T \in \mathbb{Q}(3,4)$) belong to NSM3 with $\eta(s) = ms$ (i.e., linear monotonic functions). Then, the constants $\mathbf{c}$ are extracted and are used to build other piecewise-monotonic modes with the same $\mathbf{c}$ but different $\eta(s)$. Indeed, this approach allows to extract important conclusions about the modal space of the internally resonant bar in unilateral contact.

The problem presented in (3.87) to (3.89) is derived from the CPS. Therefore, if the initial conditions $f_0(s)$ of a given 1CPP motion with $T \in (3,4)$ and $\tau \in (2,4)$ can be put in the form of an NSM3 initial condition (described in Equation (3.67)), this motion belongs to NSM3 (since it satisfies the CPS conditions by definition).

Indeed, the initial conditions $f_0(s)$ generating NSM1 on rational periods $T = n/m$ can be always formulated in the form (3.67) and constitutes a subspace of NSM3. For example, the initial condition of NSM1 motion (3.48) on $T = 3.5$ reads

$$f_0(s) = g_0 \begin{cases} s+1 & s \in [-1, 1/2] \\ 2-s & s \in [1/2, 1] \end{cases} \tag{3.90}$$

can be put in terms of (3.67) with $m = 2$, $n = 7$ and $p = 6$ by choosing $\eta(s) = 2s$ and $c_0 = c_1 = c_2 = g_0/2$ and $c_3 = -g_0/2$ which satisfy $\mathbf{G}_1(2,7,6)\mathbf{c} = g_0\mathbf{g}_1$, $\mathbf{G}_2(2,7,6)\mathbf{c} \geq g_0\mathbf{g}_2$

and $\mathbf{G}_3(2,7,6)\mathbf{c} > \mathbf{0}$ (elaboration of these equalities and inequalities is omitted for the sake of conciseness).

Furthermore, since the constants $\mathbf{c}$ answer the CPS (3.87) to (3.89), a mode of the type NSM3 can be generated by the initial conditions for $\eta(s) = 2s$

$$f_0(s) = \frac{g_0}{2}\begin{cases} \eta(s+1) & s \in [-1,-1/2] \\ 1+\eta(s+1/2) & s \in [-1/2,0] \\ 2+\eta(s) & s \in [0,1/2] \\ 3-\eta(s-1/2) & s \in [1/2,1] \end{cases} = g_0 \begin{cases} s+1 & s \in [-1,-1/2] \\ s+1 & s \in [-1/2,0] \\ s+1 & s \in [0,1/2] \\ 2-s & s \in [1/2,1] \end{cases} \tag{3.91}$$

The above procedure can be generalized for all motion of NSM1 with periods $T \in \mathbb{Q}(3,4)$, and the subspace of NSM3 is formed in Proposition 3.5.

Proposition 3.5. *Consider the set of rational periods $T = n/m \in (3,4)$ and $\tau = p/m$ where $p = 2n - 4m$. The constants*

$$c_i = \frac{g_0}{2n-6m}\begin{cases} 1 & i = 0,1,\ldots,n-2m-1 \\ -1 & i = n-2m, n-2m+1,\ldots,2m-1 \end{cases} \tag{3.92}$$

always answer conditions (3.87) to (3.89) and, therefore, generate NSM3 modes.

Proof. Proof for this proposition is provided in section Appendix A.4 □

Effectively, Proposition 3.5 details a NSM parametrized by $\eta(s)$ (subject to (3.80)) for every rational period $T \in \mathbb{Q}[3,4]$. An example of these modes is found in Figures 3.8 and 3.9. Note that the found NSMs include also the NSM1 modes at their lowest energy. From Figure 3.8, it can be noted that the modal space of the internally resonant bar is highly dense including many branches connecting to the main NSM1 branch at every rational period. In fact, it can be conjured to be even denser than presented in Figure 3.8 since the presented modes belong to a subspace of NSM3 which is, in itself, a subspace of all CPS solutions. This density of the modal space, while an interesting topic in itself, has also repercussions on the development of nonsmooth modal analysis techniques. These will be discussed in the following section.

3.3.4 Applications to non-smooth modal analysis

Via the d'Alembert function, novel NSMs, see NSM2 and NSM3, were derived. While non-smooth modes of the bar in unilateral contact were considered to consist mainly of piecewise-linear functions [12, 84, 97], it has been shown that other piecewise-smooth solutions may exist as well.

Theorem 3.6. *There exist piecewise-smooth modes of the cantilever bar in unilateral contact which are not necessarily piecewise-linear.*

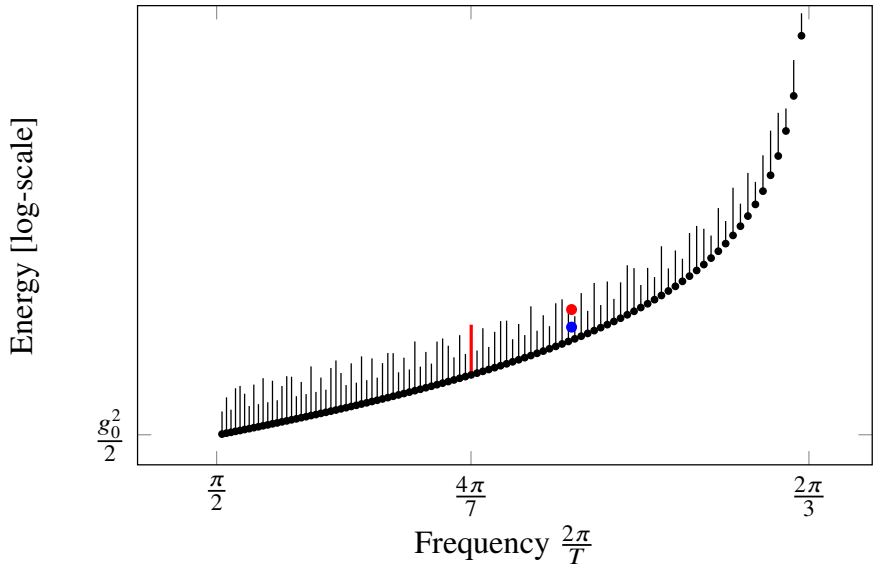

Figure 3.8: FEP of the backbone curves of NSMs satisfying Proposition 3.5 for $T_i = 3.01, 3.02, \ldots, 3.99$ and $\eta(s) = (1-\zeta)(ms)^6 + \zeta ms$ with $\zeta = (0, 1]$ (the value bounds are chosen such that condition (3.80) holds). Black lines [—] denote the NSM3 modes. Black dots [•] denotes NSM1 motions occurring for $\zeta = 1$. The red dot [•] the NSM2 motion in Figures 3.7(a) and 3.7(b) and the blue dot [•] indicates the NSM2 motion in Figures 3.7(c) and 3.7(d). The red lines [—] represent the family of 1CPP in Figure 3.9.

Proof. An example of such piecewise smooth mode is NSM2 in Section 3.3.2. Using the same methodology as presented in 3.3.2, with different values p, n and m, it is possible to find other modes of the same type (see Section 3.3.3 for a more simplified methodology). □

Conjecture 3.7. *For all $T \in \mathbb{Q}$ where a periodic motion of the cantilever bar in unilateral contact exists, there* exists *a piecewise-smooth mode of the type discussed in Theorem 3.6.*

As mentioned previously, using the methodology in Section 3.3.2, we have found solutions for other $T \in \mathbb{Q}$. In fact, Proposition 3.5 confirms there exist piecewise-smooth modes for a dense group of $T \in \mathbb{Q}[3, 4]$. Conjecture 3.7 is also supported analytically in [12, p.7] where it is stated that any mode that is not piecewise-linear would exist only for $T \in \mathbb{Q}$.

At last, the detected modes discussed in conjecture 3.7 exhibit a peculiar property: infinitely many periodic solutions for the same energy and same period. This property is proven below.

Theorem 3.8. *For the cantilever bar in unilateral contact, there exist continua of piecewise-smooth periodic solutions of the same energy and frequency.*

Proof. Contrary to proofs of preceding propositions, the proof of Theorem 3.8 will be presented here rather in the appendix since the graphical depiction of this theorem, in Figure 3.10, corresponds directly to the example in this proof.

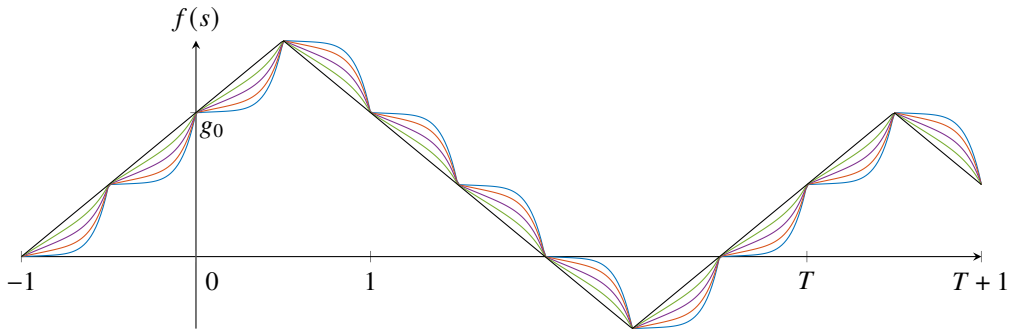

(a) D'Alembert functions for $\zeta = 0.05$ [—] $\zeta = 0.25$ [—] $\zeta = 0.5$ [—] $\zeta = 0.75$ [—], and $\zeta = 1$ [—]

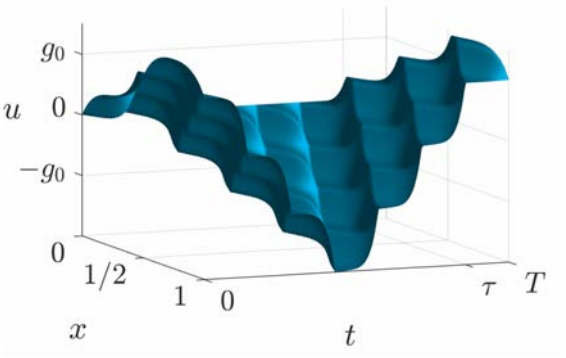

(b) Displacement field, $\zeta = 0.05$

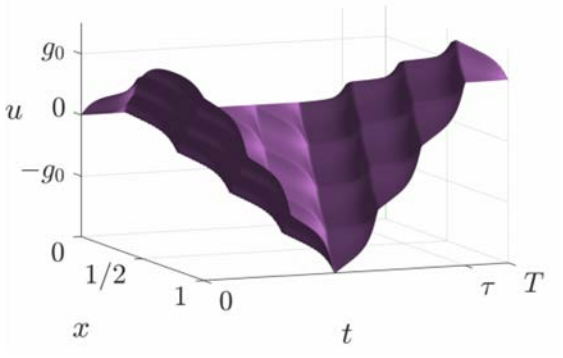

(c) Displacement field, $\zeta = 0.5$

Figure 3.9: Selected NSM3 solutions described in Proposition 3.5 for $m = 2$, $n = 7$ and $\eta(s) = (1-\zeta)(ms)^6 + \zeta ms$. The FEP of this modal family is depicted in Figure 3.8.

The proof consists of finding a family of periodic functions, subspace of NSM2, of the same energy.

To start, we consider the dimensionless energy of the cantilever bar:

$$2E(t) = \int_0^1 \partial_x u(x,t)^2 + \partial_t u(x,t)^2 \, \mathrm{d}x \tag{3.93}$$

Plugging the d'Alembert expression of the stress and velocity (3.8) gives:

$$2E(t) = \int_0^1 (f'(t+x) + f'(t-x))^2 + (f'(t+x) - f'(t-x))^2 \mathrm{d}x \tag{3.94}$$

$$= 2\int_0^1 f'^2(t+x)\mathrm{d}x + 2\int_0^1 f'^2(t-x)\,\mathrm{d}x \tag{3.95}$$

The second term can be put then in terms of $f'(t+x)$ via a basic change of variable

$$E(t) = \int_0^1 f'^2(t+x)\mathrm{d}x - \int_0^{-1} f'^2(t+x)\mathrm{d}x = \int_{-1}^1 f'^2(t+x)\mathrm{d}x = \int_{t-1}^{t+1} f'^2(s)\mathrm{d}s. \tag{3.96}$$

Also, note that the energy under unilateral contact is preserved [24, 84, 98] and can be represented in

terms of initial conditions, in the d'Alembert form f_0, exclusively

$$E(t) = E(0) = \int_{-1}^{1} f_0'^2(s)\mathrm{d}s \equiv E. \tag{3.97}$$

Plugging f_0 from NSM2 (3.65) leads to (the simplification procedure has been omitted for the sake of conciseness)

$$E = 3\int_0^{1/3} a_0'^2(s)\mathrm{d}s + 3\int_0^{1/3} a_1'^2(s)\mathrm{d}s. \tag{3.98}$$

Any functions a_1 and a_0 satisfying (3.98) generate a periodic solution with $T = 10/3$, $\tau = 8/3$ and prescribed energy E. For example, a linear function a_0 and cubic function a_1 belonging to NSM2 can be denoted as follows: (some steps in the derivation of the following expressions were omitted to facilitate reading)

$$a_0(s) = b_1 s \tag{3.99}$$

$$a_1(s) = 27\left(g_0 - \frac{b_1}{3}\right)\frac{s^3 + b_2 s}{1 + 9b_2} + \frac{b_1}{3} \tag{3.100}$$

where, to satisfy the remainder of the NSM2 conditions (3.59)-(3.64), b_1 and b_2 must abide

$$0 < b_1 \leq 3g_0, \tag{3.101}$$

$$b_2 > 0. \tag{3.102}$$

To obtain the energy of this NSM2 motion, (3.99) and (3.100) are plugged into (3.98):

$$E(b_1, b_2) = \frac{9(45b_2^2 + 10b_2 + 1)(b_1 - 3g_0)^2}{5(9b_2 + 1)^2} + b_1^2 \tag{3.103}$$

For several energy values, E, there exist infinitely many values b_1 and b_2 (i.e., infinitely many NSM2 solutions) generating motions of the same energy. For example, $E(b_1, b_2) = 9g_0^2$ is satisfied for any

$$b_1 = \frac{6g_0}{7 + 90b_2 + 405b_2^2} \tag{3.104}$$

and $0 < b_2 < \infty$ satisfies (3.101) and (3.102). Thus, $b_2 \in (0, \infty]$ with Equations (3.99), (3.100) and (3.104) represents a family of periodic solution with the same energy and period in NSM2. Several solutions from this piecewise-smooth mode are depicted in Figure 3.10. It is interesting to note that the solution presented in Figures 3.7(a) and 3.7(b) also exhibits energy $E = 9g_0^2$ and shares the same loci in the FEP of the family of solutions discovered here. Thus, it is indicative that there could exist many more families of solutions with the same energy and period. □

Similarly to Conjecture 3.7, for $\tau, T \in \mathbb{Q}$ where periodic motions can be found, there also exist energy-frequency (or period) pairs consisting of piecewise-smooth modes of the type mentioned in Theorem 3.8. This mode is also depicted as a red point in Figure 3.8.

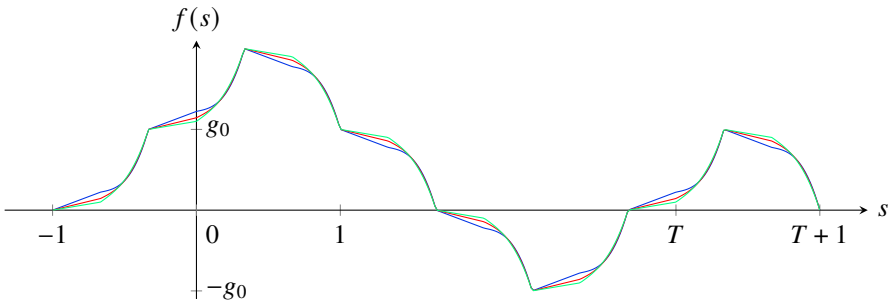

(a) D'Alembert functions for selected b_2 values. $b_2 = g_0/5$ [—] $b_2 = 3g_0/5$ [—], and $b_2 = g_0$ [—]

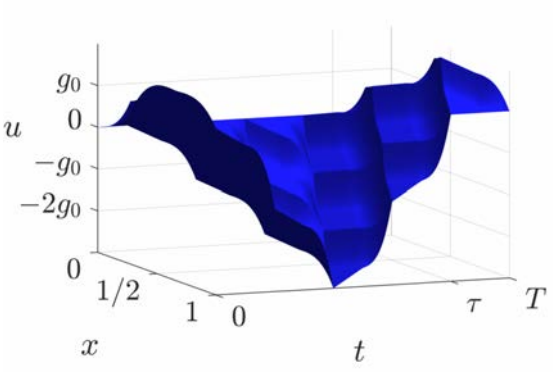

(b) Displacement field, $b_2 = g_0/5$

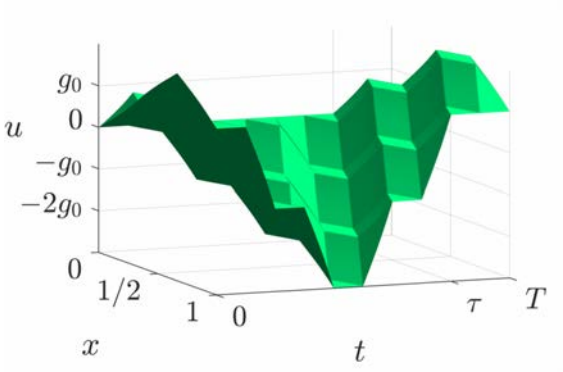

(c) Displacement field, $b_2 = g_0$

Figure 3.10: Selected solutions from the continuum of solutions of same energy and frequency described by (3.99), (3.100) and (3.104) defined by the b_2 values. All depicted solutions are motions of energy $E = 9g_0^2$ and period $T = 10/3$. Their location on the FEP diagram corresponds to the red point in Figure 3.8.

3.4 Discussion

It has been noticed that the true nonsmooth modal space of the investigated bar features a dense cluster of NSMs. For example, the NSM2 existing on convex subsets of the functional space $C^1[0, 1/3]$. Furthermore, a cluster of NSMs pertaining to NSM3 and belonging to $C^1[0, 1/m]$ (for various m) has been found to exist for the periods $T \in (3, 4)$. In fact, it can be suggested that the isolated periodic solutions discovered in [97] belong to the space of iso-periodic NSMs discussed in Section 3.3.2. This last statement is supported by the fact that the numerical method used to obtain the isolated solutions in [97] produces Signorini solutions for rational periods and inactive contact durations $T, \tau \in \mathbb{Q}$ similar to the piecewise-smooth modes discussed in Theorem 3.6.

The methodology presented here unfortunately does not extend to the nonsmooth modal analysis of other structures in unilateral contact. For example, for the bar with soft support (Robin conditions at $x = 0$), the periodicity conditions admit a set of functional equations involving integral terms in the initial conditions which could not be solved given the methodology presented here. Furthermore, for the varying area bar and two-dimensional structures in unilateral contact, there exist no d'Alembert travelling-wave function and therefore the proposed methodology is not applicable.

The results presented here also have implications on the remainder of the thesis. Specifically, the cluster of NSMs discovered in this chapter sets numerous difficulties on numerical modal analysis. These difficulties are explained in detail for the remainder of this section. The NSMs discovered here exist in functional spaces that are subsets of C^1 as shown by NSM2 and NSM3 with Theorem 3.5. However, the continuation methods presented in Section 2.1.3 are constructed to find two-dimensional manifolds. To clarify, since the numerical approximation of the nonsmooth modal space reaches the exact modal space at convergence, it is expected that the solution space to the periodicity conditions (with phase conditions) not be a two-dimensional manifold but may consist of a hyper-surface parametrized with more than two parameters (such as NSM3). In turn, as convergence is reached, the solution to the equations solved in nonlinear modal analysis (periodicity conditions, phase condition and continuation equation) may not be unique and may not be suitable for traditional gradient-based root solvers (which require solutions to exist as isolated point).

Another difficulty of numerical nonsmooth modal analysis is imposed by the existence of iso-periodic NSMs for every rational period $T \in \mathbb{Q}[3,4]$, as implied from Theorem 3.5 and shown in Figure 3.8. Specifically, both sequential and pseudo-arclength continuation methods may have difficulties in revealing the modal space. Sequential continuation, as demonstrated in Section 2.1.3, assumes a unique solution for a fixed period T_i. However, the space of iso-periodic NSMs for rational periods T contradicts this assumption. In turn, the pseudo-arclength continuation method may experience difficulties since it requires a definition of a tangent to the space of solutions of the periodicity equations. However, a tangent to the space of solutions is not defined at intersection between branches or for solution spaces that do not constitute a curve [4]. Here, intersections between branches in the investigated modal space occur on a dense set of periods and the existence of nonsmooth modal families on rational periods may therefore introduce difficulties to pseudo-arclength continuation, upon convergence of the model. While these conclusions pertain to the specific nonsmooth modal space of the internally resonant bar, precautions will be taken in the application of numerical nonsmooth modal analysis in this thesis as these behaviours may not be exclusive to the internally resonant bar.

Chapter 4

Nodal Boundary Method in One Dimension

In Chapter 3, analytical tools were employed to determine the modal space of the uniform area bar in unilateral contact. However, these analytical techniques could not have been extended to study the uniform-area bar with soft-support or the varying-area bar. Thus, to perform nonsmooth modal analysis of models of the bar other than the uniform-area bar, numerical techniques must be used. In Section 2.5, several numerical methods were inspected and it was concluded that none of the methods allow for the detection of periodic solutions without chattering and without penetration of the rigid obstacle. Thus, as stated in the introduction to this thesis (Chapter 1), the nodal boundary method (NBM) is developed for nonsmooth modal analysis. In contrast with the numerical methods mentioned in Section 2.5, the NBM has been successful in performing nonsmooth modal analysis of the varying-area bar and the two-dimensional plate.

In this chapter, the NBM will be presented for the *one-dimensional* bar in unilateral contact. The main novelty in this chapter is the nonsmooth modal analysis of the varying-area bar prone to contact. However, for comparison with existing literature, the NBM is also applied to the case of the uniform-area cantilever bar with and without soft support. It is important to note that the NBM is not limited to the one-dimensional case of the bar. Indeed, in the following chapter (Chapter 5), application of NBM for nonsmooth modal analysis of the deformable plate in unilateral contact is presented.

While most of this chapter is replicated from an article published in [87], some of the sections were modified to make for a more coherent reading in the context of this thesis. Furthermore, several new sections were added to expand on subjects presented in [87] and to provide a more robust proofs and foundation to various aspects of the NBM. These sections include: Section 4.4.1 detailing application of Crank-Nicolson and shooting method, Appendix B.5 elaborating the Crank-Nicolson algorithm, Section 4.5.2 comparing the performance of NBM against other numerical methods, Figure 4.9 which provides comparisons of forced-response curves obtained by NBM and other numerical methods, proof of invertible NBM mass matrices (Appendix B.3), and proof of uniqueness

of solutions of NBM-ODE (Appendix B.4).

In this chapter, Section 4.1 presents the problem of the nonsmooth modal analysis of the varying-area bar and introduces notation and terminology to be used in this chapter. Next, in Section 4.2 the FEM formulation is reminded to give context for the derivation of NBM. In Section 4.3, the NBM will be derived from basic principles and supporting theorems will be presented. Then, the shooting method and sequential continuation with the NBM will be discussed in Section 4.4. At last, nonsmooth modal analysis of various cases involving the bar will be performed in Section 4.5. There, proofs of convergence will be presented as well.

4.1 Problem statement

The cantilever bar of varying-area illustrated in Figure 4.1. The displacement field of the bar is

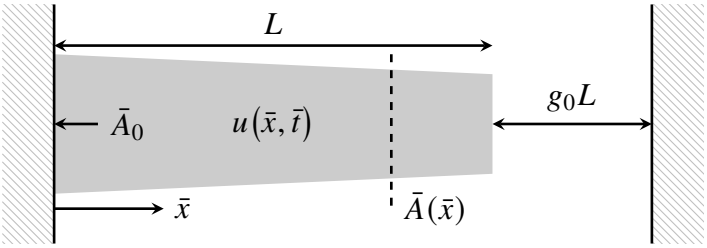

Figure 4.1: Bar of varying area prone to unilateral contact with a rigid wall.

denoted $u(\bar{x},\bar{t})$, where $\bar{x}$ and $\bar{t}$ represent the physical position and time, respectively. The bar is clamped to a wall at $\bar{x}=0$ and is prone to unilateral contact with a rigid obstacle at its other end $\bar{x}=L$, where L denotes the length of the bar. At rest, the rigid obstacle is set at a distance $g_0 L$ from the tip of the bar.

The time and space coordinates are normalized here, similarly to the normalization procedure in Equation (3.1) of Section 3.1. Upon normalization of the physical coordinates, the PDE governing the motion of the varying-area bar reads

$$\partial_{tt}u(x,t)=\partial_x(A(x)\partial_x u(x,t)),\quad \forall x\in(0,1),\quad t\in(0,\infty). \tag{4.1}$$

where subscripts denote partial differentiation with respect to the denoted variable. Furthermore, the following non-dimensional coordinates are introduced: $x=\bar{x}/L$ and $t=\alpha\bar{t}/L$. Here, α is introduced as a normalization factor $\alpha^2=Y\bar{A}_0/m$ where $Y>0$, $m>0$ and $\bar{A}_0\equiv\bar{A}(0)>0$ representing Young's modulus [N/m^2], the constant mass per unit length of the bar [kg/m], and the physical area of the bar at $x=0$ [m^2], respectively. In turn, $A(x)>0$ is a non-dimensional quantity representing the area variation in the bar and $A(0)=1$ holds. The physical cross-sectional area of the bar abides

$\bar{A}(\bar{x}) = \bar{A}(xL) = A(x)\bar{A}_0$. Moreover, we use the following Dirichlet boundary condition at $x = 0$:

$$u(0,t) = 0, \quad \forall t \in (0,\infty). \tag{4.2}$$

At $x = 1$ (ie, $\bar{x} = L$), we impose the Signorini boundary condition

$$0 \geq u(1,t) - g_0 \perp \sigma_n(u(1,t)) \leq 0 \quad \forall t \in (0,\infty), \quad \sigma_n(u(1,t)) = A(1)\partial_x u(1,t) \tag{4.3}$$

to describe contact of the bar with the rigid wall, where the non-dimensional gap distance g_0 and the stress at the contact end of the bar $\sigma_n(u(1,t))$ are introduced. Namely, the Signorini conditions (4.3), in the continuous setting, can be seen as a switching of boundary conditions at $x = 1$:

$$\text{Active contact conditions:} \quad u(1,t) = g_0 \quad \text{and } \sigma_n(u(1,t)) \leq 0 \tag{4.4}$$

$$\text{Inactive contact conditions:} \quad \sigma_n(u(1,t)) = 0 \quad \text{and } u(1,t) \leq g_0. \tag{4.5}$$

It is noted that the contact node is known a priori, and the methodology developed here is done under this assumption. While this assumption allows us to simplify the formulation, it is also valid for many engineering applications. Nevertheless, the methodology presented here can be also extended to cases where to contact nodes are not known a priori.

For nonsmooth modal analysis, it is also required to find the initial conditions $u_{\text{init}}(x)$ and $v_{\text{init}}(x)$ generating periodic solutions:

$$u(x,T) = u(x,0) \quad = u_{\text{init}}(x), \quad \forall x \in [0,1] \tag{4.6}$$

$$\partial_t u(x,T) = \partial_t u(x,0) = v_{\text{init}}(x), \quad \forall x \in [0,1] \tag{4.7}$$

where T denotes the period of motion. Accordingly, to solve the problem numerically, we use the FEM with NBM (NBM) for the treatment of boundary condition on the governing boundary value problem in Equations (4.1) and (4.5). Next, the shooting method and continuation are used to depict the continua of solutions satisfying Equations (4.6) and (4.7).

While the problem of modal analysis of the bar in unilateral contact with a constant cross-section, $A'(x) = 0$, was studied both analytically and numerically in [12, 84, 98] (and Chapter 3), the same techniques could not be implemented for the case of $A'(x) \neq 0$. Namely, analytical techniques have relied on the exact solution to the wave equation to describe both inactive and active contact phases in a closed-form manner. The WFEM exhibits numerical properties favouring the existence of periodic solutions (such as energy conservation and preservation of characteristic quantities) only for the case of the bar with constant cross-section [97]. These favourable properties no longer exist for the case of the varying area bar since the upwind-flux used in the WFEM does not accurately solve for the transfer of quantities between elements [49, chapter 9]. In contrast, it will be shown that the NBM allows for the detection of periodic solutions in the varying area bar by implementation of a Galerkin-Bubnov method and boundary shape functions to satisfy the Signorini conditions.

4.2 Finite element formulation

In order to apply FEM on the one-dimensional Signorini problem, the displacement within the bar is approximated by $u^h(x,t)$. The approximation $u^h(x,t)$ consists of a series of piecewise Lagrange polynomials $\phi_i(x)$, $i = 0, 1, 2, \ldots, N$, and corresponding nodal quantities $u_i(t)$ [34] located at the nodes $x_i = i/N$ for $i = 0, 1, 2, \ldots, N$, as classically achieved in FEM. The approximation thus reads

$$u(x,t) \approx u^h(x,t) = \sum_{i=0}^{N} \phi_i(x) u_i(t) \equiv \mathbf{P}(x)\mathbf{u}(t), \text{ where } \phi_i(x_j) = \delta_{ij} \text{ and } u_i(t) \approx u(x_i,t) \quad (4.8)$$

with $\mathbf{u}(t)$ storing the time-domain nodal displacements and δ_{ij} denoting the Kronecker Delta. Furthermore, we introduced the vector quantity $\mathbf{P}(x) \equiv \begin{pmatrix}\phi_0(x) & \phi_1(x) & \ldots & \phi_N(x)\end{pmatrix}$ to simplify the representation of the finite-element in matrix form. The FEM applies to the weak form of PDE (4.1). It requires the definition of test functions $\mathbf{w}(t)$ corresponding to the nodal displacements $\mathbf{u}(t)$. In the NBM, the test functions $\mathbf{w}(t)$ will be subject to change through time (according to the phase of contact motion), while it is not the case in classical FEM. This will be clarified in Section 4.3. Hence, application of the FE approximation on the weak form of PDE (4.1) with cantilever condition (4.2) ($u_0(t) = 0$ and such that $\phi_0(x)$ is omitted from $\mathbf{P}(x)$) yields

$$\mathbf{w}^\top(t)\mathbf{M}\ddot{\mathbf{u}}(t) + \mathbf{w}^\top(t)\mathbf{K}\mathbf{u}(t) - w_N(t)\sigma_n(u(1,t)) = 0, \quad \forall \mathbf{w}(t) \quad (4.9)$$

where $\mathbf{M}$ is the mass matrix, $\mathbf{K}$ is the stiffness matrix, with respective entries

$$\mathbf{M} = \int_0^1 \mathbf{P}(x)^\top \mathbf{P}(x)\,\mathrm{d}x, \quad \mathbf{K} = \int_0^1 A(x)\mathbf{P}'(x)^\top \mathbf{P}'(x)\,\mathrm{d}x. \quad (4.10)$$

While this notation is conventional in FE analysis, it is reminded here since the NBM formulation will rely on it significantly. Specifically, the NBM modifies the weak form (4.9) throughout the motion and the test functions $\mathbf{w}(t)$ actively participate in its formulation. We now introduce the NBM to treat the Signorini conditions (4.4) and (4.5) in the FE framework. There, the displacement and the stress at $x = 1$ will be approximated using $u^h(x,t)$

$$u(1,t) \approx u^h(1,t) = u_N(t), \quad \sigma_n(u(1,t)) \approx A(1)u_x^h(1,t) = A(1)\sum_{i=1}^{N} \phi_i'(1)u_i(t), \quad (4.11)$$

respectively. While the approximation $u(1,t) \approx u_N(t)$ is equivalent to the one used in the classical FEM, the above stress approximation $\sigma_n(u(1,t)) \approx A(1)u_x^h(1,t)$ is non-traditional. To clarify, in the classical FEM, implementation of Neumann conditions is done in a weak sense, and the motion of the nodes does not satisfy the Neumann condition for any grid. Instead, the error in satisfaction of the Neumann condition is reduced with increasing the number of elements or degree of polynomials. In the NBM, the Neumann conditions are imposed on the shape functions for any choice of number of elements or degree of polynomial such that the stress at the end of the bar is always strictly zero

and the Neumann condition is exactly satisfied throughout inactive contact motion. In fact, this is the key to the implementation of the NBM, as described below.

4.3 Nodal boundary method

In NBM, the FE approximation is obtained by inserting (4.11) into (4.3) such that

$$0 \geq u_N(t) - g_0 \perp A(1) \sum_{i=1}^{N} \phi_i'(1) u_i(t) \leq 0. \tag{4.12}$$

The main proposition in NBM is that condition (4.12) is solved by constructing shape functions capable of satisfying the inactive and active contact conditions. To do so, the boundary node $u_N(t)$ is isolated in (4.12) such that

$$g_0 \geq u_N(t), \quad u_N(t) \leq -\sum_{i=1}^{N-1} \frac{\phi_i'(1)}{\phi_N'(1)} u_i(t), \quad (u_N(t) - g_0)\left(u_N(t) - \sum_{i=1}^{N-1} \frac{\phi_i'(1)}{\phi_N'(1)} u_i(t)\right) = 0. \tag{4.13}$$

Indeed, if (4.13) holds then (4.12) holds as well. By separating $u_N(t)$, we impose that $u_N(t)$ is no longer dictated by the ODE (4.9) but is dictated exclusively by condition (4.13). The following points introduce the remaining steps of the derivation (which will be elaborated in the upcoming sections):

1. To solve for the motion during inactive contact, the Signorini conditions (4.13) require that

$$u_N(t) = -\sum_{i=1}^{N-1} \frac{\phi_i'(1)}{\phi_N'(1)} u_i(t), \quad u_N(t) \leq g_0. \tag{4.14}$$

   Substitution of the above into the FE approximation (4.8) effectively creates a family of shape functions that always satisfies the inactive contact conditions

$$u(x,t) \approx \sum_{i=1}^{N-1} \left(\phi_i(x) - \phi_N(x) \frac{\phi_i'(1)}{\phi_N'(1)}\right) u_i(t). \tag{4.15}$$

   In other words, any solution obtained using the above approximation satisfies the homogeneous Neumann condition taking place during inactive contact. In the FEM, all functions $\phi_i(x)$ have local support and are non-zero for the elements containing the node $u_i(t)$. In the case of NBM, the principle of local support is followed as well, and only the shape functions at the element including the contact node $u_N(t)$ are affected by the approximation (4.15). In turn, the inactive contact inequality in (4.14) reads

$$u_N(t) \leq g_0 \quad \Rightarrow \quad -\sum_{i=1}^{N-1} \frac{\phi_i'(1)}{\phi_N'(1)} u_i(t) \leq g_0. \tag{4.16}$$

2. To solve for the motion during active contact, we construct a family of shape functions that

always answers

$$u(L,t) \approx u_N(t) = g_0, \quad u_N(t) \leq -\sum_{i=1}^{N-1} \frac{\phi_i'(1)}{\phi_N'(1)} u_i(t). \tag{4.17}$$

Evidently, the set of shape functions answering this condition admits

$$u(x,t) \approx \sum_{i=1}^{N-1} \phi_i(x) u_i(t) - \phi_N(x) g_0. \tag{4.18}$$

Thus, any solution that is obtained using the above approximation satisfies the Dirichlet condition in (4.17). In turn, the active contact inequality in (4.17), under this approximation becomes

$$u_N(t) \leq -\sum_{i=1}^{N-1} \frac{\phi_i'(1)}{\phi_N'(1)} u_i(t) \Rightarrow -\sum_{i=1}^{N-1} \frac{\phi_i'(1)}{\phi_N'(1)} u_i(t) \geq g_0. \tag{4.19}$$

3. The different sets of shape functions described in (4.15) and (4.18) will lead to different sets of ODEs governing inactive and active contact motions, respectively. The Signorini conditions are then satisfied by switching between the two sets of functions according to inequalities (4.16) and (4.19), which are mutually exclusive, as expected from the Signorini conditions. At the moment of switch, the internal nodal displacements and velocities (internal nodes are those with indexes $i = 1, 2, \ldots, N-1$) are assumed to be continuous in time.
4. The NBM formulation results in an ODE, featuring discontinuous mass and stiffness matrices, which exhibits periodic solutions.

4.3.1 Comment on application of NBM using other shape functions

Although the NBM is derived in this manuscript using the classical FEM piecewise Lagrangian shape functions, this method can be also formulated using other shape functions. However, for other shape functions, precautions must be considered. One such precaution is that the shape functions must admit a stress approximation that is not always vanishing at the contacting end. To clarify, the NBM relies on the approximation of stress for the switching between active and inactive contact phases, as seen in Equation (4.12). In order to allow for a switching between contact phases, the shape function must be chosen such that the stress approximation at $x = 1$ does not exhibit $\phi_i'(1) = 0$ for all $i = 1, \ldots, N$.

The linear modes of the cantilever bar with uniform area

$$\phi_i(x) = \sin\left(\frac{(2i-1)\pi x}{2}\right), \quad i = 1, 2, \ldots, N. \tag{4.20}$$

will be investigated as an example of a set of shape functions that cannot be used in NBM. These mode shapes bear the undesired property $\phi_i'(1) = 0$, $\forall i$. For such shape functions, the active

contact phase cannot occur as can be seen by plugging Equation (4.20) into the Signorini conditions Equation (4.12)

$$0 \geq u_N(t) - g_0 \perp 0 \leq 0 \rightarrow g_0 \geq u_N(t). \tag{4.21}$$

In simple terms, Equation (4.21) shows that the linear modes of the cantilever bar exhibit inactive contact motions exclusively and therefore a switch between contact phases cannot occur.

The choice of shape functions is crucial for other methods in contact dynamics and not only the NBM. In fact, for the shape functions (4.20), both the mass redistribution method [40] and Nitsche's method would fail. The mass redistribution method would fail in the same fashion as NBM since it relies on strong enforcement of the Signorini boundary condition. In turn, Nitsche's method would not be able to approximate adequately the Signorini problem. This is illustrated in the remainder of this section. In Nitsche's method, the Signorini boundary conditions are enforced via the following approximation of the stress at the contact boundary

$$\sigma_n(u(1,t)) \approx -\max\left(0, \gamma(u_N(t) - g_0) - A(1)\sum_{i=1}^{N} \phi_i'(1)u_i(t)\right), \quad \gamma > 0 \tag{4.22}$$

where γ is set to be constant [19]. The Signorini condition is then satisfied as $N \rightarrow \infty$

$$\sigma_n(u(1,t)) = \lim_{N\rightarrow\infty} -\max\left(0, \gamma(u_N(t) - g_0) - A(1)\sum_{i=1}^{N} \phi_i'(1)u_i(t)\right) \tag{4.23}$$

$$\sigma_n(u(1,t)) = -\max(0, \gamma(u(1,t) - g_0) - \sigma_n(u(1,t))), \quad \gamma > 0 \tag{4.24}$$

and is equivalent to the Signorini condition (4.3) [20]. The convergence of Nitsche's method largely relies on the participation of the stress approximation in the right-hand side of Equation (4.23). This property is disrupted for the $\phi_i(x)$ in Equation (4.21). For these shape functions, the Nitsche stress approximation (4.22) reads

$$\sigma_n(u(1,t)) \approx -\gamma \max(0, u_N(t) - g_0). \tag{4.25}$$

Since the stress approximation is omitted from the right hand side of (4.25), the resulting approximation (4.25) is equivalent to a penalty force with penalty parameter γ [24]. The penalty method does not share the same convergence properties as Nitsche's method. It can be seen that by taking the limit of Equation (4.25) as $N \rightarrow \infty$:

$$\sigma_n(u(1,t)) = \lim_{N\rightarrow\infty} -\gamma \max(0, u_N(t) - g_0) = -\gamma \max(0, u(1,t) - g_0). \tag{4.26}$$

This term, in contrast to Equation (4.24), is not equivalent to the Signorini conditions.

Nevertheless, it is possible also to consider global shape functions for the NBM instead of the FEM functions of local support used in this manuscript. For example, if one wishes to use NBM

with global support functions, one may use:

$$u(x,t) \approx a(t)\sin(\pi x/2) + b(t)x \tag{4.27}$$

which admits a non-vanishing stress approximation at the contact end:

$$\partial_x u(1,t) \approx b(t). \tag{4.28}$$

and thus allows for the existence of negative stress at the contact end. To apply the NBM on approximation (4.27), it is first plugged into the inactive contact conditions of the Signorini problem (4.12) admits

$$u_x(1,t) = 0, u(1,t) \leq g_0 \rightarrow b(t) = 0, \quad a(t) \leq g_0 \tag{4.29}$$

Then, the approximation (4.27) is plugged into the active contact conditions of Equation (4.12) gives:

$$u_x(1,t) \leq 0, u(1,t) = g_0 \rightarrow b(t) = g_0 - a(t), \quad a(t) \geq g_0 \tag{4.30}$$

Finally, the NBM shape functions for the approximation (4.27) are put as follows:

$$u(x,t) \approx \begin{cases} a(t)\sin(\pi x/2) & a(t) \leq g_0 \\ a(t)(\sin(\pi x/2) - x) + g_0 x & a(t) \geq g_0 \end{cases} \tag{4.31}$$

It is noted that the FEM Lagrange functions are utilized in this manuscript rather than global functions of the type (4.27) since FEM functions are utilized frequently in structural dynamics [34].

4.3.2 Inactive contact motion

The inactive contact motion condition (4.5) in the NBM framework is

$$\sigma_n^h(\mathbf{u}(t)) \equiv A(1)u_x^h(1,t) = A(1)\sum_{i=1}^{N}\phi_i'(1)u_i(t) = 0, \quad u_N(t) \leq g_0. \tag{4.32}$$

where we use $\sigma_n^h(\mathbf{u}(t))$ to denote the FE approximation of the stress at $x = 1$. To clarify, the true stress in the bar reads $\sigma_n(u(1,t)) \approx \sigma_n^h(\mathbf{u}(t))$ according to Equation (4.11), and the homogeneous Neumann condition $\sigma_n(u(1,t)) = 0$ is satisfied by virtue of Equation (4.32). for the inactive contact motion, we impose that $u_N(t)$ satisfies equation (4.32) such that

$$u_N(t) = -\frac{1}{\phi_N'(1)}\sum_{i=1}^{N-1}\phi_i'(1)u_i(t) \equiv S(\mathbf{u}^o(t)), \quad \mathbf{u}^o(t) = \begin{pmatrix} u_1(t) & u_2(t) & \dots & u_{N-1}(t) \end{pmatrix}^\top. \tag{4.33}$$

Here, $\mathbf{u}^o(t)$ gathers internal nodal displacements whereas the contact node is represented in $u_N(t)$. This distinction is fixed and an internal node cannot turn into a contact node (or vice-versa) throughout the motion of the bar. This distinction between internal nodes and nodes prone to contact

is also used in the MRM formulation [40]. Thus, in the NBM, the loci of contact nodes must be known a priori. Although the loci of contact nodes is not always known in advance, for the case of small strains, the loci of contact nodes can be assumed to be known and fixed without loss of generality.

In Equation (4.33), we introduce the function S, acting on $\mathbf{u}^o(t)$, to simplify the notation. Actually, S appears naturally throughout the derivation of both inactive and active contact motions in NBM. Indeed, this function is of integral importance to NBM and serves for multiple purposes: it defines the conditions for the switching between phases, the motion of the contact node during inactive contact phase, and the contact force applied on the bar during active contact phase. These roles of S are illustrated in Figure 4.2 and are explicitly explained later in Section 4.3.4. For the remainder of this article, the function S will be referred to as the *switching function*.

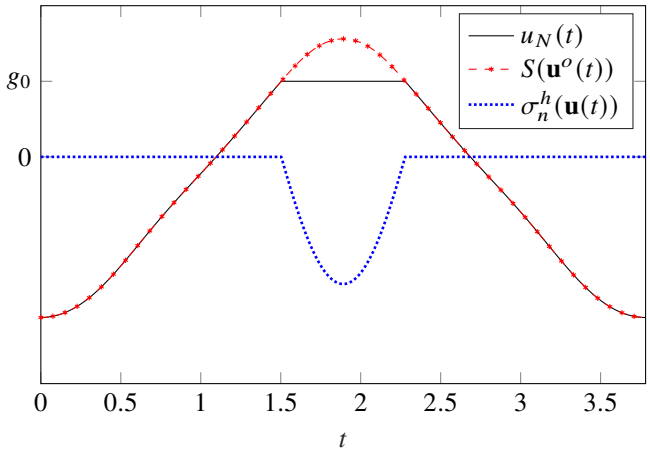

Figure 4.2: Switching function and associated quantities. The switching function dictates the phase of motion. For $S(\mathbf{u}^o(t)) \leq g_0$, inactive contact motion takes place, and active contact motion takes place otherwise. Moreover, the displacement at the contact boundary abides $u_N(t) = S(\mathbf{u}^o(t))$ during the inactive contact phase, $S(\mathbf{u}^o(t)) \leq g_0$, and the approximation of the stress at the contact boundary abides $\sigma_n^h(\mathbf{u}(t)) = A(1)\phi'_N(1)(g_0 - S(\mathbf{u}^o(t)))$ during the active contact phase.

Following the substitution $u_N(t)$ in (4.33), $\mathbf{u}(t)$ can be related to $\mathbf{u}^o(t)$ via a linear operator $\mathbf{A}^N \in \mathbb{R}^{N\times N-1}$

$$\mathbf{u}(t) = \mathbf{A}^N\mathbf{u}^o(t) \quad \mathrm{A}^N_{ij} = \begin{cases} \delta_{ij} & i = 1,\dots,N-1 \text{ and } j = 1,\dots,N-1, \\ -\dfrac{\phi'_j(1)}{\phi'_N(1)} & i = N \text{ and } j = 1,\dots,N-1. \end{cases} \tag{4.34}$$

In turn, the displacement field during inactive contact is approximated as follows:

$$u(x,t) \approx \mathbf{P}(x)\mathbf{A}^N\mathbf{u}^o(t), \quad u_N \leq g_0 \tag{4.35}$$

In fact, Equation (4.35) constitutes the matrix form of Equation (4.15) (previously presented in the overview of the NBM). The matrix form representation in Equation (4.35) will be helpful in

introducing the ODE governing the inactive contact motion.

The inequality condition for the inactive contact phase (4.32) (non-penetration) can be put in terms of the nodes $\mathbf{u}^o(t)$ via the switching function

$$u_N \leq g_0 \Rightarrow S(\mathbf{u}^o) \leq g_0. \tag{4.36}$$

To derive the ODE governing the inactive contact motion, we insert the inactive motion constraints (4.34) and (4.36) into the weak-form of the PDE, Equation (4.9),

$$\mathbf{w}^\top(t)(\mathbf{M}\mathbf{A}^N\ddot{\mathbf{u}}^o(t) + \mathbf{K}\mathbf{A}^N\mathbf{u}^o(t)) = 0 \tag{4.37}$$

$$u_N(t) = S(\mathbf{u}^o(t)), \quad \ddot{u}_N(t) = S(\ddot{\mathbf{u}}^o(t)), \quad S(\mathbf{u}^o(t)) \leq g_0. \tag{4.38}$$

In classical FEM, it is generally assumed Equation (4.37) is true for all $\mathbf{w}(t)$ and the subsequent omission of $\mathbf{w}(t)$ from the equation takes place. Here, however, omission of $\mathbf{w}(t)$ will lead to an over-defined system of ODEs ($N-1$ variables in $\mathbf{u}^o$ for N equations). To remedy this, we use the Galerkin-Bubnov method where we project the residual (the term multiplying $\mathbf{w}$ in Equation (4.37)) on the same solution space used for $\mathbf{u}(t)$ [44]. This strategy has been proven successful in other applications and is commonly used when shape functions that satisfy the boundary conditions are involved in the approximation [44, 58]; [61, p. 300]. It is further noted that the strategy taken here in deriving the NBM has also been referred to as *basis recombination* [14, p. 112]. Following the Galerkin-Bubnov method, we project the residual resulting from the approximation (4.35) on the composing trial functions. Under representation (4.9), this results effectively in modification of the test-function as follows:

$$\mathbf{w}(t) = \mathbf{A}^N\mathbf{w}^o \tag{4.39}$$

where $\mathbf{w}^o$ gathers all test function contributions corresponding to the internal nodes $\mathbf{u}^o(t)$. Then, substitution of (4.39) into (4.37) and omission of $\mathbf{w}^o$ results in the reduced ODE (of $N-1$ equations)

$$(\mathbf{M}_N\ddot{\mathbf{u}}^o(t) + \mathbf{K}_N\mathbf{u}^o(t)) = 0, \quad \mathbf{M}_N = (\mathbf{A}^N)^\top\mathbf{M}\mathbf{A}^N, \quad \mathbf{K}_N = (\mathbf{A}^N)^\top\mathbf{K}\mathbf{A}^N \tag{4.40}$$

where the subscript N in $\mathbf{M}_N$ (or $\mathbf{K}_N$) is used to denote the NBM coefficients corresponding to answering homogeneous *Neumann* conditions. We remark that, via the NBM, the displacement $u_N(t)$ has been effectively removed from the ODE such that neither the equation nor the inequality constraint in expression (4.40) includes $u_N(t)$.

In sum, the approximation of the inactive contact in NBM constitutes the most novel contribution of this methodology as it enforces the homogeneous Neumann condition in *strong* fashion. In fact, the NBM can be generally used to enforce the Neumann condition in strong fashion even outside of the context of the Signorini problem. To help the readers understand this approach more clearly, Appendix B.2 compares the enforcement of Neumann conditions in classical FEM and the NBM.

4.3.3 Active contact motion

The active contact condition in NBM, derived from Equation (4.13), reads

$$u_N(t) = g_0 \text{ implying } \dot{u}_N(t) = 0 \text{ and } w_N(t) = 0 \tag{4.41}$$

Effectively, this approximation applies in the active contact phase and the velocity of the contact node is discontinuous at the moment of contact. Here, the test function vanishes on Dirichlet boundaries (ie, $w_N(t) = 0$ during active contact) which is common practice for general FEM approximations [26, 34, 44]. Next, the complementarity condition (4.13) can be rewritten in terms of the switching function

$$A(1) \sum_{i=1}^{N} \phi_i'(L) u_i(t) \leq 0, \tag{4.42}$$

$$-\sum_{i=1}^{N-1} \frac{\phi_i'(1)}{\phi_N'(1)} u_i(t) \geq u_N(t), \tag{4.43}$$

$$S(\mathbf{u}^o(t)) \geq g_0. \tag{4.44}$$

The transition between statements (4.42) and (4.43) requires that $\phi_N'(1) > 0$ holds. Otherwise, in the case $\phi_N'(1) \leq 0$, both inactive and active contact phases would have to occur for $S(\mathbf{u}^o(t)) < 0$, that is simultaneously, which disagrees with the mutual exclusivity of the inactive and active contact conditions in the complementarity conditions (4.3). Accordingly, for $\phi_N'(1) > 0$, we note that the active contact motion occurs for $S(\mathbf{u}^o(t)) > g_0$, and the inactive contact motion occurs for $S(\mathbf{u}^o(t)) < g_0$ such that both are mutually exclusive. Fortunately, for the case of Lagrangian polynomials used here, the statement $\phi_N'(1) > 0$ has been proven to hold for any number of elements. The proof can be found in Appendix B.1.

We continue with the substitution of expressions (4.41) and (4.44) into the FEM-ODE (4.9) where (4.41) is first recast in the matrix format

$$\mathbf{w}(t) = \mathbf{A}^D \mathbf{w}^o, \quad \mathbf{u}(t) = \mathbf{A}^D \mathbf{u}^o(t) + g_0 \mathbf{d}, \qquad S(\mathbf{u}^o(t)) \geq g_0 \tag{4.45}$$

where

$$\mathrm{A}_{ij}^D = \begin{cases} \delta_{ij} & i = 1, \ldots, N-1;\ j = 1, \ldots, N-1 \\ 0 & i = N;\ j = 1, \ldots, N-1 \end{cases} \quad \text{and } d_i = \begin{cases} 0 & i = 1, \ldots, N-1 \\ 1 & i = N. \end{cases} \tag{4.46}$$

We then plug (4.45) into (4.9) to obtain an ODE in terms of $\mathbf{u}^o$ multiplied by $\mathbf{w}^o$ forming the scalar equation

$$(\mathbf{w}^o)^\top (\mathbf{M}_D \ddot{\mathbf{u}}^o(t) + \mathbf{K}_D \mathbf{u}^o(t) + g_0 \mathbf{f}_D) = 0, \quad S(\mathbf{u}^o(t)) \geq g_0 \tag{4.47}$$

where

$$\mathbf{M}_D = (\mathbf{A}^D)^\top \mathbf{M}\mathbf{A}^D, \mathbf{K}_D = (\mathbf{A}^D)^\top \mathbf{K}\mathbf{A}^D, \text{ and } \mathbf{f}_D = (\mathbf{A}^D)^\top \mathbf{K}\mathbf{d}, \tag{4.48}$$

and the subscript D is used to denote the coefficients corresponding the ODE answering the non-homogeneous *Dirichlet* conditions. Assuming equation (4.47) should be valid for all values $\mathbf{w}^o$, the following ODE formulation is obtained:

$$\mathbf{M}_D \ddot{\mathbf{u}}^o(t) + \mathbf{K}_D \mathbf{u}^o(t) + g_0 \mathbf{f}_D = \mathbf{0}, \quad S(\mathbf{u}^o(t)) \geq g_0. \tag{4.49}$$

Equation (4.49) is equivalent to the ODE obtained by application of classical FEM on the clamped-clamped bar. Furthermore, the NBM formulation of the ODE for the active contact phase is equivalent to this described by the basis recombination method for non-homogeneous boundary conditions [14, p. 112]. However, the NBM adds the restriction $S(\mathbf{u}^o(t)) > g_0$ to infer that the bar must be repulsed at all time throughout contact, as required by the active contact condition (4.4).

In the next section, we combine the ODEs corresponding to both active and inactive motions, Equations (4.40) and (4.49) respectively, to construct the ODE approximation for the original Signorini problem.

4.3.4 NBM-FEM formulation of Signorini problem

The switching method [3, 98] is used for the enforcement of the Signorini conditions in NBM. In the switching method, the Signorini complementarity conditions are answered by alternating between the boundary conditions (4.4) and (4.5) both in the test and trial functions such that the inequality constraints are satisfied. In NBM, this translates to switching between Equations (4.40) and (4.49), and the complete NBM-ODE reads

$$\begin{cases} \mathbf{M}_D \ddot{\mathbf{u}}^o(t) + \mathbf{K}_D \mathbf{u}^o(t) + g_0 \mathbf{f}_D = 0 & S(\mathbf{u}^o(t)) \geq g_0 \\ \mathbf{M}_N \ddot{\mathbf{u}}^o(t) + \mathbf{K}_N \mathbf{u}^o(t) = 0 & S(\mathbf{u}^o(t)) \leq g_0. \end{cases} \tag{4.50}$$

We note that at the moment of switch, denoted t_s such that $S(\mathbf{u}^o(t_s)) = g_0$, the resulting NBM-ODE (4.50) raises two conflicting definitions to the ODE. This conflict is resolved by extending the active and inactive contact NBM conditions as follows:

$$\text{Active contact NBM: } S(\mathbf{u}^o(t)) > g_0, \text{ or } S(\mathbf{u}^o(t)) = g_0 \text{ and } S(\dot{\mathbf{u}}^o(t^-)) > 0 \tag{4.51}$$

$$\text{Inactive contact NBM: } S(\mathbf{u}^o(t)) < g_0, \text{ or } S(\mathbf{u}^o(t)) = g_0 \text{ and } S(\dot{\mathbf{u}}^o(t^-)) < 0 \tag{4.52}$$

which is mathematically sound since the velocity at the moment of switch indicates whether an active contact or an inactive contact occurs after the switch. Furthermore, note that the case of zero velocity $S(\dot{\mathbf{u}}^o(t_s^-)) = 0$ before contact is not investigated in definitions (4.51) and (4.52). Such solutions are referred to as grazing solutions and propose a challenge that is beyond the scope

of this manuscript (the reader may refer to [16, p. 385] for some of the intricacies involved with determining grazing periodic motions). Since grazing motions are excluded, the NBM is limited in its solutions. Thus, it is important to note that the NBM is not presented as a scheme for the generation of physically accurate simulations. Rather, the NBM is used for the modal analysis and detection of periodic Signorini compliant non-grazing motions.

Next, at the instant of switch, we impose that the *internal* displacements $\mathbf{u}^o(t)$ and velocities $\dot{\mathbf{u}}^o(t_s)$ are continuous

$$\text{Continuity of internal states: } \mathbf{u}^o(t^+) = \mathbf{u}^o(t^-), \dot{\mathbf{u}}^o(t^+) = \dot{\mathbf{u}}^o(t^-), \quad S(\mathbf{u}^o(t)) = g_0 \tag{4.53}$$

while only the contact node is characterized by discontinuous velocity, as will be shown later in Equation (4.57). The condition for the continuity of the internal states (4.53) corresponds to common application of the Signorini conditions both numerically and analytically [19, 24, 40, 84, 98]. Thus, both internal displacements and internal velocities are assumed to be always continuous and only the acceleration $\ddot{\mathbf{u}}^o(t)$ is discontinuous at instants t_s (as can be deduced from Equation (4.50)). The discontinuity of *internal* accelerations at the moment of switch is a consequence of the NBM and is not expected in the true solution. However, solutions of the NBM still show good agreement with the true solution as $N \to \infty$, as illustrated in Section 4.5.

Given that the acceleration is discontinuous at the moment of switch, it is more convenient to represent the ODE (4.50) in terms of the acceleration at t^+

$$\ddot{\mathbf{u}}^o(t^+) = \begin{cases} -(\mathbf{M}_D)^{-1}(\mathbf{K}_D\mathbf{u}^o(t) + g_0\mathbf{f}_D) & \text{active contact NBM} \\ -(\mathbf{M}_N)^{-1}(\mathbf{K}_N\mathbf{u}^o(t)) & \text{inactive contact NBM} \end{cases} \tag{4.54}$$

where $\mathbf{M}_D$ and $\mathbf{M}_N$ are always invertible. See proof in Appendix B.3.

In turn, the approximation of $u(x,t)$ in NBM is defined via expressions (4.35) and (4.45)

$$u(x,t) \approx u^h(x,t) = \mathbf{P}(x)\mathbf{u}(t) = \begin{cases} \mathbf{P}(x)(\mathbf{A}^D\mathbf{u}^o(t) + g_0\mathbf{d}) & S(\mathbf{u}^o(t)) \geq g_0 \\ \mathbf{P}(x)\mathbf{A}^N\mathbf{u}^o(t) & S(\mathbf{u}^o(t)) \leq g_0. \end{cases} \tag{4.55}$$

At last, from expression (4.55), we obtain nonsmooth expressions at the contacting end (with strict inequality applied on the active contact condition) for the displacement

$$u(1,t) \approx u_N(\mathbf{u}^o(t)) = \begin{cases} g_0 & S(\mathbf{u}^o(t)) \geq g_0 \\ S(\mathbf{u}^o(t)) & S(\mathbf{u}^o(t)) \leq g_0 \end{cases} \tag{4.56}$$

velocity

$$\partial_t u(1,t) \approx \dot{u}_N(\mathbf{u}^o(t), \dot{\mathbf{u}}^o(t)) = \begin{cases} 0 & S(\mathbf{u}^o(t)) > g_0 \\ S(\dot{\mathbf{u}}^o(t)) & S(\mathbf{u}^o(t)) < g_0 \end{cases} \tag{4.57}$$

and stress

$$\sigma_n(u(1,t)) \approx \sigma_n^h(\mathbf{u}(t)) = \begin{cases} A(1)\phi_N'(1)(g_0 - S(\mathbf{u}^o(t)) & S(\mathbf{u}^o(t)) \geq g_0 \\ 0 & S(\mathbf{u}^o(t)) \leq g_0. \end{cases} \tag{4.58}$$

We note that $\sigma_n(u(1,t))$ is continuous in the NBM formulation contrarily to the discontinuous behaviour of the true solution to the Signorini problem [12, 84, 98]. However, in Section 4.5 it will be shown that the method still converges. Furthermore, it is important to note that schemes utilizing Newton's impact law with $e = 0$ are characterized by continuous contact pressure as well and still show convergence to the true solution [24].

The Signorini problem is hence formulated as the nonsmooth ODE (4.54) in $\mathbf{u}^o(t)$ with unique solutions given initial conditions $\mathbf{u}^o(0)$ and $\dot{\mathbf{u}}^o(0)$. Indeed, solutions to the ODE (4.54) are unique so long they do not describe grazing motions. For the proof of this statement, see Appendix B.4. Furthermore, the solutions generated by the NBM are characterized by *sticking phases*. Sticking phases are continuous intervals of time of non-zero measure where active contact motion occurs. To clarify, sticking phases stand in contrast to chattering exhibited by schemes utilizing a Newton impact law with $e = 1$ [84]. This is a noteworthy property of this scheme since sticking phases occur in the true solution to the Signorini problem as demonstrated in Chapter 3 and in [24, 84, 98].

On another note, the acceleration $\ddot{u}_N(t)$ obtained by differentiating Equation (4.57) involves the Dirac-delta distribution at the instance of switch, which may affect the formulation of the NBM-ODE since it participates in its definition, see Equation (4.38). However, the influence of the Dirac-delta in the NBM formulation was not investigated in this manuscript and is suppressed to simplify the formulation. Nevertheless, numerical experiments show that the NBM-ODE (4.54) admits solutions that converge to the true motion for large N. Such numerical experiment is explored in Section 4.5.1.

Next, since periodic solutions require energy conservation, we investigate the energy conservation properties of solutions to the NBM-ODE.

4.3.5 Energy conservation properties of solutions to NBM-ODE

Solutions to the NBM-ODE (4.54) are equipped with the energy metric

$$2E(t) = \int_0^1 \partial_t u(x,t)^2 + A(x)\partial_x u(x,t)^2 \, \mathrm{d}x \approx \dot{\mathbf{u}}^\top(t)\mathbf{M}\dot{\mathbf{u}}(t) + \mathbf{u}^\top(t)\mathbf{K}\mathbf{u}(t) \tag{4.59}$$

and exhibit the following properties:

1. The ODE preserves energy for $S(\mathbf{u}^o(t)) > g_0$ and $S(\mathbf{u}^o(t)) < g_0$, away from instants t_s such that $S(\mathbf{u}^o(t_s)) = g_0$.
2. At a time instant t_s, where a transition between active and inactive contact occurs (namely, at an instant where $S(\mathbf{u}^o(t_s)) = g_0$ and $S(\dot{\mathbf{u}}^o(t_i)) \neq 0$), an instantaneous change in energy ΔE

occurs

$$\Delta E = E(t_s^+) - E(t_s^-) = -|S(\dot{\mathbf{u}}^o(t_s))|\Big(\frac{1}{2}M_{NN}S(\dot{\mathbf{u}}^o(t_s)) + \sum_{j=1}^{N-1} M_{Nj}\dot{u}_j(t_s)\Big). \tag{4.60}$$

The energy after transition may either decrease ($\Delta E < 0$), increase ($\Delta E > 0$) or be conserved ($\Delta E = 0$).

For the proof, Appendix B.6.1 establishes lemmas regarding statement 1 and Appendix B.6.2 details the proof of statement 2. Thus, NBM solutions are not always energy conservative and may dissipate or gain energy at contact. From numerical experiments, it has been noticed that a large portion of NBM solutions is indeed energy dissipative. Although, similarly to Newton's impact law $e = 0$, the energy dissipation in the solution decreases with convergence to the solution, this is further discussed in Section 4.5.1.

However, statements 1 and 2 also indicate that solutions of the NBM-ODE may exhibit a periodic energy evolution in time. Indeed, this property is favourable for the detection of periodic solutions, and it is expected that the NBM can be used for the detection of periodic solutions to the Signorini problem. From numerical experiments, such periodic solutions to the NBM were found. An example of a periodic solution is shown in Figure 4.3 from which it is clear that the NBM allows for the existence of periodic solutions with sticking phases. In contrast, solutions obtained via Nitsche's

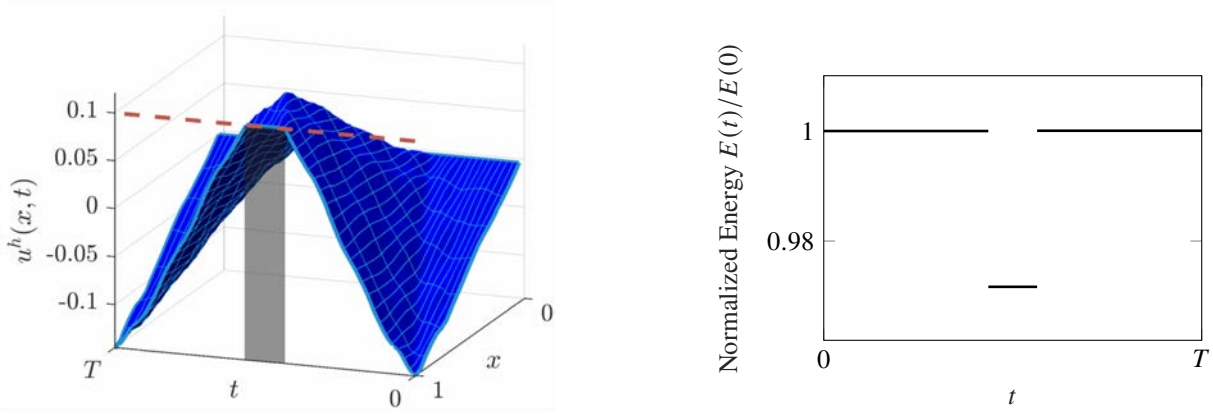

(a) Displacement field

(b) Total Energy

Figure 4.3: NBM periodic solution for the varying area bar $A(x) = 1 - x/2$ and $g_0 = 0.1$ of 10 elements and quadratic Lagrangian shape functions ($N = 20$). This model is used to illustrate different aspects of the NBM methodology (a similar model with different N is used in Figure 4.4) Note that the total energy is dissipated at the moment of contact but is completely regained at the end of the contact phase. Due to this characteristic, the NBM allows for the existence of periodic solutions with sticking phases. In Figure 4.3(a), and all the following displacement field plots, shaded rectangular surfaces and dotted lines highlight active contact phases and gap from wall, respectively.

method exhibit sticking phases only at convergence (ie, for high number of elements) [19] and solutions of scheme with Newton's impact law $e = 1$ exhibit chattering [24]. While solutions to

Newton's impact law with $e = 0$ exhibit sticking phases, they also exhibit energy dissipation for non-zero impact velocity [24] and therefore do not allow for periodic solutions. The NBM, in comparison to Newton's impact law $e = 0$, allows for a regain of energy in transition from active to inactive contact.

Indeed, the existence of periodic solutions in NBM relates largely to the fact that energy can be regained throughout the motion, as seen in Figure 4.3. We note here that the NBM does not have an explicit impact law and the energy jumps (whether loss or gain) are instead explained by the change in shape functions at the moment of switch.

In the true solution, at the instance of switch, $\partial_t u(x, t_s^+) = \partial_t u(x, t_s^-)$ holds true for $x \in (0, 1)$ [12, 84]. However, in NBM, the approximations of $\partial_t u(x, t_s^+)$ and $\partial_t u(x, t_s^-)$ involve two different sets of shape functions, described in Equations (4.16) and (4.19). For example, during closing contact (switch from inactive to active contact), the contact node's velocity $\dot{u}_N$ vanishes as dictated by the shape functions in (4.19) and a loss in energy ensues at this instance. This is similar to application of $e = 0$ using Newton's impact law in FEM. However, in opening contact (switch from active to inactive contact), there is a gain of energy since the shape functions dictating the inactive contact motion (4.16) allow for non-zero $\dot{u}_N$ after the switch. This is different than application of $e = 0$ using Newton's impact law in FEM where the velocity $\dot{u}_N$ is zero at opening contact. In sum, the regain in energy is a consequence of the switching mechanism and shape functions introduced in NBM. To better illustrate this mechanism, we use the example of the NBM model of the bar with linear shape functions.

For the NBM model of the bar with linear shape functions we have $\phi'_N(1) = 1$, $\phi'_{N-1}(1) = -1$ and $\phi'_i(1) = 0$ for $i = 1, 2, \ldots, N-2$. In turn, for the bar with linear shape functions, the displacement and velocity of the contact node during inactive contact, $S(\mathbf{u}^o(t)) < g_0$, are given as follows:

$$u(x = 1, t) \approx u_N(t) = S(\mathbf{u}^o(t)) = u_{N-1}(t) \tag{4.61}$$

$$\partial_t u(x = 1, t) \approx \dot{u}_N(t) = S(\dot{\mathbf{u}}^o(t)) = \dot{u}_{N-1}(t) \tag{4.62}$$

where Equations (4.61) and (4.62) are deduced from Equations (4.56) and (4.57) for linear Lagrange shape functions, respectively. From Equations (4.61) and (4.62), we see that, for linear shape functions, $u_N(t) = u_{N-1}(t)$ holds during inactive contact motion. Physically, it means that the last element of the bar acts as a *rigid body* throughout inactive contact motion. During active contact motion, $S(\mathbf{u}^o(t)) > g_0$, the last element of the bar acts as an elastic body similar to FEM with Newton's impact law $e = 0$ since the approximating shape functions used in Equation (4.19) are identical to implementation of a non-homogeneous Dirichlet condition in FEM. Thus, upon closing contact, the last element of the bar transforms from a rigid element to an elastic element and loses energy due to vanishing $\dot{u}_N$. However, in opening contact, the bar transforms from an elastic element to a rigid element, and the bar regains energy as the velocity of the contact node equals the velocity

of the previous node $\dot{u}_N(t) = \dot{u}_{N-1}(t)$. For higher order shape functions, a similar mechanism takes effect, however it cannot be illustrated as transformation of the last element between rigid and elastic body. Rather, the jump in energy is explained as a consequence of changing between two families of shape functions of the NBM.

Along the same line, the terms dissipation and gain of energy will be used to describe the evolution of the energy metric in time rather than implying any physical energy transfer in or out of the system. Moreover, in the NBM, it was evident from numerical experiments that the energy jump ΔE diminishes for large N. An example of such experiment is presented in Section 4.5.1. Nevertheless, an analytical proof for the convergence of ΔE to zero with higher number of elements is not presented in this manuscript.

To conclude, the behaviour of the energy metric in the NBM should be understood as a consequence of the Galerkin-Bubnov method rather than as a physical imposition on the system (as done by implementing a Newton impact law with $e = 0$, for example).

4.3.6 Notes on the NBM-FEM formulation

In this section, we will explore differences and similarities between the NBM and other existing methods for the treatment of the Signorini conditions.

The Signorini conditions are implemented in the NBM-ODE in Equation (4.54) via switching between systems of ODEs. We note that the Wave-FEM [98] also implements the Signorini conditions via switching between two discrete dynamical systems (one governing inactive contact motion and the other governing active contact motion). Also, the NBM can be considered similar to the MRM [40] since the MRM effectively modifies the stiffness matrix on the switch between active and inactive contact whereas the NBM modifies both the mass and stiffness matrix on the switch.

The solution proposed to the NBM-ODE (4.54) constitutes a Filippov solution to discontinuous ODEs [23]. In Filippov theory, the behaviour of a motion around a discontinuity ($S(\mathbf{u}^o(t)) = g_0$ in Equation (4.54)) is either *crossing* or *sliding*. Crossing solutions are solutions do not remain within the discontinuity and are not attracted to the point of discontinuity (i.e., these solutions cross the point of discontinuity). In the case of the NBM-ODE, the switching conditions (4.51)-(4.52) include only crossing solutions, since, assuming a continuous and once-differentiable solution $\mathbf{u}^o(t)$, and therefore continuous $S(\mathbf{u}^o(t))$, it is evident that a point $S(\mathbf{u}^o(t^-)) = g_0$, $S(\dot{\mathbf{u}}^o(t)) > 0$ enters active contact conditions and $S(\mathbf{u}^o(t^+)) > 0$ is expected (and vice-versa for the inactive contact conditions). However, grazing solution for which $S(\mathbf{u}^o(t)) = g_0$ and $S(\dot{\mathbf{u}}^o(t^-)) = 0$ are considered sliding Fillipov solutions since they are expected to remain at the point of discontinuity. Whilst this type of solutions is not investigated in this manuscript, it is important to note that the Filippov theory allows for solution at a discontinuity by composing a *mean* differential equations from the active contact

NBM and inactive contact NBM components of (4.54). However, this is not further investigated in this article. Moreover, while the Filippov solution is proposed for the NBM-ODE (4.54), it is not the only methodology for the solution of the NBM-ODE. Other methodologies such as regularization of the NBM around the discontinuity may be taken are possible (for more methods, see [90]). Here, it has been chosen to not consider grazing solutions which allows for the implementation of the Filippov solution in a straight-forward manner.

On another note, we would like to state that the NBM-ODE does not introduce explicitly an impact law. To clarify, in schemes utilizing Newton's impact law, different coefficients of restitutions may be used $e \in [0, 1]$ to solve the Signorini problem for a single FE model. In contrast, the NBM formulation of the Signorini conditions is unique with respect to the FE model. Still, we can draw a parallel between the NBM and FEM schemes utilizing Newton's impact law. The NBM coincides with Newton's impact law $e = 0$ during the active contact motion and away from switching instants. There, the NBM abides exactly the same ODE abided by the Newton impact law $e = 0$ since the shape functions discretizing the governing PDE are equivalent to those used in classical FEM for a fixed $u_N(t) = g_0$. However, during inactive contact motions, the ODE dictating the motion of nodes is distinct from the one used in implementation of Newton's impact law since the set of NBM shape functions to discretize the PDE (4.16) is distinct from this used in classical FEM. For example, for the case of first-order shape functions, the NBM preserves the length of the contact element during inactive contact motion: $u_N(t) = S(\mathbf{u}^o(t)) = u_{N-1}(t)$ (i.e., the contact node has the same displacement as the node before it) which does not occur in the classical FEM scheme.

4.4 Nonsmooth modal analysis

In the preceding sections, the NBM and FEM were used to approximate the solution to the initial boundary value problem exposed in Equation (4.1) to Equation (4.4). To solve for the remaining conditions, we require that $\mathbf{u}^o(t)$ and $\dot{\mathbf{u}}^o(t)$ are periodic, see Equations (4.6) and (4.7),

$$\mathbf{u}^o(0) = \mathbf{u}^o(T) \tag{4.63}$$

$$\dot{\mathbf{u}}^o(0) = \dot{\mathbf{u}}^o(T). \tag{4.64}$$

In this article, we attempt to find such solutions and corresponding period using the shooting method. Moreover, continuation is used for the detection of NSMs, i.e., families of periodic solutions [64].

4.4.1 Crank-Nicolson and shooting method in NBM

In NBM, the shooting equations require a initial displacements $\mathbf{u}_0^o$. Furthermore, all initial velocities are set to zero $\dot{\mathbf{u}}^o(t) = \mathbf{0}$ to fix the phase of the motion (see phase condition in Section 2.1.1). For

the NBM, the shooting equations read

$$\mathbf{u}^o(T) = \mathbf{u}_0^o, \quad \mathbf{v}^o(T) \equiv \dot{\mathbf{u}}^o(T) = \mathbf{0} \tag{4.65}$$

where $\mathbf{u}^o(t)$ and $\mathbf{v}^o(t)$ (introduced to denote nodal velocities) are both subject to the ODE (4.54).

To approximate $\mathbf{u}^o(T)$ and $\dot{\mathbf{u}}^o(T)$, the Crank-Nicolson (CN) scheme (or Newmark scheme with $\beta = 1/2$ and $\gamma = 1/4$ [43]) is used since it is characterized by energy conserving properties. The CN scheme in the context of NBM reads

$$\mathbf{u}_{i+1}^o = \mathbf{u}_i^o + \frac{\Delta t}{2}(\mathbf{v}_{i+1}^o + \mathbf{v}_i^o) \tag{4.66}$$

$$\mathbf{v}_{i+1}^o = \mathbf{v}_i^o + \frac{\Delta t}{2}(\mathbf{a}_{i+1}^o(\mathbf{u}_{i+1}^o, \mathbf{v}_{i+1}^o) + \mathbf{a}_i^o(\mathbf{u}_i^o, \mathbf{v}_i^o)) \tag{4.67}$$

$$\mathbf{a}_i^o(\mathbf{u}_i^o, \mathbf{v}_i^o) = \begin{cases} -(\mathbf{M}_D)^{-1}(\mathbf{K}_D\mathbf{u}_i^o + \mathbf{f}_D) & S(\mathbf{u}_i^o) > g_0 \text{ or } S(\mathbf{u}_i^o) = g, S(\mathbf{v}_i^o) > 0 \\ -(\mathbf{M}_N)^{-1}(\mathbf{K}_N\mathbf{u}_i^o) & S(\mathbf{u}_i^o) < g_0 \text{ or } S(\mathbf{u}_i^o) = g, S(\mathbf{v}_i^o) < 0. \end{cases} \tag{4.68}$$

It is important to note that the CN scheme is proven to conserve energy for classical FEM models in dynamics of autonomous and undamped structures [43]. In principle, any other ODE scheme could be chosen. Although, in NBM, it is of interest to conserve the energy of the structure away from contact in order to be able to obtain an overall accurate motion. The CN scheme is implicit and requires the implementation of a root solving procedure to find $\mathbf{u}_{i+1}^o$ and $\mathbf{v}_{i+1}^o$ in Equations (4.66) and (4.67). The root solving method used here is a Newton algorithm referred to as inexact Newton (or semismooth Newton) [18, 27]. The semismooth-Newton algorithm is detailed in Appendix B.5.

To approximate the final states $\mathbf{u}^o(T)$ and $\mathbf{v}^o(T)$, a discretization of the time span $t \in [0, T]$ into N_t steps is considered with the time-step $\Delta t = T/N_t$. The approximated time-marching solutions are denoted $\mathbf{u}^o(T) \approx \mathbf{u}_{N_t}^o$ and $\mathbf{v}^o(T) \approx \mathbf{v}_{N_t}^o$. Substitution of these approximations into Equation (4.65) reads

$$\mathbf{u}_{N_t}^o(\mathbf{u}_0^o, T) - \mathbf{u}_0^o = \mathbf{0} \tag{4.69}$$

$$\mathbf{v}_{N_t}^o(\mathbf{u}_0^o, T) = \mathbf{0} \tag{4.70}$$

where it is emphasized that the final states $\mathbf{u}_{N_t}^o$ and $\mathbf{v}_{N_t}^o$ are both functions of the initial displacements $\mathbf{u}_0^o$ and period of motion T. The shooting equations can be then solved using MATLAB's `fsolve` via a semismooth Newton procedure. The derivation of the Jacobian for the shooting equations describing a nonsmooth motion is explained in length in [8]. Furthermore, it is worth noting that the CN method is also known as the $\theta = 1/2$ implicit method and is commonly used for the solution of discontinuous ODEs arising in mechanical and electrical engineering [2].

4.4.2 Error estimation

For cases where the solution $u(x,t)$ exists, a proper error estimate of the NBM solution is the L_2 norm $||u-u^h||_2$ where $u^h(x,t)$ is defined in Equation (4.55). However, in the absence of closed-form solution, such as the periodic solutions sought for the varying-area bar, other error metrics are needed. While the error in the residual resulting from the approximation constitutes a common error metric for the Galerkin-Bubnov method [44, 79], the residual of the PDE (4.1) under the NBM-FEM approximation requires knowledge of $\phi_i''(x)$ for $x \in [0,1]$. However, since $\phi_i(x)$ is described using the piecewise Lagrangian used in FE framework, the double derivative of $\phi_i(x)$ is not defined on element boundaries. Therefore, to quantify the error, the *residual estimator* [79, p. 93]

$$R(t) = h^4 \sum_{j=1}^{N_e} \int_{\mathcal{E}_j} \left(\sum_{i=1}^{N} \phi_i(x)\ddot{u}_i(t) - \phi_i''(x)u_i(t) \right)^2 \mathrm{d}x \tag{4.71}$$

is used, where h describes the length of the element, N_e denotes the total number of elements and $\mathcal{E}_j$ is the domain of the element j excluding its boundaries such that any given $\phi_i''(x)$ is defined everywhere in $\mathcal{E}_j$, and the boundary of the elements are excluded from the error metric (4.71). It is noted, that while the error metric effectively excludes points of discontinuity, it evaluates the accuracy of the solution in ranges where the approximation of $u(x,t)$ is clearly defined. Thus, it is considered a proper metric for the evaluation of the solution's accuracy. For the NBM, we must evaluate the integral of $R(t)$ for $t \in [0,T]$. Since the acceleration $\ddot{\mathbf{u}}(t)$ is discontinuous at the moment of switch t_s, we define the *residual error* by excluding instances of discontinuity, similarly to the residual estimator,

$$R_\epsilon = \int_0^{t_s^{1-}} R(t)\,\mathrm{d}t + \int_{t_s^{(N_s-1)+}}^{T} R(t)\,\mathrm{d}t + \sum_{j=1}^{N_s} \int_{t_s^{j+}}^{t_s^{(j+1)-}} R(t)\,\mathrm{d}t \tag{4.72}$$

where t_s^j denote various distinct instants of switch through the motion and N_s defines the total instances of switch in $[0,T]$. We duly note that the residual error does not take into account the discontinuities in time, and may be an inaccurate error metric for the Signorini problem. However, the metric R_ϵ does define the quality of the approximation of inactive and active phases of motion by their respective shape functions. Thus, R_ϵ is useful in determining the accuracy in the approximation of the active and inactive contact phases. Nevertheless, if the exact solution to the problem is known, the more accurate error norm $||u-u^h||_2$ will be used instead of R_ϵ.

4.4.3 Sequential continuation with correction

As discussed in Section 3.4, methods useful for numerical nonsmooth modal analysis of the bar may not be suitable for nonsmooth modal analysis of the varying-area bar or the multi-dimensional cases

due to the existence of a dense modal space. Nevertheless, it was reported in [51] that sequential continuation led to successfully revealing the NSMs of the bar prone to unilateral contact for a FD-BEM. Similarly, application of sequential continuation on the NBM shooting equations, leads to successful detection of NSMs. Although, application of sequential continuation in the NBM was accompanied with significant numerical error and large computation times. Rather, a different approach to sequential continuation was deemed more successful: *sequential continuation with correction*. This approach and its motivation are explained in the remainder of this section.

The space of solutions of the system (4.69) to (4.70) [51,98] describing the NSM is denoted $(\mathbf{q}_0(T), T)$ where $\mathbf{q}_0$ is introduced to simplify the notation and it denotes the initial guess $\mathbf{q}_0 = \mathbf{u}_0^o$. In the solution of the NBM shooting equations (4.69) to (4.70), it has been noticed that the sequential continuation of curves with $N \geq 10$ faces difficulties in obtaining solutions on the backbone curve $(\mathbf{q}_0(T), T)$ such as long computation times and non-convergence. It is conjured that continuation these difficulties ensue from the dense modal space of the bar and insufficiency of the initial guess.

However, it was found that for large N, it is more efficient to obtain solutions by first finding solution with a low N and then apply a shooting algorithm while recursively increasing the number of nodes for each point in the low-N curve. We refer to this method as *sequential continuation with correction* (SCC). To distinguish between curves approximated using different N, we will denote a solution continuum as follows: $(\mathbf{q}_0(T), T)^N$. The steps of sequential continuation with correction are:

1. Obtain the nonlinear normal mode with low N (for instance, $N = 4$), stored as the series $(\mathbf{q}_0^k, T^k)^4$, $k = 1, 2, \ldots, N_c$.
2. For the point $i = 1$ in the series $(\mathbf{q}_0^1, T^1)^N$, perform shooting on a system with higher number of nodes N^+. First, interpolate $(\mathbf{q}_0^1)^N$ using the shape functions $\mathbf{P}(x)$ to obtain an initial guess for the desired N^+ approximation.
3. Solve the shooting equations with N^+ nodes with period T^1 and obtain $(\mathbf{q}_0^1, T^1)^{N+}$.
4. Steps 2 and 3 may be repeated for higher number of nodes with the period T^1 constant.
5. Repeat 2, 3 and 4 for all points in the series discovered in step 1, i.e., $k = 2, 3, \ldots, N_c$.

Figures 4.4 and 4.5 are used to illustrate the method.

It is important to note that failure of sequential continuation was expected due to existence of iso-periodic solutions, as explained in Section 2.5. Nevertheless, sequential continuation with correction seems to detect periodic solutions successfully. It is estimated that for finite N, the space of periodic solution of the bar in unilateral contact is less dense than the solutions described in Section 3.3.4. Furthermore, since sequential continuation with correction is used, it is possible to focus on specific solutions of the modal space and thus avoid any continuation issues emanating from the dense solution space Section 3.3.4. For example, in Figure 4.4, large portions of the backbone curves $N = 20$ and $N = 30$ are almost congruent which indicates convergence to specific periodic

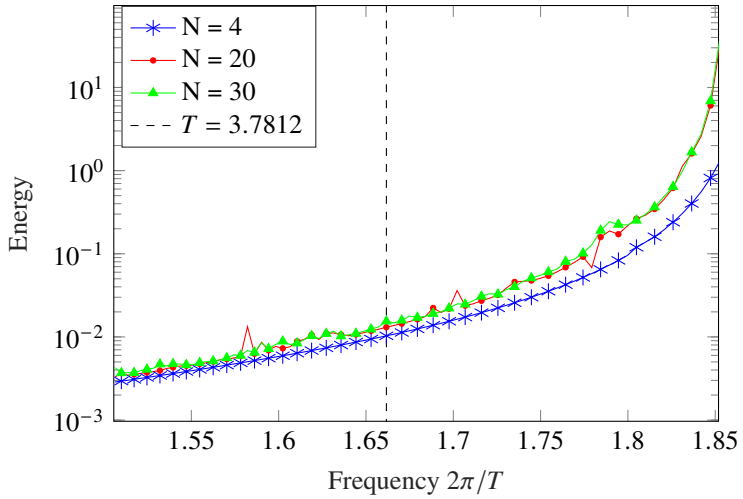

Figure 4.4: Sequential continuation with correction (SCC): every point represents a periodic solution of specific frequency and energy. The curve for $N = 4$ is found using sequential continuation. For each point on this curve, a shooting algorithm is applied to obtain a periodic solution in higher N and the same frequency. Dotted line relates to Figure 4.5 depicting solutions along this line. The results in this figure and in Figure 4.5 were obtained using CN and NBM with $g_0 = 0.1$ and $A(x) = 1 - x/2$.

solutions in the modal space. Furthermore, the solutions for small N seem to exhibit backbone curves that are two-dimensional manifolds. Thus, the backbone curve can be readily detected for NBM-ODEs of small N (for example, $N = 4$) and improved by correction for higher N.

4.5 Results

4.5.1 Convergence of Crank-Nicolson and NBM

In this section, we verify the validity of the NBM for the cantilever bar of uniform area, i.e., $A(x) = 1$, $\forall x \in [0, 1]$ and $g_0 = 0.1$. For this model, analytical solutions and nonsmooth modal analysis results were derived in the form of NSM1 in Section 3.3.1. Here, a motion from the exact NSM1, with period $T = 3.5$, is compared with its NBM approximation. The corresponding NSM displacement field can be obtained from Equation (3.48) as follows:

$$u(x,t) = f(t+x) - f(t-x) \quad \text{with} \quad f(s) = 0.1 \begin{cases} -s & s \in [-1,1], \\ s-2 & s \in [1,2.5], \\ 3-s & s \in [2.5,4.5]. \end{cases} \tag{4.73}$$

The NBM model is assigned the initial conditions generating the exact periodic solutions. The exact initial conditions are discretized and their values are taken at loci x_i corresponding to the

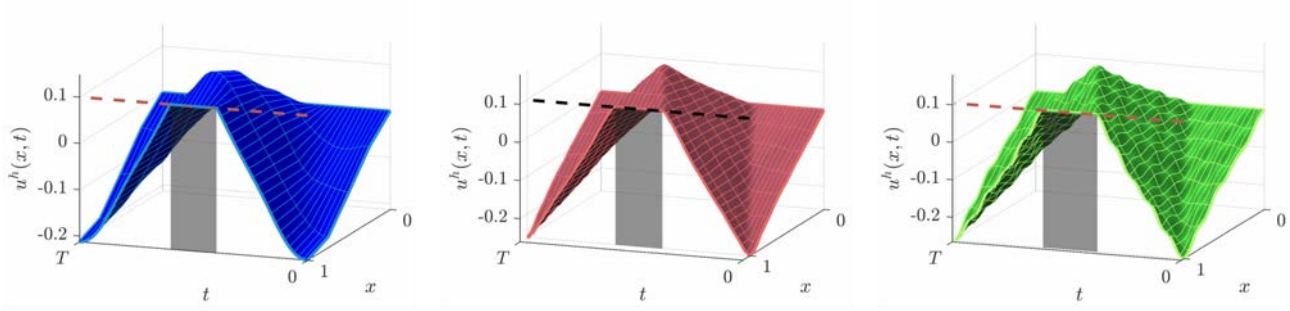

(a) $N = 4$, $R_\epsilon = 1.75 \times 10^{-2}$ (b) $N = 20$, $R_\epsilon = 2.8433 \times 10^{-4}$ (c) $N = 30$, $R_\epsilon = 1.0904 \times 10^{-4}$

Figure 4.5: Periodic displacement field corresponding to Figure 4.4, for period $T = 3.7812$. With higher number of nodes, the obtained displacement field is more accurate as evident by the lower R_ϵ value.

NBM-FEM nodes $u_i(t)$

$$u_i^o(0) = f(x_i) - f(-x_i) = -0.2x_i \quad \text{and} \quad v_i^o(0) = f'(x_i) - f'(-x_i) = 0 \tag{4.74}$$

inserted in the implicit CN time-marching with $N_t = 2000$ steps and $\Delta t = 1.75 \cdot 10^{-3}$. The error used in the convergence analysis is expressed in the L_2-norm

$$||u - u^h||_2 = \frac{1}{T}\sqrt{\int_0^1 \int_0^T (u(x,t) - \sum_{i=1}^{N-1} \phi_i(x) u_i^o(t) + \phi_N(x) u_N(\mathbf{u}^o(t)))^2 \, \mathrm{d}t \, \mathrm{d}x} \tag{4.75}$$

where $u_N(\mathbf{u}^o(t))$ is defined in Equation (4.56). A sample of the solution for $N = 200$ is illustrated in Figure 4.6. The motion plotted in Figure 4.6 shows very close to piecewise linear surface which is indeed the expected solution for the given initial conditions as presented in Equation (4.73).

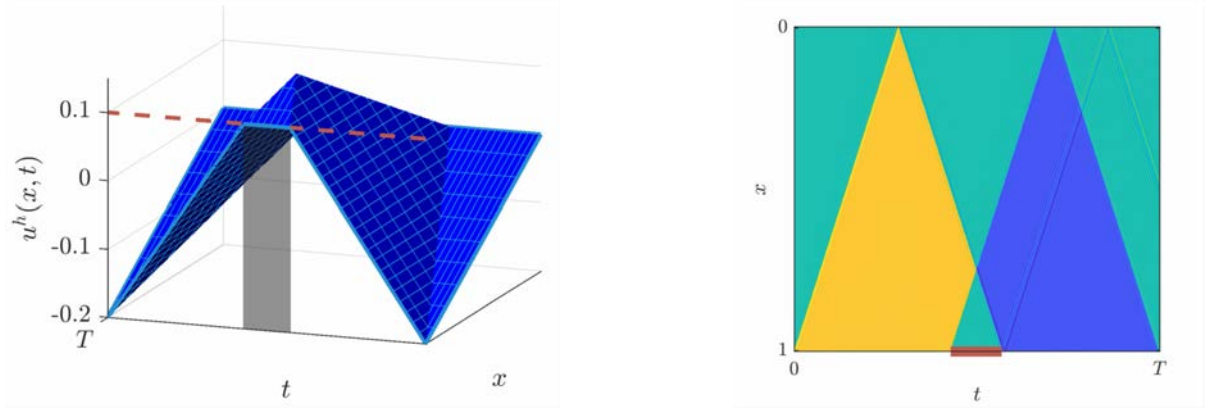

(a) Displacement field (b) Velocity field

Figure 4.6: NBM solution emerging from initial conditions (4.74) for 100 elements and quadratic shape functions ($N = 200$). We note a small disturbance in the velocity field Figure 4.6(b). This disturbance in the velocity field seems to travel along characteristic lines and diminishes progressively as higher number of elements and degree of polynomials are used. In Figure 4.6(b), and all following velocity field plots, a bolded line on the t axis highlights active contact phases.

Figure 4.7 denotes convergence of L_2 error and ΔE for the cantilever bar solution with NBM and C-N algorithm. From Figure 4.7(a), we note that, for any shape function polynomial degree, convergence is approximately of first order in terms of the number of elements. Indeed, since the

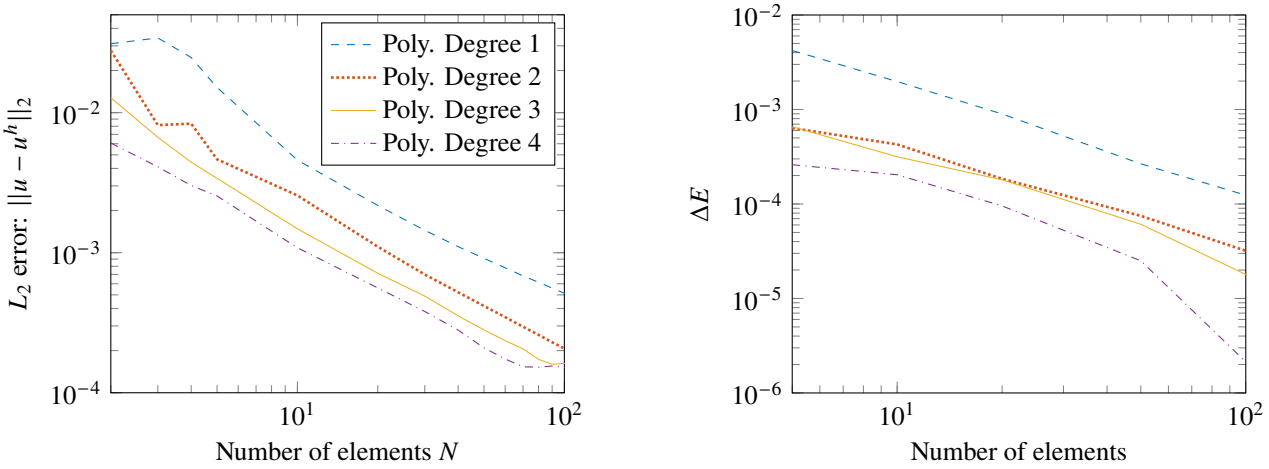

(a) Error in NBM approximation. Rates of convergence in the region of 70 elements are: Poly. Degree 1 $\approx O(N^{-0.65})$, Poly. Degree 2 $\approx O(N^{-1.1})$, Poly. Degree 3 $\approx O(N^{-0.7})$, Poly. Degree 4 $\approx O(N^{-1.4})$

(b) Error in energy jump ΔE, see Equation (4.60), occurring at the first switching instance from inactive to active contact

Figure 4.7: Error plots for the NBM with CN algorithm solution of a nonsmooth motion of the cantilever barr. Curves denote different order of Lagrangian shape function in the FE approximation

exact solution is only once piecewise differentiable as evident from Equation (4.73), the order of convergence of the FE methods is limited to first order [34, p. 117]. Since the order of convergence in FE based method is expected to be linear, it can be said that the number of elements affects the solution's accuracy more than the order of shape functions. However, it was found that for the application of shooting method, dealing with higher shape functions has allowed to reduce the number of variables while reducing both the residual error and computation time. Thus, in the upcoming nonsmooth modal analysis Section 4.5.3, the authors deemed a set of 20 elements with quadratic shape functions ideal in terms of accuracy and computation time.

Furthermore, in Figure 4.7(b), we see that as the number of elements or order of shape functions increases, the energy jump ΔE (discussed previously in Section 4.3.5) decreases. Compared to the L_2 convergence rate in Figure 4.7(a), the rate of convergence $\Delta E \to 0$ seems to be affected by the order of shape functions and shows a higher rate with increasing polynomial order. This indicates that, in NBM, a higher order of shape functions or higher number of elements allows for better energy conservation throughout the motion. Although, besides the empirical evidence shown here, no analytical investigation was done to prove this statement.

4.5.2 Comparison of NBM with other numerical techniques

The NBM exhibits numerical non-grazing solutions that converge to the exact solution. Although, it is of interest to compare the NBM to other numerical techniques. Here, the convergence of NBM will be compared to other FEM treatments of the Signorini problem, presented in Section 2.5.3, for the same exact solution presented in Equation (4.73). Furthermore, advantages of the NBM over existing methods are discussed in this section. Figure 4.8 shows the different rates of convergence for the FEM methods discussed in this manuscript in comparison to the NBM.

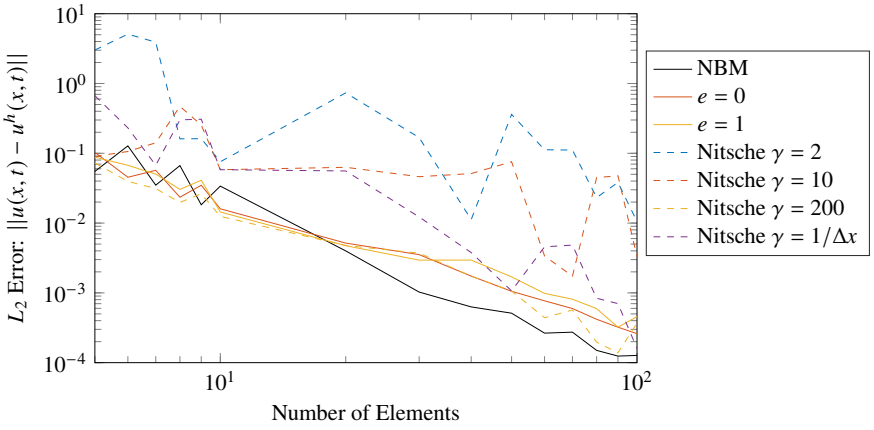

Figure 4.8: Comparison of rates of convergence of FEM treatments to the Signorini problem. In all tests, the FEM approximation consists of quadratic (degree 2 polynomial) Lagrangian shape functions.

From Figure 4.8, it is evident that the NBM exhibits a comparable rate of convergence to the other investigated methods. Nevertheless, the NBM also offers other advantages in regard to other methods. The remainder of this section shall focus on those advantages in the context of the results presented in Figure 4.8.

To start, the NBM is compared to Nitsche's method. For low N, the NBM exhibits lower L_2 errors than Nitsche's method in Figure 4.8. Evidently, the Nitsche method allows penetration of the obstacle for finite N. The penetration of the obstacle is controlled by the parameters γ and Δx (the length of the element). In fact, from our results in Figure 4.8, it can be shown that the parameter γ affects the error with respect to the true solution. Thus, the lower L_2 error of NBM for low N can be explained the fact that the NBM restricts penetration for any N while the penetration in Nitsche's method is sensitive to the value of γ at low N. Next, NBM is compared to the implementation of Newton's impact law with $e = 0, 1$. From Figure 4.8 the NBM exhibits similar convergence rate to Newton's impact law schemes. However, as previously discussed in Section 2.5.3, motions generated by implementation of Newton's impact law either exhibits artificial chattering ($e = 1$) or dissipates energy at contact ($e = 0$). In contrast, the NBM is capable of generating periodic solutions without artificial chattering at contact. An overview of the discussed advantages of NBM

over existing numerical techniques is outlined in Table 4.1.

	Convergence	No-Penetration	No-Chattering	Periodic Solutions
Nitsche	✓	✗	N/A	✓
$e = 0$	✓	✓	✓	✗
$e = 1$	✓	✓	✗	✓
NBM	✓	✓	✓	✓

Table 4.1: Comparison of desired properties of different FEM treatments to the Signorini problem.

It is also worth mentioning that the MRM (see Section 2.5.3) is not analyzed in this section. In fact, the NBM is similar in many aspects to the MRM: both exhibit a continuous active contact phase by restricting the motion $u_N(t)$ such that the Signorini conditions are satisfied. Although, the advantage of the NBM over the MRM lays in its implementation. While the MRM requires solution of an optimization problem in order to formulate the reduced mass matrix [40], the NBM does not require to do so and the formulation of the NBM mass matrices $\mathbf{M}_N$ and $\mathbf{M}_D$ is done via row and column operations on the classical FEM mass matrix $\mathbf{M}$ (eg, the formation of $\mathbf{M}_N$ in 4.40).

4.5.3 Nonsmooth modes

In this section, the nonsmooth modal analysis techniques developed in Section 4.4 are used on three variations of the bar: the internally resonant cantilever uniform area bar, the uniform area cantilever bar with soft support, and the varying area cantilever bar. To verify the validity of the NSMs presented here, we will compare each NSM with its corresponding forced-response diagram since it is expected that the backbone branch will align with the frequency and energy at resonance [64, 97]. All results in Section 4.5.3 are generated for a gap distance $g_0 = 0.001$ to comply with the models investigated in [51, 97]. Furthermore, all NSMs were generated via FE models of 20 elements and quadratic shape functions for which the backbone branches were depicting resonant points sufficiently.

Forced-response curves

The forced response-curves are generated by solving the equation

$$\partial_{tt}u(x,t) + \xi\partial_t u(x,t) + \partial_x(A(x)\partial_x u(x,t)) = \bar{F}\cos(\omega t) \tag{4.76}$$

where ξ, $\bar{F}$ and ω denote the damping coefficient, forcing amplitude and the forcing frequency, respectively. This governing PDE is complemented with the Signorini boundary conditions (4.5) and (4.4) as well as the boundary conditions imposed at $x = 0$ by the model in questions. The resulting Signorini problem is then solved for $\xi = 0.1, 0.2, \ldots, 0.7$ and for frequencies ω within

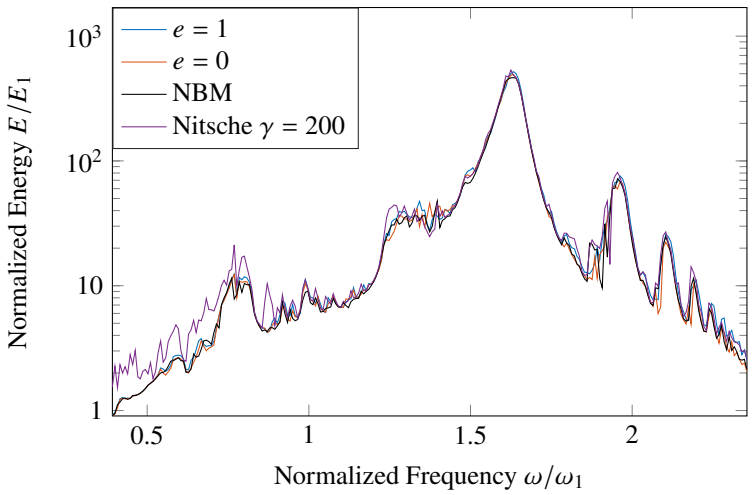

Figure 4.9: Agreement in forced-response diagram ($\bar{F} = 0.05$ and $\xi = 0.1$) for the internally resonant bar bar with 20 elements and Quadratic shape functions ($N = 40$) across different numerical methods in FEM.

the range of the detected NSM. For each set of values ξ and ω, we record the sum of kinetic and potential energies of the structure at steady state to plot the forced-response diagrams.

In practice, it is assumed a steady state is reached as $t \to \infty$. Although we often expect a forced motion to reach a periodic steady state, for some frequencies, quasi-periodic or chaotic solutions take place [98]. Thus, to obtain the forced-response curve, the Signorini problem is solved until a periodic motion is obtained or until the energy's mean value throughout a forcing period is sufficiently stable.

All forced-response curves were obtained using the FEM framework with 20 elements and quadratic shape functions and solved via SICONOS [1]. SICONOS uses a Moreau-Jean scheme to implement the Newton-impact law in the resulting system of ODEs. Here, the Newton-impact law is applied on a classical FEM approximation of the model in question, that is without application of NBM. The coefficient of restitution used to generate the forced responses in sections 4.5.3 to 4.5.3 is $e = 0$. It is important to note that forced-response diagrams for the models have been also obtained using SICONOS with $e = 1$, Nitsche's method, and NBM. Nevertheless, for the choice of 20 elements and quadratic Lagrange shape functions, all the forced-response curves yielded very similar results. An example of the comparison between forced-response diagram is presented in Figure 4.9. Figure 4.9 shows that the forced-response obtained by all numerical schemes are relatively similar, and their resonance peaks lie on approximatively same frequencies. In Sections 4.5.3, 4.5.3 and 4.5.3, the detected NBM NSMs lie on resonance peaks that are common to forced-response curves by all numerical schemes. Thus, in these sections, only forced response curves generated via SICONOS with $e = 0$ are shown for the sake of conciseness.

Internally resonant bar

The internally resonant bar of uniform area $A(x) = 1$ is an example that has been investigated both numerically [51, 98] and analytically in Chapter 3 and in [12, 84]. The system is known to manifest an intricate modal space consisting of families of iso-periodic periodic solutions in a dense set of periods and families of periodic solutions of the same frequency and energy.

In Figure 4.10(a), we compare the curve obtained by NBM to the curve of piecewise-linear analytical solutions obtained in [97]. It is clear that the NSM obtained from NBM lays closely to

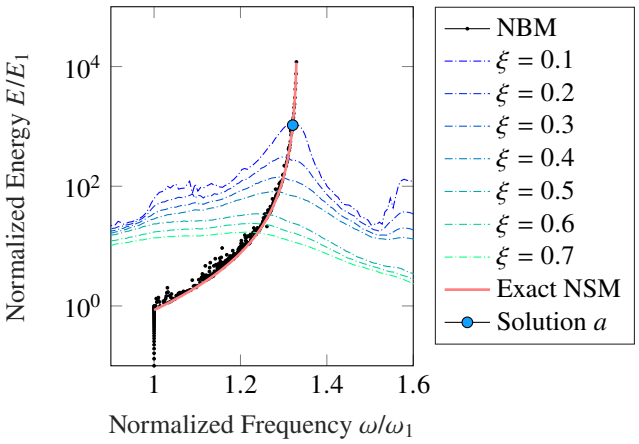

(a) Forced response curves

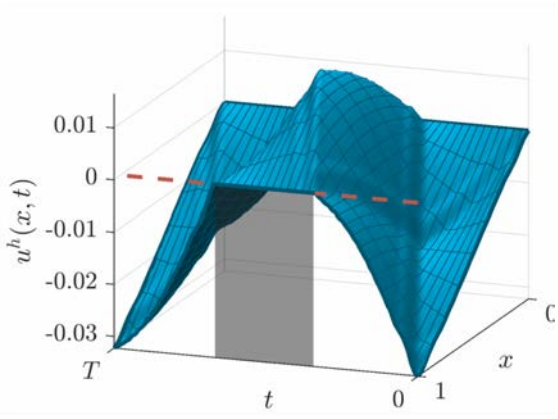

(b) Displacement field of solution a, forced and damped motion generated by SICONOS with $e = 0$

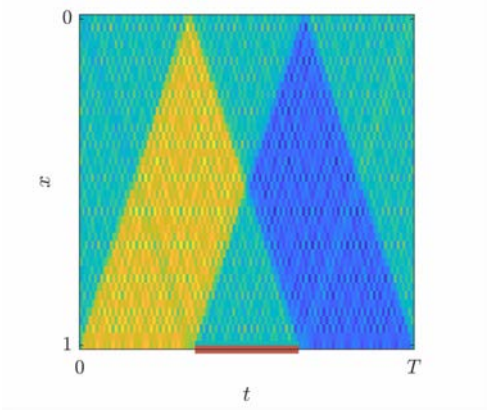

(c) Velocity field of solution a, autonomous motion generated using NBM with CN time-marching

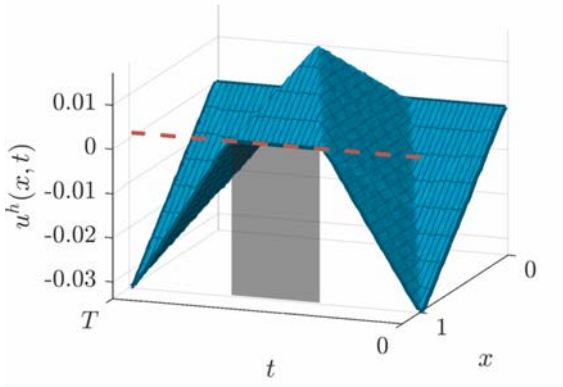

(d) Displacement field of solution a, autonomous motion using NBM with CN time-marching

Figure 4.10: NSM of the internally resonant bar detected by the NBM. ($\bar{F} = 0.05$). Exact NSM is the piecewise-linear NSM1 detected for the internally resonant bar in Section 3.3.1. $\omega_1 = \pi/2$ and $E_1 \approx 5.9\times10^{-7}$. We note here that the velocity field Figure 4.10(c) involves porous oscillations which are common to methods in the FE framework. However, a heat-map representation of the velocity field is useful in demonstrating that the found solution follows (approximately) the characteristic lines, exhibited by the exact solution [97].

the exact piecewise-linear NSM1 from Section 3.3.1. We note that there exist other exact periodic solutions with higher energies to the NSM1 curve as was concluded in Chapter 3. To clarify, it

is stated in Section 3.3.4, that the spectrum of the internally resonant bar consists of iso-periodic NSMs existing as lines above the exact NSM branch in the frequency-energy diagram. Therefore, the group of solutions found by NBM may be considered numerically accurate due to the existence of solutions above the Exact NSM curve. Nevertheless, we note that the NBM backbone curve does cross all points of resonance in the forced-response diagram. This shows that the NBM is useful for the modal analysis of the Signorini problem.

Constant cross-section bar with soft support

Similarly to [51, 97], the bar with soft support features a uniform cross-sectional area $A(x) = 1$ where the homogeneous Dirichlet condition at $x = 0$ is replaced with the Robin condition

$$ku(0,t) = \partial_x u(0,t), \quad k = \bar{k}L/(EA_0) \tag{4.77}$$

where k is the physical stiffness coefficient of the spring. The NBM was used to handle the Signorini boundary condition at $x = 1$ while the soft support condition (4.77) was treated using the classical FE technique.

For this experiment, we set $k = 0.5$ to replicate the results in [51, 97]. Corresponding results are shown in Figure 4.11. Again, as in the case of the internally resonant bar, the alignment between occurrences of resonance and the NSM detected by NBM is clear. The motions obtained in the NBM analysis are similar to those obtained in [51] for the same values. Specifically, the displacement fields depicted in Figures 4.11(b) and 4.11(c) are similar to those presented in [51, (a) and (b) in Figure 11].

In Figure 4.11(a), it seems apparent that both displacements relate to two different branches of the solution. Moreover, the forced response curves of less damped motions have two peaks which may indicate the existence of two distinct NSM branches. Here, the branch corresponding to solution q_2 has been detected until a maximal energy point. Backward sequential continuation has then revealed a distinct a set of points to which the solution q_1 belongs. These points seem to consist of a curve and the origin of this curve coincides with a subharmonic 4 of the second fundamental frequency ω_2. This coincidence with the subharmonic $\omega_2/4$ may suggest the existence of an internal resonance in the proximity of both curves. Further attempts using sequential continuation to reveal the internal resonance between the curves were not successful. Indeed, the use of sequential continuation prevents us from confirming confidently the existence of the two distinct branches since the method does distinguish between branches belonging to different continua [4]. In order to affirm this hypothesis, a continuation method capable of resolving internal resonances is required.

A method generally used for the detection of internal resonances is the pseudo-arclength continuation [64]. However, the use of pseudo-arclength continuation relies on the a tangent to the backbone curve to formulate the next solution along the curve [4]. Due to the nonsmoothness

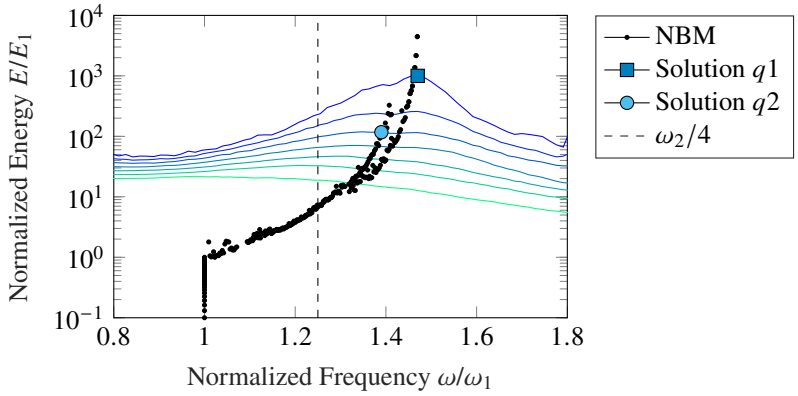

(a) Forced response curves

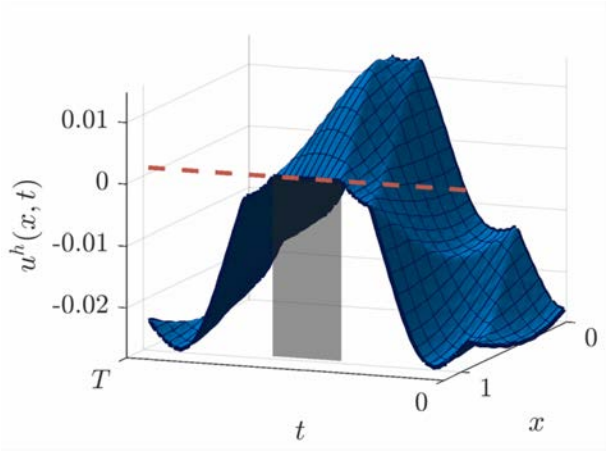

(b) Solution q_1, autonomous NBM motion

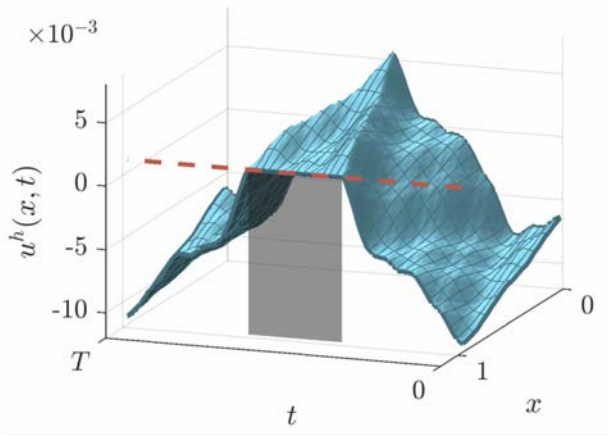

(c) Solution q_2, autonomous NBM motion

Figure 4.11: NSM of the bar with soft support with $k = 0.5$ detected by the NBM. Forced response curves with $\bar{F} = 0.025$ and $\xi = 0.1, 0.2, \ldots, 0.7$. First natural frequency $\omega_1 \approx 0.65$, second natural frequency $\omega_2 \approx 3.3$ and grazing energy $E_1 \approx 5.9 \times 10^{-7}$.

of the motions in NSMs, such tangent cannot be formulated at every point on the branch. In fact, pseudo-arclength continuation was applied in [51, p. 9] for the detection of NSMs. While some continuous sections of the NSM were detected, pseudo-arclength continuation has failed to reveal internal resonances and could not reveal backbone curves for long ranges of frequencies [51, p. 10].

Varying-area bar

While modal analysis of the bar of uniform area has been the subject of both analytical or numerical analysis [51, 97], it required knowledge of the d'Alembert function or Green's function or characteristic lines. Here, the NBM allows for modal analysis of the varying-area bar since it allows detection of periodic solutions in the autonomous varying-area bar prone to contact. For the varying area bar in Figure 4.1, several area functions $A(x)$ were considered. In order to simplify the discussion for the remainder of this section, the following terminology is introduced to distinguish

between the investigated models:

$$\textbf{heav-bar} \quad A(x) = 1 - 0.5\Theta(x - 0.5) \equiv A_h(x) \tag{4.78}$$

$$\textbf{lin-bar} \quad A(x) = 1 - x/2 \equiv A_l(x) \tag{4.79}$$

$$\textbf{quad-bar} \quad A(x) = 0.5x(2 - x) \equiv A_q(x) \tag{4.80}$$

where $\Theta(x)$ denotes the Heaviside function, and the heav-bar hence exhibits two cross-sectional areas: A_0 for $\bar{x} \in [0, 0.5L]$ and $0.5A_0$ for $\bar{x} \in (0.5L, 1]$. Furthermore, it is worth noting that all models consist of bars with decreasing areas such that $A(0) = 1$ and $A(1) = 0.5$. The corresponding NSM is illustrated in Figure 4.12(a). The detected NSMs of the lin- and quad-bars are illustrated

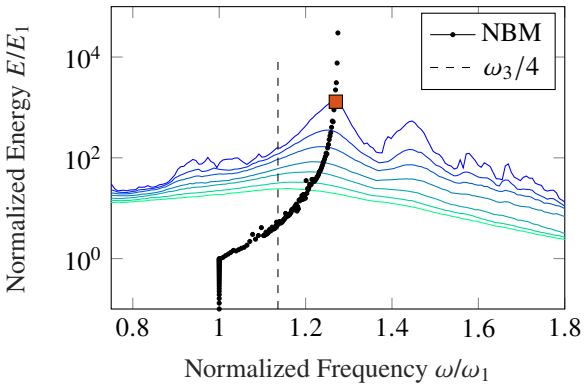

(a) heav-bar ($A(x) = A_h(x)$). $\omega_1 \approx 1.44$, $\omega_3 \approx 6.54$ and $E_1 \approx 4.43 \times 10^{-7}$

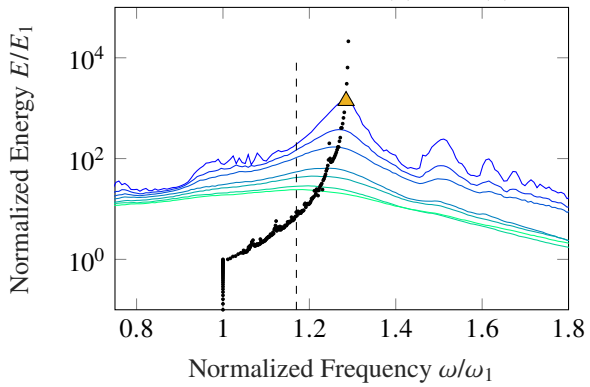

(b) lin-bar ($A(x) = A_l(x)$). $\omega_1 \approx 1.44$, $\omega_3 \approx 6.72$ and $E_1 \approx 4.98 \times 10^{-7}$

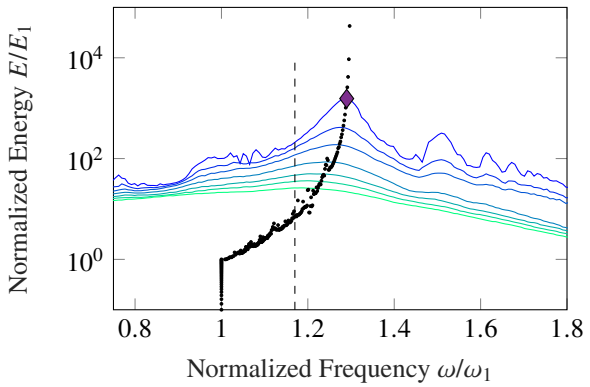

(c) quad-bar ($A(x) = A_q(x)$). $\omega_1 \approx 1.35$, $\omega_3 \approx 6.32$ and $E_1 \approx 4.31 \times 10^{-7}$

Figure 4.12: Backbone and forced response curves ($\bar{F} = 0.05$) for the varying area bars. NSMs detected by the NBM with 20 elements of quadratic shape functions. The depicted points in sub-figures (a), (b) and (c) correspond respectively to solutions b, c, and d investigated in Figure 4.13(b).

in Figures 4.12(b) and 4.12(c), respectively. Indeed, the NSMs obtained by the NBM coincide the resonant points in the forced-response diagrams as expected from theory of nonlinear modal analysis [64, 84].

The effect of area variation on the modal space of the bar in unilateral contact is of interest. In

contrast to the conclusions from the bar with soft support in Section 4.5.3, no internal resonances were detected for the cases of the varying area bar around the subharmonic $\omega_3/4$ or other subharmonics within spectrum of the backbone curve. Next, Figure 4.13 illustrates the backbone curves of all varying area models and that of the uniform area investigated in Section 4.5.3. In Figure 4.13(a), the backbones of the varying area bars exhibit higher energies for the same normalized frequencies when compared to the uniform area bar (investigated in Section 4.5.3). In other terms, the behaviour of the varying area bars can be characterized as "softer" in relation to the uniform area bar. Along the same line, it is noted that while the lin- and quad-bars exhibit a similar stiffening pattern, the heav-bar is characterized by the softest stiffening. Thus, it is indicative that the varying area function affects the stiffening behaviour and, in turn, the range size of resonant frequencies. Next, in Figure 4.13(b), comparison of the varying-area bar NSMs with respect to their true (not normalized) frequencies shows that the area variation causes backward shifts in the backbone curves towards lower frequency ranges. We note that the backward shifts in Figure 11(b) originates in the vertical line portions of the backbone curves below normalized energy 1. These vertical line portions depict linear modes of vibrations where no contact occurs and $u_N(t) < g_0$ throughout the whole duration of motion. Since the sections of linear vibration modes of the varying area bars are shifted backwards in frequency, we conjure that the backward shifts are a consequence of the area variation's effect on the linear mode shapes of the bar rather than the contact dynamics introduced to the system.

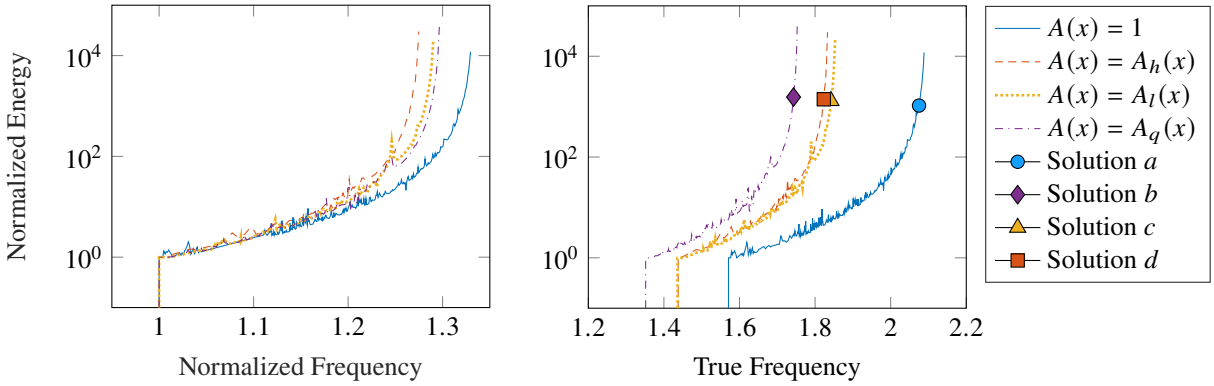

(a) Comparison in normalized frequency

(b) Comparison in true frequency

Figure 4.13: Backbone curves of different area cantilever bars corresponding to Figures 4.10(a) and 4.12.

At last, specific motions on the NSMs of the heav-bar, quad-bar and lin-bar are plotted in Figure 4.14. it is noted that the NSM motions of the varying area bar models, while qualitatively similar to the NSM motions of the uniform area bar depicted in Figures 4.10(c) and 4.10(d), exhibit piecewise nonlinear displacement fields in space-time rather than piecewise-linear displacement field of the uniform area bar.

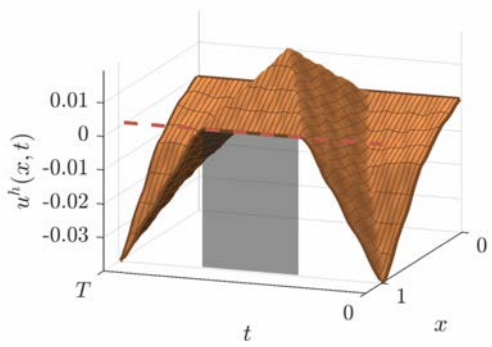

(a) Displacement field solution b

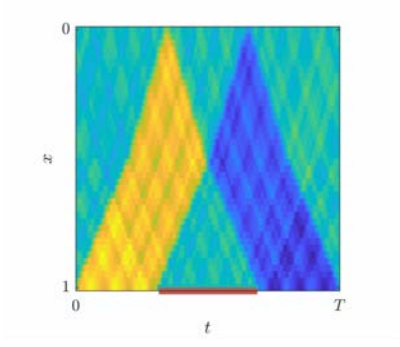

(b) Velocity field solution b

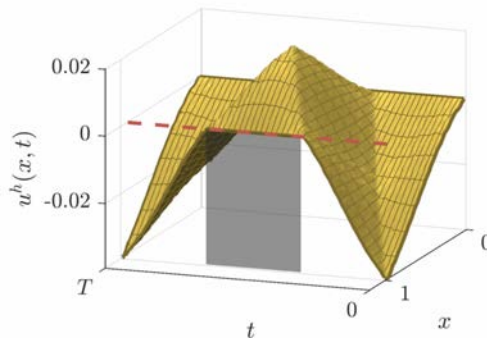

(c) Displacement field solution c

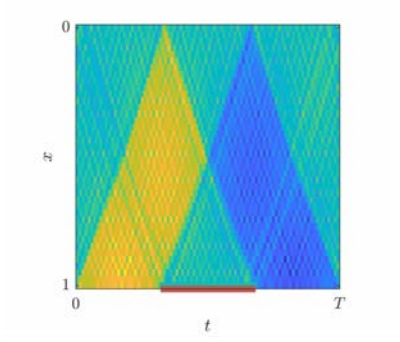

(d) Velocity field solution c

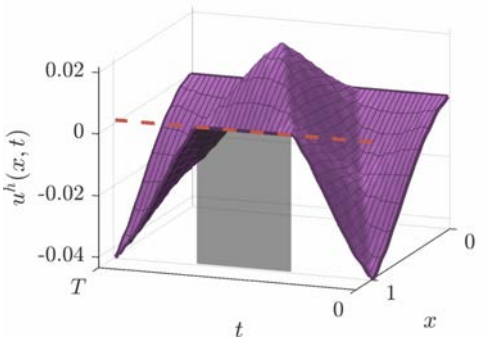

(e) Displacement field solution d

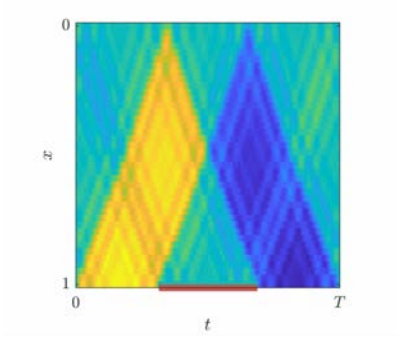

(f) Velocity field solution d

Figure 4.14: Comparison of selected autonomous NBM motions from the backbone curves of all varying-area bars. The locations of the selected motions on the FEP is noted in Figures 4.12 and 4.13(b).

4.6 Limitations of NBM

In this section, we provide a summery of all limitations to NBM and include possible spectrum of applications of NBM to other structures.

The limitations of NBM can be summarized as follows:

1. The choice of shape functions to approximate $u(x,t)$, in the NBM, must be able to exhibit non-zero and negative stress $A(1)\partial_x u(1,t)$. This limitation is common to the Nitsche method and MRM as well. See Section 4.3.1 for further elaboration.

2. The NBM relies on distinction between internal nodes and nodes prone to contact. Furthermore, those are fixed in throughout the motion and must be known a priori. See Section 4.3.2 for context and further discussion.
3. The NBM formulation does not cover the case of grazing motions as they were beyond the scope of this paper. Currently, the rules for implementing active or inactive contact are (4.51) and (4.52). It is suspected that additional rules are required to allow NBM to capture grazing motions. This is further discussed in Section 4.3.4.
4. The acceleration term $\ddot{u}_N(t)$ exhibits a dirac-delta function at the switch between inactive and active contact by definition (obtained by differentiating Equation (4.57)). The dirac-delta does not appear in the NBM-ODE formulation and its effects were yet explored. Further elaboration on the matter is given at the last paragraph of Section 4.3.4.

4.7 Discussion

The NBM for the treatment of Signorini boundary conditions in the framework of FEM was presented. The method was developed for nonsmooth modal analysis purposes entailing the detection of periodic solutions to the autonomous Signorini problem. Compared to application of Newton's impact law in FEM or WFEM, the resulting ODE from the NBM formulation for the varying area bar allows for the existence of periodic solutions with a continuous sticking phase at contact.

The NBM assumes different approximations of the contacting nodal displacement $u_N(t)$ during inactive and active contact phases. The state $u_N(t)$ is dictated by (1) boundary conditions and (2) nodes that are not prone to contact (internal nodes). While the treatment of active contact is done similarly to classical FEM (clamped condition at end of bar), in the treatment of inactive contact, the homogeneous Neumann boundary condition is enforced in a strong sense such that the approximation of the contact stress vanishes, that is $\sigma_n(u(1,t)) = 0$, throughout the entire inactive contact duration. The two associated approximations of the quantity $u_N(t)$ can be seen as constituting two distinct sets of shape functions. The residuals for the inactive and active motion approximations are then projected onto their respective set of shape functions to form two distinct ODEs. The Signorini problem is then solved by switching between the sets of shape functions both in trial and test functions.

Moreover, nonsmooth modal analysis via NBM resulted in valid backbone curves aligning with resonances of forced-response diagrams. These results were obtained for three cases: the cantilever bar of uniform area, the cantilever bar with soft support, and the cantilever bar of varying area.

The results presented for the uniform area bar and the bar with soft support have agreed with previous research on the topic. Furthermore, the NBM has allowed for the characterization of two distinct NSMs of the bar with soft support. The two distinct curves seem to relate via an

internal resonance as one of the curves originates from a sub-harmonic of the motion. However, affirmation of this result could not be achieved with sequential continuation and the detection of internal resonances in NSMs is subject for future research (this is further discussed in Chapter 6) Furthermore, application of the NBM to discover the modal space of the bar of varying area in unilateral contact has been proven successful and the results show good agreement with the forced-response curves.

The NBM has been expanded to the framework of multidimensional Signorini problems successfully. Furthermore, the NBM was proven to exhibit periodic solutions to the Signorini problem in two dimensions and NSMs were found. The NBM formulation for multidimensional problems enjoys the same advantages of this in the one-dimensional case (1) mass and stiffness matrix of the FE models are modified via a series of column and row operation (similar to definition of $\mathbf{M}_N$ and $\mathbf{K}_N$ in (4.40)) (2) the resulting composite ODE can be solved via explicit or implicit time marching techniques and (3) existence of a continuous contact phase. These will be discussed in the next chapter.

Supplementary Material

Excerpts of scripts and algorithms used to perform the analysis and generate figures in this chapter are available on Zenodo [86].

Chapter 5

Nodal Boundary Method in Two Dimensions

In Chapter 4, the NBM was derived in the context of the bar prone to unilateral contact with a rigid foundation. The NBM was proven successful for the nonsmooth modal analysis of various bar geometries. In this chapter, the formulation of the NBM is extended for the nonsmooth modal analysis of two-dimensional structures.

Nonsmooth modal analysis of two-dimensional structure has been attempted prior in [97]. In [97], the FVM was used to determine periodic solutions to the cantilever plate prone to unilateral contact. However, the FVM has yet been able to detect periodic solutions to the Signorini problem in two-dimensions due to high energy dissipation exhibited by numerical solutions [97]. Thus, this chapter answers the most challenging topic in this thesis: nonsmooth modal analysis of multi-dimensional structures. To this end, the NBM formulation is extended to two-dimensional structures and is used for nonsmooth modal analysis. Still, it should be noted that the NBM is not extended beyond two-dimensions even though notes regarding three-dimensional extensions are presented in Section 5.8.

This chapter follows a structure similar to Chapter 4. Section 5.1 lays the Signorini problem of the two-dimensional plate and necessary terminology for this chapter. Next, Section 5.2 discusses briefly the FEM formulation and sets the framework for the 2D-NBM. In turn, Section 5.3 derives the switching algorithm responsible for the treatment of Signorini conditions in NBM (this section is equivalent to sections 4.3.2 and 4.3.3 of the 1D-NBM). In Section 5.4, the 2D-NBM is derived and its properties are discussed. Then, techniques for the nonsmooth modal analysis in 2D-NBM are presented in Section 5.6, and nonsmooth modal analysis of the plate via NBM is performed in Section 5.7. The scope and limitation of the presented 2D-NBM methodology are discussed in Section 5.8. Section 5.9 constitutes of the conclusion of this chapter.

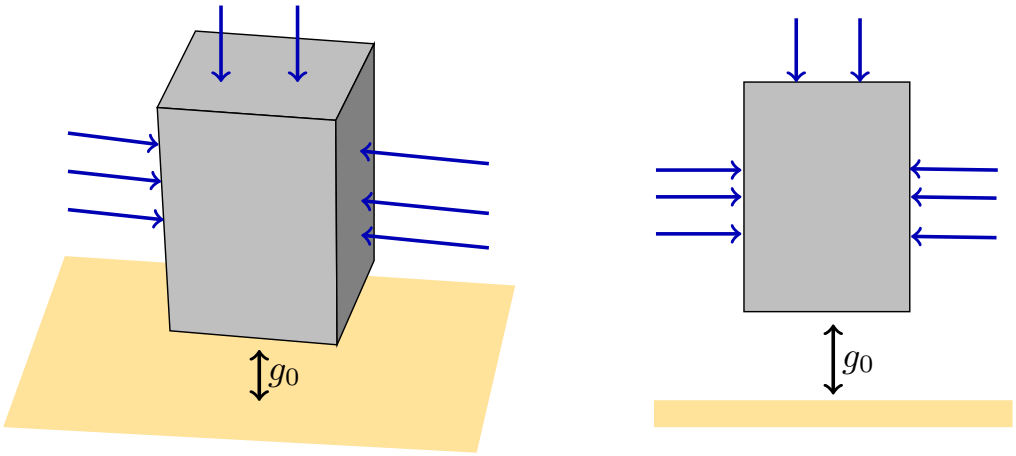

Figure 5.1: A plate in unilateral contact with rigid obstacle (in yellow) under plane stress assumptions. The plane stress assumption is valid for thin plates and no net out-of-plane forces acting on the plate.

5.1 Signorini problem

We investigate the problem of a two-dimensional mechanical system prone to unilateral contact with a rigid foundation. Let the structure be defined by a domain $\Omega \subset \mathbb{R}^2$. The displacement field of the structure $\mathbf{u}(\mathbf{x}, t) : \Omega \times \mathbb{R}^+ \to \mathbb{R}^2$ obeys the partial differential equation

$$\rho \partial_{tt} \mathbf{u}(\mathbf{x}, t) - \nabla \cdot \boldsymbol{\sigma}(\mathbf{u}(\mathbf{x}, t)) = \mathbf{0}, \quad (\mathbf{x}, t) \in \Omega \times [0, \infty) \tag{5.1}$$

where ρ describes the density of the structure and the stress field $\boldsymbol{\sigma}(\mathbf{u}(\mathbf{x}, t)) : \Omega \times \mathbb{R}^+ \to \mathbb{R}^{2\times 2}$ is formulated assuming plane stress and isotropic material [34]. Using Voigt's notation, the stress-strain relationship is

$$\begin{pmatrix} \sigma_{11}(\mathbf{u}(\mathbf{x}, t)) \\ \sigma_{22}(\mathbf{u}(\mathbf{x}, t)) \\ \sigma_{12}(\mathbf{u}(\mathbf{x}, t)) \end{pmatrix} = \frac{Y}{1-\nu^2} \begin{bmatrix} 1 & \nu & 0 \\ \nu & 1 & 0 \\ 0 & 0 & \frac{1}{2}(1-\nu) \end{bmatrix} \begin{pmatrix} \epsilon_{11}(\mathbf{u}(\mathbf{x}, t)) \\ \epsilon_{22}(\mathbf{u}(\mathbf{x}, t)) \\ \epsilon_{12}(\mathbf{u}(\mathbf{x}, t)) \end{pmatrix} \to \underline{\boldsymbol{\sigma}}(\mathbf{u}(\mathbf{x}, t)) = \mathbf{D}\underline{\boldsymbol{\epsilon}}(\mathbf{u}(\mathbf{x}, t)) \tag{5.2}$$

where both the stress and strain fields consist of symmetric tensors such that $\sigma_{21} = \sigma_{12}$ and $\epsilon_{21} = \epsilon_{12}$. According to Voigt's notation, $\underline{\boldsymbol{\sigma}}$ and $\underline{\boldsymbol{\epsilon}}$ gather the non-redundant terms in the stress (σ_{11}, σ_{22} and σ_{12}) and strain tensors ($\epsilon_{11}, \epsilon_{22}$ and ϵ_{12}), respectively. Furthermore, $\mathbf{D}$ gathers the constant physical properties Y and ν and defines the strain-stress relationship for the plane-stress approximation. Illustration of a structure approximated by plane stress and prone to unilateral contact is portrayed in Figure 5.1. Nevertheless, the presented formulation is not limited to the plane-stress assumption and is applicable to other linear relationships between stress and strain. However, similarly to the 1D-NBM, the 2D-NBM does not apply to nonlinear relationship stress-strain relationship.

The boundary of the structure is defined by Γ and is further partitioned as follows: $\Gamma = \Gamma_D \cup \Gamma_N \cup \Gamma_C$. The portions Γ_N and Γ_D denote parts where homogeneous Neumann and Dirichlet

BCs are applied, respectively,

$$\boldsymbol{\sigma}(\mathbf{u}(\mathbf{x},t))\mathbf{n} = 0, \quad (\mathbf{x},t) \in \Gamma_{\mathrm{N}} \times [0,\infty) \tag{5.3}$$

$$\mathbf{u}(\mathbf{x},t) = 0, \quad (\mathbf{x},t) \in \Gamma_{\mathrm{D}} \times [0,\infty) \tag{5.4}$$

where $\mathbf{n}$ denotes the outward normal to the boundary Γ. Γ_{C} describes the portion of the boundary prone to unilateral contact. For $(\mathbf{x},t) \in \Gamma_{\mathrm{C}} \times \mathbb{R}^{+}$, the Signorini complementarity conditions apply [96], that is

$$0 \leq g_0 - \mathbf{u}(\mathbf{x},t)\cdot\mathbf{n}, \quad \sigma_n(\mathbf{u}(\mathbf{x},t)) \leq 0, \quad (g_0 - \mathbf{u}(\mathbf{x},t)\cdot\mathbf{n})\sigma_n(\mathbf{u}(\mathbf{x},t)) = 0 \tag{5.5}$$

where $\sigma_n = \mathbf{n}^{\top}\boldsymbol{\sigma}(\mathbf{u}(\mathbf{x},t))\mathbf{n}$ denotes the contact pressure defined on Γ_{C}. Moreover, g_0 defines the distance between the non-deformed boundary Γ_{C} and the rigid obstacle. For the rectangular plate, the boundary Γ_{C} constitutes a constant gap g_0 (ie, the initial gap with the rigid obstacle does not vary in space or time) and forms a straight line parallel to the contact boundary of the structure (see Figure 5.1 for the illustration of a fixed constant-gap with the rigid obstacle). Curved boundaries of the rigid obstacle or variable gap functions (of the type $g_0(t,\mathbf{x})$) are not considered in this work.

In what follows, the dynamic Signorini problem in (5.1) to (5.5) is solved using NBM within the FEM framework. The next section discusses the NBM treatment of the Signorini condition complementarity conditions (5.5).

5.2 Nodal Boundary Method

Similarly to the 1D-NBM, the formulation of the 2D-NBM relies on the FEM Lagrangian shape functions. In this section, a brief overview of the FEM formulation of the plate is given. Important terminology for the derivation of the 2D-NBM is also introduced.

In FEM, the displacement field is approximated using piecewise continuous Lagrange polynomial shape functions, stored in $\mathbf{P}(\mathbf{x}) : \mathbb{R}^2 \to \mathbb{R}^{2\times N}$, and nodal quantities $\mathbf{u}(t) \in \mathbb{R}^N$ where N denotes the total number of nodes for a given number of elements and order of Lagrange polynomials such that the displacements are approximated as follows:

$$\mathbf{u}(\mathbf{x},t) \approx \mathbf{P}(\mathbf{x})\mathbf{u}(t), \quad (\mathbf{x},t) \in \Omega \times [0,\infty). \tag{5.6}$$

For conciseness, the arrays $\mathbf{u}(t)$ and $\mathbf{P}(\mathbf{x})$ exclude nodal quantities relating to homogeneous Dirichlet boundaries Γ_{D}. These quantities are naturally omitted from Equation (5.6) and do not participate in the ODE formulation of the FEM.

The 2D-NBM also uses the stress field approximation of the FEM. The stress field in the FE model is represented as a linear function of the nodal quantities $\mathbf{u}(t)$. Specifically, the FEM

approximation of Equation (5.2) reads

$$\underline{\boldsymbol{\epsilon}}(\mathbf{P}(\mathbf{x})\mathbf{u}(t)) = \mathbf{B}(\mathbf{x})\mathbf{u}(t) \tag{5.7}$$

$$\underline{\boldsymbol{\sigma}}(\mathbf{P}(\mathbf{x})\mathbf{u}(t)) = \mathbf{D}\mathbf{B}(\mathbf{x})\mathbf{u}(t) \tag{5.8}$$

where $\mathbf{B}(\mathbf{x})$ stores the space-differentiated Lagrangian polynomials within the element, as done traditionally in the FEM [34]. Similarly to the 1D-NBM derivation, we shall distinguish between internal nodal displacements $\mathbf{u}^o(t)$ and displacements of nodes prone to unilateral contact denoted $\mathbf{u}^c(t)$. In the multidimensional framework, there exist multiple nodes that are prone to unilateral contact on Γ_C. Accordingly, the displacement vector reads $\mathbf{u}(t) = (\mathbf{u}^o(t)\ \mathbf{u}^c(t))^\top$ with $N = N_\mathrm{O} + N_\mathrm{C}$. The weak formulation of Equation (5.1) uses test functions $\mathbf{w}$ corresponding to nodal quantities and reads

$$\mathbf{w}(t)^\top(\mathbf{M}\ddot{\mathbf{u}}(t) + \mathbf{K}\mathbf{u}(t)) - \mathbf{w}^c(t)^\top\boldsymbol{\lambda} = \mathbf{0}, \quad \mathbf{w}(t) = \begin{pmatrix}\mathbf{w}^o(t)\\ \mathbf{w}^c(t)\end{pmatrix} \tag{5.9}$$

where $\mathbf{w}^c(t)$ and $\mathbf{w}^o(t)$ denote the test function corresponding to nodes prone to contact and internal nodes, respectively. Similarly to the 1D-NBM (see Equation (4.9)), the quantities in $\mathbf{w}(t)$ vary depending on the contact phase of the structure and play an active role in the derivation of the NBM-ODE. In Equation (5.9), $\mathbf{M}$, $\mathbf{K}$ and $\boldsymbol{\lambda}$ are the FE mass matrix, stiffness matrix and vector of contact forces, respectively, and are defined as

$$\mathbf{M} = \rho\int_\Omega \mathbf{P}(\mathbf{x})^\top\mathbf{P}(\mathbf{x})\mathrm{d}\mathbf{x}, \quad \mathbf{K} = \int_\Omega \mathbf{B}(\mathbf{x})^\top\mathbf{D}\mathbf{B}(\mathbf{x})\mathrm{d}\mathbf{x}, \quad \boldsymbol{\lambda} = \int_{\Gamma_\mathrm{C}} \mathbf{P}(\mathbf{x})^\top\boldsymbol{\sigma}(\mathbf{u}(\mathbf{x},t))\mathbf{n}\mathrm{d}\mathbf{x}. \tag{5.10}$$

The FE approximation of the Signorini conditions (5.5) reads

$$0 \le g_0\mathbf{1} - \mathbf{u}^c(t), \quad \boldsymbol{\lambda} \le 0, \quad (g_0\mathbf{1} - \mathbf{u}^c(t))^\top\boldsymbol{\lambda} = 0 \tag{5.11}$$

where $\mathbf{1}$ is a vector of size $N_\mathrm{C} \times 1$ with all entries being 1.

In the NBM, the contact forces $\boldsymbol{\lambda}$ are first approximated using the FE Lagrange shape functions as

$$\boldsymbol{\lambda} = \int_{\Gamma_\mathrm{C}} \mathbf{P}(\mathbf{x})^\top\boldsymbol{\sigma}(\mathbf{u}(\mathbf{x},t))\mathbf{n}\mathrm{d}\mathbf{x} \approx \int_{\Gamma_\mathrm{C}} \mathbf{P}(\mathbf{x})^\top\boldsymbol{\sigma}(\mathbf{P}(\mathbf{x})\mathbf{u}(t))\mathbf{n}\mathrm{d}\mathbf{x} \equiv \boldsymbol{\lambda}^{\mathrm{NBM}}(\mathbf{u}(t)) \tag{5.12}$$

where $\boldsymbol{\lambda}^{\mathrm{NBM}}(\mathbf{u}(t))$ denotes the NBM approximation of contact forces (approximation (5.12) is equivalent to the use of the FEM stress as the boundary stress in the 1D-NBM in Equation (4.32)). Similarly to the 1D-NBM, this approximation is not traditional to the FEM, where usually λ is usually used to denote prescribed Neumann conditions [34].

Then, the contact forces in Equation (5.12) are inserted into Equation (5.11) to form the Signorini conditions in NBM in $\mathbf{u}(t)$ exclusively:

$$0 \le g_0\mathbf{1} - \mathbf{u}^c(t), \quad \boldsymbol{\lambda}^{\mathrm{NBM}}(\mathbf{u}(t)) \le 0, \quad (g_0\mathbf{1} - \mathbf{u}^c(t))^\top\boldsymbol{\lambda}^{\mathrm{NBM}}(\mathbf{u}(t)) = 0. \tag{5.13}$$

Finally, given $\mathbf{u}^o(t)$, the Signorini conditions are applied on the contact nodes in a strong manner by solving Equation (5.13) for $\mathbf{u}^c(t)$. This procedure will be elaborated in the next sections.

It is noted that the derivations of both 2D-NBM and 1D-NBM methodologies follow similar steps such as the definition of the stress on the contact boundary in Equation (5.12) and the application of the switching method. Therefore, it is useful to first discuss the similarities and differences between the 1D and 2D NBM.

5.2.1 Analogy between the 1D and 2D NBM

The NBM-ODE in the multidimensional case takes a similar form to the NBM-ODE in the one-dimensional case (4.54). The general form of the NBM-ODE in both the one- and multi- dimensional cases can be put as follows:

$$\ddot{\mathbf{u}}^o(t^+) = -\mathbf{M}^*(\mathbf{u}^o(t))^{-1}(\mathbf{K}^*(\mathbf{u}^o(t))\mathbf{u}^o(t) + \mathbf{f}^*(\mathbf{u}^o(t))) \tag{5.14}$$

where

$$\mathbf{M}^*(\mathbf{u}^o(t)) = \mathbf{A}^*(\mathbf{u}^o(t))^\top \mathbf{M}\mathbf{A}^*(\mathbf{u}^o(t)) \tag{5.15}$$

$$\mathbf{K}^*(\mathbf{u}^o(t)) = \mathbf{A}^*(\mathbf{u}^o(t))^\top \mathbf{K}\mathbf{A}^*(\mathbf{u}^o(t)) \tag{5.16}$$

$$\mathbf{f}^*(\mathbf{u}^o(t)) = \mathbf{A}^*(\mathbf{u}^o(t))^\top \mathbf{K}\mathbf{d}^*(\mathbf{u}^o(t)). \tag{5.17}$$

For example, in the 1D case, $\mathbf{A}^*(\mathbf{u}^o(t))$ and $\mathbf{d}^*(\mathbf{u}^o(t))$ are defined as

$$\mathbf{A}^*(\mathbf{u}^o(t)) = \begin{cases} \mathbf{A}^D & \text{active contact} \\ \mathbf{A}^N & \text{inactive contact} \end{cases} \text{ and } \mathbf{d}^*(\mathbf{u}^o(t)) = \begin{cases} \mathbf{d} & \text{active contact} \\ \mathbf{0} & \text{inactive contact} \end{cases} \tag{5.18}$$

where the quantities $\mathbf{A}^D$, $\mathbf{A}^N$ and $\mathbf{d}$ are defined in Equations (4.34) and (4.46). In both the 1D-NBM and 2D-NBM, the form of $\mathbf{A}^*(\mathbf{u}^o(t))$ and $\mathbf{d}^*(\mathbf{u}^o(t))$ depends on the contact phase of the structure. However, in comparison to the 1D-NBM, there are now more than two possible phases. In the 2D-NBM, each contact node in $\mathbf{u}^c(t)$ can be either in active or inactive contact phase, and there effectively exist 2^{N_C} distinct contact phase configurations (all possible permutations for the set of nodes N_C being either in active or inactive contact). In this chapter, the contact phases of all nodes prone to contact are collectively referred to as *contact configurations*.

As a consequence, the definition of $\mathbf{A}^*(\mathbf{u}^o(t))$ and $\mathbf{d}^*(\mathbf{u}^o(t))$ (and the definition of the 2D-NBM-ODE (5.14)) depends on the notion contact configurations.

Definition 5.1 (Contact configuration)**.** *Consider a FE model of a deformable structure consisting of N_C nodes that are prone to contact, with corresponding displacements $\mathbf{u}^c(t)$. At any given instant t, each of the nodes is either in active or inactive contact phase (grazing motions are ignored in this manuscript). A contact configuration is defined as the collection of active and inactive contact*

phases corresponding to each node prone to contact. The boolean variable p_i, $i = 1, 2, \ldots, N_C$, *denotes the contact phase applied on the displacement of a given contact node* $u_i^c(t)$*:*

$$p_i(\mathbf{u}^c(t)) = \begin{cases} 1 & \text{if } u_i^c(t) \text{ in active contact} \\ 0 & \text{if } u_i^c(t) \text{ in inactive contact.} \end{cases} \tag{5.19}$$

As a result, each contact configuration corresponds to a unique array $\mathbf{p}$*.*

Definition 5.2 (Configuration space)**.** *The configuration space denotes the space of all possible displacements* $\mathbf{u}^c(t)$ *belonging to a specific configuration* $\mathbf{p}(\mathbf{u}^c(t))$*. The configuration space is denoted* $\mathcal{S}(\mathbf{p})$ *such that for a given* $\mathbf{p}^*$*,* $\mathcal{S}(\mathbf{p}^*) = \{\mathbf{u}^c(t) : \mathbf{p}(\mathbf{u}^c(t)) = \mathbf{p}^*\}$*.*

Definition 5.3 (Configuration phase)**.** *Assume a FE model with contact node displacement* $\mathbf{u}^c(t)$ *and a given contact configuration* $\mathbf{p}_i$ *starting from some time* t_0 *and lasting for a duration* $\tau > 0$*. The time interval* $t \in (t_0, t_0 + \tau)$ *is referred to as the configuration phase if and only if*

1. $\mathbf{u}^c(t) \in \mathcal{S}(\mathbf{p}_i)$ *for all* $t \in (t_0, t_0 + \tau)$*.*
2. *The interval* $(t_0, t_0 + \tau)$ *is defined such that a switch between contact configurations occurs outside of it. Otherwise put,* $\mathbf{u}^c(t_0^-) \notin \mathcal{S}(\mathbf{p}_i)$ *and* $\mathbf{u}^c(t_0^+ + \tau) \notin \mathcal{S}(\mathbf{p}_i)$ *must hold.*

To simplify further the notation, $\mathcal{T}(\mathbf{p})$ *denotes the configuration phase* $(t_0, t_0 + \tau)$ *corresponding to a configuration* $\mathbf{p}$*.*

An example illustrating all possible contact configurations for the case $N_C = 2$ is found in Figure 5.2.

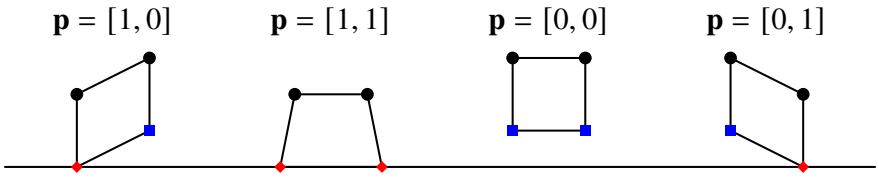

Figure 5.2: All possible contact configurations for a model of two contact nodes $N_C = 2$ ($2^{N_C} = 4$ contact configurations). Nodes shapes and colors: diamond-red (♦) denotes active contact, square-blue (■) denotes inactive contact and circle-black (●) denotes internal nodes $\mathbf{u}^o$. Each contact configuration is represented using a distinct $\mathbf{p}$ defined in Equation (5.19).

As stated previously, each contact configuration admits a distinct set of ODEs. Indeed, for a given FE model, there exist 2^{N_C} distinct ODEs each describing the motion of a specific contact configuration. To determine the NBM-ODE for a given contact configuration, an algorithmic approach is taken. This algorithmic approach is referred to as the *switching algorithm*, direct extension to the switching function $S(\mathbf{u}^o(t))$ in the 1D-NBM. Also, in the 1D-NBM, the contact phase of motion and the definition of the NBM-ODE at a specific instant t are dictated by the value of the switching function $S(\mathbf{u}^o(t))$ (see Equations (4.51) and (4.52)). Analogously, in 2D-NBM,

the role of the switching algorithm is to define the NBM-ODE and the contact configuration at any instant t. This algorithm is illustrated in Figure 5.3(a).

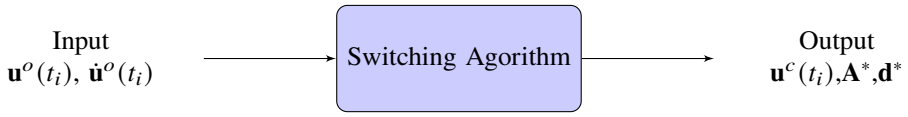

(a) Switching algorithm: inputs and outputs. This algorithm is used extensively in the 2D-NBM. The inputs are the displacement and velocities of internal nodes at a specific time t_i and the outputs are the contact nodes $\mathbf{u}^c(t_i)$ and the quantities $\mathbf{A}^*$ and $\mathbf{d}^*$. The quantities $\mathbf{A}^*$ and $\mathbf{d}^*$ are mainly used for constructing the NBM-ODE as described in Equations (5.14) to (5.17)

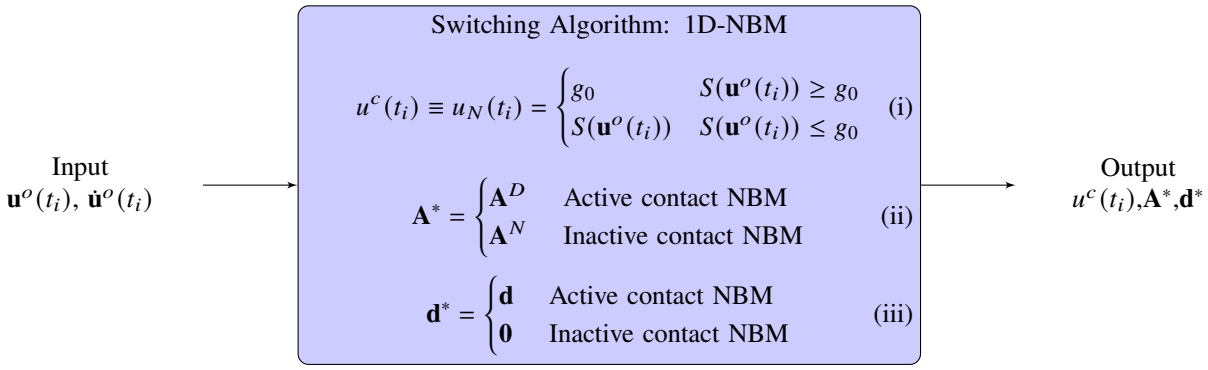

(b) Switching algorithm: illustration of the 1D-NBM case. This representation borrows expressions from Chapter 4 to construct the algorithm: Equation (i) to Equation (4.56), the Equations (ii) and (iii) refer to Equation (5.18). In the 1D-NBM, the notion of switching algorithm is not a necessity since the switching mechanism is governed by $S(\mathbf{u}^o(t))$ and all outputs are readily obtained for any value of $S(\mathbf{u}^o(t))$. Instead, in the 2D-NBM, a switching function (of the type $S(\mathbf{u}^o(t))$) does not exist, and a numerical root-solving algorithm is necessary to derive the outputs

Figure 5.3: Switching algorithm for the 2D-NBM and 1D-NBM.

The switching algorithm takes as input the internal displacements $\mathbf{u}^o(t)$. Then, for a given finite element model, it outputs $\mathbf{u}^c(t)$ and quantities $\mathbf{A}^*(\mathbf{u}^o(t))$ and $\mathbf{d}^*(\mathbf{u}^o(t))$ for the contact configuration. The switching algorithm is presented in the context of the 1D-NBM in Figure 5.3(b): $u^c(t)$ is readily defined from the switching function $S(\mathbf{u}^o(t))$, and the formulation of the quantities $\mathbf{A}^*$ and $\mathbf{d}^*$ directly follows from it as well. Since $S(\mathbf{u}^o(t))$ can be derived and has a closed-form expression (see Equation (4.33)), the notion of a switching algorithm is not necessary. However, in the 2D-NBM, the solution to the Signorini conditions requires a root-solving algorithm to obtain $\mathbf{u}^c(t)$ from the Signorini complementarity conditions (5.13). Furthermore, the construction of $\mathbf{A}^*$ and $\mathbf{d}^*$ necessitates an application of a matrix-inverse algorithm. In sum, both numerical algorithms are used in the *switching algorithm* which is presented in the following section.

5.3 Switching algorithm

The switching algorithm enforces the Signorini conditions (5.11) in a strong sense. To this end, the latter must be put in terms of the nodal displacements $\mathbf{u}(t)$. Specifically, the term $\boldsymbol{\lambda}$ in (5.11)

must be expressed in terms of $\mathbf{u}(t)$. This is achieved in Equation (5.12) by introducing the quantity $\boldsymbol{\lambda}^{\mathrm{NBM}}(\mathbf{u}(t))$ which is an expression of the linear elasticity constitutive law on the contact boundary, that is the FE approximation of the contact forces. In this section, Equation (5.12) is revisited and $\boldsymbol{\lambda}^{\mathrm{NBM}}(\mathbf{u}(t))$ is developed, before proceeding with the derivation of the switching algorithm. In Equation (5.12), it is possible to ignore the tangential stress contributions which are zero $\forall \mathbf{x} \in \Gamma_{\mathrm{C}}$ due to frictionless contact: $\boldsymbol{\sigma}(\mathbf{P}(\mathbf{x})\mathbf{u}(t))\mathbf{n} = \sigma_n(\mathbf{P}(\mathbf{x})\mathbf{u}(t))\mathbf{n}$. This implies the suppression of the tangential stress in Equation (5.9) in a *weak* manner. Although the main motivation for the conception of the NBM is the strong enforcement of the contact condition, only conditions in the normal direction are considered in this manuscript. Equation (5.12) thus simplifies to

$$\boldsymbol{\lambda}^{\mathrm{NBM}}(\mathbf{u}(t)) = \int_{\Gamma_{\mathrm{C}}} \mathbf{P}(\mathbf{x})^{\top} \sigma_n(\mathbf{P}(\mathbf{x})\mathbf{u}(t))\mathbf{n} \mathrm{d}\mathbf{x} \tag{5.20}$$

that is

$$\boldsymbol{\lambda}^{\mathrm{NBM}}(\mathbf{u}(t)) = \mathbf{N}\mathbf{u}(t) \quad \text{with} \quad \mathbf{N} = \left(\int_{\Gamma_{\mathrm{C}}} \mathbf{P}(\mathbf{x})^{\top} (\mathbf{n}\mathbf{n}^{\top}) \tilde{\mathbf{V}}(\mathbf{n}) \mathbf{D}\mathbf{B}(\mathbf{x}) \mathrm{d}\mathbf{x} \right) \tag{5.21}$$

where the expression for $\mathbf{N}$ is derived in Appendix C.1 and the term $\tilde{\mathbf{V}}(\mathbf{n})$ is defined in Equation (C.3) of Appendix C.1. $\mathbf{N}^c$ and $\mathbf{N}^o$ are introduced as the contributions of $\mathbf{N}$ corresponding to the contact nodes and internal nodes, respectively, such that Equation (5.21) reads

$$\boldsymbol{\lambda}^{\mathrm{NBM}}(\mathbf{u}(t)) = \mathbf{N}^o \mathbf{u}^o(t) + \mathbf{N}^c \mathbf{u}^c(t), \qquad \mathbf{N} = \begin{bmatrix} \mathbf{N}^c \\ \mathbf{N}^o \end{bmatrix}. \tag{5.22}$$

The operator $\mathbf{N}$ in Equation (5.21) is critical to the formulation of the 2D-NBM. Plugging Equation (5.22) into (5.13) yields

$$0 \leq g_0 \mathbf{1} - \mathbf{u}^c(t) \perp \mathbf{N}^o \mathbf{u}^o(t) + \mathbf{N}^c \mathbf{u}^c(t) \leq 0. \tag{5.23}$$

Equation (5.23) formulates a linear complementarity problem (LCP) in $\mathbf{u}^c(t)$. To simplify upcoming notation, the general LCP is defined in Definition 5.4.

Definition 5.4 (Linear Complementarity Problem)**.** *A LCP is defined as follows:*

$$\textit{Find } \mathbf{z} \textit{ such that: } \mathbf{0} \leq \mathbf{C}\mathbf{z} + \mathbf{q} \perp \mathbf{z} \geq \mathbf{0}. \tag{5.24}$$

The LCP has a unique solution for any $\mathbf{q}$ *if the matrix* $\mathbf{C}$ *is a P-matrix, that is if every minor of* $\mathbf{C}$ *is positive-definite [11]. In this work, the solution to the linear complementarity problem* (5.24) *is denoted*

$$\mathbf{z} = LC(\mathbf{C}, \mathbf{q}) \tag{5.25}$$

Under the notation in Equation (5.24), Equation (5.23) constitutes a LCP in $\mathbf{u}^c(t)$ where the

quantities $\mathbf{C}$, $\mathbf{z}$ and $\mathbf{q}$ are defined as follows:

$$\mathbf{C} = \mathbf{N}^c, \quad \mathbf{z} = \mathbf{1}g_0 - \mathbf{u}^c(t), \quad \mathbf{q} = -\mathbf{N}^o\mathbf{u}^o(t) - g_0\mathbf{N}^c\mathbf{1} \tag{5.26}$$

It is noted that Equation (5.23) is equivalent to the complementarity conditions of the 1D-NBM enforced on $u_N(t)$ in Equation (4.13). In contrast to the 1D-NBM complementarity conditions, the solution of Equation (5.23) cannot be obtained in closed form and instead requires the use of dedicated numerical solvers [11,28]. In Section 5.3.1, it will be shown that LCP (5.23) can be solved numerically for any given $\mathbf{u}^o(t)$. It is important to note that in the MRM, the Signorini problem is also converted into an LCP in $\mathbf{u}^c(t)$ [40]. Indeed, the formulation of the Signorini condition as an LCP in $\mathbf{u}^c(t)$ is only possible by formulating $\mathbf{N}$ in Equation (5.22).

In what follows, Equation (5.23) is solved numerically to obtain $\mathbf{u}^c(t_i)$ for any given $\mathbf{u}^o(t_i)$. The quantities $\mathbf{A}^*$ and $\mathbf{d}^*$ are obtained by inspecting the resulting contact forces $\boldsymbol{\lambda}^{\mathrm{NBM}}(\mathbf{u}(t_i))$ and $\mathbf{u}^c(t_i)$. This is illustrated in the algorithm's flow chart in Figure 5.4.

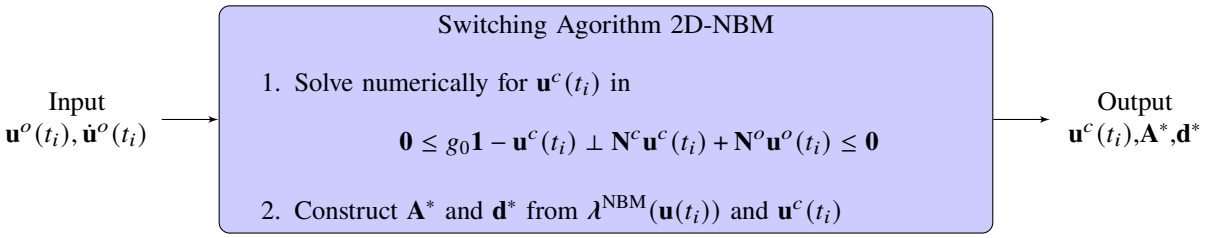

Figure 5.4: Steps for the switching algorithm in 2D-NBM. Steps 1 and 2 of this algorithm are described in Sections 5.3.1 and 5.3.2, respectively.

To facilitate the exposition, both outputs of the switching algorithm, $\mathbf{u}^c(t_i)$ and $(\mathbf{A}^*, \mathbf{d}^*)$, are discussed separately in Sections 5.3.1 and 5.3.2, respectively.

5.3.1 Step 1: Obtain $\mathbf{u}^c(t_i)$

In the 2D-NBM, the motion of the contact nodes is dictated by the solution to the linear complementarity problem defined in Equation (5.23). Specifically, Equation (5.23) is solved for $\mathbf{u}^c(t)$ for any $\mathbf{u}^o(t)$. The solution to (5.23) is presented according to Equation (5.25) where the components $\mathbf{C}$, $\mathbf{q}$ and $\mathbf{z}$ were defined in Equation (5.26) as follows:

$$\mathbf{u}^c(\mathbf{u}^o(t)) = g_0\mathbf{1} - \mathrm{LC}(\mathbf{N}^c, -\mathbf{N}^o\mathbf{u}^o(t) - g_0\mathbf{N}^c\mathbf{1}). \tag{5.27}$$

Equation (5.27) defines the displacement $\mathbf{u}^c(t)$ in the NBM and constitutes the strong enforcement of the NBM Signorini conditions (5.23). As explained in Definition 5.4, $\mathbf{u}^c(\mathbf{u}^o(t))$ in Equation (5.27) exists and is unique for any $\mathbf{u}^o(t)$ if the matrix $\mathbf{N}^c$ is a P-matrix. Particularly, distinct finite element models, consisting of a specific number of elements and specific polynomial degree of shape function, admit distinct $\mathbf{N}^c$. Since the NBM formulation relies on the existence and uniqueness of solutions of

the LCP (5.23), it is necessary to prove that *any* finite element approximation results in $\mathbf{N}^c$ that is a P-matrix. For the single dimensional case, the LCP problem is a scalar equation and the proof required to show that the shape function of the last element always exhibits $\phi'_N(1) > 0$ (this is proven in B.1). However, a general proof of $\mathbf{N}^c$ being a P-matrix for any FE model is not further explored. Instead, for all cases considered, the $\mathbf{N}^c$ is verified numerically to be a P-matrix numerically via eigenvalue algorithms (specifically, MATLAB's `eig` algorithm [55]). The implications of the existence and uniqueness of solutions of the LCP (5.23) are further discussed in Section 5.8.

In practice, the solution to Equation (5.27) for a given $\mathbf{u}^o(t_i)$ is found numerically via the semismooth Newton's method [10, 18, 28]. It is applied on the "max" formulation of the LCP (5.23), which reads:

$$\mathbf{u}^c(t_i) - g_0\mathbf{1} + \mathbf{max}(\mathbf{0}, g_0\mathbf{1} - \mathbf{u}^c(t_i) + \mathbf{N}^c\mathbf{u}^c(t_i) + \mathbf{N}^o\mathbf{u}^o(t_i)) = \mathbf{0}. \tag{5.28}$$

For all numerical experiments, the semismooth Newton algorithm applied on Equation (5.28) always converged to satisfactory accuracy.

In what follows, the displacements of contact nodes are denoted $\mathbf{u}^c(\mathbf{u}^o(t))$ since $\mathbf{u}^c(t)$ depends exclusively on $\mathbf{u}^o(t)$ for any time instant t_i, as seen in Equation (5.27). Given $\mathbf{u}^c(\mathbf{u}^o(t))$, the corresponding contact pressures (5.22) are obtained as follows:

$$\boldsymbol{\lambda}^{\mathrm{NBM}}(\mathbf{u}^o(t)) = \mathbf{N}^c\mathbf{u}^c(\mathbf{u}^o(t)) + \mathbf{N}^o\mathbf{u}^o(t) \tag{5.29}$$

$$= \mathbf{N}^c(g_0\mathbf{1} - \mathrm{LC}(\mathbf{N}^c, -\mathbf{N}^o\mathbf{u}^o(t) - g_0\mathbf{N}^c\mathbf{1})) + \mathbf{N}^o\mathbf{u}^o(t). \tag{5.30}$$

5.3.2 Step 2: Construct $\mathbf{A}^*$ and $\mathbf{d}^*$

Before deriving the quantities $\mathbf{A}^*$ and $\mathbf{d}^*$, their role in the NBM formulation is established. It is stated in Section 5.2.1 that the quantities $\mathbf{A}^*$ and $\mathbf{d}^*$ depend exclusively on the contact configuration of the structure. Thus, the notation $\mathbf{A}^*(\mathbf{p})$ and $\mathbf{d}^*(\mathbf{p})$ will apply in this section for the sake of consistency. The role of the quantities $\mathbf{A}^*(\mathbf{p})$ and $\mathbf{d}^*(\mathbf{p})$ is to primarily define the 2D-NBM approximation of the displacement corresponding to a contact configuration $\mathbf{p}$ (similarly to the roles of $\mathbf{B}$ and $\mathbf{B}^d$ in Equation (4.55) of the 1D-NBM):

$$\mathbf{u}(\mathbf{x}, t) \approx \mathbf{P}(\mathbf{x})\mathbf{u}(t) = \mathbf{P}(\mathbf{x})(\mathbf{A}^*(\mathbf{p})\mathbf{u}^o(t) + \mathbf{d}^*(\mathbf{p})). \tag{5.31}$$

Specifically, the quantities $\mathbf{A}^*(\mathbf{p}) \in \mathbb{R}^{N \times N_O}$ and $\mathbf{d}^*(\mathbf{p}) \in \mathbb{R}^N$ are defined by the relationship between the displacements of contact nodes $\mathbf{u}^c(t)$ and internal nodes $\mathbf{u}^o(t)$ as follows:

$$\mathbf{u}(t) = \mathbf{A}^*(\mathbf{p})\mathbf{u}^o(t) + \mathbf{d}^*(\mathbf{p}) \rightarrow \begin{pmatrix} \mathbf{u}^o(t) \\ \mathbf{u}^c(t) \end{pmatrix} = \underbrace{\begin{bmatrix} \mathbf{I} \\ \mathbf{A}(\mathbf{p}) \end{bmatrix}}_{\mathbf{A}^*(\mathbf{p})} \mathbf{u}^o(t) + \underbrace{\begin{pmatrix} \mathbf{0} \\ \mathbf{d}(\mathbf{p}) \end{pmatrix}}_{\mathbf{d}^*(\mathbf{p})} \tag{5.32}$$

where $\mathbf{A}(\mathbf{p})$ is a $N_C \times N_O$ matrix and $\mathbf{d}(\mathbf{p})$ is a vector of size N_C. The matrices $\mathbf{A}(\mathbf{p})$ and $\mathbf{d}(\mathbf{p})$ are linear operators that are used to define relationships between $\mathbf{u}^c(t)$ and $\mathbf{u}^o(t)$ for a given contact configuration $\mathbf{p}$, that is

$$\mathbf{u}^c(t) = \mathbf{A}(\mathbf{p})\mathbf{u}^o(t) + \mathbf{d}(\mathbf{p}). \tag{5.33}$$

They are defined such that $\mathbf{u}^c(t)$ in Equation (5.33) also satisfies the conditions implied by the contact configuration $\mathbf{p}$ (see Definition 5.1)

$$\begin{cases} \text{Active contact phase} & u_i^c(t) = g_0 & \text{if } p_i = 1 \\ \text{Inactive contact phase} & \lambda_i^{\text{NBM}}(\mathbf{u}(t)) = 0 & \text{if } p_i = 0 \end{cases} \qquad i = 1, 2, \ldots, N_C. \tag{5.34}$$

In sum, $\mathbf{A}^*(\mathbf{p})$ and $\mathbf{d}^*(\mathbf{p})$ create a displacement approximation that satisfies that contact configuration conditions (5.34). It is important to note that the contact configuration does not enforce physical admissibility to the Signorini conditions (ie, the inequality conditions of the NBM-LCP (5.23) are not addressed). In order to define $\mathbf{A}^*(\mathbf{p})$ and $\mathbf{d}^*(\mathbf{p})$ resulting in a physically admissible approximation, the following must be achieved:

1. Definition of $\mathbf{A}(\mathbf{p})$ and $\mathbf{d}(\mathbf{p})$ (see Equation (5.32))
2. Definition of a contact configuration $\mathbf{p}$ that always satisfies the LCP (5.23)

In what follows, $\mathbf{A}(\mathbf{p})$ and $\mathbf{d}(\mathbf{p})$ are first determined for arbitrary contact configuration $\mathbf{p}$. Then, a contact configuration $\mathbf{p}$ that always satisfies the LCP (5.23), denoted $\mathbf{p}^{\text{NBM}}(\mathbf{u}^o(t))$, is derived in order to finally culminate in a formulation of $\mathbf{A}^*(\mathbf{p}^{\text{NBM}}(\mathbf{u}^o(t)))$ and $\mathbf{d}^*(\mathbf{p}^{\text{NBM}}(\mathbf{u}^o(t)))$ that is always physically admissible.

Definition of $\mathbf{A}(\mathbf{p})$ and $\mathbf{d}(\mathbf{p})$

For a given contact configuration $\mathbf{p}$, the quantities $\mathbf{A}(\mathbf{p})$ and $\mathbf{d}(\mathbf{p})$ are derived from the affine relationship between $\mathbf{u}^c(t)$ and $\mathbf{u}^o(t)$ described in Equation (5.34). To illustrate clearly the derivation, Equation (5.34) (while recalling the definition of $\boldsymbol{\lambda}^{\text{NBM}}(\mathbf{u}(t))$ from Equation (5.22)) is put in matrix form

$$\mathbf{L}^c(\mathbf{p})\mathbf{u}^c(t) + \mathbf{L}^o(\mathbf{p})\mathbf{u}^o(t) = \mathbf{l}(\mathbf{p}) \tag{5.35}$$

where

$$L_{ij}^c = \begin{cases} \delta_{ij} & p_i = 1 \\ (N_C)_{ij} & p_i = 0 \end{cases} \qquad i = 1, 2, \ldots, N_C, \quad j = 1, 2, \ldots, N_C \tag{5.36a}$$

$$L_{ij}^o = \begin{cases} 0 & p_i = 1 \\ (N_O)_{ij} & p_i = 0 \end{cases} \qquad i = 1, 2, \ldots, N_C, \quad j = 1, 2, \ldots, N_O \tag{5.36b}$$

and

$$l_i = \begin{cases} g_0 & p_i = 1 \\ 0 & p_i = 0 \end{cases} \qquad i = 1, 2, \ldots, N_C. \tag{5.36c}$$

By isolating $\mathbf{u}^c(t)$ using representation (5.35), $\mathbf{A}(\mathbf{p})$ and $\mathbf{d}(\mathbf{p})$ are obtained (as they are defined in Equation (5.32))

$$\mathbf{u}^c(t) = \mathbf{A}(\mathbf{p})\mathbf{u}^o(t) + \mathbf{d}(\mathbf{p}) \qquad \mathbf{u}^c(t_i) \in \mathcal{S}(\mathbf{p}) \tag{5.37}$$

$$\mathbf{A}(\mathbf{p}) = -(\mathbf{L}^c(\mathbf{p}))^{-1}\mathbf{L}^o(\mathbf{p}) \qquad \mathbf{d}(\mathbf{p}) = (\mathbf{L}^c(\mathbf{p}))^{-1}\mathbf{l}(\mathbf{p}). \tag{5.38}$$

At last, $\mathbf{A}^*(\mathbf{p})$ and $\mathbf{d}^*(\mathbf{p})$ are obtained by inserting expression (5.38) into expression (5.32):

$$\mathbf{A}^*(\mathbf{p}) = \begin{bmatrix} \mathbf{I} \\ -(\mathbf{L}^c(\mathbf{p}))^{-1}\mathbf{L}^o(\mathbf{p}) \end{bmatrix}, \qquad \mathbf{d}^*(\mathbf{p}) = \begin{pmatrix} \mathbf{0} \\ (\mathbf{L}^c(\mathbf{p}))^{-1}\mathbf{l}(\mathbf{p}) \end{pmatrix}. \tag{5.39}$$

It is clear here that $\mathbf{A}^*(\mathbf{p})$ and $\mathbf{d}^*(\mathbf{p})$ are defined by the contact configuration of the deformable structure.

Ambiguity at the instant of switch

It is important to note that $\mathbf{A}^*(\mathbf{p})$ and $\mathbf{d}^*(\mathbf{p})$, as defined in Equation (5.39), are ill-defined for switching instants t_s where, at a given node i, the contact force and gap are zero:

$$u_i^c(\mathbf{u}^o(t_s)) - g_0 = \lambda_i^{\mathrm{NBM}}(\mathbf{u}^o(t_s)) = 0. \tag{5.40}$$

At an instant of switch, according to Equation (5.34), both contact phases $p_i = 1$ and $p_i = 0$ may apply. Thus, at the moment of switch, there exist distinct definitions of $\mathbf{L}^c(\mathbf{p})$, $\mathbf{L}^o(\mathbf{p})$ and $\mathbf{l}(\mathbf{p})$ and, by virtue of Equation (5.39), distinct definitions of $\mathbf{A}^*(\mathbf{p})$ and $\mathbf{d}^*(\mathbf{p})$. To illustrate this aspect, Figure 5.5 presents an instance of ambiguity of contact configurations in the case of two contact nodes, $N_C = 2$. In what follows, the contact phase definition (5.34) is enforced in order to avoid

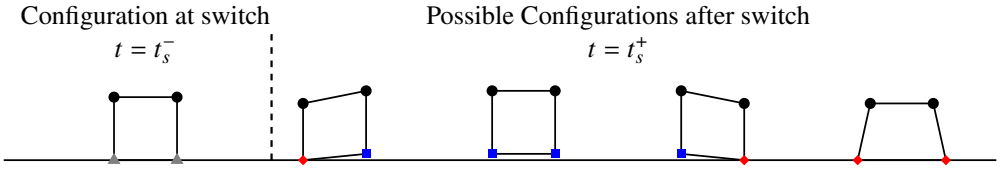

Figure 5.5: Possible contact configurations after a switch for $N_C = 2$. The case where both contact nodes experience a switch (▲) is illustrated. When both contact nodes experience a switch, there exist four possible distinct contact configurations that the element can take after contact. Thus, at the moment of switch itself, there exist four distinct sets of quantities $\mathbf{A}^*$ and $\mathbf{d}^*$ to generate the NBM-ODE (5.14). However, given the velocities of contact nodes $\dot{\mathbf{u}}^c(t)$ and the rate of change of contact forces $\dot{\boldsymbol{\lambda}}^{\mathrm{NBM}}(t)$, it is possible to determine a unique contact configuration immediately after the switch. This is done by refining the definitions of active and inactive contact phases in Equations (5.43) and (5.44).

ambiguity in the definition of $\mathbf{A}^*(\mathbf{p})$ and $\mathbf{d}^*(\mathbf{p})$ at the switch.

Before treating $\mathbf{A}^*(\mathbf{p})$ and $\mathbf{d}^*(\mathbf{p})$ at the instant of switch, we recall that a similar ambiguity at the instant of switch occurred in the 1D-NBM (see discussion in the first paragraph of Section 4.3.4). In the 1D-NBM, this ambiguity is resolved by complementing the definitions of active and inactive contact phases with conditions on $S(\dot{\mathbf{u}}^o(t_s))$ at the switch, see Equations (4.51) and (4.52).

For the 2D-NBM, a similar approach is taken. The active and inactive contact conditions at the switch are complemented with additional restrictions on the velocity of the contact node and rate of change of the contact force at the switch. After the switch, if the motion is non-grazing, one of two outcomes is expected: (1) either the contact forces will decrease ($\lambda_i^{\mathrm{NBM}}(t_s^+) < 0$) while the contact node enters an active contact phase or (2) the velocity of the contact node will be negative (separation of the contact node from the obstacle) while the contact node enters inactive contact phase. Mathematically, the definition of active and inactive contact phases now reads

$$\begin{cases} \text{Active contact:} & u_i^c(t) = g_0 \text{ or } \dot{\lambda}_i^{\mathrm{NBM}}(\mathbf{u}(t_s^+)) < 0 \\ \text{Inactive contact:} & \lambda_i^{\mathrm{NBM}}(\mathbf{u}(t)) = 0 \text{ or } \dot{u}_i^c(t_s^+) < 0 \end{cases} \tag{5.41}$$

$$t_s = \{t : u_i^c(t) - g_0 = \lambda_i^{\mathrm{NBM}}(\mathbf{u}(t)) = 0\} \tag{5.42}$$

for $i = 1, 2, \ldots, N_{\mathrm{C}}$.

Definition of contact configuration from solution to LCP

To define matrices $\mathbf{A}^*(\mathbf{p})$ and $\mathbf{d}^*(\mathbf{p})$ such that a physically admissible displacement approximation (5.31) is obtained, it is necessary to define $\mathbf{p}$ based on the solution to the NBM-LCP (5.23). The contact displacement and contact force solutions to the NBM-LCP (5.23) (see also Equations (5.27) and (5.29)) are inserted into the contact configuration definition (5.41) admitting the NBM conditions

$$\text{Active NBM contact:} \quad \lambda_i^{\mathrm{NBM}}(\mathbf{u}^o(t)) < 0 \text{ or } \dot{\lambda}_i^{\mathrm{NBM}}(t_s^+) < 0 \tag{5.43}$$

$$\text{Inactive NBM contact:} \quad u_i^c(\mathbf{u}^o(t)) < g_0 \text{ or } \dot{u}_i^c(\mathbf{u}^o(t_s^+), \dot{\mathbf{u}}^o(t_s^+), t_s^+) < 0 \tag{5.44}$$

$$t_s = \{t : u_i^c(\mathbf{u}^o(t)) - g_0 = \lambda_i^{\mathrm{NBM}}(\mathbf{u}^o(t)) = 0\} \tag{5.45}$$

where the time-derivative of $\mathbf{u}^c(\mathbf{u}^o(t))$ after the switch, $\dot{u}_i^c(\mathbf{u}^o(t_s), \dot{\mathbf{u}}^o(t_s), t_s^+)$, is obtained by differentiating expression (5.27)

$$\dot{\mathbf{u}}^c(\mathbf{u}^o(t_s), \dot{\mathbf{u}}^o(t_s), t_s^+) = -\lim_{t \to t_s^+} \frac{\mathrm{d}}{\mathrm{d}t} \mathrm{LC}(\mathbf{N}^c, -\mathbf{N}^o\mathbf{u}^o(t) - \mathbf{N}^c\mathbf{1}g_0), \tag{5.46}$$

and the time-derivative of the contact force after the switch is defined by differentiating Equation (5.29)

$$\dot{\boldsymbol{\lambda}}(\mathbf{u}^o(t_s), \dot{\mathbf{u}}^o(t_s), t_s^+) = \mathbf{N}^c\dot{\mathbf{u}}^c(\mathbf{u}^o(t_s), \dot{\mathbf{u}}^o(t_s), t_s^+) + \mathbf{N}^o\dot{\mathbf{u}}^o(t_s). \tag{5.47}$$

It is important to note that the derivative in Equation (5.46) (which also participates in Equation (5.47)) is not trivial to calculate. In fact, the LCP solution $\mathrm{LC}(\mathbf{C}, \mathbf{q}(t))$ can exhibit a discontinuous derivative at the instant of switch, and the operation $\frac{\mathrm{d}}{\mathrm{d}t}\mathrm{LC}(\mathbf{C}, \mathbf{q}(t))$ requires an algorithmic approach. This algorithm is derived in Appendix C.2.

Next, the definition of contact configuration is updated with conditions (5.43) and (5.44)

$$p_i^{\mathrm{NBM}}(\mathbf{u}^o(t), \dot{\mathbf{u}}^o(t)) = \begin{cases} 1 & \text{Active NBM contact (5.43)} \\ 0 & \text{Inactive NBM contact (5.44)} \end{cases} \tag{5.48}$$

and $\mathbf{A}^*(\mathbf{p}^{\mathrm{NBM}}(\mathbf{u}^o(t), \dot{\mathbf{u}}^o(t)))$ and $\mathbf{d}^*(\mathbf{p}^{\mathrm{NBM}}(\mathbf{u}^o(t), \dot{\mathbf{u}}^o(t)))$ are now defined uniquely for all states except for grazing motions where the velocity and stress at the moment of switch are zero

$$u_i^c(\mathbf{u}^o(t)) = g_0, \quad \dot{\lambda}_i^{\mathrm{NBM}}(\mathbf{u}^o(t_s), \dot{\mathbf{u}}^o(t_s), t_s^+) = \dot{u}_i^c(\mathbf{u}^o(t_s), \dot{\mathbf{u}}^o(t_s), t_s^+) = 0. \tag{5.49}$$

Thus, it is important to note that the NBM formulation in this manuscript does not apply to grazing motions.

To simplify the notations, $\mathbf{A}^*(\mathbf{p}^{\mathrm{NBM}}(\mathbf{u}^o(t), \dot{\mathbf{u}}^o(t)))$ and $\mathbf{d}^*(\mathbf{p}^{\mathrm{NBM}}(\mathbf{u}^o(t), \dot{\mathbf{u}}^o(t)))$ are denoted as functions in $\mathbf{u}^o(t)$ only, that is $\mathbf{A}^*(\mathbf{u}^o(t))$, $\mathbf{d}^*(\mathbf{u}^o(t))$ for the remainder of this chapter.

5.4 NBM-ODE

The formulation of the NBM-ODE relies on the NBM displacement approximation (recall Equations (5.31) and (5.32))

$$\mathbf{u}(\mathbf{x}, t) \approx \mathbf{u}^h(\mathbf{x}, t) \equiv \mathbf{P}(\mathbf{x})\mathbf{u}(t) = \mathbf{P}(\mathbf{x})(\mathbf{A}^*(\mathbf{u}^o(t))\mathbf{u}^o(t) + \mathbf{d}^*(\mathbf{u}^o(t))). \tag{5.50}$$

Specifically, the 2D-NBM-ODE uses the Galerkin-Bubnov method in its formulation (similarly to the 1D-NBM-ODE in Sections 4.3.2 and 4.3.3) as described in the remainder of this section.

Application of the Galerkin-Bubnov is presented first in the context of a given configuration phase, where $\mathbf{A}^*(\mathbf{u}^o(t))$ and $\mathbf{d}^*(\mathbf{u}^o(t))$ are constant (recall, $\mathbf{A}^*(\mathbf{u}^o(t))$ and $\mathbf{d}^*(\mathbf{u}^o(t))$ depend on the contact configuration). Then, the switching method is used to formulate the general NBM-ODE.

To formulate the NBM-ODE, The weak form of the PDE (5.1) is first exposed

$$\begin{aligned} \int_\Omega \mathbf{w}(\mathbf{x}, t)^\top \rho \partial_t t \mathbf{u}(\mathbf{x}, t) \mathrm{d}\mathbf{x} + \int_\Omega \boldsymbol{\epsilon}(\mathbf{w}(\mathbf{x}, t)) : \boldsymbol{\sigma}(\mathbf{u}(\mathbf{x}, t)) \mathrm{d}\mathbf{x} \ldots \\ - \int_{\Gamma_C} \mathbf{w}(\mathbf{x}, t)^\top \boldsymbol{\sigma}(\mathbf{u}(\mathbf{x}, t)) \mathbf{n} \mathrm{d}\mathbf{x} = 0 \end{aligned} \tag{5.51}$$

Here, it is noted that the test functions, $\mathbf{w}(\mathbf{x}, t)$ are time dependent which is not customary. However, as form of the test function in the 1D-NBM depends on the contact phase, it shall depend on the configuration phase for the 2D-NBM. Next, by application of the Galerkin-Bubnov method [44, 79]

requires that shape functions composing the displacement approximation (5.50) are also used for the test-functions. For a given configuration phase, the test function approximation reads:

$$\mathbf{w}(\mathbf{x},t) = \mathbf{P}(\mathbf{x})\mathbf{A}^*(\mathbf{u}^o(t))\mathbf{w}^o, t \in \mathcal{T}(\mathbf{p}^{\mathrm{NBM}}) \tag{5.52}$$

where $\mathbf{d}^*(\mathbf{u}^o(t))$ does not participate since it represents a particular solution to the non-homogeneous Dirichlet boundary where the test functions vanish. Plugging Equations (5.50) and (5.52) into the weak form (5.51) then admits

$$\mathbf{w}^{o\top}(\mathbf{A}^*)^\top(\mathbf{M}\partial_{tt}(\mathbf{A}^*\mathbf{u}^o(t)+\mathbf{d}^*)+\mathbf{K}(\mathbf{A}^*\mathbf{u}^o(t)+\mathbf{d}^*))-\mathbf{w}^{c\top}\boldsymbol{\lambda}^{\mathrm{NBM}}(\mathbf{u}^o(t)) = \mathbf{0},\ \forall t \in \mathcal{T}(\mathbf{p}^{\mathrm{NBM}}) \tag{5.53}$$

where the dependence of $\mathbf{A}^*(\mathbf{u}^o(t))$ and $\mathbf{d}^*(\mathbf{u}^o(t))$ on $\mathbf{u}^o(t)$ is omitted for the sake of conciseness. The choice of test functions in Equation (5.52) also eliminates the last term in Equation (5.53) since the test function vanishes ($w_i^c = 0$) for all nodes in active contact, and $\lambda_i^{\mathrm{NBM}}(\mathbf{u}^o(t)) = 0$ for all nodes in inactive contact (see Equation (5.34)). Hence, Equation (5.53) can be further simplified as follows:

$$\mathbf{w}^{o\top}(\mathbf{A}^*)^\top(\mathbf{M}\partial_{tt}(\mathbf{A}^*\mathbf{u}^o(t)+\mathbf{d}^*)+\mathbf{K}(\mathbf{A}^*\mathbf{u}^o(t)+\mathbf{d}^*)) = \mathbf{0},\ \forall t \in \mathcal{T}(\mathbf{p}^{\mathrm{NBM}}) \tag{5.54}$$

Next, it is noted that the quantities $\mathbf{A}^*(\mathbf{u}^o(t))$ and $\mathbf{d}^*(\mathbf{u}^o(t))$ depend on the contact configuration and are constant for $t \in \mathcal{T}(\mathbf{p}^{\mathrm{NBM}})$. Therefore, for a given configuration phase, the following holds

$$\partial_{tt}(\mathbf{A}^*(\mathbf{u}^o(t))\mathbf{u}^o(t)+\mathbf{d}^*) = \mathbf{A}^*(\mathbf{u}^o(t))\ddot{\mathbf{u}}^o(t),\ \forall t \in \mathcal{T}(\mathbf{p}^{\mathrm{NBM}}) \tag{5.55}$$

Then, plugging Equation (5.55) into Equation (5.54) and generalizing for any $\mathbf{w}^o$ admits

$$\mathbf{M}^*(\mathbf{u}^o(t))\ddot{\mathbf{u}}^o(t)+\mathbf{K}^*(\mathbf{u}^o(t))\mathbf{u}^o(t)+\mathbf{f}^*(\mathbf{u}^o(t)) = \mathbf{0} \qquad \forall t \in \mathcal{T}(\mathbf{p}^{\mathrm{NBM}}) \tag{5.56}$$

where

$$\mathbf{M}^*(\mathbf{u}^o(t)) = \mathbf{A}^*(\mathbf{u}^o(t))^\top\mathbf{M}\mathbf{A}^*(\mathbf{u}^o(t)) \tag{5.57}$$

$$\mathbf{K}^*(\mathbf{u}^o(t)) = \mathbf{A}^*(\mathbf{u}^o(t))^\top\mathbf{K}\mathbf{A}^*(\mathbf{u}^o(t)) \tag{5.58}$$

$$\mathbf{f}^*(\mathbf{u}^o(t)) = \mathbf{A}^*(\mathbf{u}^o(t))^\top\mathbf{K}\mathbf{d}^*(\mathbf{u}^o(t)). \tag{5.59}$$

Equations (5.56) to (5.59) correspond directly to Equations (5.14) to (5.17). Similarly to the quantities $\mathbf{A}^*(\mathbf{u}^o(t))$ and $\mathbf{d}^*(\mathbf{u}^o(t))$, the quantities $\mathbf{M}^*(\mathbf{u}^o(t))$, $\mathbf{K}^*(\mathbf{u}^o(t))$ and $\mathbf{f}^*(\mathbf{u}^o(t))$ are constant for $t \in \mathcal{T}(\mathbf{p}^{\mathrm{NBM}})$.

The general 2D-NBM-ODE is expressed by applying the switching method on the ODEs formed by the Galerkin-Bubnov method Equation (5.56). Application of the switching method implies that the NBM-ODE always satisfies the Signorini conditions. This results in switching the displacement approximation according to the NBM contact phase conditions (5.44) and (5.43). This switching procedure for the displacement approximation is already embedded in the definition of $\mathbf{A}^*(\mathbf{u}^o(t))$ and $\mathbf{d}^*(\mathbf{u}^o(t))$. It is important to note that at the time of switch, the acceleration term

(see Equation (5.55)) exhibits a Dirac-delta function due to the appearance of a Dirac-delta in the acceleration of contact nodes. In this manuscript, this Dirac-delta function is ignored (similar approach is taken for the 1D-NBM in Section 4.3.4), and the general NBM-ODE is formed by simply generalizing Equation (5.56) to any configuration phase, as follows:

$$\mathbf{M}^*(\mathbf{u}^o(t))\ddot{\mathbf{u}}^o(t) + \mathbf{K}^*(\mathbf{u}^o(t))\mathbf{u}^o(t) + \mathbf{f}^*(\mathbf{u}^o(t)) = \mathbf{0}. \tag{5.60}$$

This system of ODEs is piecewise-linear and discontinuous due to $\mathbf{A}^*(\mathbf{u}^o(t))$ and $\mathbf{d}^*(\mathbf{u}^o(t))$ which are embedded in the coefficients $\mathbf{M}^*(\mathbf{u}^o(t))$, $\mathbf{K}^*(\mathbf{u}^o(t))$ and $\mathbf{f}^*(\mathbf{u}^o(t))$. At the instant of switch, it is required that both the internal displacements $\mathbf{u}^o(t)$ and velocities $\dot{\mathbf{u}}^o(t)$ remain continuous (the same condition is applied in the 1D NBM-ODE in Equation (4.53))

$$u_i^o(t_s^+) = u_i^o(t_s^-), \quad \dot{u}_i^o(t_s^+) = \dot{u}_i^o(t_s^-) \tag{5.61}$$

Since the system of ODEs is discontinuous in time, it is assumed that the internal accelerations $\ddot{\mathbf{u}}^o(t)$ are discontinuous as well. The NBM-ODE (5.60) is thus better formulated as follows:

$$\begin{aligned} \ddot{\mathbf{u}}^o(t^+) &= \mathbf{M}^*(\mathbf{u}^o(t))^{-1}(\mathbf{K}^*(\mathbf{u}^o(t))\mathbf{u}^o(t) + \mathbf{f}^*(\mathbf{u}^o(t))) \\ \dot{u}_i^o(t_s^+) &= \dot{u}_i^o(t_s^-) \end{aligned} \tag{5.62}$$

where t_s denotes the time of switch (defined in Equation (5.45)), and the coefficients $\mathbf{M}^*(\mathbf{u}^o(t))$, $\mathbf{K}^*(\mathbf{u}^o(t))$ and $\mathbf{f}^*(\mathbf{u}^o(t)))$ vary according to the contact configuration at the limit t^+ (the contact configuration $\mathbf{p}^{\text{NBM}}$ is defined in Equation (5.48)).

The energy metric in 2D-NBM is

$$2E(t) = \int_\Omega \rho\partial_t\mathbf{u}(\mathbf{x},t)^\top\partial_t\mathbf{u}(\mathbf{x},t) + \boldsymbol{\sigma}(\mathbf{u}(\mathbf{x},t)):\boldsymbol{\epsilon}(\mathbf{u}(\mathbf{x},t))\mathrm{d}\mathbf{x} \approx \dot{\mathbf{u}}(t)^\top\mathbf{M}\dot{\mathbf{u}}(t) + \mathbf{u}(t)^\top\mathbf{K}\mathbf{u}(t). \tag{5.63}$$

Otherwise, the energy metric can be also represented in terms of internal quantities $\mathbf{u}^o(t)$ and $\dot{\mathbf{u}}^o(t)$ by plugging Equation (5.50) into Equation (5.63) as follows:

$$E(t) \approx \frac{1}{2}(\dot{\mathbf{u}}^o(t)^\top\mathbf{M}^*\dot{\mathbf{u}}^o(t) + \mathbf{u}^o(t)^\top\mathbf{K}^*\mathbf{u}^o(t) + (\mathbf{d}^*)^\top\mathbf{K}\mathbf{d}^*) + \mathbf{u}^o(t)^\top\mathbf{f}^* \tag{5.64}$$

Similarly to solutions of the 1D-NBM ODE, solutions to the 2D-NBM ODE are expected to preserve energy away from instants of switch. The fact that $\dot{E}(t) = 0$ for $t \in \mathcal{T}(\mathbf{p}^{\text{NBM}})$ (energy is preserved away from instants of switch) is proven in Appendix C.3. In fact, when a 2D-NBM solution passes through different contact configurations in its motion, it exhibits a piecewise-constant energy (see Figure 5.9 in the next section). In a similar fashion to the 1D-NBM, the 2D-NBM allows for a regain in energy throughout the motion. Thanks to this property, periodic solutions of the 2D-NBM exist and nonsmooth modal analysis via 2D-NBM is possible.

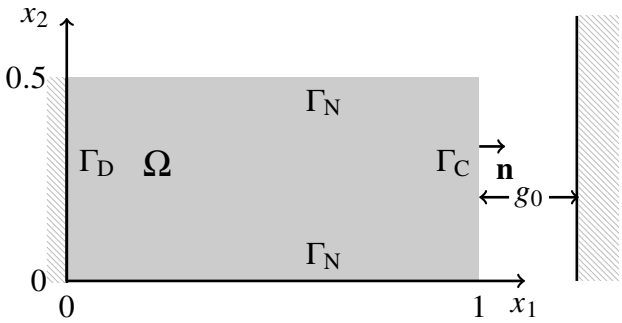

Figure 5.6: Investigated plate defined in Definition 5.5

5.5 Comparative analysis of 2D NBM

In this section, the 2D NBM-ODE is solved via time marching and compared to other methodologies such as Nitsche's method and the various Newton's impact law methods. For the solution of the 2D-NBM ODE, the CN scheme is used and its application to (5.62) is similar to that for the 1D-NBM ODE (see Section 4.4.1). However, the CN scheme application specifically to the 2D-NBM-ODE is not detailed in this manuscript for the sake of conciseness. In the remainder of this chapter, the system of interest is investigated via different FE models and the same physical configurations are used in all numerical experiments.

Definition 5.5 (Investigated plate)**.** *The investigated plate has dimensions* $\Omega = \{x_1 \in [0,1]; x_2 \in [0,0.5]\}$ *and its boundary conditions span*

$$\Gamma_D = \{x_1 = 0; x_2 \in (0,0.5)\} \tag{5.65}$$

$$\Gamma_N = \{x_2 = 0; x_1 \in (0,1)\} \text{ and } \{x_2 = 0.5; x_1 \in (0,1)\} \tag{5.66}$$

$$\Gamma_C = \{x_1 = 1; x_2 \in 0,0.5\} \tag{5.67}$$

with physical properties $\rho = Y = 1$ *and* $\nu = 0.2$*. The initial gap between the obstacle and the plate is constant and set to* $g_0 = 0.01$*. The investigated plate is illustrated in Figure 5.6.*

Since both the comparative study and nonsmooth modal analysis of the investigated plate are computationally expensive, the analysis is limited to a single model of the plate. The suggested model provides practical and novel insights that are sufficient for this thesis. Nevertheless, other possible avenues are discussed in Section 5.8. At last, numerical solutions obtained using schemes involving Newton's impact laws are obtained using SICONOS [1] and are denoted by the corresponding coefficient of restitution: $e = 0$ and $e = 1$.

5.5.1 Comparison of numerical schemes

The NBM and other FEM-based schemes are implemented on the investigated plate to demonstrate the capabilities of the NBM in comparison to existing methods. The results shown in this section were generated via the discretization of the domain Ω into a 20×20 square element grid with each element consisting of linear shape functions. The implicit CN scheme (or Newmark scheme with $\beta = 1/2$ and $\gamma = 1/4$ [43]) is used across all numerical schemes. The scheme is chosen since it preserves the discrete energy for linear motions in elastodynamics [43].

The time-step for all shown solutions is chosen in the plateau of convergence. This, it is assumed that numerical errors related to the truncation error of the CN scheme are minimized. Furthermore, $\gamma = 2000$ is chosen in Nitsche's method since the resulting solutions exhibit adequately small penetration while admitting a relatively non-stiff ODE (Nitsche's method leads to a stiff ODE for higher values of γ).

The initial conditions are:

$$\mathbf{u}(\mathbf{x}, 0) = \mathbf{0}, \quad \partial_t \mathbf{u}(\mathbf{x}, 0) = \begin{pmatrix} 0.05 x_1 \\ 0 \end{pmatrix}, \qquad \mathbf{x} \in \Omega. \tag{5.68}$$

The resulting motion of the plate is presented in Figure 5.7 to Figure 5.9. Figure 5.7 consists of different snapshots of the motion for $t \in [0, 5]$. In Figure 5.8, the motion of the node located at $\mathbf{x} = (1 \; 0.25)^\top$ on the boundary Γ_C is illustrated. At last, Figure 5.9 shows the energy through time for various FEM Signorini treatments.

In Figure 5.8(a), the NBM shows good agreement in the displacement field with other methods. Moreover, the NBM shows a behaviour similar to Newton's impact law $e = 0$. It is noted that the energy loss in NBM is considerably larger than $e = 0$. However, it is noted that the NBM is primarily conceived for the detection of periodic solutions for nonsmooth modal analysis. Thus, the NBM is primarily used for the depiction of periodic solutions (which are possible at any grid) and is not intended for the purposes of general initial-value problem solutions. Nevertheless, the NBM does converge to solutions generated by other FEM methodologies and the energy dissipation is expected to reduce upon convergence. This is further discussed in Section 5.5.2. Otherwise, the Nitsche solution exhibits significant penetration of the obstacle (situated at 0.01 in the x_1 direction), and Newton's impact law $e = 1$ exhibits considerable chattering. The difference between the numerical schemes is more prevalent in Figure 5.8(b) showing contact node velocity. Qualitatively, this figure shows that the NBM suffers the least from spurious oscillations. Indeed, application of Newton's impact law $e = 1$ is known to exhibit chattering behaviour which contributes to the existence of spurious oscillation [24]. It is also evident in Figure 5.8(b) that Nitsche's method exhibits spurious oscillations, known to exist when applied for relatively coarse grids [20]. While application of Newton's impact law $e = 0$ exhibits less dispersion than either Nitsche or $e = 1$, the NBM exhibits

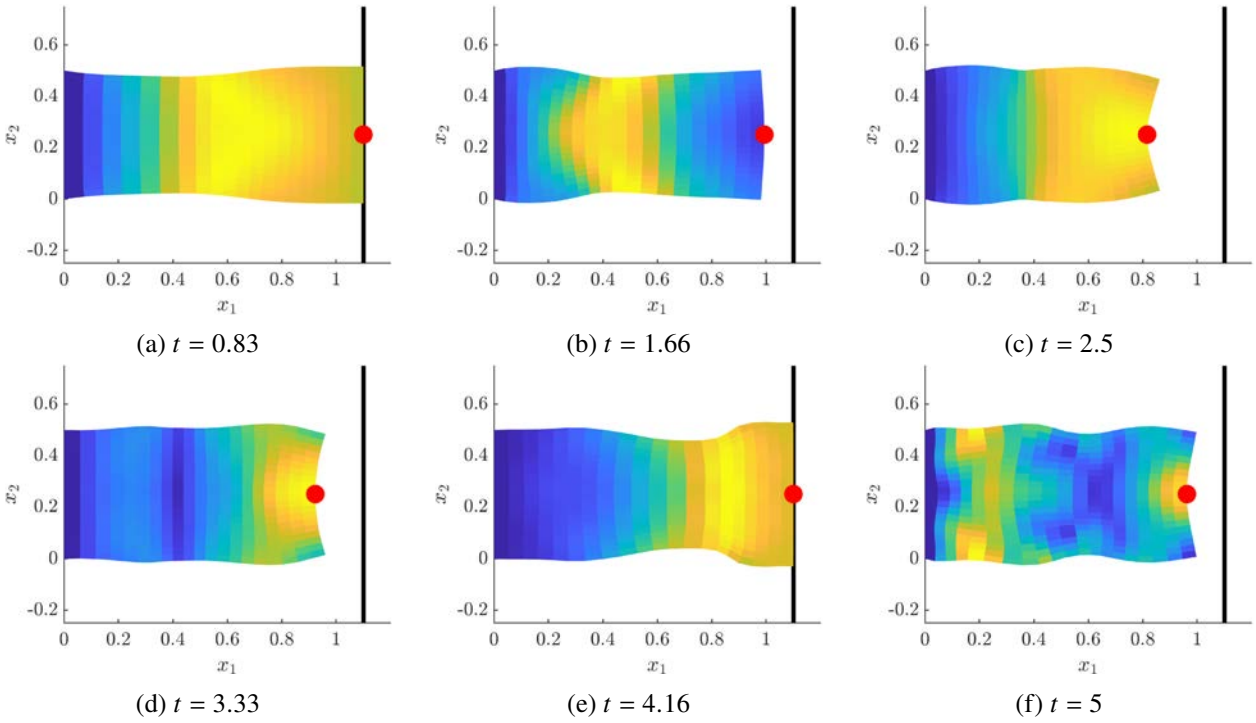

(a) $t = 0.83$ (b) $t = 1.66$ (c) $t = 2.5$

(d) $t = 3.33$ (e) $t = 4.16$ (f) $t = 5$

Figure 5.7: Snapshots of the NBM solution to the investigated plate (Definition 5.5) with initial conditions (5.68). Displacements along the x_1 and x_2 directions are multiplied by 10 (as well as the rigid obstacle's location relative to the structure) for illustration purposes. Motion of the red node presented in Figure 5.8. Colour gradient represents the field $||10\mathbf{P}(\mathbf{x})\mathbf{u}(t_i)||_2$ where t_i represents the snapshot time.

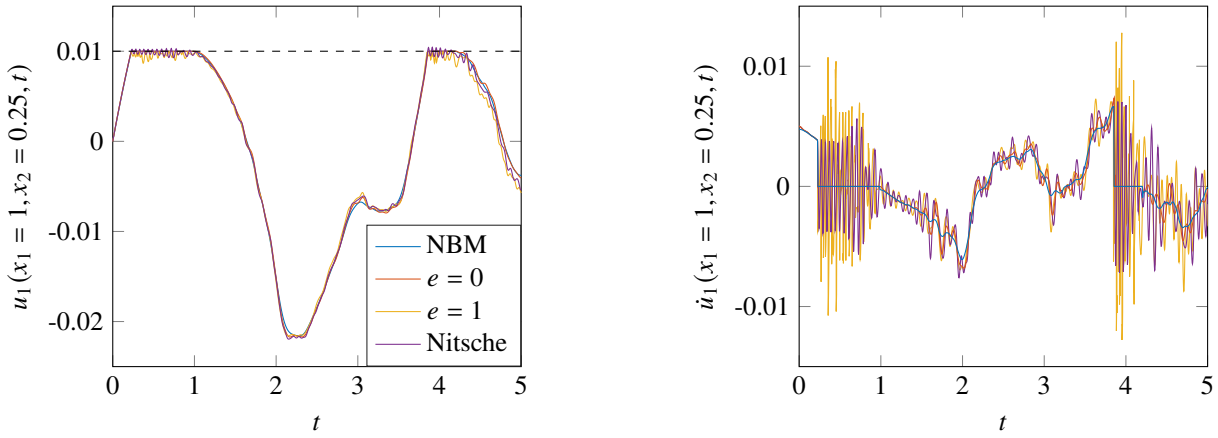

(a) Displacement (b) Velocity

Figure 5.8: Contact node motion for various Signorini FEM solvers of the investigated plate (Definition 5.5) with initial conditions (5.68). Location of the contact node indicated in Figure 5.7.

qualitatively the least spurious oscillations among all schemes, as evidenced in Figure 5.8(b).

In Figure 5.9, we remark that Newton's impact law $e = 1$ is energy-conservative while both the NBM and $e = 0$ are energy dissipative during contact occurrences. On the other hand, the solution

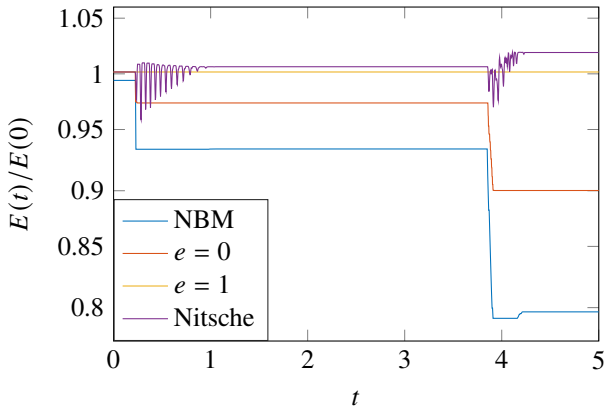

Figure 5.9: Energy of various Signorini FEM solvers for the investigated plate with initial conditions (5.68)

generated by Nitsche's method increases in energy with time. It is important to note that Nitsche's method does not always exhibit increase in energy and may exhibit energy dissipation as well [20]. Although the 2D-NBM largely dissipates in energy, small regains are noticeable slightly after $t = 4$ which correspond to changes of configuration phase and separation of the center contact node from the obstacle (see Figure 5.8(a)).

From this comparative analysis, the 2D-NBM shows advantages similar to the ones exhibited by the 1D-NBM: continuous active contact phases, energy regains, no chattering and no penetration of the obstacle. However, the 2D-NBM is shown to exhibit less spurious oscillations. It is important to note that elimination of spurious oscillations is advantageous numerically. For example, motions with spurious oscillations often necessitate a smaller time-step (to resolve the oscillations) than their less spurious equivalents and are generally avoided [56]. Nevertheless, it is yet unknown whether the NBM always exhibits less spurious oscillations than other schemes. In order to affirm this proposition, a thorough stability analysis of the 2D-NBM scheme needs to be conducted. This analysis is beyond the scope of this thesis and is therefore not conducted.

5.5.2 Convergence of FEM based schemes

In section Section 5.5, an example of FEM schemes for the solution of the Signorini problem is given. From numerical testing, it is revealed that the various numerical approximations, including NBM, converge to the same solutions for a fixed number of contact nodes. To demonstrate this, a convergence test is conducted. In this convergence test, the investigated plate is discretized using four contact nodes ($N_C = 4$) and a varying number of internal nodes N_O through the following grid: 5×3 ($N_O = 16$), 10×3 ($N_O = 36$), 20×3 ($N_O = 76$), 30×3 ($N_O = 116$), 40×3 ($N_O = 156$) and 50×3 ($N_O = 196$). The 2D-NBM solutions are compared to $e = 0, 1$ and Nitsche's schemes. Since no closed-form solution is available, the solution generated by $e = 0$ and the 60×3 grid constitutes the

baseline for the converged solution. The convergence error in each grid configuration is measured by computing the L_2 norm of the difference in displacements with respect to the baseline.

The L_2 error and attendant convergence rate for all schemes and grids are presented in Figure 5.10. It is noted that all schemes have a relatively similar rate of convergence. Another evidence to

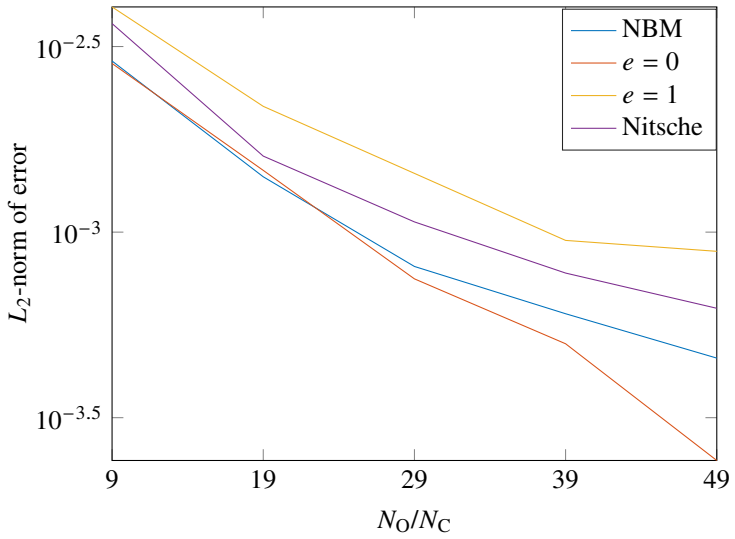

Figure 5.10: Approximation error for a fixed number of contact nodes. In all tests, the approximation error assuming convergence to the model generated by Newton's impact law with $e = 0$ and 60×3 grid. The models are varying in internal nodes N_O while the number of contact nodes is fixed $N_C = 4$. Note that all method converge to the solution generated by Newton's impact law with $e = 0$ and 60×3 grid.

convergence is in Section 5.7.1 which shows that all forced-response diagrams obtained by different FEM schemes with a 50×3 grid are virtually equivalent.

From this convergence test, it is possible to conjure that different FE schemas of the Signorini problem converge to the same solution for a fixed number of nodes. Although this conjectures is not investigated further in this thesis, its repercussions are discussed in Chapter 6.

5.6 Detection of NSM via HBM

To perform nonsmooth modal analysis using the 2D-NBM, periodic solutions to Equation (5.62) should be found. Although the shooting method can be used to find periodic solutions using 2D-NBM (similarly to the 1D-NBM), numerical experiments showed it was computationally expensive. Instead, a combination of HBM and 2D-NBM was shown to be more efficient. This section serves to elaborate on these aspects. The resulting HBM-NBM approach is then used for the nonsmooth modal analysis of the investigated plate.

for the application of HBM, the displacement of internal nodes $\mathbf{u}^o(t)$ is approximated as a series

of N_h cosine functions of frequency ω

$$u_i^o(t) \approx \sum_{j=1}^{N_h} H_{ij} \cos((j-1)\omega t) \equiv u_i^{N_h}(\mathbf{H}, \omega, t) \tag{5.69}$$

where the cosine coefficients are H_{ij} stored in $\mathbf{H}$ and $\mathbf{u}^{N_h}(\mathbf{H}, \omega, t)$ is used to denote the HBM approximation of $\mathbf{u}^o(t)$. The trial solution (5.69) is plugged into Equation (5.62) to form the residual

$$\mathbf{R}^{N_h}(\mathbf{H}, \omega, t) = \mathbf{M}^*(\mathbf{u}^{N_h}(\mathbf{H}, \omega, t))\ddot{\mathbf{u}}^{N_h}(\mathbf{H}, \omega, t) + \ldots \tag{5.70}$$

$$\mathbf{K}^*(\mathbf{u}^{N_h}(\mathbf{H}, \omega, t))\mathbf{u}^{N_h}(\mathbf{H}, \omega, t) + \mathbf{f}^*(\mathbf{u}^{N_h}(\mathbf{H}, \omega, t)). \tag{5.71}$$

To find a solution to the 2D-NBM-ODE, $\mathbf{H}$ and ω are found by projecting the residual onto the composing cosine functions and equating this projection to zero. This procedure yields

$$\mathbf{F}_i^{N_h}(\mathbf{H}, \omega) = \int_0^T \cos(i\omega t)\mathbf{R}^{N_h}(\mathbf{H}, \omega, t)\mathrm{d}t = \mathbf{0}, \quad i = 0, 1, 2, \ldots, N_h \tag{5.72}$$

where $T = 2\pi/\omega$.

The integration quadrature operation in (5.72) is done via trapezoidal integration with $20N_h$ as it was proved sufficient for finding accurate solutions. In Section 2.1.3, it is noted that the HBM must be complemented with continuation methods in order to find nonsmooth modes of the 2D-NBM ODE (5.62). In this section, the SCC, explained in Section 4.4.3, is used in order to determine periodic solutions. However, compared to Section 4.4.3, for the 2D-NBM-HBM, SCC is conducted by fixing the initial energy of the motion (5.63) rather than the period of motion. It was found the SCC in the frequency domain did not result in solutions for all frequencies. However, fixing the energy of motion was proven successful and the algorithm almost always resulted in a periodic solution. It is important to note that the reason for which fixing the energy of the motion results more often in successful solutions rather than fixing the period of motion is yet unknown and further investigation of the topic is not conducted in this manuscript. To clarify, in the root solving problem, the set of equations to be solved consists of Equation (5.72) and the continuation equation

$$F_{\text{cont}}^{N_h}(\mathbf{H}, \omega) = E(\mathbf{u}^{N_h}(\mathbf{H}, \omega, t = 0)) - E^i \tag{5.73}$$

$$E(\mathbf{u}^o(t)) = \frac{1}{2}(\dot{\mathbf{u}}^o(t)^\top \mathbf{M}^* \dot{\mathbf{u}}^o(t) + \mathbf{u}^o(t)^\top \mathbf{K}^* \mathbf{u}^o(t) + (\mathbf{d}^*)^\top \mathbf{K}\mathbf{d}^*) + \mathbf{u}^o(t)^\top \mathbf{f}^* \tag{5.74}$$

where E^i is the energy level sought and the energy metric (5.64) is reminded in Equation (5.74).

As a consequence, application of SCC to the above system follows the steps:

1. For small N_h (say $N_h = 3$), SCC is performed on Equation (5.72) for a range of energies E^k to find the corresponding HBM coefficients $\mathbf{H}$. For low N_h, periodic solutions are generally found with relative ease. The resulting HBM coefficients are denoted $\mathbf{H}^{N_h,k}$.
2. The HBM approximation for each E^k is improved by considering a higher number of harmonics N_h using the previous solution with fewer harmonics as initial guess, the new harmonics being

set to zero.

3. Repeat step 2 for higher values of N_h, using the previous solution as initial guess.

Although Equation (5.72) is non-smooth due to NBM-ODE, it was solved using MATLAB's `fsolve` [66].

5.6.1 Convergence of HBM

To measure the accuracy of the HBM approximation, the residual error in Section 4.4.2 is formulated. It is defined as

$$\text{Residual Error} = \left\| \sqrt{\frac{1}{T}\int_0^T \mathbf{R}^{N_h}(\mathbf{H},\omega,t)^2 \mathrm{d}t} \right\|_2 \tag{5.75}$$

It is worth noting that Bernung and Haller in [15] have shown numerous cases where the HBM approximation for large N_h does not converge to a true periodic solution of the approximated system. In order to guarantee that the HBM produces solutions that are representative of NBM-ODE motions, it is proposed to compare the HBM solution to the time-marched solution via the metric

$$\text{Approximation Error} = \left\| \sqrt{\frac{\omega}{2\pi N_t}\sum_{i=0}^{N_t}(\mathbf{u}^{N_h}(\mathbf{H},\omega,t_i) - \mathbf{u}^o(t_i))^2} \right\|_2 \tag{5.76}$$

$$\mathbf{u}^o(0) = \mathbf{u}^{N_h}(\mathbf{H},\omega,0), \quad \dot{\mathbf{u}}^o(0) = \dot{\mathbf{u}}^{N_h}(\mathbf{H},\omega,0) = \mathbf{0} \tag{5.77}$$

where the quantities $\mathbf{u}^o(t_i)$ are approximated using a CN algorithm with N_t time-steps where N_t is sufficiently large.

For the FEM approximation of the plate, a 10×10 grid of square elements and linear Lagrangian shape functions are used. In order to study the convergence, it is important to focus on a specific solution of HBM equations (5.72) (recall from Section 2.1.2 that the set of HBM equations describes a continuum of solutions). Therefore, it is necessary to provide an additional condition to the HBM equations (5.72) so that the complete set of equations is well-determined. The additional constraint is implemented on the energy of the motion via Equation (5.73) with energy fixed at 0.002: this value is chosen since it is high enough to guarantee contact with the rigid obstacle.

The set of HBM conditions developed in Equations (5.72) and (5.73) was successfully solved for increasing number of harmonics $N_h = 3, 5, \ldots, 19$. The residual and approximation errors are illustrated in Figure 5.11. They are both characterized by slow convergence rates. This is expected when HBM is used to approximate nonsmooth solutions [42, 51]. Still, the solution obtained via HBM fits closely the NBM-ODE solution and the reduction in residual error and approximation error is expected to improve with increasing N_h.

In Figure 5.13, the HBM solution with $N_h = 19$ is compared against the time-marched solution starting with the initial state of the approximated HBM motion (i.e., the initial guess in Equation (5.77)

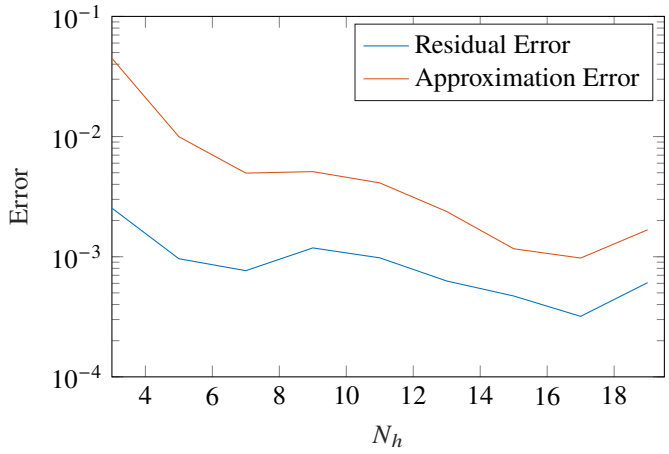

Figure 5.11: Convergence of HBM-NBM for the investigated plate approximated via a 10×10 grid and linear shape functions.

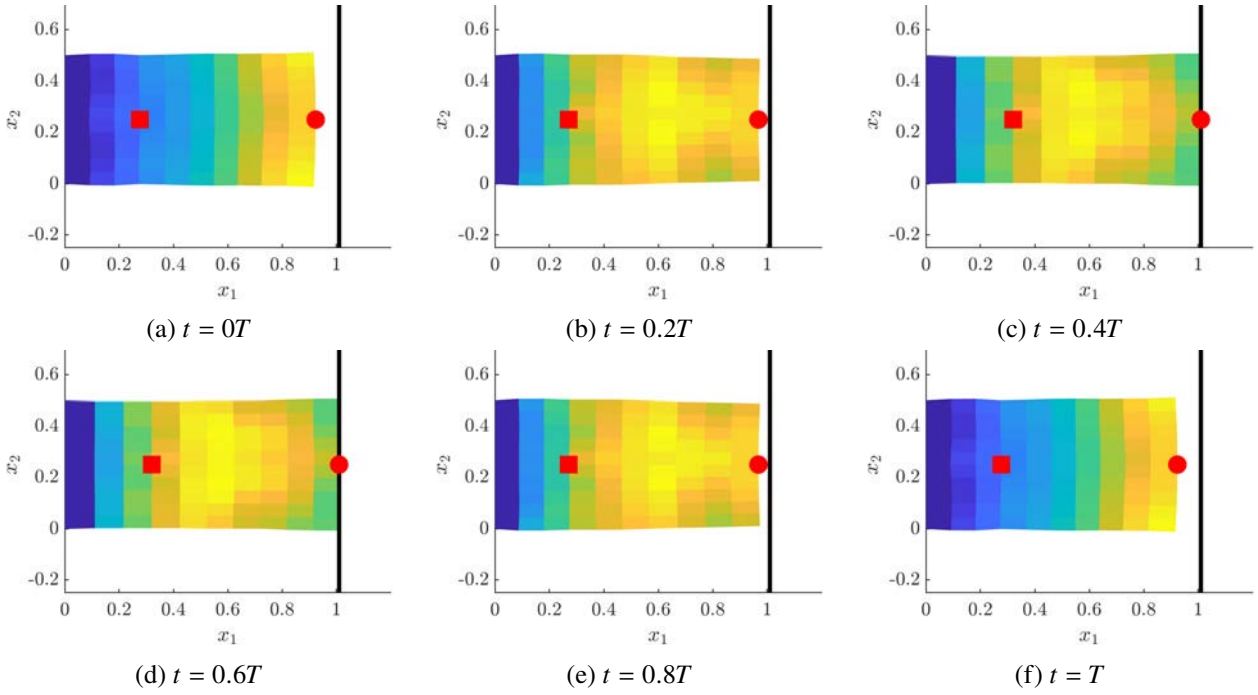

(a) $t = 0T$ (b) $t = 0.2T$ (c) $t = 0.4T$

(d) $t = 0.6T$ (e) $t = 0.8T$ (f) $t = T$

Figure 5.12: Instances of a HBM-NBM plate motion throughout a period of motion with $T \approx 3.0962$. The displacement of the contact node marked with a red dot (•) is presented in Figure 5.13(a). The displacement of the internal node marked with a red square (■) is presented in Figure 5.13(b). Colour gradient represents the field $||\mathbf{P}(\mathbf{x})\mathbf{u}(t_i)||_2$ where t_i is the snapshot time.

is used). While there exist some fitting error (see Figure 5.11 for $N_h = 19$) between the time-marched and HBM solutions and a noticeable error in energy, see Figure 5.13(c), it is evident from Figures 5.13(a) and 5.13(b) that the displacements generated by both HBM and CN fit closely and the HBM motion still generates a relatively accurate motion to the NBM-ODE.

Furthermore, it can be clearly seen that the HBM approximation to the NBM-ODE still admits a

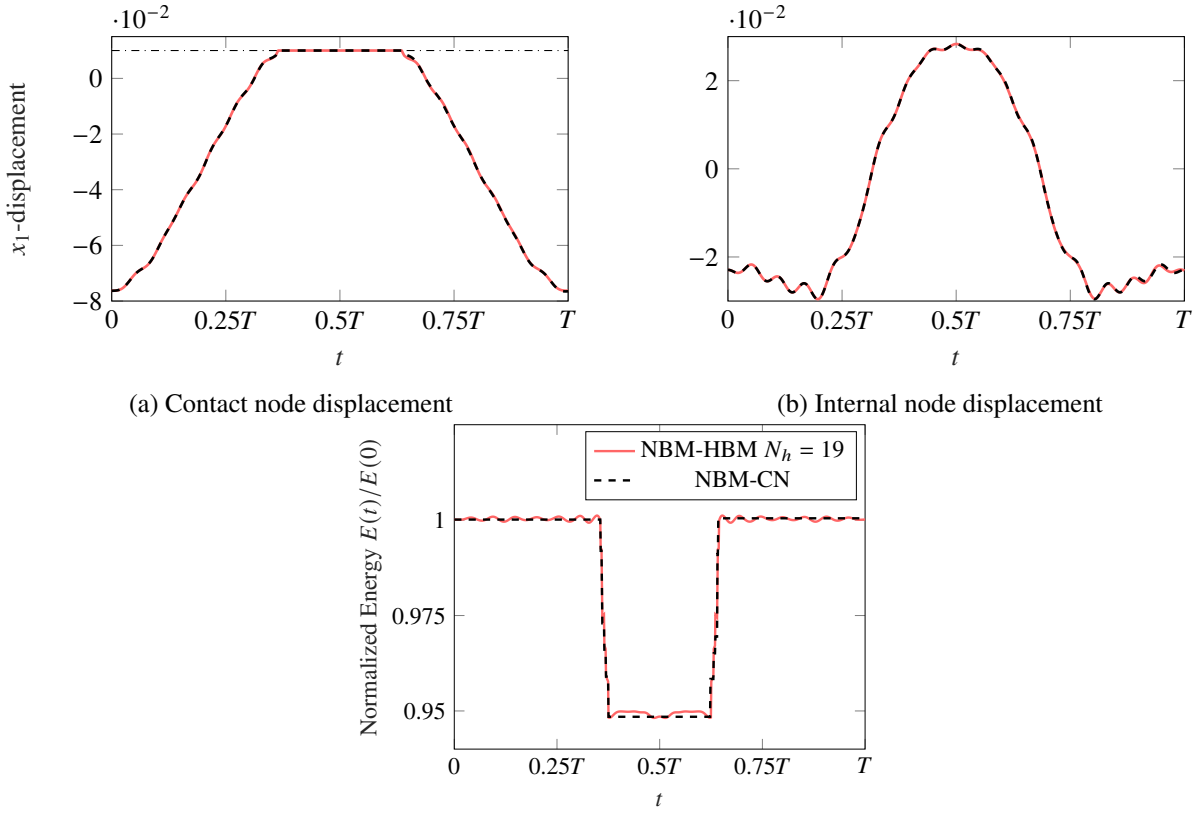

(a) Contact node displacement

(b) Internal node displacement

(c) Normalized Energy, $E(0) = 0.002$

Figure 5.13: Comparison of HBM and CN (time-marched solution) solutions to the NBM-ODE for a period of motion $T \approx 3.0962$, The nodes plotted in Figures 5.13(a) and 5.13(b) are marked in Figure 5.12.

non-smooth contact node motions, see Figures 5.13(a) and 5.13(b). In fact, the NBM-ODE can exhibit nonsmooth displacements and velocities at the contact boundary even when HBM is used to approximate the motion of internal nodes. This is largely due to the fact that the nonsmoothness in the displacement of contact node is dictated by the switching of the contact configuration and does not depend on the HBM approximation. While the nonsmooth behaviour of contact nodes is not affected by the HBM approximation, the location of discontinuities in nodal velocities (i.e., the instants of switch) are affected by the HBM approximation.

5.7 Nonsmooth modal analysis

To perform nonsmooth modal analysis of the investigated plate in unilateral contact with a rigid obstacle, the HBM and SCC are used. The nonsmooth modes of the plate are compared against forced responses.

In Section 5.7.1, the forced-response motion is defined for validation of the resonance points detected by the NSMs. Then, two NSMs are discussed: longitudinal in Section 5.7.2 and transverse

in Section 5.7.3. The longitudinal NSM originates from the second natural frequency of the underlying linear plate system ($\omega_2 \approx 1.57$) and consists of displacement mainly in the longitudinal direction (normal to the obstacle). The transverse NSM originates from the third natural frequency of the underlying linear plate system ($\omega_3 \approx 1.73$) and consists of displacement in transverse direction (tangent to the obstacle). It is important to note that an NSM exists around the first natural frequency ω_1 which consists also of motions in the transverse direction however it is not discussed for the sake of conciseness.

5.7.1 Forced-response curves

The nonsmooth mode of the investigated plate is compared against the forced-responses obtained from the PDE

$$\rho\partial_{tt}\mathbf{u}(\mathbf{x},t) + \xi\partial_t\mathbf{u}(\mathbf{x},t) - \nabla\cdot\boldsymbol{\sigma}(\mathbf{u}(\mathbf{x},t)) = \mathbf{f}\cos(\omega_f t), \quad (\mathbf{x},t) \in \Omega\times[0,\infty) \tag{5.78}$$

where $\mathbf{f}$ describes the amplitude and direction of the applied force and ω_f is the forcing frequency. In the forced response diagrams, the ranges of damping coefficients ξ and forcing magnitudes are chosen such that resonances occur in the same range of energies as the detected NSM. The forced-response curves are obtained by solving the PDE (5.78) through 20 periods $2\pi/\omega_f$, considered sufficient to reach a steady state.

To compare between forced-response and NSM energies, the root mean square of mechanical energy throughout a period of motion is used

$$\tilde{E}(T) = \sqrt{\frac{\int_0^T E(\mathbf{u}(t))^2 \mathrm{d}t}{T}} \tag{5.79}$$

where $E(\mathbf{u}(t))$ is defined in Equation (5.63) and T is the period of the motion in question. for the forced-response motions, the value $\tilde{E}$ is calculated at the steady state.

The forced-response curves were generated using three different treatments of the Signorini conditions: 2D-NBM, Newton's impact law, and Nitsche's method. In all methods, a finite element grid of 50 by 3 elements was chosen. Figure 5.14 displays a comparison of the forced-response curves generated by the different treatments of the Signorini conditions.

All forced-response curves in Figure 5.14 show good agreement in terms of the loci of resonant points. From numerical experiments, this agreement also carries for other values of $\mathbf{f}$. Indeed, the fact the 2D-NBM generates forced-response curves that lie closely to forced-response curves by other techniques constitutes a proof of work for the 2D-NBM. Since the forced-response curves closely align, those generated by SICONOS with $e = 0$ are chosen for the comparison against the detected NSMs.

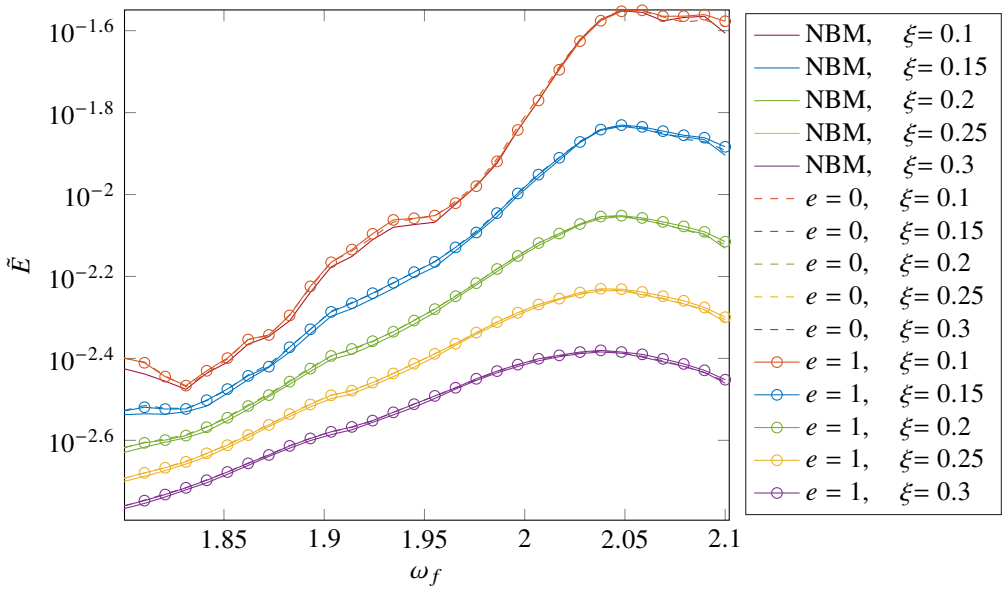

Figure 5.14: Forced-response diagrams obtained for the 50 by 3 model of the plate in unilateral contact, $\mathbf{f} = \begin{pmatrix} 0.05 & 0 \end{pmatrix}$ for varying frequencies ω_f and damping coefficients ξ. $\tilde{E}$ is defined in Equation (5.79) and is calculated throughout the last period of motion $t \in [19(2\pi/\omega_f), 20(2\pi/\omega_f)]$. This figure portrays the equivalence between the forced response diagrams obtained via different FEM based methodologies.

5.7.2 Longitudinal NSM

This NSM is excited by applying forces oscillating in the longitudinal direction and, at low energies, this NSM coincides with the second linear mode of vibration (see Mode 2 in C.7) of the investigated plate. To determine the NSM, a 50 by 3 FEM model is used with HBM-NBM algorithm consisting of 10 harmonics (judged sufficient for the convergence of the backbone curve). The NSM is illustrated in Figure 5.15.

In this section, the contribution of linear normal modes and the corresponding forced-response diagrams will be used to analyse the obtained NSM following the procedure in [97, p.75] is used. In brief, the contribution of a linear mode i, denoted $\mathbf{u}_i^{\text{lin}}(\mathbf{x})$ in a given motion j of the NSM, denoted $\mathbf{u}_j^{\text{NSM}}(\mathbf{x}, t)$, is quantified by the projection of the NSM motion onto the linear mode. This admits a time dependent coefficient

$$a_{ij}^{\text{lin}}(t) = \frac{\int_\Omega \mathbf{u}_i^{\text{lin}}(\mathbf{x}) \cdot \mathbf{u}_j^{\text{NSM}}(\mathbf{x}, t) \mathrm{d}\mathbf{x}}{\int_\Omega \mathbf{u}_i^{\text{lin}}(\mathbf{x}) \cdot \mathbf{u}_i^{\text{lin}}(\mathbf{x}) \mathrm{d}\mathbf{x}}. \tag{5.80}$$

Then, the numerical metric representing the linear mode's participation in a given NSM motion is obtained by taking the root mean square value of $a_{ij}^{\text{lin}}(t)$ over a period T_j of the NSM motion j:

$$\tilde{a}_{ij} \equiv \frac{1}{T_j} \sqrt{\int_0^{T_j} a_{ij}^{\text{lin}}(t)}. \tag{5.81}$$

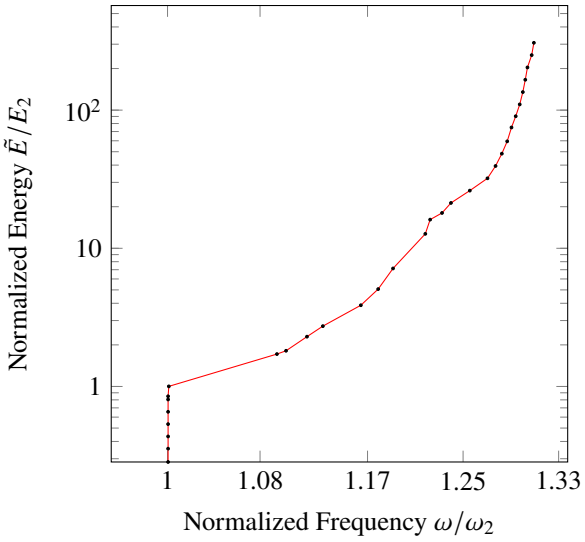

Figure 5.15: FEP of longitudinal NSM of the plate originating from the 2nd linear mode. The NSM is found using NBM-HBM with $N_h = 10$. The grazing energy is $E_2 \approx 3.5 \times 10^{-5}$ and the corresponding natural frequency at grazing is $\omega_2 \approx 1.57$.

The participation of linear mode i in an NSM motion j is represented using the quantity

$$\tilde{p}_{ij} \equiv \frac{|\tilde{a}_{ij}|}{\sum_{i=0}^{N_l} |\tilde{a}_{ij}|} \tag{5.82}$$

where N_l represents the number of linear modes of vibration used for the approximation. The participation of linear modes in the longitudinal NSM is presented in Figure 5.16. Figure 5.16 shows a significant participation of other linear modes than the second linear mode in the NSM. The participation of more than one linear mode in NSM motions is characteristic and is expected in

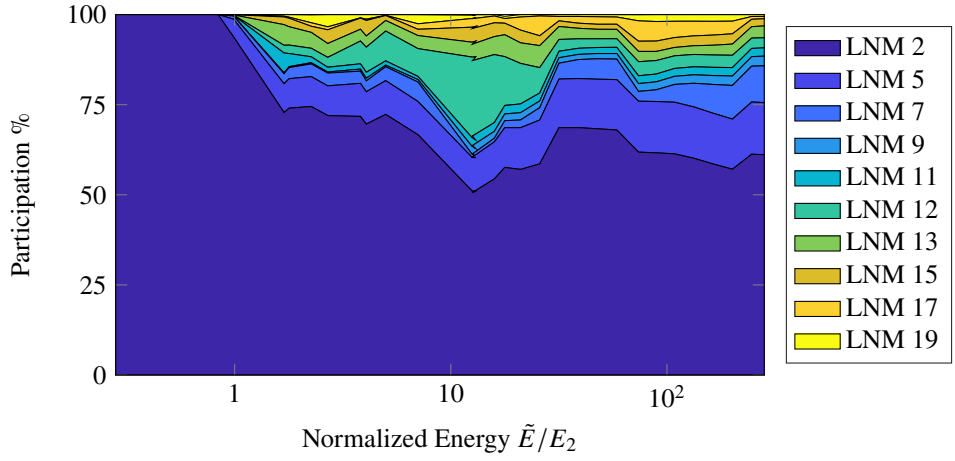

Figure 5.16: Participation (defined in Equation (5.82)) of 10 first linear modes in the longitudinal NSM. $\tilde{E}$ stands for the root-mean-square value of $E(t)$ through a period of motion. Grazing energy $E_2 \approx 3.25 \times 10^{-5}$. Modes illustrated in Appendix C.6.

nonlinear normal modes in general [97]. It is worth noting that the participation of longitudinal modes (modes excited by longitudinal forces) is dominant compared to transverse modes. For example, the 2nd, 5th 7th and all other linear modes appearing in Figure 5.16 are longitudinal modes (see illustrations of linear modes in Appendix C.6). Nevertheless, it is important to note that other transverse modes (such as 1st and 3rd modes) participate in the NSM but their participation is negligible compared to the participation of longitudinal modes.

Next, the NSM is compared to the forced response diagrams in Figure 5.17. To generate these forced response curves, a force oscillating exclusively in the longitudinal direction with amplitude $\mathbf{f} = (0.02 \quad 0)^\top$ was used. Furthermore, Figure 5.17 shows that the NSM passes closely to all resonances detected in the forced response curve.

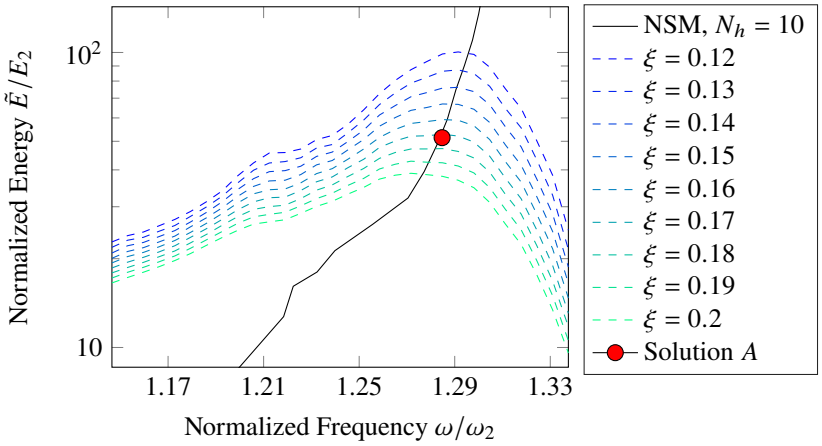

Figure 5.17: Longitudinal NSM emanating from 2nd linear mode from Figure 5.15 against forced response curves generated for $\mathbf{f} = \begin{pmatrix} 0.02 & 0 \end{pmatrix}^\top$. Solution A ($T \approx 3.12, \tilde{E} \approx 0.0018$) is illustrated in Figure 5.18 and in Figure 5.19.

Figures 5.18 and 5.19 depict the NSM motion at the intersection between the backbone curve and the forced response for $\xi = 0.17$ (see Solution A in Figure 5.17). The figures depict the second linear mode at the same energy as the NSM motion for comparison purposes. The motions are compared at fractions of their respective periods rather than in exact times. Both NSM and linear motion show close resemblance away from contact. For example, in Figure 5.18, the plate follows the linear mode's trajectory for the most part until a contact with the obstacle is achieved. Furthermore, Figure 5.19 shows that a similar negative amplitude is reached by the structure for the same energy. However, the contribution of other modes can be seen along the t axis in Figure 5.19. Even away from contact, it is evident that the NSM solution (solution A) does not follow a cosine trajectory (like the second linear mode) and has contribution from higher harmonics in time.

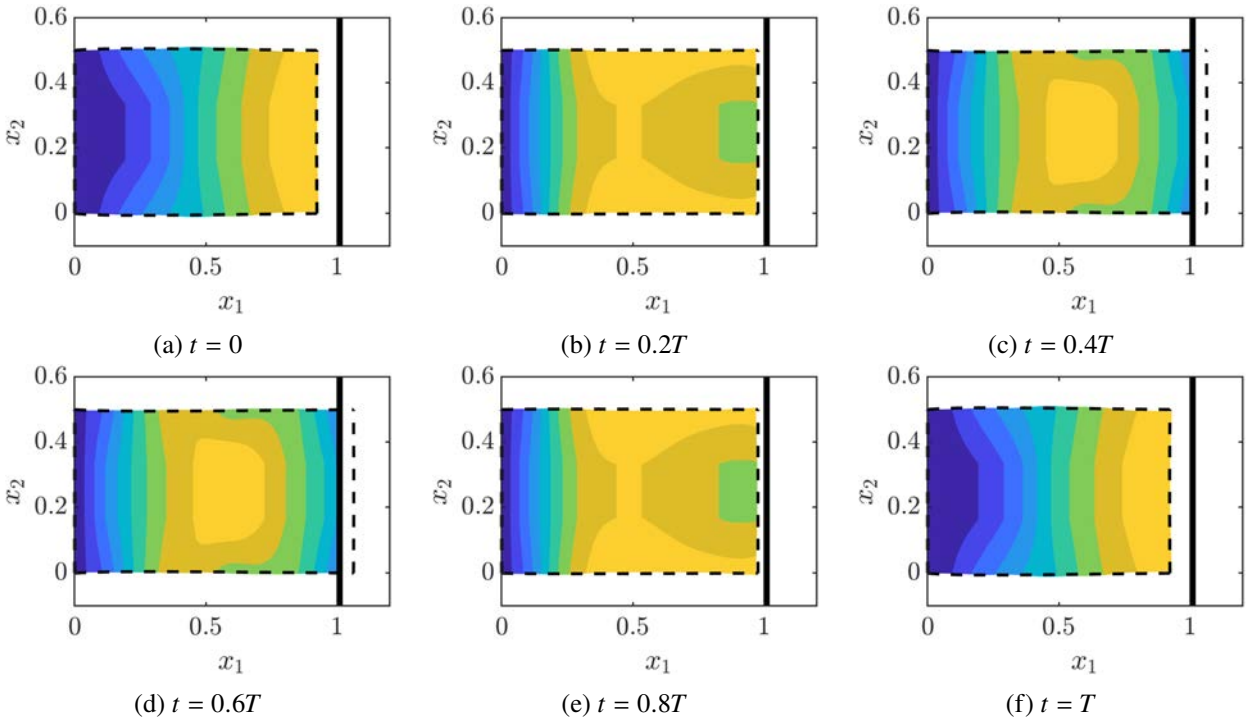

(a) $t = 0$ (b) $t = 0.2T$ (c) $t = 0.4T$

(d) $t = 0.6T$ (e) $t = 0.8T$ (f) $t = T$

Figure 5.18: Instances of the longitudinal NSM motion in solution A (see Figure 5.21, $T \approx 3.12$, $\tilde{E} \approx 0.0018$). Colour gradient represents the field $||\mathbf{P}(\mathbf{x})\mathbf{u}(t_i)||_2$ where t_i denotes an instant time. The black-dashed outline represents the motion of the linear mode with frequency ω_2 ($T \approx 3.98$) and energy $E(t) = 0.0018$ (same level of energy as solution A). Other motions on of the longitudinal NSM are presented in Appendix C.4

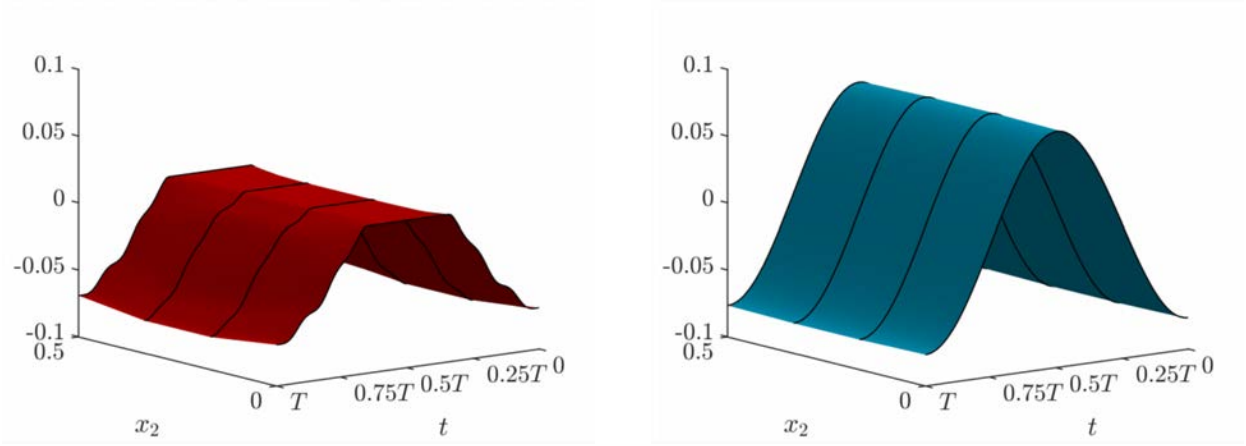

(a) Solution A, $T \approx 3.12$, $\tilde{E} \approx 0.0018$ (b) Linear mode, $T \approx 3.98$, $\tilde{E} = 0.0018$

Figure 5.19: Motion of contact boundary for the solution A and third linear mode of vibration at the same energy. Snapshots of both solution A and the linear mode's motions are presented in Figure 5.18.

5.7.3 Transverse NSM

The transverse NSM is excited by applying a force oscillating in the transverse direction x_2 and, at low energies, coincides with the third linear mode of vibration of the investigated plate, shown in C.7.

To identify the NSM, a 50 by 3 FEM model of the approximated plate is used with HBM-NBM algorithm consisting of 10 harmonics (similarly to the Longitudinal NSM, the curve sufficiently converged for 10 harmonics). The NSM is illustrated in Figure 5.20 together with the contribution of the first ten linear modes of vibration in the NSM. From Section 5.7.3, it is evident that the presence of unilateral contact admits an NSM where energy increases with increasing frequency and it is expected that excitation with higher frequencies would result in a higher energy of motion at resonance (for frequencies within the range of NSM frequencies, of course).

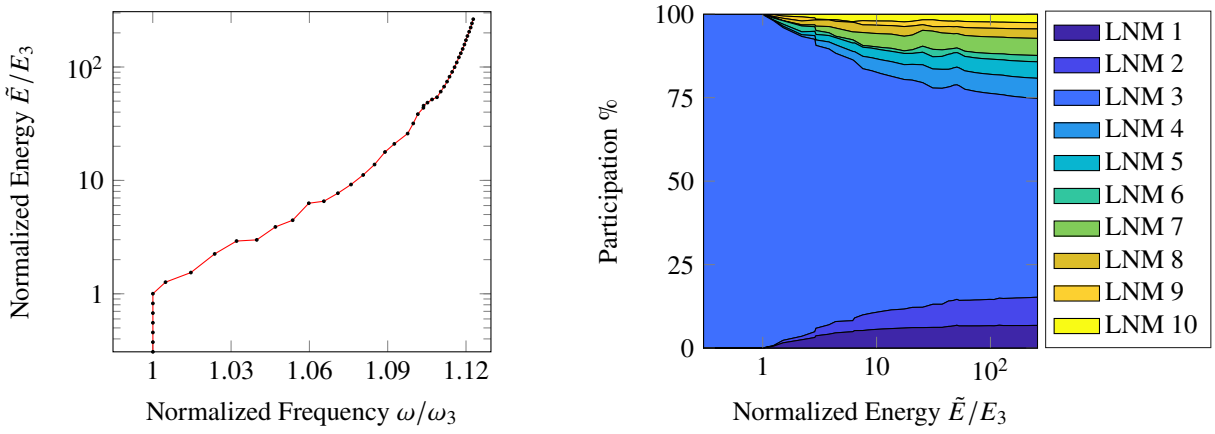

(a) FEP of NSM

(b) Linear mode participation in NSM

Figure 5.20: FEP of transverse NSM originating from the third linear mode and participation (defined in Equation (5.82)) of ten first linear modes in the NSM. The NSM is found using NBM-HBM with $N_h = 10$. Grazing energy $E_3 \approx 3.25 \times 10^{-5}$ and natural frequency at grazing $\omega_3 \approx 1.73$.

From the modal participations in Figure 5.20(b), it is clear that the third linear mode has the largest participation within the NSM throughout all energy levels. At energies higher than the grazing energy, other modal contribution are present. Interestingly, even though the plate is excited using exclusively transverse forces, it can be seen that the unilateral contact condition triggers exclusively longitudinal modes of vibration, see Figure C.7. While in linear systems, only the third mode will be present, the contribution of longitudinal modes in the NSM motion are expected due to the contact pressure acting in the longitudinal direction.

The NSM is compared to the forced response in Figure 5.21. A force oscillating exclusively in the transverse direction with amplitude $\mathbf{f} = (0 \;\; 0.05)^\top$ was chosen. The NSM passes closely to all resonances detected in the forced response curve which validates the accuracy of the NBM-HBM method in detecting the NSMs.

The plates vibration profile of the NSM close to the resonant peak of the $\xi = 0.2$ curve is presented in Figure 5.22 and contact boundary motion in the x_1 direction for this specific motion is presented in Figure 5.23.

In Figure 5.22, the vibration is characterized by a collision of a single corner of the plate against

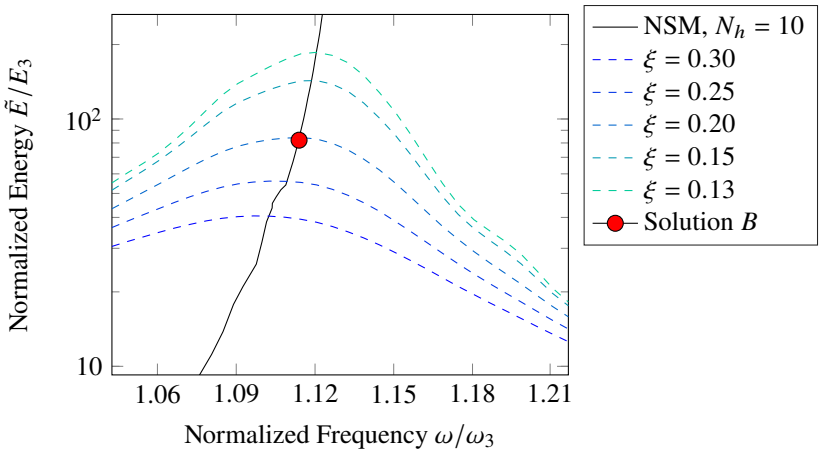

Figure 5.21: NSM emanating from the third linear mode from Figure 5.20 against forced response curves generated for $\mathbf{f} = (0 \;\; 0.05)^\top$. Solution B ($T \approx 3.27$, $\tilde{E} \approx 0.0027$) shown in Figures 5.22 and 5.23.

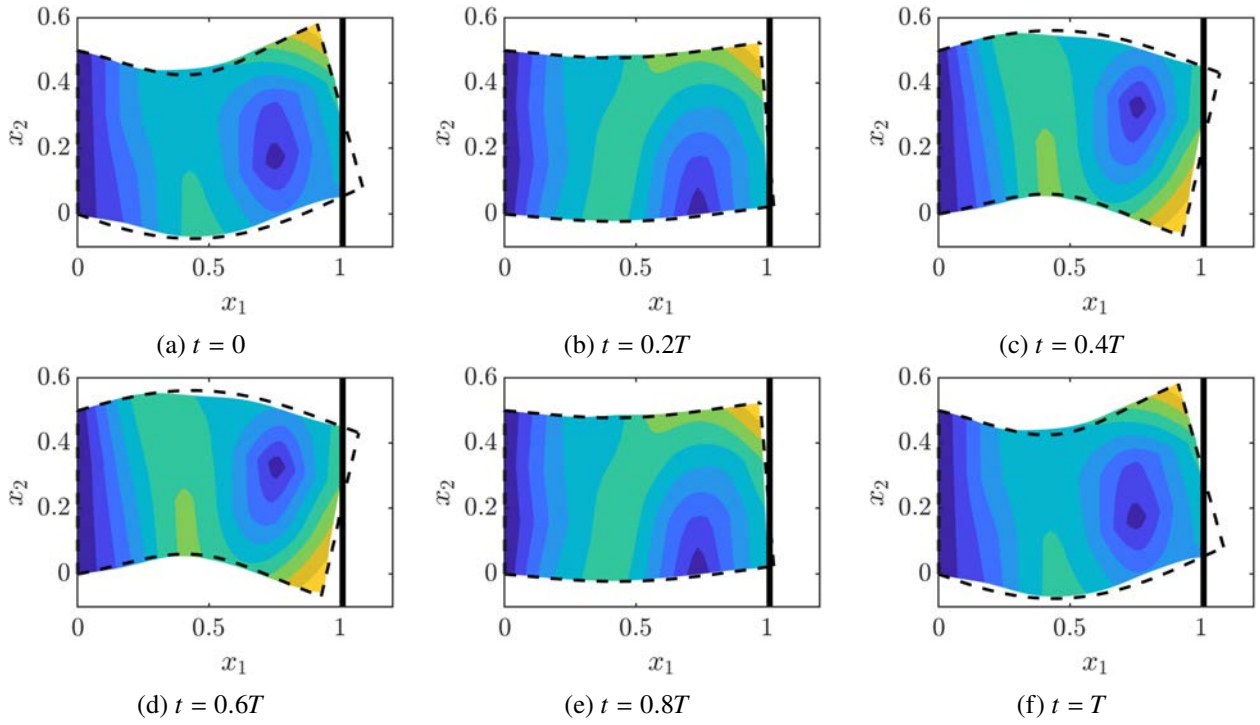

(a) $t = 0$ (b) $t = 0.2T$ (c) $t = 0.4T$

(d) $t = 0.6T$ (e) $t = 0.8T$ (f) $t = T$

Figure 5.22: Instances of the Transverse NSM motion in solution B (see Figure 5.21, $T \approx 3.27$, $\tilde{E} \approx 0.0027$). Colour gradient represents the field $||\mathbf{P}(\mathbf{x})\mathbf{u}(t_i)||_2$ where t_i represents the snapshot time. The black-dashed outline represents the motion of the linear mode with frequency ω_{tan} ($T \approx 3.64$) and energy $E(t) = 0.0027$ (same level of energy as solution B). Other motions of the longitudinal NSM are presented in Appendix C.5

the rigid obstacle and never a simultaneous collision of all stencils on the contact boundary against the obstacle (compared to the longitudinal NSM in Figure 5.19). Comparing the NSM and the third linear mode in Figure 5.22, it is noted that the NSM motion follows closely the third linear mode's trajectory. This is also indicated in the large contribution of the third linear in the NSM in

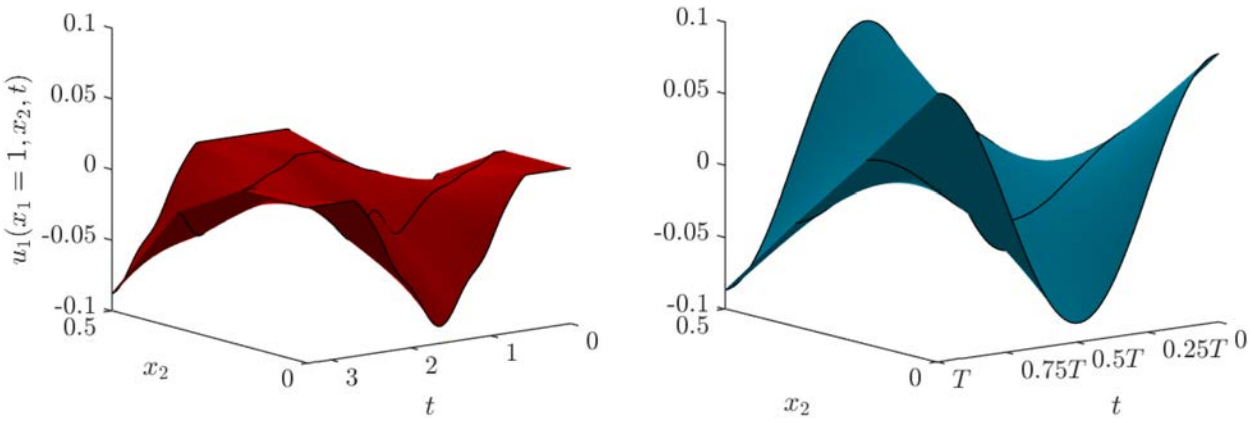

(a) Solution B, $T \approx 3.27$, $\tilde{E} \approx 0.0027$

(b) Linear mode, $T \approx 3.64$, $\tilde{E} = 0.0027$

Figure 5.23: Motion of contact boundary for the solution B and third linear mode of vibration at the same energy. Snapshots of both motions are presented in Figure 5.22.

Figure 5.20(b). Nevertheless, the deformation profiles of NSM and linear motions in the phase-space differ and are not entirely congruent which is likely related to the participation of other linear modes in the motion. Furthermore, Figure 5.23 shows that the contact boundary reaches a minimum of the same magnitude in both the NSM motion and in the linear mode. In the presence of unilateral contact, the minimal amplitude of the contact node is equivalent to that of the third linear mode.

Both longitudinal and transverse NSMs show that the NBM-HBM approach is successful in predicting resonance points in forced responses. It is noted that the presence of unilateral contact conditions with a positive gap has a hardening effect on the backbone curve. The NSM motion also shows contributions from other linear modes, although the contribution of the mode from which the NSM emanates still carries dominant participation.

Both NSMs were shown as proof of work of the NBM-HBM approach. However, given the proposed methodology, nonsmooth modal analysis of the investigated plate can be done for varying thickness, varying forces and in a larger frequency spectrum.

5.8 Scope and Limitations

In this chapter, the 2D-NBM was applied successfully for the nonsmooth modal analysis of a rectangular plate in unilateral contact with a rigid obstacle situated at a fixed gap g_0 from the non-deformed structure. Although not explored, the proposed 2D-NBM formulation may also apply for rectangular plates with Robin boundary conditions or varying density, dimensions, Young's modulus or Poison's ratio. The methodology can also apply to plane-strain approximations and is not exclusive to plane-stress.

It should be said that the presented formulation of the 2D-NBM does not readily apply to

non-rectangular plates or non-constant gap functions. Assuming non-rectangular plate affects the formulation of the NBM approximation of contact forces (5.20) and, consequentially, the formulation of the matrix $\mathbf{N}^c$ in the LCP solution (5.26). Thus, it is of primary importance to verify that the resulting $\mathbf{N}^c$ for curved boundary conditions is a P-matrix to guarantee a unique solution exists for the NBM-LCP (5.25). For non-constant gap functions, the Signorini complementarity conditions involve a more intricate Signorini problem as both the normal $\mathbf{n}$ in the NBM approximation of contact forces (5.20) and the gap function in the Signorini problem (5.13) must involve restrictions on both x_1 and x_2 axes [96, p. 126]. Thus, the NBM must produce a $\mathbf{N}^c$ that is a P-matrix for any possible configuration. In this case, one cannot resort to numerically verify every possible $\mathbf{N}^c$ for any possible normal to the rigid boundary $\mathbf{n}$. Thus, a more generic proof of $\mathbf{N}^c$ being a P-matrix for any possible $\mathbf{n}$ is necessary for this case.

Also, the formulation has been tested for rectangular elements only but is general to any type of elements as long as the choice of shape functions permits an approximation of a non-zero contact force (5.21). A similar notion is explored in the 1D-NBM in Section 4.3.6. It is also worth noting that the 2D-NBM approximation categorically requires that the NBM-LCP Equation (5.23) always admits a unique solution $\mathbf{u}^c(t)$ for any $\mathbf{u}^o(t)$. The uniqueness and existence of solutions to Equation (5.23) depends on the type and number of shape functions.

In all examples, the uniqueness of LCP solutions was affirmed by verifying numerically that $\mathbf{N}^c$ is a P-matrix, see Section 5.3.1. However, a general proof of uniqueness and existence of solution to the NBM-LCP 5.23 for any type of finite elements is not yet developed.

At last, the current NBM approximation is not limited to the two-dimensional case only but may apply to three-dimensional settings as well. The uniqueness and existence of the NBM-LCP 5.23 solutions must be affirmed for this case.

We note that application of NBM on problems involving tangential forces (such as friction [96]) is currently under question and the proposed NBM approach applies only on the normal direction of contact forces. The linear complementarity problem resulting from the NBM implementation of the Signorini conditions with friction is more intricate and sets additional restrictions on the choice of shape functions. Specifically, the Signorini complementarity problem (5.13) will involve also a complementarity condition on the velocity of contact nodes, normal forces and tangential forces at the contact boundary [96, Eq. 4.45]. for the application of NBM, the tangential forces must be approximated using the FEM formulations such that they result as functions of the nodal displacement (similar to the treatment of contact pressures in Equation (5.29)). While it is possible to approach this problem using NBM, it is unknown whether the NBM will result in admissible solutions for the friction problem. Thus, application of NBM to problems involving friction or tangential forces remains in question and necessitates a thorough examination.

5.9 Discussion

Nonsmooth modal analysis of two-dimensional structures requires (1) accurate simulation of the motion prone to unilateral contact, (2) ability to depict periodic solutions of the investigated system, and (3) continuation of periodic solutions for the detection of families of periodic solutions. The 2D-NBM with HBM and SCC have been proposed for numerical nonsmooth modal analysis and to answer these challenges.

While there exist numerous approaches for the simulation of two-dimensional structures in unilateral contact, most do not admit accurate solutions for low grid models. Current numerical schemes either allow penetration, exhibit numerical chattering or suffer from dissipation of energy, and thus do not allow for the detection of periodic solutions. The 1D-NBM has been proposed in Chapter 4 to remedy those issues for one-dimensional problems, and its formulation is extended in this chapter to two-dimensional structure. Compared to existing methods, the 2D-NBM features favourable properties such as continuous active contact phases and non-penetration of the obstacle at any grid. The NBM is derived by applying the Signorini conditions on the contact nodes in a strong sense. Thus, motion of nodes in the contact boundary is restricted such that the conditions of active and inactive contact are enforced exactly by the NBM approximation of the displacement. In turn, similarly to the 1D-NBM, the displacement of nodal quantities on the contact boundary is dictated solely by the Signorini complementarity conditions and displacement of internal nodes. As a result, the contact nodes do not participate in the NBM-ODE. The NBM-ODE admits a set of nonsmooth ODEs with coefficients that depend on the contact configuration of the structure. In comparison to the 1D-NBM where the contact problem is solved by switching between two distinct ODEs (describing either active or inactive contact phases), in the 2D-NBM, there exist 2^{N_C} possible distinct ODEs to describe each contact configuration. A switching algorithm which allows choosing the appropriate ODEs among all possible 2^{N_C} distinct ODEs is developed for the 2D-NBM. The switching algorithm consists of an LCP solver which determines the current contact configuration and of linear matrix operations to determine proper mass and stiffness matrix to be used in the contact configuration.

The 2D-NBM is used to generate periodic solutions for nonsmooth modal analysis. To demonstrate the validity of the proposed 2D-NBM scheme, its solution of the Signorini problem involving the plate in unilateral contact is compared to other FEM schemes. The results of these comparisons show that the NBM successfully exhibits non-penetration and continuous active contact phases. Furthermore, the results suggest that the 2D-NBM exhibits less spurious oscillations than existing methods. Most importantly, the 2D-NBM allows for a regain of energy throughout the motion and, thus, for the detection of periodic solutions with sticking phases and no-penetration. Also, a convergence analysis of the 2D-NBM with respect to other FE schemes showed that, for a

fixed number of contact nodes, all schemes converge to the same solution. This convergence test also confirms the validity of the 2D-NBM solution to Signorini problem.

The HBM is applied to the 2D-NBM for the detection of periodic solutions. Specifically, it is shown that the HBM converges for increasing number of harmonics and successfully determines an accurate periodic solution of 2D-NBM-ODE. Nonsmooth modal analysis is then preformed by applying HBM with sequential continuation on the 2D-NBM-ODE. Nonsmooth modes were successfully determined and two modes are demonstrated in this manuscript: a NSM excited by longitudinal force (Longitudinal NSM) and a NSM excited by transverse force (Transverse NSM). Both NSMs were found to be in close proximity to resonance peaks in the corresponding force-response diagrams. Also, both NSMs showed a hardening behaviour of the backbone curve.

Analysis of the participation of linear modes in the detected NSMs allowed for better understanding of the motions within the NSM. For example, it was shown that the longitudinal NSM mostly consists of linear longitudinal modes. Meanwhile, the transverse NSM demonstrate strong participation of both transverse and longitudinal modes due to contact forces applied on the structure (the contact force applies in the longitudinal direction). Furthermore, selected NSM motions are compared to the linear mode with the dominant contribution. The comparison showed that NSM motions have similar amplitudes during inactive contact phases, and the linear mode and generally follow a similar trajectory to the dominant participating linear mode. However, the contribution of other modes in the motion are non-negligible and can be seen in the time evolution which differs significantly between NSM motions the linear mode.

Although it was yet attempted, the presented formulation of the 2D-NBN is generic enough to readily extend to research avenues including arbitrarily shaped-boundaries and three spatial dimensions.

Supplementary Material

Excerpts of scripts and algorithms used to perform the analysis and generate figures in this chapter are available on Zenodo [88].

Chapter 6

Conclusion

6.1 Summary of thesis

This thesis is focused on nonsmooth modal analysis of structures prone to unilateral contact and the Signorini complementarity conditions are used to describe the unilateral contact conditions. In the field of mechanical engineering, applications involving vibrations and unilateral contact are common. Nevertheless, the nonsmooth modal analysis of such structures is an academically challenging topic, and the methodologies for nonsmooth modal analysis in literature are not readily applicable.

Since closed-form solutions are not generally available for the Signorini problem, numerical approaches must be used for the nonsmooth modal analysis. While linear modal analysis relies on the superposition principle to derive the natural frequencies and modes of vibration, these cannot be derived for nonsmooth systems where the principle fails.

Nonsmooth modes are families of periodic solutions to the autonomous structure and constitute an extension of the notion of linear modes of vibration to nonsmooth systems. Like linear modes, detection of resonance frequencies and behaviours in the forced system are possible. In this thesis, the detection of nonsmooth modes requires the accurate simulation of contact mechanics, detection of periodic solutions, continuation of nonsmooth modes.

The work in this thesis focused on two different approaches for nonsmooth modal analysis: (1) analytical nonsmooth modal analysis via d'Alembert functions and (2) numerical nonsmooth modal analysis of the one-dimensional bar and the two-dimensional plate.

An elaborate introduction to the nonsmooth modal analysis and the current state of numerical methods for nonsmooth modal analysis of structures prone to unilateral contact is given in Chapter 2.

In Chapter 3, the analytical study of the nonsmooth modal space of the internally resonant bar takes place. The motivation behind analytical modal analysis of the bar was to understand the difficulties in nonsmooth modal analysis given a closed-form solution. Specifically, the accurate simulation of contact mechanics is obtained by application of the method of steps on the d'Alembert

traveling-wave solution of the bar. In this approach, the conditions for periodic solutions are formed based on d'Alembert solution. This constitutes a set of linear functional equations (the CPS), of which the solutions are families of periodic solutions (i.e., NSMs). It is shown that the previously defined piecewise-linear modes of the bar constitutes a part of a larger solution space to the CPS and new nonsmooth modes were derived using the CPS. Particularly, piecewise-smooth modes that are iso-periodic and exist in a dense set of periods and a set of nonsmooth modes of the same frequency and energy were exhibited. Furthermore, it was shown that such nonsmooth modal spaces cannot be readily discovered by existing numerical methods. Specifically, the widely used pseudo-arclength continuation method is not readily applicable to the dense space of periodic solution families which includes infinitely many branching points since the notion of a tangent to the curve does not exist. Thus, in the numerical modal analysis section of this thesis, alternative continuation methods were considered such as sequential continuation with correction (SCC). The SCC, presented in Chapter 4, relies on the fact that, for low order approximations, the nonsmooth modal space does not include as many branching points as higher order approximations. Consequently, continuation methods can be applied for low order approximations to determine low order NSMs. Then, corrections to the low order periodic solutions within the NSM are obtained by increasing the order of approximation while fixing either the frequency or energy of the solution.

The larger portion of this thesis focuses on numerical modal analysis of structures prone to unilateral contact. In current literature, such methods are limited to a narrow set of models. For example, the WFEM and TD-BEM were proven successful for nonsmooth modal analysis of the bar with constant cross-sectional area. However, extension to other models such the varying-area bar or two-dimensional plate failed due to significant dissipation of energy through time in the developed schemes. One objective of this is thesis is primarily to conceive a numerical scheme for nonsmooth modal analysis of multi-dimensional structures. To this end, a new numerical treatment of the Signorini boundary conditions, the nodal boundary method, was introduced. The suggested method treats the Signorini conditions in the framework of finite elements. Existing treatments of the Signorini conditions suffer from numerical deficiencies such as: dissipation of energy, non-physical chattering, or penetration of the rigid obstacle. These deficiencies prevent the detection of periodic solutions. The NBM is developed for purposes of nonsmooth modal analysis and resolves the deficiencies in existing FE schemes. It can find periodic motions with continuous contact phases (sticking phases). Using the NBM, nonsmooth modal analysis of both the varying area bar and the two-dimensional plate in unilateral contact were performed.

In Chapter 4, the 1D-NBM is developed in the context of the bar prone to unilateral contact. It considers separate approximations (separate families of shape functions) to treat the inactive contact conditions (boundary conditions describing the structure away from rigid obstacle) and active contact boundary conditions (describing the boundary when contact with rigid obstacle

is imposed). The discretized PDE is solved by switching between these sets of shape functions where the switching procedure is responsible for detection of contact. In sum, the nodal boundary method culminates in a nonsmooth ODE where only the nodes internal to the considered system participate. The nonsmooth modes are successfully detected using the SCC and shooting method for the internally resonant bar, the bar with soft support and the varying area bar. For all models, the nonsmooth modes aligned closely with resonance peaks in the forced response. As well, the internally resonant bar and the bar with soft support featured periodic solutions that were previously obtained using WFEM and TD-BEM.

In Chapter 5, the 2D-NBM is developed in the context of a plate prone to unilateral contact. The 2D-NBM relies on similar principles as that of 1D-NBM: implementation of Signorini conditions in a strong manner and exclusion of contact nodes by switching between different ODE systems describing different contact conditions. However, the NBM implementation on multidimensional structures presents another challenge: switching between more than two systems of ODEs. Thus, while the 1D-NBM required switching between two ODEs describing distinct contact phases, the switching in the 2D-NBM requires depiction of an ODE out of 2_C^N potential ODEs describing different contact configurations. The switching mechanism in the 2D-NBM is implemented using root solving algorithms. A dedicated switching procedure is developed to both obtain the displacement of contact nodes based on internal nodes (i.e., solution of the Signorini problem for a given instance in time), and formulation of the corresponding ODE for the contact configuration. Comparison of the 2D-NBM to other FE based schemes shows that the 2D-NBM exhibits favourable properties such as: elimination of chattering and low spurious oscillations. Also, the 2D-NBM was shown to converge to motions generated by other schemes for a high enough number of internal nodes.

Periodic solutions in the 2D-NBM were detected using the HBM since shooting method proved to be too expensive. Besides the 2D-NBM being able to generate solutions via time-marching techniques, it can also accommodate spectral methods such as the HBM. The resulting 2D-NBM-HBM solution is used to detect NSMs of the plate via the SCC. Two NSMs are explored in this thesis: Longitudinal NSM and Transverse NSM. Both NSMs are found in proximity to the resonance peaks of forced response.

6.2 Possible future avenues

6.2.1 Exact nonsmooth modal analysis using d'Alembert functions

The methodology for exact nonsmooth modal analysis presented in Chapter 3 relies on the d'Alembert solution described in Equation (3.8) to the wave equation and the method of steps. While the d'Alembert solution describes the motion of the bar for either homogeneous Neumann conditions

or non-homogeneous Dirichlet conditions (which are the inactive and active phases of contact, respectively), the switching mechanism is implemented using the method of steps. While the methodology was not developed for other configurations of the bar, it may be possible to apply it on the bar with soft-support (i.e., Robin condition on that non-contacting end) or the two colliding bars [51] since both enjoy the existence of d'Alembert function. However, the described methodology does not apply to the bar of varying area or the two-dimensional case where the d'Alembert solution does not apply. Moreover, the methodology used for exact nonsmooth modal analysis is not limited to 1CPP and may extend to include more contact phases per period. In fact, experiments done for more contact phases per period show that the strategy for finding iso-periodic nonsmooth modes (described in Section 3.3.2) also works for kCPP solutions. These experiments were not shown in this thesis for sake of conciseness.

The results brought forward in this context also present avenues for future research. For example, it is revealed that the nonsmooth modal space of the bar is dense and infinitely many NSMs exist within a short span of frequencies. It is of interest to determine how the density of the modal space affects the forced-response of the internally resonant bar. While it is known that the NSMs correspond to resonance behaviour of the structure, it is not known how the existence of dense iso-periodic solutions of the type in NSM3 or NSM2, which include multiple periodic solutions at given frequency-energy points, relate to a resonant behaviour. Stability analysis of the discovered NSMs is also of interest as it can give further knowledge on the motions of the bar prone to unilateral contact.

Another interesting direction for future research using the methodology presented here is in the reduction of the density of the modal space by depicting solutions of specific types. The density of the modal space, as noted in [51, 97], does not allow to outline trends in behaviours in the modal space. For example, restriction of the CPS to synchronous motions of the type discussed by Rosenberg [70] may be beneficial in outlining specific behaviours in the modal space.

6.2.2 Nodal boundary method

It is noted that the scope and limitations of NBM are discussed in depth in Sections 4.6 and 5.8. However, it is important to add that the 1D-NBM can be applied for contact problems involving the one-dimensional bar with varying Young's modulus E, density ρ, or area A and with any boundary conditions on the non-contacting ends (so long that these can be implemented via classical finite-element). Furthermore, application to contact problems involving a moving wall or collision between two bars is also possible with 1D-NBM. In turn, the 2D-NBM formulation in Chapter 5 can be readily applied for contact problems involving the plate with different boundary conditions on the non-contacting boundaries and varying density or shape or varying shape of plate, given

that the gap distance remains constant. Currently, the 2D-NBM applies to a variety of useful cases and may be applied to practical applications such as one/two-dimensional simplifications of blade-casing contact [9] or drills [62]. However, it is of interest to determine whether the application of NBM easily extends to three-dimensions or other governing equations (such as the beams or shell structures) and thus extend the usage of NBM to any practical application. At last, the 2D-NBM scheme suffers from long computation times due to semismooth-Newton method called for both solution of the NBM-LCP in Section 5.3.1 and solution of the CN time-step [43]. The 2D-NBM may be improved by assuming other time-marching schemes for LCP solution schemes. An analysis of the performance of the 2D-NBM for different numerical scheme may lead less computationally intensive technique and, thus, improvement of nonsmooth modal analysis capabilities with the NBM.

6.2.3 Numerical nonsmooth modal analysis

The dense modal space discovered in Chapter 3 has significant implications on the implementation of numerical nonsmooth modal analysis techniques. Specifically, the general solution space does not allow for simple implementation of continuation methods [51,97]. However, in the numerical analysis portion of this thesis exposed in Chapters 4 and 5, it was revealed that low order approximations allow for simple application of sequential continuation culminating in the formulation of SCC in Section 4.4.3. Although the SCC is based on sequential continuation, application of pseudo-arclength on low order approximation may be possible as well since the detected NSMs did not exhibit any disturbances or branching points for low order approximation. Another possible continuation method is the asymptotic numerical method (ANM) [21] which allows detection of large sections of the backbone curve via a quadratic approximation in the arclength parameter of the solution curve. Implementation of this methodology to the continuation problem in the NBM faces two issues: (1) the solution space involves many branching points, and a quadratic approximation may not be successful in detecting (2) the set of equations is non-smooth and thus a quadratic form of the approximation is not readily obtained (although probable given some regularization of the discontinuous NBM-ODE). Although, it was shown in [51,84] that the backbone curve for a discrete approximation of the bar equation involves a piecewise-differentiable backbone curve. Thus, it may be possible to apply ANM (or pseudo-arclength continuation) on differentiable portions of the backbone curve and thus discover the space of solutions via detection of separate branches.

However, it is also worth to investigate alternatives to continuation methods. For example, the simplex method [54] is a non-gradient optimization method and may be able to discover more than multiple periodic solutions. Although the continuation problem is generally formulated as a root-solving problem rather than an optimization problem, it can be formulated as an optimization problem by minimizing the norm of the participating functions in the root-solving problem. Because

it does not rely on gradients, the simplex method is a good candidate for determining periodic solution in a dense modal space.

The NBM formulation allows for usage both the HBM, used in 2D-NBM, and shooting method, used in 1D-NBM, for detection of periodic solutions. Although the shooting method may theoretically apply to both the one dimensional and two-dimensional cases, it was noticed, through numerical experiments, that the HBM may determine a periodic solution for a larger space of initial guesses than the shooting method. Specifically, the HBM, in the SCC approach, resulted in a more efficient computational algorithm than the shooting method (which took a significantly higher number of iterations to find a solution). Nevertheless, it is important to note that the shooting method relies on the accuracy of the ODE solver to determine a periodic solution whilst the HBM requires the usage of many shape functions to approximate the ODE solution appropriately. Moreover, the HBM utilizes smooth functions to describe the ODE solution (which is non-smooth and only once differentiable). Although, from a practical standpoint, as the number of degrees-of-freedom increases, the HBM has reached a sufficiently accurate solution in a feasible computation time (number of iterations).

Furthermore, it is noted that the phase condition chosen requires all velocities to reach a zero point. It is possible that by choosing this phase condition other solutions are neglected. Therefore, it may be beneficial to consider other phase conditions such as the one presented in Section 3.1.1 or Poincaré orthogonality condition [13, p. 156].

It is important to remind the convergence of FEM schemes for a fixed number of nodes in Section 5.5.2. In this convergence test, it was shown the various FEM treatments of the Signorini problem applied for a fixed number of contact nodes converge to the same solution. It is of interest to examine whether the convergence of different schemes for a fixed number of contact nodes can be generalized to any FE model. If proven true, this conjecture could point to a unique solution to the Signorini problem in FE. A unique solution of the Signorini problem for a fixed number of contact nodes would allow to perform a convergence analysis with respect to the number of contact nodes. Since the number of contact nodes affects directly the size of the grid (and in turn, the computational effort necessary), this would allow for better estimation of the necessary computational effort in reaching a suitable approximation of the solution to the Signorini problem.

6.3 List of publications

The following publications resulted from this dissertation:

1. D. Urman and M. Legrand. Nonlinear modal analysis of the bar in unilateral contact via analytical weak-solutions to the wave equation. *27th Canadian Congress of Applied Mechanics*. Sherbrooke, Canada, 2019.
2. D. Urman and M. Legrand. Nodal-boundary finite-element method for periodic solutions of

Signorini problems. *XI International Conference on Structural Dynamics*. Athens, Greece, 2020.

3. D. Urman and M. Legrand. Nodal-boundary finite-element method for the Signorini problem in two dimensions. *ASME 2021 International Design Engineering Technical Conferences & Computers and Information in Engineering Conference*. Online, 2021.
4. D. Urman, M. Legrand, and S. Junca. D'Alembert function for exact non-smooth modal analysis of the bar in unilateral contact. *Nonlinear Analysis: Hybrid Systems*, 43, 2021. doi:10.1016/j.nahs.2021.101115.
5. D. Urman and M. Legrand. Nonsmooth modal analysis of a rectangular plate in unilateral contact. *10th European Nonlinear Dynamics Conference*. Lyon, France, 2022.
6. D. Urman and M. Legrand. Nonsmooth modal analysis of a varying cross-sectional area bar in unilateral contact. *Journal of Sound and Vibration*, 2022. doi:10.1016/j.jsv.2022.117385.

Bibliography

[1] V. Acary, O. Bonnefon, M. Brémond, O. Huber, F. Pérignon, and S. Sinclair. An introduction to Siconos. Technical Report RT-0340, INRIA, 2019. oai:inria-00162911.

[2] V. Acary and B. Brogliato. Time-stepping schemes for systems with AC solutions. In *Numerical Methods for Nonsmooth Dynamical Systems: Applications in Mechanics and Electronics*, chapter 9, pages 243–284. Springer, 2008. doi:10.1007/978-3-540-75392-6_9.

[3] J. M. Aitchison and M. W. Poole. A numerical algorithm for the solution of Signorini problems. *Journal of Computational and Applied Mathematics*, 94(1):55–67, 1998. doi:10.1016/S0377-0427(98)00030-2.

[4] E. L. Allgower and K. Georg. *Numerical Continuation Methods: an Introduction*, volume 13. Springer, 2012. doi:10.1007/978-3-642-61257-2.

[5] B. Alzubaidi and R. K. Németh. Modal analysis-based calculation of periodic nonlinear responses of harmonically forced piecewise linear elastic systems. *Journal of Sound and Vibration*, 549:117576, 2023. doi:10.1016/j.jsv.2023.117576.

[6] R. Arquier, S. Bellizzi, R. Bouc, and B. Cochelin. Two methods for the computation of nonlinear modes of vibrating systems at large amplitudes. *Computers & Structures*, 84(24):1565–1576, 2006. oai:hal-01580935. doi:10.1016/j.compstruc.2006.01.011.

[7] M. Attar, A. Karrech, and K. Regenauer-Lieb. Non-linear modal analysis of structural components subjected to unilateral constraints. *Journal of Sound and Vibration*, 389:380–410, 2017. oai:hal-01513216. doi:10.1016/j.jsv.2016.11.012.

[8] M. Attar, A. Karrech, and K. Regenauer-Lieb. Non-linear modal analysis of structural components subjected to unilateral constraints. *Journal of Sound and Vibration*, 389(17):380–410, 2017. oai:hal-01513216. doi:10.1016/j.jsv.2016.11.012.

[9] A. Batailly, M. Legrand, and C. Pierre. Full three-dimensional rotor/stator interaction simulations in aircraft engines with time-dependent angular speed. *Journal of Engineering for Gas Turbines and Power*, 139(3):031202, 2017. doi:10.1115/1.4034503.

[10] J. Y. Bello Cruz, O. P. Ferreira, S. Z. Németh, and L. F. Prudente. A semi-smooth newton method for projection equations and linear complementarity problems with respect to the second order cone. *Linear Algebra and its Applications*, 513:160–181, 2017. doi:10.1016/j.laa.2016.10.007.

[11] A. Berman and R. J. Plemmons. The linear complementarity problem. In *Nonnegative Matrices in the Mathematical Sciences*, chapter 10, pages 270–297. Academic Press, 1979. doi:10.1016/

B978-0-12-092250-5.50017-5.

[12] C. Bertrand. Periodic solutions of a one-dimensional elastic bar subject to a unilateral constraint. Technical report, ENTPE, 2020. oai:hal-02897846.

[13] W.-J. Beyn, A. Champneys, E. Doedel, W. Govaerts, Y. A. Kuznetsov, and B. Sandstede. Numerical continuation, and computation of normal forms. In *Handbook of Dynamical Systems*, volume 2 of *Handbook of Dynamical Systems*, chapter 4, pages 149–219. Elsevier, 2002. doi:10.1016/S1874-575X(02)80025-X.

[14] J. P. Boyd. *Chebyshev and Fourier spectral methods*, volume 49. Springer, 2001.

[15] T. Breunung and G. Haller. When does a periodic response exist in a periodically forced multi-degree-of-freedom mechanical system? *Nonlinear Dynamics*, 98:1761–1780, 2019. doi:10.1007/s11071-019-05284-z.

[16] B. Brogliato. *Nonsmooth Mechanics: Models, Dynamics and Control*, volume 2. Springer, 1999. doi:10.1007/978-1-4471-0557-2.

[17] D. Cartwright and D. E. Beskos. Underlying Principles of the Boundary Element Method. *Applied Mechanics Reviews*, 55(2):B25–B26, 2002. doi:10.1115/1.1451159.

[18] Z. Chen and L. Qi. A semismooth Newton method for tensor eigenvalue complementarity problem. *Computational Optimization and Applications*, 65(1):109–126, 2016. doi:10.1007/s10589-016-9838-9.

[19] F. Chouly, M. Fabre, P. Hild, R. Mlika, J. Pousin, and Y. Renard. An overview of recent results on Nitsche's method for contact problems. In *Geometrically Unfitted Finite Element Methods and Applications*, pages 93–141. Springer, 2017. oai:hal-01403003. doi:10.1007/978-3-319-71431-8_4.

[20] F. Chouly and Y. Renard. Explicit Verlet time-integration for a Nitsche-based approximation of elastodynamic contact problems. *Advanced Modeling and Simulation in Engineering Sciences*, 5(31), 2018. doi:10.1186/s40323-018-0124-5.

[21] B. Cochelin, N. Damil, and M. Potier-Ferry. The asymptotic-numerical method: an efficient perturbation technique for nonlinear structural mechanics. *Revue Européenne des Éléments Finis*, 3(2):281–297, 1994. doi:10.1080/12506559.1994.10511124.

[22] B. Cockburn, S. Hou, and C.-W. Shu. The Runge-Kutta local projection discontinuous Galerkin finite element method for conservation laws. IV. the multidimensional case. *Mathematics of Computation*, 54:545–581, 1990. doi:10.2307/2008501.

[23] L. Dieci, C. Elia, and L. Lopez. On filippov solutions of discontinuous daes of index 1. *Communications in Nonlinear Science and Numerical Simulation*, 95:105656, 2021. doi:10.1016/j.cnsns.2020.105656.

[24] D. Doyen, A. Ern, and S. Piperno. Time-integration schemes for the finite element dynamic Signorini problem. *SIAM Journal on Scientific Computing*, 33(1):223–249, 2011. oai:hal-00440128. doi:10.1137/100791440.

[25] T. Erneux. *Applied Delay Differential Equations*. Springer, 2009. doi:10.1007/978-0-387-74372-1.

[26] L. C. Evans. *Partial Differential Equations*. American Mathematical Society, 2010.

[27] F. Facchinei, A. Fisher, and M. Herrich. A family of Newton methods for nonsmooth constrained systems with nonisolated solutions. *Mathematical Methods of Operations Research*, 77:433–443, 2013. doi:10.1007/s00186-012-0419-0.

[28] A. Fischer. A Newton-type method for positive-semidefinite linear complementarity problems. *Journal of Optimization Theory and Applications*, 86:585–608, 1995. doi:10.1007/BF02192160.

[29] F. Georgiades, M. Peeters, G. Kerschen, J.-C. Golinval, and M. Ruzzene. Modal analysis of a nonlinear periodic structure with cyclic symmetry. *AIAA Journal*, 47:1014–1025, 2009. oai:hal-01385735. doi:10.2514/1.40461.

[30] G. Gilardi and I. Sharf. Literature survey of contact dynamics modelling. *Mechanism and Machine Theory*, 37(10):1213–1239, 2002. doi:10.1016/S0094-114X(02)00045-9.

[31] C. Hager, S. Hüeber, and B. I. Wohlmuth. A stable energy-conserving approach for frictional contact problems based on quadrature formulas. *International Journal for Numerical Methods in Engineering*, 73(2):205–225, 2008. doi:10.1002/nme.2069.

[32] C. Hager and B. I. Wohlmuth. Analysis of a space-time discretization for dynamic elasticity problems based on mass-free surface elements. *SIAM Journal on Numerical Analysis*, 47(3):1863–1885, 2009. oai:hal-03349902. doi:10.1137/080715627.

[33] J. S. Hesthaven and T. Warburton. *Nodal Discontinuous Galerkin Methods: Algorithms, Analysis, and Applications*. Springer, 2007. doi:10.1007/978-0-387-72067-8.

[34] T. J. R. Hughes. *Finite Element Method - Linear Static and Dynamic Finite Element Analysis*. Dover Publications, 2000.

[35] G. James, V. Acary, and F. Pérignon. Periodic motions of coupled impact oscillators. In *Advanced Topics in Nonsmooth Dynamics: Transactions of the European Network for Nonsmooth Dynamics*, pages 93–134. Springer, 2018. oai:hal-01660891. doi:10.1007/978-3-319-75972-2_3.

[36] Z. Ji, H. Shi, G. Li, and H. Song. Improved drifting oscillator model for dynamical bit-rock interaction in percussive drilling under high-temperature condition. *Journal of Petroleum Science and Engineering*, 186:106772, 2020. doi:10.1016/j.petrol.2019.106772.

[37] C. Joannin, B. Chouvion, F. Thouverez, J.-P. Ousty, and M. Mbaye. A nonlinear component mode synthesis method for the computation of steady-state vibrations in non-conservative systems. *Mechanical Systems and Signal Processing*, 83:75–92, 2017. doi:10.1016/j.ymssp.2016.05.044.

[38] G. Kerschen. Definition and fundamental properties of nonlinear normal modes. In G. Kerschen, editor, *Modal Analysis of Nonlinear Mechanical Systems*, volume 555, pages 1–46. Springer, 2014. doi:10.1007/978-3-7091-1791-0_1.

[39] G. Kerschen, M. Peeters, J.-C. Golinval, and A. Vakakis. Nonlinear normal modes, part I: A useful framework for the structural dynamicist. *Mechanical Systems and Signal Processing*, 23(1):170–194, 2009. oai:hal-01357931. doi:10.1016/j.ymssp.2008.04.002.

[40] H. B. Khenous, P. Laborde, and Y. Renard. Mass redistribution method for finite element contact problems in elastodynamics. *European Journal of Mechanics-A/Solids*, 27(5):918–932, 2008. oai:

hal-00582045. doi:10.1016/j.euromechsol.2008.01.001.

[41] W.-J. Kim and N.C. Perkins. Harmonic balance/galerkin method for non-smooth dynamic systems. *Journal of Sound and Vibration*, 261(2):213–224, 2003. oai:hal-01693093. doi:10.1016/S0022-460X(02)00949-5.

[42] M. Krack and J. Gross. *Harmonic Balance for Nonlinear Vibration Problems*. Springer, 2019. doi:10.1007/978-3-030-14023-6.

[43] S. Krenk. Energy conservation in Newmark based time integration algorithms. *Computer Methods in Applied Mechanics and Engineering*, 195(44):6110–6124, 2006. doi:10.1016/j.cma.2005.12.001.

[44] V. A. Krys'ko, J. Awrejcewicz, and G. G. Narkaitis. Nonlinear vibration and characteristics of flexible plate-strips with non-symmetric boundary conditions. *Communications in Nonlinear Science and Numerical Simulation*, 11(1):95–124, 2006. doi:10.1016/j.cnsns.2003.11.002.

[45] R.J. Kuether, L. Renson, T. Detroux, C. Grappasonni, G. Kerschen, and M.S. Allen. Nonlinear normal modes, modal interactions and isolated resonance curves. *Journal of Sound and Vibration*, 351:299–310, 2015. doi:10.1016/j.jsv.2015.04.035.

[46] G. Lebeau and M. Schatzman. A wave problem in a half-space with a unilateral constraint at the boundary. *Journal of Differential Equations*, 53(3):309–361, 1984. oai:hal-01294216. doi:10.1016/0022-0396(84)90030-5.

[47] C. H. Lee, A. J. Gil, and J. Bonet. Development of a cell centred upwind finite volume algorithm for a new conservation law formulation in structural dynamics. *Computers & Structures*, 118:13–38, 2013. doi:10.1016/j.compstruc.2012.12.008.

[48] M. Legrand, S. Junca, and S. Heng. Nonsmooth modal analysis of a N-degree-of-freedom system undergoing a purely elastic impact law. *Communications in Nonlinear Science and Numerical Simulation*, 45:190–219, 2017. oai:hal-01185980. doi:10.1016/j.cnsns.2016.08.022.

[49] R. J. LeVeque et al. *Finite volume methods for hyperbolic problems*, volume 31. Cambridge University Press, 2002.

[50] T. Lu and M. Legrand. Nonsmooth modal analysis with boundary element method. In *XI International Conference on Structural Dynamics*, pages 205–212, Athènes, Greece, 2020. oai:hal-03136267. doi:10.47964/1120.9016.19060.

[51] T. Lu and M. Legrand. Nonsmooth modal analysis via the boundary element method for one-dimensional bar systems. *Nonlinear Dynamics*, page 227–246, 2021. oai:hal-03206114. doi:10.1007/s11071-021-06994-z.

[52] M. Lukáčová-Medvid'ová, K. Morton, and G. Warnecke. Evolution galerkin methods for hyperbolic systems in two space dimensions. *Mathematics of Computation of the American Mathematical Society*, 69(232):1355–1384, 2000. doi:10.1090/S0025-5718-00-01228-X.

[53] O. L. Mangasarian and T.-H. Shiau. Lipschitz continuity of solutions of linear inequalities, programs and complementarity problems. *SIAM Journal on Control and Optimization*, 25(3):583–595, 1987. doi:10.1137/0325033.

[54] S. Z. Martínez, A. A. Montaño, and C. A. C. Coello. A nonlinear simplex search approach for

multi-objective optimization. In *2011 IEEE Congress of Evolutionary Computation (CEC)*, pages 2367–2374, 2011. doi:10.1109/CEC.2011.5949910.

[55] MATLAB. *version 9.10.0.1602886 (R2021a)*. The MathWorks Inc., Natick, Massachusetts, 2021.

[56] Y. Mirbagheri, H. Nahvi, J. Parvizian, and A. Düster. Reducing spurious oscillations in discontinuous wave propagation simulation using high-order finite elements. *Computers & Mathematics with Applications*, 70(7):1640–1658, 2015. doi:10.1016/j.camwa.2015.06.022.

[57] Z. Moche. Two-spatial dimensional elastic wave propagation by the theory of characteristics. *International Journal of Solids and Structures*, 5(10):1135–1151, 1969. doi:10.1016/0020-7683(69)90008-0.

[58] Y. Modarres-Sadeghi and M. P. Païdoussis. Nonlinear dynamics of extensible fluid-conveying pipes, supported at both ends. *Journal of Fluids and Structures*, 25(3):535–543, 2009. doi:10.1016/j.jfluidstructs.2008.09.005.

[59] J. J. Moré. The Levenberg-Marquardt algorithm: Implementation and theory. In *Numerical Analysis*, pages 105–116. Springer, 1978. doi:10.1007/BFb0067700.

[60] E. H. Moussi, S. Bellizzi, B. Cochelin, and I. Nistor. Nonlinear normal modes of a two degrees-of-freedom piecewise linear system. *Mechanical Systems and Signal Processing*, 64-65:266–281, 2015. oai:hal-00783088. doi:10.1016/j.ymssp.2015.03.017.

[61] M. P. Paidoussis. Pipes conveying fluid: Nonlinear and chaotic dynamics. In M. P. Païdoussis, editor, *Slender Structures and Axial Flow*, volume 1 of *Fluid-Structure Interactions*, chapter 5, pages 277–414. Academic Press, 1998. doi:10.1016/S1874-5652(98)80007-0.

[62] E. Pavlovskaia, D. C. Hendry, and M. Wiercigroch. Modelling of high frequency vibro-impact drilling. *International Journal of Mechanical Sciences*, 91:110–119, 2015. doi:10.1016/j.ijmecsci.2013.08.009.

[63] M. P. Païdoussis and G.X. Li. Cross-flow-induced chaotic vibrations of heat-exchanger tubes impacting on loose supports. *Journal of Sound and Vibration*, 152(2):305–326, 1992. doi:10.1016/0022-460X(92)90363-3.

[64] M. Peeters, R. Viguié, G. Sérandour, G. Kerschen, and J.-C. Golinval. Nonlinear normal modes, part II: Toward a practical computation using numerical continuation techniques. *Mechanical Systems and Signal Processing*, 23(1):195–216, 2009. oai:hal-01581480. doi:10.1016/j.ymssp.2008.04.003.

[65] S. Peter, F. Schreyer, and R. I. Leine. A method for numerical and experimental nonlinear modal analysis of nonsmooth systems. *Mechanical Systems and Signal Processing*, 120:793–807, 2019. doi:10.1016/j.ymssp.2018.11.009.

[66] M. J. D. Powell. A FORTRAN subroutine for solving systems of non-linear algebraic equations. Technical report, Theoretical Physics Division, Atomic Energy Research Establishement, 1968.

[67] D. L. Powers. *Boundary Value Problems and Partial Differential Equations*. Academic Press, 1972.

[68] G. Rawitscher, V. dos Santos Filho, and T. C. Peixoto. *Galerkin and Collocation Methods*, pages 17–31. Springer, 2018. doi:10.1007/978-3-319-42703-4_3.

[69] P. Ribeiro. Non-linear forced vibrations of thin/thick beams and plates by the finite element and shooting

methods. *Computers & Structures*, 82(17):1413–1423, 2004. Computational Mechanics in Portugal. doi:10.1016/j.compstruc.2004.03.037.

[70] R. M. Rosenberg. The normal modes of nonlinear n-degree-of-freedom systems. *Journal of Applied Mechanics*, 29:7–14, 1962. oai:hal-01344457.

[71] S. Samukham, S. N. Khaderi, and C. P. Vyasarayani. Galerkin–Ivanov transformation for nonsmooth modeling of vibro-impacts in continuous structures. *Journal of Vibration and Control*, 27(13-14):1548–1560, 2021. doi:10.1177/1077546320945441.

[72] A. Saood, A. K. Zain, T. P. Mohd, and H. K. Arshad. On the large amplitude forced vibration analysis of composite sectorial plates. *Journal of Composites Science*, 5(3):83, 2021. doi:10.3390/jcs5030083.

[73] M. Schatzman and M. Bercovier. Numerical approximation of a wave equation with unilateral constraints. *Mathematics of Computation*, 53(187):55–79, 1989. oai:hal-01295436. doi:10.1090/S0025-5718-1989-0969491-5.

[74] F. Schreyer and R. Leine. A mixed shooting - harmonic balance method for unilaterally constrained mechanical systems. *Archive of Mechanical Engineering*, 63(2):297–314, 2016. oai:hal-01356796.

[75] S. Shaw and C. Pierre. Normal modes of vibration for non-linear continuous systems. *Journal of Sound and Vibration*, 169(3):319–347, 1994. oai:hal-01471098.

[76] S. W. Shaw. Invariant manifold representations of nonlinear modes of vibration. In *Modal Analysis of Nonlinear Mechanical Systems*, volume 555, pages 47–74. Springer, 2014. doi:10.1007/978-3-7091-1791-0_2.

[77] B. F. Shorr. *The Wave Finite Element Method*. Springer, 2004. doi:10.1007/978-3-540-44579-1.

[78] M. W. Sracic and M. S. Allen. Numerical continuation of periodic orbits for harmonically forced nonlinear systems. In *Civil Engineering Topics*, volume 4, pages 51–69. Springer, 2011. doi:10.1007/978-1-4419-9316-8_5.

[79] E. Süli. *Finite element methods for partial differential equations*. Oxford University Computing Laboratory Oxford, 2002.

[80] H. Tao and J. Gibert. Periodic orbits of a conservative 2-DOF vibro-impact system by piecewise continuation: bifurcations and fractals. *Nonlinear Dynamics*, 95:2963–2993, 2019. doi:10.1007/s11071-018-04734-4.

[81] A. Ten Eyck and A. Lew. Discontinuous galerkin methods for non-linear elasticity. *International Journal for Numerical Methods in Engineering*, 67(9):1204–1243, 2006. doi:10.1002/nme.1667.

[82] H. Le Thi, S. Junca, and M. Legrand. Periodic solutions of a two-degree-of-freedom autonomous vibro-impact oscillator with sticking phases. *Nonlinear Analysis: Hybrid Systems*, 28:54–74, 2018. oai:hal-01305719. doi:10.1016/j.nahs.2017.10.009.

[83] A. Thorin, P. Delezoide, and M. Legrand. Periodic solutions of n-dof autonomous vibro-impactoscillators with one lasting contact phase. *Nonlinear Dynamics*, 90:1771–1783, 2017. oai:hal-01505888. doi:10.1007/s11071-017-3763-z.

[84] A. Thorin and M. Legrand. Nonsmooth modal analysis: From the discrete to the continuous settings. In *Advanced Topics in Nonsmooth Dynamics: Transactions of the European Network*

for Nonsmooth Dynamics, pages 191–234. Springer, 2018. oai:hal-01771849. doi:10.1007/978-3-319-75972-2_5.

[85] D. Urman and M. Legrand. Nonlinear modal analysis of the bar in unilateral contact via analytical weak-solutions to the wave equation. In *27th Canadian Congress of Applied Mechanics*, 2019. oai:hal-02151373.

[86] D. Urman and M. Legrand. MATLAB Scripts for nonsmooth modal analysis of the bar via nodal boundary method, 2022. doi:10.5281/zenodo.6382948.

[87] D. Urman and M. Legrand. Nonsmooth modal analysis of a varying cross-sectional area bar in unilateral contact. *Journal of Sound and Vibration*, page 117385, 2022. oai:hal-03619197. doi:10.1016/j.jsv.2022.117385.

[88] D. Urman and M. Legrand. MATLAB scripts for two-dimensional nodal boundary method and harmonic balance method, 2023. doi:10.5281/zenodo.8237611.

[89] D. Urman, M. Legrand, and S. Junca. D'Alembert function for exact non-smooth modal analysis of the bar in unilateral contact. *Nonlinear Analysis: Hybrid Systems*, 43:101115, 2021. oai:hal-02984137. doi:10.1016/j.nahs.2021.101115.

[90] V. I. Utkin. *Sliding Modes in Control and Optimization*. Springer, 2013. doi:10.1007/978-3-642-84379-2.

[91] J. Venkatesh. Boundary element method for nonlinear modal analysis of systems undergoing unilateral contact conditions. Master's thesis, McGill University, 2017. [pdf].

[92] L. Vitagliano. Characteristics, bicharacteristics and geometric singularities of solutions of PDEs. *International Journal of Geometric Methods in Modern Physics*, 11(09):1460039, 2014. doi:10.1142/s0219887814600391.

[93] G. von Groll and D.J. Ewins. The harmonic balance method with arc-length continuation in rotor/stator contact problems. *Journal of Sound and Vibration*, 241(2):223–233, 2001. doi:10.1006/jsvi.2000.3298.

[94] L. Wang and Q. Ni. Hopf bifurcation and chaotic motions of a tubular cantilever subject to cross flow and loose support. *Nonlinear Dynamics*, 59(329):305–326, 2010. doi:10.1007/s11071-009-9542-8.

[95] P. Wriggers and G. Zavarise. *Computational Contact Mechanics*, chapter 6. American Cancer Society, 2004. doi:10.1002/0470091355.ecm033.

[96] V. A. Yastrebov. *Numerical Methods in Contact Mechanics*. Wiley, 2013. doi:10.1002/9781118647974.

[97] C. Yoong. *Nonsmooth modal analysis of a finite linear elastic bar subject to unilateral contact constraint*. PhD thesis, McGill University, 2018. [pdf].

[98] C. Yoong, A. Thorin, and M. Legrand. Nonsmooth modal analysis of an elastic bar subject to a unilateral contact constraint. *Nonlinear Dynamics*, 91(4):2453–2476, 2018. oai:hal-01471341. doi:10.1007/s11071-017-4025-9.

[99] J. Yuan, Y. Sun, C. Schwingshackl, and L. Salles. Computation of damped nonlinear normal modes for large scale nonlinear systems in a self-adaptive modal subspace. *Mechanical Systems and Signal*

Processing, 162:108082, 2022. doi:10.1016/j.ymssp.2021.108082.

Appendix A

Proofs for propositions on 1CPP NSMs of the uniform-area bar

A.1 Proof of Proposition 3.2

Proof. First, we will show that a 1CPP motion cannot occur for $\tau \geq 4$. To this end, we show that a motion with $\tau = 4$ will never initiate an active contact phase. Then, by extension, we will show that motions with $\tau > 4$ will not initiate an active contact phase either.

To start, we note that a duration $\tau = 4$ coincides exactly with the period of the bar if it were *always* in inactive contact motion (a motion of the bar where $\partial_x u(1,t) = 0$ for all $t \in [0,\infty)$). Thus, a motion with $\tau = 4$ could hypothetically repeat for $t \in [4,\infty)$ in periods of 4, as shown in Equation (3.20), and still satisfy the wave equation (3.1), cantilever condition (3.2), and the set of Signorini conditions describing inactive contact motion: $u(1,t) \leq g_0$ and $\partial_x u(1,t) = 0$ for all $t \in [0,\infty)$. Specifically, such a motion would be a solution to Signorini problem while never initiating an active contact phase. Using the uniqueness theorem for this Signorini problem [73], we can then justify that a motion that never initiates an active contact phase for $t \in [4,\infty)$ (following the inactive contact motion taking place for $t \in [0,\tau]$ with $\tau = 4$) is the only possible solution. To clarify, since (I) there must exist a unique solution to the considered initial-value problem [73], and (II) there always exists a solution that is exclusively in inactive contact for $t > \tau = 4$; there cannot exist any motion with $\tau = 4$ that enters into an active contact phase. By the same logic, we can conclude that any inactive motion that lasts from $t = 0$ until some time $t > 4$ - for example, a motion with $\tau > 4$ - must also be exclusively an inactive contact motion that never initiates active contact. Accordingly, we conclude that a motion with $\tau \geq 4$ never initiates active contact (the stress at $x = 1$ is always zero) and, therefore, cannot pertain to the group of 1CPP motions.

Next, the constraints (3.22)-(3.23) are derived by plugging the resulting d'Alembert function for

inactive contact into the inactive contact inequality constraint (3.3): $\bar{u}(1,t) = f(t+1) - f(t-1) \leq g_0$ $\forall t \in [0,\tau]$. Starting with the d'Alembert function (3.17) for $\tau \leq 2$, we obtain

$$f(t+1) - f(t-1) = g_0 - 2f_0(t-1) \leq d \quad \forall t \in [0,\tau],\ 0 < \tau < 2 \tag{A.1}$$

which can be simplified into

$$f_0(t) \geq 0 \quad \forall t \in [-1,\tau-1],\ 0 < \tau \leq 2. \tag{A.2}$$

Next, plugging (3.17) for $2 < \tau < 4$ into $f(t+1) - f(t-1) \leq g_0$, $\forall t \in [0,\tau]$, we obtain

$$g_0 \geq f(t+1) - f(t-1) = \begin{cases} g_0 - 2f_0(t-1) & t \in [0,2] \\ 2f_0(t-3) - g_0 & t \in [2,\tau] \end{cases} \quad 2 < \tau < 4. \tag{A.3}$$

The inequality constraint is then assigned separately in $t \in [0,2]$ and $t \in [2,\tau]$ and, with further simplification, admits

$$0 \leq f_0(t) \quad t \in [-1,1], \qquad 2 < \tau < 4 \tag{A.4}$$

$$g_0 \geq f_0(t) \quad t \in [-1,\tau-3], \quad 2 < \tau < 4. \tag{A.5}$$

At last, conditions (A.2) and (A.4) lead to (3.22) and condition (A.5) is (3.23) verbatim, which concludes the proof. □

A.2 Proof of Proposition 3.3

Proof. By contradiction, it is shown that for $T - \tau \geq 2$ a non-grazing 1CPP periodic motion cannot occur.

For $T - \tau = 2$, the active contact duration equals the period of $\partial_x \bar{u}(1,t)$, which is 2-periodic through (3.27). In future time $t > T$, $\partial_x \bar{u}(1,t)$ can therefore be described using active contact conditions exclusively. The same applies for $T - \tau > 2$. Since uniqueness is guaranteed, any motion with $T - \tau \geq 2$ remains in active contact motion for any $t > T$ and therefore never switches to inactive contact (such motion, by definition, would not be periodic). Thus, the bound (3.28) must hold to guarantee the existence of 1CPP.

The restriction (3.29) is derived by plugging (3.26) into the active contact inequality condition (3.4). □

A.3 Proof of Proposition 3.4

Proof. The proof is divided into three parts. First, it is shown that (3.30) can be derived from the periodicity conditions (3.5) and (3.6) (in their d'Alembert form). Second, we show Equation (3.30)

implies that f' is T-periodic. Third, it is shown if f abides (3.30) then $u(x,t)$ is T-periodic (in time) by virtue of uniqueness of the solution to the Signorini problem

It is shown that (3.30) can be derived from (3.5) and (3.6) (in their d'Alembert form) and vice-versa. A periodic solution, such that (3.5) and (3.6) are valid, requires that

$$f(T+x) - f(T-x) = f_0(x) + f_0(-x) \quad \forall x \in [0,1] \tag{A.6}$$

$$f'(T+x) - f'(T-x) = f_0'(x) + f_0'(-x) \quad x \in [0,1] \text{ a.e.} \tag{A.7}$$

respectively. Differentiating Equation (A.6) with respect to x yields:

$$f'(T+x) + f'(T-x) = f_0'(x) - f_0'(-x) \quad x \in [0,1] \text{ a.e.} \tag{A.8}$$

In turn, adding (A.7) to (A.8) and subtracting (A.7) from (A.8) results in

$$f'(T+x) = f_0'(x) \qquad x \in [0,1] \text{ a.e.} \tag{A.9}$$

$$f'(T-x) = f_0'(-x) \quad x \in [0,1] \text{ a.e.} \tag{A.10}$$

respectively. Next, $s = x$ and $s = -x$ are substituted into (A.9) and (A.10), respectively

$$f'(T+s) = f_0'(s) \quad s \in [0,1] \text{ a.e.} \tag{A.11}$$

$$f'(T+s) = f_0'(s) \quad s \in [-1,0] \text{ a.e.} \tag{A.12}$$

which can then be assembled to (3.30).

Also, f' abiding (3.30) is periodic. To prove this, we show that $f'(s+T) = f'(s)$ for $s \in [-1, T+1]$ a.e. by assuming that $f'(s+T)$ and $f'(s)$ are defined by the same NDDEs and initial conditions (formulated as problem I and II).

Problem 1 The determination of $f'(s)$ for $s \in [1, T+1]$ can be obtained from an NDDE problem formed by the inactive boundary conditions (3.12) and the derivative of the active contact boundary conditions (3.13)

NDDE I

$$f'(s) = \begin{cases} -f'(s-2) & s \in [1, \tau+1] \text{ a.e.} \\ f'(s-2) & s \in [\tau+1, T+1] \text{ a.e.} \end{cases} \tag{A.13}$$

Initial conditions I

$$f'(s) = f_0'(s) \quad s \in [-1,1] \text{ a.e.} \tag{A.14}$$

Problem II Similarly, for $s \geq T+1$, it is expected that the same boundary conditions apply. Namely, determining $f'(s)$ for $s \in [T+1, 2T+1]$ requires solving

NDDE II

$$f'(s) = \begin{cases} -f'(s-2) & s \in [1+T, \tau+T+1] \text{ a.e.} \\ f'(s-2) & s \in [\tau+T+1, 2T+1] \text{ a.e.} \end{cases} \tag{A.15}$$

where the initial conditions are assumed to be known from Equation (3.30)

Initial conditions II

$$f'(s) = f_0'(s-T) \quad s \in [T-1, T+1] \text{ a.e.} \tag{A.16}$$

Note that both initial conditions I and II are given by the same function $f_0'(s)$ for $s \in [-1,1]$ a.e. Similarly, NDDEs I and II are equivalent up to a phase difference T. As shown in sections 3.2.1 and 3.2.1, the solution to NDDE I is unique with respect to initial conditions (given $f_0(-1) = 0$ as in (3.9)). Similarly, using the method of steps, one can show that NDDE II produces a unique solution with respect to initial conditions (given $f_0(-1) = 0$). Therefore, the solutions $f'(s)$ for $s \in [-1, T+1]$ and $f'(s)$ for $s \in [T-1, 2T+1]$, must be equal, that is $f'(T+s) = f'(s)$, $s \in [-1, T+1]$ a.e. and, by induction, we can show the relationship holds for the extensions of f' in $s > 2T+1$: $f'(nT+s) = f'((n-1)T+s)$, $s \in [-1, T+1]$ a.e., $n = 2, 3, \ldots, \infty$ which also means that f' is periodic: $f'(T+s) = f'(s)$, $s \in [-1, \infty)$ a.e.

Finally, to show that statement (3.30) leads to $\bar{u}(x,t)$ T-periodic, we integrate (3.30) to obtain

$$f_0(s) = f(s+T) - f(T-1) \quad \forall s \in [-1,1] \tag{A.17}$$

which, in turn, admits the identities $\bar{u}(x,T) = f(T+x) - f(T-x) = f_0(x) - f_0(-x) = \bar{u}(x,0)$, $\forall x \in [0,1]$ and $\partial_t \bar{u}(x,T) = f'(T+x) - f'(T-x) = f_0'(x) - f_0'(-x) = \partial_t \bar{u}(x,0)$, $x \in [0,1]$ a.e.. Through uniqueness [73], conditions (3.30) implies a T-periodic motion of the bar in dimensionless time. □

A.4 Proof of Proposition 3.5

Proof. The proof consists of first converting the initial conditions of NSM1 motions on rational periods into the formulation of initial conditions presented in Equation (3.67). Following this conversion, it will be shown that NSM1 motions on rational periods belong to NSM3 motions with $\mathbf{c}$ abiding Equation (3.92) and $\eta(s) = ms$ as stated in Proposition 3.5. Second, it will be shown that c_i defined in Equation (3.92) are solutions of Equations (3.87) to (3.89) since they are produced from a NSM of the bar: NSM1 (all NSMs of the bar must answer the CPS conditions). Thus, instead of solving CPS in Equations (3.87) to (3.89) for a particular solution $\mathbf{c}$, the solution $\mathbf{c}$ is derived from the known NSM1 which already answers the CPS conditions.

First, it is desired to convert NSM1 motions to NSM3 motions on rational periods. Thus, the

rational period $T = n/m$ is plugged into the initial conditions for NSM1 from Equation (3.47) to derive the initial conditions of NSM1 for rational periods

$$f_{0,\text{NSM1}}(s) \equiv \frac{g_0 m}{2n-6m}\begin{cases} s+1 & s \in [-1, n/m-3] \\ 2n/m-5-s & s \in [n/m-3, 1] \end{cases} \tag{A.18}$$

where $f_{0,\text{NSM1}}(s)$ is used to simplify upcoming notation. Next, to convert $f_{0,\text{NSM1}}$ to initial conditions of NSM3 (Equation (3.67)), the function $\eta(s)$ must be linear to result in a piecewise linear function like described in Equation (A.18). Therefore, $\eta(s) = ms$ is imposed since it is the only linear function that satisfies the conditions on $\eta(s)$ (3.80). Consequentially, the initial conditions for NSM3 (3.67) for $\eta(s) = ms$ are denoted $f_{0,\text{NSM3}}(s, \mathbf{c})$

$$f_{0,\text{NSM3}}(s, \mathbf{c}) \equiv \begin{cases} mc_0(s+1) & s \in [-1, -1+1/m] \\ c_0 + mc_1(s+1-1/m) & s \in [-1+1/m, -1+2/m] \\ \vdots & \\ \sum_{i=0}^{2m-2} c_i + mc_{2m-1}(s-1-1/m) & s \in [-1+(2m-1)/m, 1] \end{cases} \tag{A.19}$$

In order to convert $f_{0,\text{NSM1}}(s)$ to $f_{0,\text{NSM3}}(s, \mathbf{c})$, the quantity $\mathbf{c}$ such that $f_{0,\text{NSM3}}(s, \mathbf{c}) = f_{0,\text{NSM1}}(s)$ must be determined.

To simplify the derivation of the value $\mathbf{c}$ from $f_{0,\text{NSM3}}(s, \mathbf{c}) = f_{0,\text{NSM1}}(s)$, it can be shown that $f'_{0,\text{NSM3}}(s, \mathbf{c}) = f'_{0,\text{NSM1}}(s) \Rightarrow f_{0,\text{NSM3}}(s, \mathbf{c}) = f_{0,\text{NSM1}}(s)$. To prove the last statement, it is noted that both $f_{0,\text{NSM3}}(s, \mathbf{c})$ and $f_{0,\text{NSM1}}(s)$ functions are assumed to be continuous, piecewise differentiable, and integrable with $f_{0,\text{NSM3}}(-1, \mathbf{c}) = f_{0,\text{NSM1}}(-1) = 0$, $f_{0,\text{NSM3}}(s, \mathbf{c}) = f_{0,\text{NSM1}}(s)$. Thus, the following procedure is valid

$$f'_{0,\text{NSM3}}(s) = f'_{0,\text{NSM1}}(s) \qquad \forall s \in (-1, 1) \text{ a.e.} \tag{A.20}$$

$$\int_{-1}^{s} f'_{0,\text{NSM3}}(\mu)\,\mathrm{d}\mu = \int_{-1}^{s} f'_{0,\text{NSM1}}(\mu)\,\mathrm{d}\mu \qquad \forall s \in [-1, 1] \tag{A.21}$$

$$f_{0,\text{NSM3}}(s) + f_{0,\text{NSM3}}(-1) = f_{0,\text{NSM1}}(s) + f_{0,\text{NSM1}}(-1) \qquad \forall s \in [-1, 1] \tag{A.22}$$

$$f_{0,\text{NSM3}}(s) = f_{0,\text{NSM1}}(s) \qquad \forall s \in [-1, 1] \tag{A.23}$$

Hence, the coefficients c_i which satisfy $f'_{0,\text{NSM3}}(s, \mathbf{c}) = f'_{0,\text{NSM1}}(s)$ also satisfy $f_{0,\text{NSM3}}(s, \mathbf{c}) = f_{0,\text{NSM1}}(s)$.

To obtain the functions $f'_{0,\text{NSM3}}(s, \mathbf{c})$ and $f'_{0,\text{NSM1}}(s)$, Equations (A.18) and (A.19) are differenti-

ated

$$f'_{0,\mathrm{NSM3}}(s,\mathbf{c}) = \begin{cases} mc_0 & s \in [-1, -1+1/m] \\ mc_1 & s \in [-1+1/m, -1+2/m] \\ \vdots & \\ mc_{n-2m} & s \in [-1+(n-2m)/m, -1+(n-2m+1)/m] \\ \vdots & \\ mc_{2m-1} & s \in [-1+(2m-1)/m, 1] \end{cases} \tag{A.24}$$

$$f'_{0,\mathrm{NSM1}}(s) = \frac{g_0 m}{2n-6m} \begin{cases} 1 & s \in [-1, -1+(n-2m)/m] \\ -1 & s \in [-1+(n-2m)/m, 1] \end{cases} \tag{A.25}$$

Here, equating the same components in $f'_{0,\mathrm{NSM3}}(s,\mathbf{c}) = f'_{0,\mathrm{NSM1}}(s)$ admits $\mathbf{c}$ as defined in Equation (3.92) and the equality $f_{0,\mathrm{NSM3}}(s) = f_{0,\mathrm{NSM1}}(s)$ is obtained. In what follows, the values $\mathbf{c}$ that satisfy Equation (3.92) and $f'_{0,\mathrm{NSM3}}(s,\mathbf{c}^*) = f'_{0,\mathrm{NSM1}}(s)$ are denoted $\mathbf{c}^*$.

Next, since the $f'_{0,\mathrm{NSM3}}(s,\mathbf{c}^*) = f_{0,NSM1}(s)$ was shown to satisfy the CPS conditions (as elaborated in Section 3.3.1), the quantity $\mathbf{c}^*$ also satisfies the system of CPS equations and inequalities (3.87) to (3.89) which ends to proof. □

Appendix B

Proofs and supplementary material on the 1D-NBM

B.1 Proof of $\phi'_N(1) > 0$

Lemma B.1. *Consider the Lagrangian shape functions $\phi_i(x)$ for $i = 1, 2, \ldots, N$ consisting of uniformly spaced nodes on loci $x_i = i/N$ used in the classical FE treatment of the PDE (4.1). For these shape functions $\phi_i(x)$, the value of $\phi'_N(1)$ depends on the order of shape functions only.*

Proof. The proof follows from the construction of shape functions in the FEM. In the classical FEM, the structure is divided into elements and each element consists of a set of shape functions that are piecewise Lagrange polynomials. These shape functions are local to the element and their definition depends only on the order of the polynomial chosen for this specific element [34]. Thus, the value $\phi'_N(1)$ is dependent only on the order of shape functions used. □

This lemma will be necessary in the generalization of the theorem below to any number of elements and any order of shape functions.

Theorem B.2. *For the classical FE approximation for the PDE (4.1) with Lagrangian shape functions $\phi_i(x)$ $i = 1, 2, \ldots, N$ based on uniformly spaced nodes $x_i = i/N$, the statement*

$$\phi'_N(1) > 0 \tag{B.1}$$

always holds.

Proof. The proof consists of first proving Inequality (B.1) for the case of a single element by inspecting the exact expression of the Lagrangian function. Then, the proof is expanded to any number of elements and/or shape functions by virtue of Lemma B.1.

We start by approximating the bar's displacement using a single element. It follows then that the parameter N ($N \geq 1$) corresponds to the order of the shape function such that

$$\phi_i(x) = \prod_{\substack{0 \leq m \leq N \\ m \neq i}} \frac{x - x_m}{x_i - x_m}, \quad x \in [0, 1]. \tag{B.2}$$

Then, for $\phi_N(x)$, we can simplify the expression using $x_i = i/N$ to simplify the denominator

$$\phi_N(x) = \prod_{m=0}^{N-1} \frac{x - x_m}{x_N - x_m} = N^N \prod_{m=0}^{N-1} \frac{x - x_m}{N - m}. \tag{B.3}$$

Then, we take the derivative of $\phi_N(x)$ to obtain

$$\phi'_N(x) = N^N \sum_{j=0}^{N-1} \frac{1}{N - j} \prod_{\substack{0 \leq m \leq N-1 \\ m \neq j}} \frac{x - x_m}{N - m}. \tag{B.4}$$

To show $\phi'_N(1) > 0$, we simply evaluate every term in the expression

$$\begin{aligned} \phi'_N(1) &= N^N \sum_{j=0}^{N-1} \frac{1}{N - j} \prod_{\substack{0 \leq m \leq N-1 \\ m \neq j}} \frac{1 - x_m}{N - m} = N^N \sum_{j=0}^{N-1} \frac{1}{N - j} \prod_{\substack{0 \leq m \leq N-1 \\ m \neq j}} \frac{1}{N} \frac{N - m}{N - m} \\ &= \left(\frac{N^N}{N^{N-1}} \right) \sum_{j=0}^{N-1} \frac{1}{N - j} = N \sum_{j=1}^{N-1} \frac{1}{N - j} = N \sum_{j=1}^{N} \frac{1}{j}. \end{aligned} \tag{B.5}$$

We note that all the quantities presented here are exclusively positive and that their sum and product will also be positive such that $\phi'_N(1) > 0$ holds. By virtue of Lemma B.1, we may conclude that if $\phi'_N(1) > 0$ holds for a single element, it will hold for any number of elements as well. □

B.2 Neumann conditions in NBM and classical FEM

This section compares the treatment of Neumann conditions in NBM and FEM in order to emphasize the novelty in the NBM. For sake of simplicity, the NBM and classical FEM are both applied on the cantilever bar PDE (4.1), boundary condition (4.2) and

$$\partial_x u(1, t) = 0, \tag{B.6}$$

for a constant cross-section area $A(x) = 1$. The discussion also applies for the case of varying area.

Both classical FEM and NBM are derived from the weak formulation:

$$\forall w(x), \quad \int_0^1 w(x) \partial_{tt} u(x, t) \mathrm{d}x + \int_0^1 \partial_x w(x) \partial_x u(x, t) \mathrm{d}x - w(1) \partial_x u(1, t) = 0. \tag{B.7}$$

Both methodologies are derived using the same set of Lagrangian shape functions and nodal quantities defined in Equation (4.8).

B.2.1 Classical FEM

The set of Lagrangian functions is used both to approximate the nodal displacements and test functions as

$$u(x,t) \approx \mathbf{P}(x)\mathbf{u}(t), \quad w(x) \approx \mathbf{P}(x)\mathbf{w}. \tag{B.8}$$

Plugging Equation (B.8) into Equation (B.7) results in

$$\mathbf{w}^\top \mathbf{M}\ddot{\mathbf{u}}(t) + \mathbf{w}^\top \mathbf{K}\mathbf{u}(t) - w_N \partial_x u(1,t) = 0. \tag{B.9}$$

In Equation (B.9), it is assumed that the homogeneous Dirichlet condition at $x = 0$ has been treated by omitting u_0 and w_0. In turn, the enforcement of Equation (B.6) results in the elimination of the last term in Equation (B.9). Followed by the generalization to any $\mathbf{w}$ yields:

$$\mathbf{w}^\top \mathbf{M}\ddot{\mathbf{u}}(t) + \mathbf{w}^\top \mathbf{K}\mathbf{u}(t) - w_N \cancel{\partial_x u(1,t)} = 0, \tag{B.10}$$

$$\mathbf{w}^\top \mathbf{M}\ddot{\mathbf{u}}(t) + \mathbf{w}^\top \mathbf{K}\mathbf{u}(t) = 0, \quad \forall \mathbf{w}, \tag{B.11}$$

$$\mathbf{M}\ddot{\mathbf{u}}(t) + \mathbf{K}\mathbf{u}(t) = \mathbf{0}. \tag{B.12}$$

It should be notet that the elimination of the last term in (B.10) leads to a *weak* enforcement only of the homogeneous Neumann condition since $\partial_x u(1,t) \approx \mathbf{P}'(1)\mathbf{u}(t) \equiv \sigma_n^{\mathrm{FEM}}(\mathbf{u}(t))$ does not necessarily vanish, as specified in the strong formulation. However, it is generally understood that $\sigma_n^{\mathrm{FEM}}(\mathbf{u}(t)) \longrightarrow 0$ as the number of nodes or order of shape function increases.

B.2.2 NBM treatment of the weak formulation

In the NBM treatment, a set of shape functions is built such that the Neumann conditions are enforced in a strong manner. To this end, the FEM approximation of $\partial_x u(1,t)$ is restricted to satisfy Equation (B.6) in the following manner:

$$\partial_x u(1,t) \approx \mathbf{P}'(1)\mathbf{u}(t) = 0, \quad \forall t. \tag{B.13}$$

This restriction is implemented by isolating the last nodal displacement in Equation (B.13) such that the term $u_N(t)$ reads

$$u_N(t) = S(\mathbf{u}^o(t)) \tag{B.14}$$

where $S(\mathbf{u}^o(t))$ is recalled from Equation (4.33). Plugging Equation (B.14) into the original approximation of $u(x,t)$ leads to

$$u(x,t) \approx \mathbf{P}(x)\mathbf{A}^N \mathbf{u}^o(t) \equiv u^{\mathrm{NBM}}(x,t) \tag{B.15}$$

where $\mathbf{A}^N$ is recalled from Equation (4.34). The approximation in Equation (B.15) satifies $\partial_x u^{\mathrm{NBM}}(1,t) = 0$ which implies that the Neumann condition is enforced strongly. Application of

the Galerkin-Bubnov method [44, 79] on Equation (B.15) requires that the test function $w(x)$ is approximated using the same set of shape functions, ie

$$w(x) = \mathbf{P}(x)\mathbf{A}^N\mathbf{w}^o. \tag{B.16}$$

In Equations (B.15) and (B.16), it is assumed that the homogeneous Dirichlet condition on $x = 0$ has been treated by omitting u_0 and w_0. Plugging Equation (B.15) into Equation (B.7) and generalizing for any $\mathbf{w}^o$ implies

$$\mathbf{M}^N\ddot{\mathbf{u}}^o(t) + \mathbf{K}^N\mathbf{u}(t) = \mathbf{0} \tag{B.17}$$

which, for any initial conditions, admits an approximation that satisfies the Neumann condition (B.6) strongly.

By enforcing strongly the contact condition for active and inactive contact phases, the NBM admits two distinct system of ODEs in terms of the internal displacements $\mathbf{u}^o$. This allows for simple implementation of the switching method as the same nodal quantities are involved in both systems, as shown in Section 4.3.4.

B.3 Proof of invertible $\mathbf{M}_N$ and $\mathbf{M}_D$

Theorem B.3. *The matrices $\mathbf{M}_N$ and $\mathbf{M}_D$ defined in Equation (4.40) and Equation (4.48), respectively, are non-singular.*

Proof. The proof is established by showing that $\mathbf{M}_N$ and $\mathbf{M}_D$ by showing that they are positive-definite (and thus do not exhibit zero eigenvalues), such that for any $\mathbf{y} \neq \mathbf{0}$ ($\mathbf{y} \in \mathbb{R}^{N-1}$)

$$\mathbf{y}^\top\mathbf{M}_N\mathbf{y} > 0 \tag{B.18}$$

$$\mathbf{y}^\top\mathbf{M}_D\mathbf{y} > 0. \tag{B.19}$$

To prove that $\mathbf{M}_N$ and $\mathbf{M}_D$ are positive-definite, it is first noted that the mass matrix $\mathbf{M}$ is positive-definite. To demonstrate that $\mathbf{M}$ is positive-definite, the product $\mathbf{z}^\top\mathbf{M}\mathbf{z}$ ($\mathbb{R}^N \ni \mathbf{z} \neq \mathbf{0}$) is first put in terms of the Lagrangian functions composing it

$$\mathbf{z}^\top\mathbf{M}\mathbf{z} = \int_0^1 \mathbf{y}^\top\mathbf{P}(x)^\top\mathbf{P}(x)\mathbf{y}\mathrm{d}x = \int_0^1 (\mathbf{y}\mathbf{P}(x))^\top(\mathbf{P}(x)\mathbf{z})\mathrm{d}x = \int_0^1 ||\mathbf{P}(x)\mathbf{z}||_2^2\mathrm{d}x. \tag{B.20}$$

From Equation (B.20), it can be shown that $\mathbf{M}$ is positive definite if $\mathbf{P}(x)\mathbf{z} \neq \mathbf{0}$ for any $\mathbf{z} \neq \mathbf{0}$. Since Lagrangian functions are used in $\mathbf{P}(x)$, $\mathbf{z}$ can be seen as standing for nodal values. Also, it is known that if any of the nodal values is non-zero, the value of the function $\mathbf{P}(x)\mathbf{z}$ must be non-zero at least for a single element. Thus, for any vector $\mathbf{z} \neq \mathbf{0}$, $\mathbf{P}(x)\mathbf{z} \neq \mathbf{0}$ for $x \in [0, 1]$ holds and the mass matrix is positive-definite by virtue of (B.20).

Next, from Equation (4.40) and Equation (4.48), $\mathbf{M}_N$ and $\mathbf{M}_D$ can be written in terms of $\mathbf{M}$

$$\mathbf{y}^\top \mathbf{M}_N \mathbf{y} = (\mathbf{A}^N \mathbf{y})^\top \mathbf{M} \mathbf{A}^N \mathbf{y} \tag{B.21}$$

$$\mathbf{y}^\top \mathbf{M}_D \mathbf{y} = (\mathbf{A}^D \mathbf{y})^\top \mathbf{M} \mathbf{A}^D \mathbf{y}. \tag{B.22}$$

Thus, to show that inequalities (B.19) and (B.18) hold, it is required to show that $\mathbf{A}^N \mathbf{y} \neq \mathbf{0}$ and $\mathbf{A}^D \mathbf{y} \neq \mathbf{0}$ for $\mathbf{y} \neq \mathbf{0}$. Then, the positive-definiteness of $\mathbf{M}_N$ and $\mathbf{M}_D$ follows from $\mathbf{M}$ being positive-definite (which was already shown in expression (B.20)).

It is noted that for $\mathbf{A}^D \mathbf{y} \neq \mathbf{0}$ and $\mathbf{A}^N \mathbf{y} \neq \mathbf{0}$ for any $\mathbf{y} \neq \mathbf{0}$ to hold, $\mathbf{A}^D$ and $\mathbf{A}^N$ must consist of linearly independent columns ($\mathbf{A}^D$ and $\mathbf{A}^N$ must be full-rank). The columns of these matrices are revealed from expressions (4.34) and (4.46) as follows

$$\mathbf{A}^N = \begin{bmatrix} \mathbf{e}_1^{N-1} & \mathbf{e}_2^{N-1} & \dots & \mathbf{e}_{N-1}^{N-1} \\ -\dfrac{\phi_1'(1)}{\phi_N'(1)} & -\dfrac{\phi_2'(1)}{\phi_N'(1)} & \dots & -\dfrac{\phi_{N-1}'(1)}{\phi_N'(1)} \end{bmatrix} \tag{B.23}$$

$$\mathbf{A}^D = \begin{bmatrix} \mathbf{e}_1^{N-1} & \mathbf{e}_2^{N-1} & \dots & \mathbf{e}_{N-1}^{N-1} \\ 0 & 0 & \dots & 0 \end{bmatrix} = \begin{bmatrix} \mathbf{e}_1^{N} & \mathbf{e}_2^{N} & \dots & \mathbf{e}_{N-1}^{N} \end{bmatrix} \tag{B.24}$$

where $\mathbf{e}_i^{N-1} \in \mathbb{R}^{N-1}$ are the standard basis vectors in $N-1$ space. From Equation (B.23) and Equation (B.24), it can be noted that the first $N-1$ rows of either $\mathbf{A}^N$ or $\mathbf{A}^D$ consists of all standard basis vectors in $N-1$. These standard basis vectors remain linearly independent regardless of any values on the last row. Thus, $\mathbf{A}^N$ and $\mathbf{A}^D$ are full-rank due to the linear independence of the standard basis columns composing them. At last, since $\mathbf{A}^N$ and $\mathbf{A}^D$ are full-rank and $\mathbf{M}$ is positive definite,

$$\mathbf{y}^\top \mathbf{M}_D \mathbf{y} = (\mathbf{A}^D \mathbf{y})^\top \mathbf{M} \mathbf{A}^D \mathbf{y} > 0 \tag{B.25}$$

$$\mathbf{y}^\top \mathbf{M}_N \mathbf{y} = (\mathbf{A}^N \mathbf{y})^\top \mathbf{M} \mathbf{A}^N \mathbf{y} > 0. \tag{B.26}$$

for any $\mathbf{y} \neq \mathbf{0}$, and both $\mathbf{M}_D$ and $\mathbf{M}_N$ are positive-definite and non-singular.

□

B.4 Uniqueness of non-grazing solutions to NBM-ODE

In order to prove the uniqueness of the NBM-ODE non-grazing solutions, a formal definition of non-grazing solutions in NBM is first established.

Definition B.4 (non-grazing NBM motion)**.** *A motion $\mathbf{u}^o(t)$ that is solution of Equation (4.54) is said to be non-grazing if for every switch instant $t_s : S(\mathbf{u}^o(t_s) = g_0$ it is always true that $S(\dot{\mathbf{u}}^o(t_s)) \neq 0$.*

In laymen terms, at any switching instant, the value of $S(\dot{\mathbf{u}}^o(t_s))$ represents the velocity before the beginning of the active contact phase (see Equation (4.57)) or the derivative of the stress function

before the beginning of the inactive contact phase (see Equation (4.58)). Next, the theorem of uniqueness for such non-grazing solutions is stated below with a proof.

Theorem B.5 (Uniqueness of non-grazing NBM motions solutions to the NBM-ODE)**.** *Consider the NBM-ODE defined in Equation* (4.54) *with initial conditions* $\mathbf{u}^o(0) = \mathbf{u}_0^o$ *and* $\dot{\mathbf{u}}^o(0) = \mathbf{v}_0^o$ *which pertain non-grazing NBM motions. If the NBM-ODE generates a non-grazing NBM motion, it is unique with respect to initial conditions.*

Proof. The proof follows from the uniqueness of solutions to both components of Equation (4.54). It starts by noting that the initial conditions are non-grazing and therefore if $S(\mathbf{u}_0^o) = g_0$ then $S(\mathbf{v}_0^o) \neq 0$ and the structure's contact phase is determined by the NBM inactive or active contact conditions (4.52) or (4.51), respectively. Next, it is assumed that the initial conditions answer the inactive contact NBM conditions stated in Equation (4.52). Nevertheless, the proof can be formulated in a similar fashion with initial conditions answering active contact NBM conditions (4.51).

Case 1: Inactive contact motion For the duration of inactive contact, the NBM-ODE is:

$$\ddot{\mathbf{u}}^o(t) = -\mathbf{M}_N^{-1}\mathbf{K}_N\mathbf{u}^o(t), \quad \mathbf{u}^o(0) = \mathbf{u}_0^o \text{ and } \dot{\mathbf{u}}^o(0) = \mathbf{v}_0^o \tag{B.27}$$

This system is well-posed as it consists of a linear ODE. Regarding the possible outcomes for the solution, there exist two possibilities: either (1) a switching moment occurs such that $S(\mathbf{u}^o(t)) = g_0$ for some $t > 0$ or (2) $S(\mathbf{u}^o(t)) < g_0$ for $t \in [0, \infty)$ at which case the solution is unique by well-posedness. For case (1), the time of switch is t_s and the solution to

$$\ddot{\mathbf{u}}^o(t) = -\mathbf{M}_N^{-1}\mathbf{K}_N\mathbf{u}^o(t), \quad \mathbf{u}^o(0) = \mathbf{u}_0^o \text{ and } \dot{\mathbf{u}}^o(0) = \mathbf{v}_0^o \quad \forall t \in [0, t_s) \tag{B.28}$$

is a unique, continuous and differentiable motion $\mathbf{u}^o(t)$ for $t \in [0, t_s)$. Since the solution is differentiable for $t \in (0, t_s)$ and starts with $S(\mathbf{u}_0^o) < g_0$ (or with $S(\mathbf{u}_0^o) = g_0$ and $S(\mathbf{v}_0^o) < 0$), the velocity a t_s must abide $S(\dot{\mathbf{u}}^o(t_s)) \geq 0$. Furthermore, since non-grazing NBM motions are considered, it is assumed that $S(\dot{\mathbf{u}}^o(t_s)) > 0$ occurs at the moment of switch. Then, for $t > t_s$, the active contact NBM motion (4.51) takes effect. This is described in Case 2 below. Here, the initial displacement and velocity should be assigned with the displacement and velocity at the moment of switch: $\mathbf{u}_0^o \leftarrow \mathbf{u}^o(t_s)$ and $\mathbf{v}_0^o \leftarrow \dot{\mathbf{u}}^o(t_s)$.

Case 2: Active contact motion For the duration of active contact, the NBM-ODE is:

$$\ddot{\mathbf{u}}^o(t) = -\mathbf{M}_D^{-1}(\mathbf{K}_D\mathbf{u}^o(t) + \mathbf{f}_D), \quad \mathbf{u}^o(0) = \mathbf{u}_0^o \text{ and } \dot{\mathbf{u}}^o(0) = \mathbf{v}_0^o \tag{B.29}$$

This system is well-posed as a linear ODE. Regarding the possible routes for the solution of the NBM-ODE, there exist two possibilities: either (1) a switching moment occurs such that $S(\mathbf{u}^o(t)) = g_0$ for some $t > 0$ or (2) $S(\mathbf{u}^o(t)) > g_0$ for $t \in [0, \infty]$ in which case the solution is unique by well-posedness. For (1), we denote the moment of switch t_s and the solution to

$$\ddot{\mathbf{u}}^o(t) = -\mathbf{M}_D^{-1}(\mathbf{K}_D\mathbf{u}^o(t) + \mathbf{f}_D), \quad \mathbf{u}^o(0) = \mathbf{u}_0^o \text{ and } \dot{\mathbf{u}}^o(0) = \mathbf{v}_0^o, \quad \forall t \in [0, t_s) \tag{B.30}$$

is a unique, continuous and differentiable motion $\mathbf{u}^o(t)$ for $t \in [0, t_s)$. Since the solution is differentiable for $t \in (0, t_s)$ and $S(\mathbf{u}^o(t_s)) > g_0$ (or with $S(\mathbf{u}_0^o) = g_0$ and $S(\mathbf{v}_0^o) > 0$), the velocity at t_s must abide $S(\dot{\mathbf{u}}^o(t_s)) \leq 0$. Furthermore, since non-grazing motions are discussed, it is assumed that $S(\dot{\mathbf{u}}^o(t_1)) < 0$ occurs at the moment of switch. Then, for $t > t_s$, the inactive contact NBM motion (4.52) takes effect. This is described in Case 1 above. Here, the initial displacement and velocity should be assigned with the displacement and velocity at the moment of switch: $\mathbf{u}_0^o \leftarrow \mathbf{u}^o(t_s)$ and $\mathbf{v}_0^o \leftarrow \dot{\mathbf{u}}^o(t_s)$.

From Cases 1 and 2, it is noted that the motion is composed of unique solutions to the inactive and active contact conditions with respect to their initial or switching conditions. Thus, starting from an initial condition, the sequence of inactive and active motions is unique for non-grazing motions. □

For grazing motions, the NBM-ODE is ill-posed and definitions (4.52) and (4.51) must be extended to include the case $S(\dot{\mathbf{u}}^o(t_s)) = 0$. This requires inspection of the acceleration term (similar to Newton's impact law with $e = 0$). However, since grazing motions are not considered in this thesis, this extension is avoided for sake of conciseness.

B.5 Semismooth-Newton and Crank-Nicolson schemes in NBM

To find $\mathbf{u}^* \equiv \mathbf{u}_{i+1}^o$ and $\mathbf{v}^* \equiv \mathbf{v}_{i+1}^o$ such that Equation (4.66) and Equation (4.67) are answered, the following problem is solved

$$\mathbf{F}(\mathbf{u}^*, \mathbf{v}^*) \equiv \begin{pmatrix} \mathbf{F}_1(\mathbf{u}^*, \mathbf{v}^*) \\ \mathbf{F}_2(\mathbf{u}^*, \mathbf{v}^*) \end{pmatrix} \equiv \begin{pmatrix} -\mathbf{u}^* + \mathbf{u}_i^o + \dfrac{\Delta t}{2}(\mathbf{v}^* + \mathbf{v}_i^o) \\ -\mathbf{v}^* + \mathbf{v}_i^o + \dfrac{\Delta t}{2}(\mathbf{a}(\mathbf{u}^*, \mathbf{v}^*) + \mathbf{a}(\mathbf{u}_i^o, \mathbf{v}_i^o)) \end{pmatrix} = \mathbf{0} \tag{B.31}$$

where $\mathbf{F}_1(\mathbf{u}^*, \mathbf{v}^*)$ and $\mathbf{F}_2(\mathbf{u}^*, \mathbf{v}^*)$ were introduced to simplify the notation in the upcoming derivations of the semismooth-Newton solver. Next, we recall from Equation (4.68) the definition of the acceleration for a given displacement and velocity pair $(\mathbf{u}^*, \mathbf{v}^*)$

$$\mathbf{a}(\mathbf{u}^*, \mathbf{v}^*) = \begin{cases} -(\mathbf{M}_D)^{-1}(\mathbf{K}_D\mathbf{u}^* + \mathbf{f}_D) & S(\mathbf{u}^*) > g_0 \text{ or } S(\mathbf{u}^*) = g_0, S(\mathbf{v}^*) > 0 \\ -(\mathbf{M}_N)^{-1}(\mathbf{K}_N\mathbf{u}^*) & S(\mathbf{u}^*) < g_0 \text{ or } S(\mathbf{u}^*) = g_0, S(\mathbf{v}^*) < 0. \end{cases} \tag{B.32}$$

In the Newton-Raphson method, the root of $\mathbf{F}(\mathbf{u}^*, \mathbf{v}^*)$ is found via the iterative scheme:

$$\mathbf{q}_{j+1} = \mathbf{q}_j - \mathbf{J}^{-1}(\mathbf{q}_j)\mathbf{F}(\mathbf{q}_j), \quad \mathbf{q}_j = \begin{pmatrix} \mathbf{u}_j^* \\ \mathbf{v}_j^* \end{pmatrix}. \tag{B.33}$$

where $\mathbf{q}_j$ is introduced to simplify upcoming notation and $\mathbf{J}(\mathbf{u}^*, \mathbf{v}^*)$ denotes the Jacobian of $\mathbf{F}(\mathbf{u}^*, \mathbf{v}^*)$

$$\mathbf{J}(\mathbf{u}^*, \mathbf{v}^*) = \begin{bmatrix} \partial_{\mathbf{u}^*}\mathbf{F}_1(\mathbf{u}^*, \mathbf{v}^*) & \partial_{\mathbf{v}^*}\mathbf{F}_1(\mathbf{u}^*, \mathbf{v}^*) \\ \partial_{\mathbf{u}^*}\partial\mathbf{F}_2(\mathbf{u}^*, \mathbf{v}^*) & \partial_{\mathbf{v}^*}\mathbf{F}_2(\mathbf{u}^*, \mathbf{v}^*) \end{bmatrix}. \tag{B.34}$$

In what follows, each of the components in $\mathbf{J}(\mathbf{u}^*, \mathbf{v}^*)$ will be identified. First, determination of the derivatives of $\mathbf{F}_1(\mathbf{u}^*, \mathbf{v}^*)$ is a trivial matter

$$\partial_{\mathbf{u}^*}\mathbf{F}_1(\mathbf{u}^*, \mathbf{v}^*) = -\mathbf{I}, \quad \partial_{\mathbf{v}^*}\mathbf{F}_1(\mathbf{u}^*, \mathbf{v}^*) = \frac{\Delta t}{2}\mathbf{I}. \tag{B.35}$$

Then, the derivatives of $\mathbf{F}_2(\mathbf{u}^*, \mathbf{v}^*)$ read

$$\partial_{\mathbf{u}^*}\mathbf{F}_2(\mathbf{u}^*, \mathbf{v}^*) = \frac{\Delta t}{2}\partial_{\mathbf{u}^*}\mathbf{a}(\mathbf{u}^*, \mathbf{v}^*), \quad \partial_{\mathbf{v}^*}\mathbf{F}_2(\mathbf{u}^*, \mathbf{v}^*) = -\mathbf{I} + \frac{\Delta t}{2}\partial_{\mathbf{v}^*}\mathbf{a}(\mathbf{u}^*, \mathbf{v}^*) \tag{B.36}$$

and require more attention due to the derivative of the nonsmooth acceleration term $\mathbf{a}(\mathbf{u}^*, \mathbf{v}^*)$. Here, the semismooth-Newton approach is introduced. Newton-Raphson methods require that the Jacobian be defined everywhere near the root. However, due to the existence of the nonsmooth term $\mathbf{a}(\mathbf{u}^*, \mathbf{v}^*)$, the existence of the Jacobian cannot be always guaranteed. Thus, the semismooth-Newton method allows usage of the derivatives of $\mathbf{a}(\mathbf{u}^*, \mathbf{v}^*)$ locally, assuming that the current guess is situated away from any discontinuities [27]. As such, the derivatives of $\mathbf{a}(\mathbf{u}^*, \mathbf{v}^*)$ are obtained by differentiating Equation (4.54) (and plugging the definitions of NBM Inactive and Active contact in Equation (4.52) and Equation (4.51))

$$\partial_{\mathbf{u}^*}\mathbf{a}(\mathbf{u}^*, \mathbf{v}^*) = \begin{cases} -(\mathbf{M}_D)^{-1}\mathbf{K}_D & S(\mathbf{u}^*) > g_0 \text{ or } S(\mathbf{u}^*) = g_0, S(\mathbf{v}^*) > 0 \\ -(\mathbf{M}_N)^{-1}\mathbf{K}_N & S(\mathbf{u}^*) < g_0 \text{ or } S(\mathbf{u}^*) = g_0, S(\mathbf{v}^*) < 0 \end{cases} \tag{B.37}$$

$$\partial_{\mathbf{v}^*}\mathbf{a}(\mathbf{u}^*, \mathbf{v}^*) = \mathbf{0}. \tag{B.38}$$

Then, plugging Equations (B.35) to (B.38) into the Equation (B.34), the local-Jacobian is obtained

$$\mathbf{J}(\mathbf{u}^*, \mathbf{v}^*) = \begin{bmatrix} -\mathbf{I} & \frac{\Delta t}{2}\mathbf{I} \\ -\frac{\Delta t}{2}(\mathbf{M}_N)^{-1}\mathbf{K}_N & -\mathbf{I} \end{bmatrix} \quad \text{if } S(\mathbf{u}^*) > g_0 \text{ or } S(\mathbf{u}^*) = g_0, S(\mathbf{v}^*) > 0 \tag{B.39}$$

and

$$\mathbf{J}(\mathbf{u}^*, \mathbf{v}^*) = \begin{bmatrix} -\mathbf{I} & \frac{\Delta t}{2}\mathbf{I} \\ -\frac{\Delta t}{2}(\mathbf{M}_D)^{-1}\mathbf{K}_D & -\mathbf{I} \end{bmatrix} \quad \text{if } S(\mathbf{u}^*) < g_0 \text{ or } S(\mathbf{u}^*) = g_0, S(\mathbf{v}^*) < 0. \tag{B.40}$$

We note during the process of nonsmooth modal analysis, the specific state $S(\mathbf{u}^*) = g_0$ with $S(\mathbf{v}^*) = 0$ is rarely reached and the definition of the Jacobian above is rarely an issue. However, it is possible that for large time steps, the semismooth-Newton method does not find a solution (or, in fact, a solution does not exist). In such cases, the time step Δt is reduced to a finite threshold in order to determine whether a grazing solution is reached (a grazing solution exhibits $S(\mathbf{u}^*) = g_0$ with $S(\mathbf{v}^*) = 0$). If a grazing solution is reached, the motion is rejected. Nevertheless, it is conjured that for a small enough Δt, the method converges if the initial conditions generate a non-grazing motion. However, a proof for the convergence of the semismooth-Newton procedure for non-grazing motions is not provided in this manuscript.

B.6 Proofs related to energy behaviour in NBM

B.6.1 Conservation of energy away from instants of switch

In order to answer item 1 in Section 4.3.5, we introduce two lemmas on the energy conservation during active and inactive contact motions, away from a switch (t_s such that $S(\mathbf{u}^o(t_s)) = g_0$).

Lemma B.6. *For the FEM-NBM ODE* (4.40) *developed for a cantilever bar in inactive contact conditions, the energy (involving boundary nodes and non reduced matrices) term*

$$2E(t) = \ddot{\mathbf{u}}^\top(t)\mathbf{M}\ddot{\mathbf{u}}(t) + \mathbf{u}^\top(t)\mathbf{K}\mathbf{u}(t) \tag{B.41}$$

is conserved, that is $\dot{E}(t) = 0$ *for* $S(\mathbf{u}^o(t)) < g_0$.

Proof. This lemma is proven by developing the term $\dot{E}$ from Equation (B.41) and plugging the solution of Equation (4.40).

First, we differentiate equation (B.41) with respect to t, and for symmetric $\mathbf{M}$ and $\mathbf{K}$ (as they are in the given in the FE formulation [34]) we obtain

$$2\dot{E}(t) = \ddot{\mathbf{u}}^\top(t)(\mathbf{M}\dddot{\mathbf{u}}(t) + \mathbf{K}\dot{\mathbf{u}}(t)). \tag{B.42}$$

Next, we note that for inactive contact $S(\mathbf{u}^o(t)) < g_0$, the NBM formulation of u_N in (4.33) admits $\dot{u}_N = S(\dot{\mathbf{u}}^o(t))$. Under this restriction, the relationship between $\dot{\mathbf{u}}(t)$ and $\dot{\mathbf{u}}^o(t)$ can be described via $\dot{\mathbf{u}}(t) = \mathbf{A}^N\dot{\mathbf{u}}^o(t)$. Next, substitution of the previous identity into expression (B.42) admits $\dot{E}(t) = \dot{\mathbf{u}}^{o\top}(t)(\mathbf{M}_N\ddot{\mathbf{u}}^o(t) + \mathbf{K}_N\mathbf{u}^o(t)) = 0$, for $S(\mathbf{u}^o(t)) < g_0$ where the last equality completes this proof by virtue of (4.40). □

Lemma B.7. *For the FEM-NBM ODE* (4.49) *developed for a cantilever bar with non-homogeneous Dirichlet conditions, the energy metric* (B.41) *(similar to the energy metric used in lemma B.6) is conserved, that is* $\dot{E}(t) = 0$ *for* $S(\mathbf{u}^o(t)) > g_0$.

Proof. This theorem is proven by developing the term $\dot{E}(t)$ from equation (B.41) and plugging the solution of equation (4.49). We note that application of (4.41) implies that

$$\dot{u}_N(t) = 0. \tag{B.43}$$

We can conclude that $\mathbf{u}(t)$ belongs to the same space as $\mathbf{w}$ in (4.45), ie

$$\dot{\mathbf{u}}(t) = \mathbf{A}^D\dot{\mathbf{u}}^o(t). \tag{B.44}$$

Thus, we plug-in the identities (4.45) and (B.44) into (B.42) such that $\dot{E}(t) = \dot{\mathbf{u}}^{o\top}(t)(\mathbf{M}_D\ddot{\mathbf{u}}^o(t) + \mathbf{K}_D\mathbf{u}^o(t) + g_0\mathbf{f}_D) = 0$, for $S(\mathbf{u}^o(t)) > g_0$ where the last equality is obtained by virtue of (4.49). □

B.6.2 Derivation of energy jump at switch

In this section, the jump in energy in NBM solutions (see item 2 in Section 4.3.5), ΔE, is developed mathematically to obtain the relation in Equation (4.60). This jump in energy occurs upon switching between active to inactive contact.

In what follows, the energy jump is derived for the case opening contact (transition *from* active to inactive contact) and is denoted $\Delta E_{A/I}$. This derivation procedure can be then replicated for the case of closing contact (transition *from* inactive to active contact) denoted $\Delta E_{I/A}$. In this paper, the term $\Delta E_{I/A}$ is presented but not its derivation. Finally, the general term ΔE describing the energy jump between active and inactive contact (regardless of the order of contact phases) is derived from both $\Delta E_{A/I}$ and $\Delta E_{I/A}$.

To develop the term $\Delta E_{A/I}$, we first denote t_s as the time of switch at opening contact. At opening contact, the stress at the contacting end of the bar, $\sigma_n^h(\mathbf{u}(t_s))$, is zero

$$\sigma_n^h(\mathbf{u}(t_s)) = A(1)\phi_N'(1)(g_0 - S(\mathbf{u}^o(t_s))) = 0. \tag{B.45}$$

Furthermore, the following statements hold

1. The bar is in contact with the wall during the moment of switch (see Equation (4.56))

$$u_N(t_s) = g_0. \tag{B.46}$$

2. The velocity of the contact node during active contact (just before the switch) is zero (see Equation (4.57))

$$\dot{u}_N(t_s^-) = 0. \tag{B.47}$$

3. The derivative of the stress function at the tip of the bar is positive

$$\dot{\sigma}_n^h(\mathbf{u}(t_s^-)) = A(1)\phi_N'(1)(g_0 - S(\dot{\mathbf{u}}^o(t_s)) > 0. \tag{B.48}$$

   since the stress before the switch must be strictly negative during active contact (by Equation (4.58) and assuming non-grazing motion), zero at the switch (see Equation (B.45)), and $\sigma_n^h(\mathbf{u}(t))$ is continuous at all times (see Section 4.3.4). From Equation (B.48) we can also deduce that

$$S(\dot{\mathbf{u}}^o(t_s)) < 0 \tag{B.49}$$

   since $A(1) > 0$ by definition, and $\phi_N'(1) > 0$ holds as proven in Appendix B.1.

4. After the switch, the system is in inactive contact, and the velocity of the contact node is negative by virtue of Equations (4.57) and (B.49):

$$\dot{u}_N(t_s^+) = S(\dot{\mathbf{u}}^o(t_s)) < 0. \tag{B.50}$$

   In fact, it is expected that the velocity after the switch is negative as after the transition from

active to inactive contact, the bar should separate from the wall (for non-grazing motions).

To simplify the notations in the upcoming equations, we present the energy of System (4.59) using block matrices:

$$2E(t) = \begin{bmatrix} \dot{\mathbf{u}}^o(t)^\top & \dot{u}_N(t) \end{bmatrix} \begin{bmatrix} \mathbf{M}_{oo} & \mathbf{M}_{oN} \\ \mathbf{M}_{oN}^\top & M_{NN} \end{bmatrix} \begin{bmatrix} \dot{\mathbf{u}}^o(t_s) \\ \dot{u}_N(t) \end{bmatrix} + \begin{bmatrix} \mathbf{u}^o(t_s)^\top & u_N(t) \end{bmatrix} \begin{bmatrix} \mathbf{K}_{oo} & \mathbf{K}_{oN} \\ \mathbf{K}_{oN}^\top & K_{NN} \end{bmatrix} \begin{bmatrix} \mathbf{u}^o(t_s) \\ u_N(t) \end{bmatrix}. \tag{B.51}$$

Then, we can describe the system's energy just before the moment of switch (during active contact) by plugging Equations (B.46) and (B.47) into Equation (B.51)

$$2E(t_s^-) = \begin{bmatrix} \dot{\mathbf{u}}^o(t_s)^\top & 0 \end{bmatrix} \begin{bmatrix} \mathbf{M}_{oo} & \mathbf{M}_{oN} \\ \mathbf{M}_{oN}^\top & M_{NN} \end{bmatrix} \begin{bmatrix} \dot{\mathbf{u}}^o(t_s) \\ 0 \end{bmatrix} + \begin{bmatrix} \mathbf{u}^o(t_s)^\top & g_0 \end{bmatrix} \begin{bmatrix} \mathbf{K}_{oo} & \mathbf{K}_{oN} \\ \mathbf{K}_{oN}^\top & K_{NN} \end{bmatrix} \begin{bmatrix} \mathbf{u}^o(t_s) \\ g_0 \end{bmatrix}. \tag{B.52}$$

Next, the energy of the system at t_s^+, presuming that the bar is in inactive contact motion, is given by plugging Equations (B.46) and (B.50) into Equation (B.51):

$$\begin{aligned} 2E(t_s^+) = &\begin{bmatrix} \dot{\mathbf{u}}^o(t_s)^\top & S(\dot{\mathbf{u}}^o(t_s)) \end{bmatrix} \begin{bmatrix} \mathbf{M}_{oo} & \mathbf{M}_{oN} \\ \mathbf{M}_{oN}^\top & M_{NN} \end{bmatrix} \begin{bmatrix} \dot{\mathbf{u}}^o(t_s) \\ S(\dot{\mathbf{u}}^o(t_s)) \end{bmatrix} + \dots \\ &\begin{bmatrix} \mathbf{u}^o(t_s)^\top & g_0 \end{bmatrix} \begin{bmatrix} \mathbf{K}_{oo} & \mathbf{K}_{oN} \\ \mathbf{K}_{oN}^\top & K_{NN} \end{bmatrix} \begin{bmatrix} \mathbf{u}^o(t_s) \\ g_0 \end{bmatrix}, \quad S(\dot{\mathbf{u}}^o(t_s)) < 0. \end{aligned} \tag{B.53}$$

Then, the term $\Delta E_{A/I}$ is given as follows (where calculations where omitted for sake of conciseness)

$$\Delta E_{A/I} = E(t_s^+) - E(t_s^-) = S(\dot{\mathbf{u}}^o(t_s)) \left[\mathbf{M}_{oN}^\top \dot{\mathbf{u}}^o(t_s) + \tfrac{1}{2} M_{NN} S(\dot{\mathbf{u}}^o(t_s)) \right], \quad S(\dot{\mathbf{u}}^o(t_s)) < 0. \tag{B.54}$$

Similarly, if we would have started our derivation with the assumption that t_s denotes a instance of closing contact, we would find that the energy jump satisfies

$$\Delta E_{I/A} = -S(\dot{\mathbf{u}}^o(t_s)) \left[\mathbf{M}_{oN}^\top \dot{\mathbf{u}}^o(t_s) + \tfrac{1}{2} M_{NN} S(\dot{\mathbf{u}}^o(t_s)) \right], \quad S(\dot{\mathbf{u}}^o(t_s)) > 0. \tag{B.55}$$

At last, we derive the general term for the energy jump ΔE by combining Equations (B.54) and (B.55)

$$\Delta E = -|S(\dot{\mathbf{u}}^o(t_s))| \left[\mathbf{M}_{oN}^\top \dot{\mathbf{u}}^o(t_s) + \tfrac{1}{2} M_{NN} S(\dot{\mathbf{u}}^o(t_s)) \right]. \tag{B.56}$$

This term is presented using the elements of $\mathbf{M}$ in Equation (4.60).

Appendix C

Proofs and supplementary material on the 2D-NBM

C.1 NBM approximation of contact forces

In this section, the NBM approximation of the contact forces,

$$\boldsymbol{\lambda}(\mathbf{u}(t)) \approx \int_{\Gamma_C} \mathbf{P}(\mathbf{x})^\top \sigma_n(\mathbf{P}(\mathbf{x})\mathbf{u}(t))\mathbf{n}\mathrm{d}\mathbf{x} \tag{5.20}$$

is developed in order to define $\boldsymbol{\lambda}(\mathbf{u}(t))$ as a linear operation on $\mathbf{u}(t)$. The objective is to determine $\mathbf{N}$ such that

$$\mathbf{N}\mathbf{u}(t) = \int_{\Gamma_C} \mathbf{P}(\mathbf{x})^\top \sigma_n(\mathbf{P}(\mathbf{x})\mathbf{u}(t))\mathbf{n}\mathrm{d}\mathbf{x}. \tag{5.20}$$

The formulation of $\mathbf{N}$ allows then to formulate the Signorini conditions (5.11) as an LCP in $\mathbf{u}$ (as shown in Equation (5.23)) and is therefore crucial for the NBM formulation.

To determine $\mathbf{N}$, the term encapsulated by the function $\sigma_n\mathbf{n}$ in Equation (5.20) (the argument $\mathbf{P}(\mathbf{x})\mathbf{u}(t)$ is omitted for most of this section for sake of conciseness) is first expanded. To do so, it is first recalled the $\sigma_n\mathbf{n}$ constitutes the contribution of $\boldsymbol{\sigma}\mathbf{n}$ in the normal direction

$$\boldsymbol{\sigma}\mathbf{n} = \sigma_n\mathbf{n} + \boldsymbol{\sigma}_\tau. \tag{C.1}$$

Otherwise put, $\sigma_n\mathbf{n}$ constitutes the projection of $\boldsymbol{\sigma}\mathbf{n}$ on the direction $\mathbf{n}$

$$\sigma_n\mathbf{n} = \mathrm{proj}_{\mathbf{n}}(\boldsymbol{\sigma}\mathbf{n}) = \mathbf{n}(\mathbf{n}^\top\boldsymbol{\sigma}\mathbf{n}) = (\mathbf{n}\mathbf{n}^\top)\boldsymbol{\sigma}\mathbf{n}. \tag{C.2}$$

Thus, it is only required to evaluate the term $\boldsymbol{\sigma}\mathbf{n}$ in terms of $\mathbf{u}(t)$. Since the relationship between stress and displacement is given using Voigt's notation (5.8), the term $\boldsymbol{\sigma}\mathbf{n}$ is put in to its Voigt

notation form:

$$\boldsymbol{\sigma}\mathbf{n} = \tilde{\mathbf{V}}_{\mathbf{n}}\underline{\boldsymbol{\sigma}}, \quad \tilde{\mathbf{V}}_{\mathbf{n}} = \begin{bmatrix} n_1 & 0 & n_2 \\ 0 & n_2 & n_1 \end{bmatrix} \tag{C.3}$$

where n_1 and n_2 are the components of the normal vector $\mathbf{n} = \begin{pmatrix} n_1 & n_2 \end{pmatrix}^\top$. Then, substitution of the FE stress approximation (5.8) into Equation (C.2) and further into Equation (5.20) reads

$$\boldsymbol{\lambda} \approx \mathbf{N}\mathbf{u}(t), \quad \mathbf{N} = \left(\int_{\Gamma_C} \mathbf{P}(\mathbf{x})^\top (\mathbf{n}\mathbf{n}^\top) \tilde{\mathbf{V}}(\mathbf{n}) \mathbf{D}\mathbf{B}(\mathbf{x}) \mathrm{d}\mathbf{x} \right). \tag{C.4}$$

C.2 Time-derivative of LC($\mathbf{C}, q(t)$)

A methodology to define the derivative of a time-dependent LCP is given. Consider a continuous and differentiable vector function $\mathbf{q}(t) : \mathbb{R} \to \mathbb{R}^{N_C}$ for an arbitrary integer $N_C > 0$ and the P-matrix $\mathbf{C}$ such that the function

$$\mathbf{z}(\mathbf{q}(t)) = \mathrm{LC}(\mathbf{C}, \mathbf{q}(t)) \tag{C.5}$$

is well-defined for any t. It is also known that the function LC($\mathbf{C}, \mathbf{q}$) is Lipschitz continuous for any in $\mathbf{q}$ [53, p. 592]. Therefore, it can also be deduced that $\mathbf{z}(\mathbf{q}(t))$ is Lipschitz continuous as well for continuous $\mathbf{q}(t)$. In what follows, $\mathbf{z}(\mathbf{q}(t))$ is referred to as $\mathbf{z}(t)$ in short.

We develop a methodology to define the derivative of $\mathbf{z}(t)$

$$\dot{\mathbf{z}}(t) = \frac{\mathrm{d}}{\mathrm{d}t}\mathrm{LC}(\mathbf{C}, \mathbf{q}(t)). \tag{C.6}$$

It is recalled that $\mathbf{z}(t)$ satisfies the complementarity condition (5.24) for any t.

To determine the derivative of $\mathbf{z}(t)$, the elements of $\mathbf{z}(t)$ are categorized with respect to the equalities they answer in the complementarity conditions:

1. Type 1 elements are indexed $i \in \mathcal{I}_1$ and exhibit

$$q_i(t) + \sum_{j=1}^{N_C} C_{ij} z_j(t) = 0, \text{ and } z_i(t) > 0. \tag{C.7}$$

   Type 1 elements are collected under $\mathbf{z}^1(t)$.

2. Type 2 elements are indexed $i \in \mathcal{I}_2$ and exhibit

$$q_i(t) + \sum_{j=1}^{N_C} C_{ij} z_j(t) > 0, \text{ and } z_i(t) = 0. \tag{C.8}$$

   Type 2 elements are collected under $\mathbf{z}^2(t)$.

3. Type 3 elements are at a switching instance where both components of the LCP are zero

$$z_i(t) = q_i(t) + \sum_{j=1}^{N_C} C_{ij} z_j(t) = 0 \tag{C.9}$$

and are indexed $i \in \mathcal{I}_3$. Type 3 elements are collected under $\mathbf{z}^3(t)$. Elements in $\mathbf{z}^3(t)$ experience a switch between type 1 and type 2.

In this formulation, $\mathbf{z}(t)$ is the union of $\mathbf{z}^i$ $i = 1, 2, 3$ where for any t at least one element types is present. To clarify, for some instances t, it is possible to have $\mathcal{I}_1 = \mathcal{I}_3 = \emptyset$ and $\mathbf{z}(t) = \mathbf{z}^2(t)$.

Although this section deals with the general LCP rather than the Signorini complementarity conditions, it is useful to present a physical interpretation to the general LCP in terms of the NBM Signorini conditions (5.23). Hence, type 1 elements correspond to nodes in inactive contact motion, type 2 elements correspond to nodes in active contact motion and type 3 elements experiences a switch (ie, contact with the obstacle is made and the NBM stress at the instance of contact is zero). Also, for non-grazing motions, instances of switch where Equation (C.9) holds are expected to be instantaneous and not last of continuous interval of times. Thus, in this section, it is assumed that $\mathbf{z}^3(t)$ transition between type 1 and type 2 elements and that Equation (C.9) holds for stencil of time rather than intervals of time.

Here, the derivative of $\mathbf{z}(t)$ away from instances of switch (ie $\mathcal{I}_3 = \emptyset$) is derived in Appendix C.2.1. Next, the behaviour of the $\dot{\mathbf{z}}(t)$ at the moment of switch where $\mathcal{I}_3 \neq \emptyset$ is described in Appendix C.2.2.

To simplify the derivation of this methodology, block quantities $\mathbf{C}^{ij}$ and $\mathbf{q}^j$ corresponding to elements on indices $\mathcal{I}^j$ are introduced and the components of the LCP problem read

$$\mathbf{z}(t) = \begin{pmatrix} \mathbf{z}^1(t) \\ \mathbf{z}^2(t) \\ \mathbf{z}^3(t) \end{pmatrix}, \quad \mathbf{C} = \begin{bmatrix} \mathbf{C}^{11} & \mathbf{C}^{12} & \mathbf{C}^{13} \\ \mathbf{C}^{21} & \mathbf{C}^{22} & \mathbf{C}^{23} \\ \mathbf{C}^{31} & \mathbf{C}^{32} & \mathbf{C}^{33} \end{bmatrix} \quad \mathbf{q}(t) = \begin{pmatrix} \mathbf{q}^1(t) \\ \mathbf{q}^2(t) \\ \mathbf{q}^3(t) \end{pmatrix}. \tag{C.10}$$

C.2.1 $\dot{\mathbf{z}}(t)$ away from instant of switch

For LCPs the elements in $\mathbf{z}(t)$ are either of type 1 or type 2 and $\mathcal{I}_3 = \emptyset$ since no element of $\mathbf{z}(t)$ experiences a switch. For those instances, the LCP according to notation (C.10) reads

$$\begin{bmatrix} \mathbf{C}^{11} & \mathbf{C}^{12} \\ \mathbf{C}^{21} & \mathbf{C}^{22} \end{bmatrix} \begin{pmatrix} \mathbf{z}^1(t) \\ \mathbf{z}^2(t) \end{pmatrix} + \begin{pmatrix} \mathbf{q}^1(t) \\ \mathbf{q}^2(t) \end{pmatrix} \perp \begin{pmatrix} \mathbf{z}^1(t) \\ \mathbf{z}^2(t) \end{pmatrix} \geq \begin{pmatrix} \mathbf{0} \\ \mathbf{0} \end{pmatrix}. \tag{C.11}$$

Given the element types 1 and 2, the equalities in Equation (C.7) and Equation (C.8) hold respectively. This equalities are put in the block form (C.10)

$$\mathbf{C}^{11}\mathbf{z}^1(t) + \mathbf{C}^{12}\mathbf{z}^2(t) = \mathbf{q}^1(t) \tag{C.12}$$

$$\mathbf{z}^2(t) = \mathbf{0} \tag{C.13}$$

from which the solution to the LCP is readily available and reads

$$\begin{pmatrix} \mathbf{z}^1(t) \\ \mathbf{z}^2(t) \end{pmatrix} = \begin{pmatrix} (\mathbf{C}^{11})^{-1}\mathbf{q}^1(t) \\ \mathbf{0} \end{pmatrix} \tag{C.14}$$

In turn, the derivative $\dot{z}(t)$ is obtained by differentiating (C.14) as follows

$$\dot{\mathbf{z}}(\mathbf{q}(t), \dot{\mathbf{q}}(t), t) = \frac{\mathrm{d}}{\mathrm{d}t}\mathrm{LC}(\mathbf{C}, \mathbf{q}(t)) = \begin{pmatrix} -(\mathbf{C}^{11})^{-1}\dot{\mathbf{q}}^1(t) \\ \mathbf{0} \end{pmatrix} \tag{C.15}$$

where $\mathbf{C}^{11}$ is invertible since it is a minor of $\mathbf{C}$ which is established to be a P-matrix.

C.2.2 $\dot{\mathbf{z}}(t)$ at instant of switch

At switching instants, $\mathcal{I}_3 \neq \emptyset$ holds and elements $i \in \mathcal{I}_3$ answer the condition Equation (C.9).

To simplify further discussion, the instant of switch is denoted t_s. At t_s, $\dot{z}_i(t_s^-) = \dot{z}_i(t_s^+)$ may not necessarily hold for all i since elements in $\mathbf{z}^3(t)$ experience a switch between type 1 and type 2. However, it is demonstrated in this section that, for a given state $\mathbf{q}(t_s)$ and $\dot{\mathbf{q}}(t_s)$ (both are assumed to be continuous quantities in t), the states $\dot{z}_i(t_s^+)$ and $\dot{z}_i(t_s^-)$ can be found by solving an additional LCP problem in the derivatives. This methodology is developed here. Specifically, the proposed methodology is focused on finding $\dot{z}_i(t_s^+)$. Guidelines for determining $\dot{z}_i(t_s^-)$ follow a similar procedure which is explained briefly at the end of this section.

By definition, $\mathbf{z}^1(t_s)$ and $\mathbf{z}^2(t_s)$ and $\mathbf{z}^3(t_s)$ answer respectively Equation (C.7), Equation (C.8) and Equation (C.9). Here, the items $\mathbf{z}^i(t)$ $i = 1, 2, 3$ are isolated from Equation (C.7) to Equation (C.9) (this procedure is omitted for sake of conciseness) and are represented using the block notation introduced in Equation (C.10)

$$\mathbf{z}^1(t_s) = -(\mathbf{C}^{11})^{-1}(\mathbf{C}^{13}\mathbf{z}^3(t_s) + \mathbf{q}^1(t_s)) \tag{C.16}$$

$$\mathbf{z}^2(t_s) = \mathbf{0} \tag{C.17}$$

$$\mathbf{z}^3(t_s) = -(\mathbf{C}^{33})^{-1}(\mathbf{C}^{31}\mathbf{z}^1(t_s) + \mathbf{q}^3(t_s)) = \mathbf{0}. \tag{C.18}$$

With the given the block notation, the derivatives $\dot{\mathbf{z}}^1(t_s)$ and $\dot{\mathbf{z}}^2(t_s)$ is first established for the moment of switch. Then, the LCP problem to solve for $\dot{\mathbf{z}}^3(t_s)$ is formed. It is first noted that $\mathbf{z}^1(t)$ abides Equation (C.16) for both $t = t_s^-$ and $t = t_s^+$. Thus, the derivative of $\dot{\mathbf{z}}^1(t)$ takes the form:

$$\dot{\mathbf{z}}^1(t_s^+) = -(\mathbf{C}^{11})^{-1}(\mathbf{C}^{31}\dot{\mathbf{z}}^3(t_s^+) + \dot{\mathbf{q}}^1(t_s)). \tag{C.19}$$

It is noted that the value of $\dot{\mathbf{z}}^1(t_s^+)$ is affected by $\dot{\mathbf{z}}^3(t_s^+)$. However, the value of $\dot{\mathbf{z}}^3(t_s^+)$ is ambiguous, since $\mathbf{z}^3(t_s^+)$ may become either a type 1 or a type 2 element. Therefore, $\dot{\mathbf{z}}^1(t_s^+) = \dot{\mathbf{z}}^1(t_s^-)$ may not hold due to the behaviour of $\dot{\mathbf{z}}^3(t)$ at t_s. Thus, determination of $\dot{\mathbf{z}}^1(t_s^+)$ requires knowledge of $\dot{\mathbf{z}}^3(t_s^+)$. Next, it is noted that $\mathbf{z}^2(t_s)$ is expected to remain constant at t_s since it does not experience a switch

by definition and

$$\dot{\mathbf{z}}^2(t_s^+) = \dot{\mathbf{z}}^2(t_s^-) = \mathbf{0} \tag{C.20}$$

holds for the switching instant.

To derive the quantity $\dot{\mathbf{z}}^3(t_s^+)$, it is recalled that $\mathbf{z}^3$ can become either a type 1 or a type 2 element. In block form (C.10), this is put as follows

$$\lim_{\Delta t \to 0} \mathbf{0} \leq \mathbf{C}^{31}\mathbf{z}^1(t_s + \Delta t) + \mathbf{C}^{33}\mathbf{z}^3(t_s + \Delta t) + \mathbf{q}^3(t_s + \Delta t) \perp \mathbf{z}^3(t_s + \Delta t) \geq \mathbf{0}. \tag{C.21}$$

Then, given (1) Equation (C.21) holds and that $\mathbf{z}^3(t)$ is (2) Lipschitz continuous and (3) abides (C.9), the derivative $\dot{\mathbf{z}}^3(t_s^+)$ must abide the following restrictions

$$\mathbf{C}^{31}\dot{\mathbf{z}}^1(t_s^+) + \mathbf{C}^{33}\dot{\mathbf{z}}^3(t_s^+) + \dot{\mathbf{q}}^3(t_s) \geq \mathbf{0} \tag{C.22}$$

$$\dot{\mathbf{z}}^3(t_s^+) \geq \mathbf{0} \tag{C.23}$$

$$(\dot{\mathbf{z}}^3(t_s^+))(\mathbf{C}^{31}\dot{\mathbf{z}}^1(t_s^+) + \mathbf{C}^{33}\dot{\mathbf{z}}^3(t_s^+) + \dot{\mathbf{q}}^3(t_s)) = \mathbf{0} \tag{C.24}$$

which form an LCP problem in $\dot{\mathbf{z}}^3(t_s^+)$

$$\mathbf{0} \leq \mathbf{C}^{31}\dot{\mathbf{z}}^1(t_s^+) + \mathbf{C}^{33}\dot{\mathbf{z}}^3(t_s^+) + \dot{\mathbf{q}}^3(t_s) \perp \dot{\mathbf{z}}^3(t_s^+) \geq \mathbf{0} \tag{C.25}$$

Plugging Equation (C.19) into Equation (C.25) then admits

$$\mathbf{0} \leq -\mathbf{C}^{31}(\mathbf{C}^{11})^{-1}(\mathbf{C}^{13}\dot{\mathbf{z}}^3(t_s^+) + \dot{\mathbf{q}}^1(t_s)) + \mathbf{C}^{33}\dot{\mathbf{z}}^3(t_s^+) + \dot{\mathbf{q}}^3(t_s) \perp \dot{\mathbf{z}}^3(t_s^+) \geq \mathbf{0} \tag{C.26}$$

the solution to this LCP is denoted

$$\dot{\mathbf{z}}^3(t_s^+) = \mathrm{LC}(\tilde{\mathbf{C}}, \tilde{q}) \tag{C.27}$$

$$\tilde{\mathbf{C}} = -\mathbf{C}^{31}(\mathbf{C}^{11})^{-1}(\mathbf{C}^{13}) + \mathbf{C}^{33}, \qquad \tilde{\mathbf{q}} = -\mathbf{C}^{31}(\mathbf{C}^{11})^{-1}\dot{\mathbf{q}}^1(t_s) + \dot{\mathbf{q}}^3(t_s). \tag{C.28}$$

Furthermore, the solution (C.27) exists and is unique, since $\mathbf{z}^3(t)$ is Lipschitz continuous and the derivatives $\mathbf{z}^3(t_s^+)$ and $\mathbf{z}^3(t_s^-)$ exist everywhere. In practice, the solution (C.27) can be found via the semismooth Newton method. Thus, the term $\dot{\mathbf{z}}(t_s^+)$ is obtained by combining Equation (C.19), Equation (C.20) and Equation (C.27) as follows

$$\dot{\mathbf{z}}(t_s^+) = \frac{\mathrm{d}}{\mathrm{d}t}\mathrm{LC}(\mathbf{C}, \mathbf{q}(t)) = \begin{pmatrix} -(\mathbf{C}^{11})^{-1}(\mathbf{C}^{31}\mathrm{LC}(\tilde{\mathbf{C}}, \tilde{\mathbf{q}}) + \mathbf{q}^1(t_s)) \\ \mathbf{0} \\ \mathrm{LC}(\tilde{\mathbf{C}}, \tilde{\mathbf{q}}) \end{pmatrix} \tag{C.29}$$

$$\tilde{\mathbf{C}} = -\mathbf{C}^{31}(\mathbf{C}^{11})^{-1}(\mathbf{C}^{13}) + \mathbf{C}^{33}, \qquad \tilde{\mathbf{q}} = -\mathbf{C}^{31}(\mathbf{C}^{11})^{-1}\dot{\mathbf{q}}^1(t_s) + \dot{\mathbf{q}}^3(t_s). \tag{C.30}$$

It is noted that the derivative $\dot{\mathbf{z}}^3(t_s^-)$ can be found by looking at the problem in reverse time $\tilde{t} = -t$. In this case, the LCP condition to Equation (C.25) would exhibit sign changes since the derivative $\dot{\mathbf{z}}^3$ is expected to be negative prior to the switch. However, the result $\dot{\mathbf{z}}^3(t_s^-)$ is not relevant

for the derivation NBM and is omitted from this manuscript for sake of conciseness.

C.3 Proof of piecewise-constant energy

The proof for energy conservation in a given configuration phase is similar to the proof of energy conservation away from switching instants in Appendix B.6.1. To prove conservation of the NBM-ODE in a given configuration phase $\mathcal{T}(\mathbf{p}^{\mathrm{NBM}})$, the derivative of the energy metric in time $\mathrm{d}E/\mathrm{d}t$ is developed and the energy of NBM-ODE solution is shown to exhibit constant energy for a given configuration phase, away from switching instant.

First, let us recall the energy metric

$$2E(t) = \dot{\mathbf{u}}(t)^\top \mathbf{M}\dot{\mathbf{u}}(t) + \mathbf{u}(t)^\top \mathbf{K}\mathbf{u}(t). \tag{C.31}$$

Plugging the NBM approximation of the displacement (5.50) to the energy metric, we obtain

$$2E(t) = \dot{\mathbf{u}}^o(t)^\top (\mathbf{A}^*)^\top \mathbf{M}(\mathbf{A}^*)\dot{\mathbf{u}}^o(t) + (\mathbf{A}^*\mathbf{u}^o(t) + \mathbf{d}^*)^\top \mathbf{K}(\mathbf{A}^*\mathbf{u}^o(t) + \mathbf{d}^*) \tag{C.32}$$

for all $t \in \mathcal{T}(\mathbf{p}^{\mathrm{NBM}})$. As stated in Section 5.4, for a given configuration phase, $\mathbf{A}^*$ and $\mathbf{d}^*$ are constant. Thus, differentiation of Equation (C.32) reads

$$\dot{E}(t) = \dot{\mathbf{u}}^o(t)^\top (\mathbf{A}^*)^\top \mathbf{M}(\mathbf{A}^*)\ddot{\mathbf{u}}^o(t) + \dot{\mathbf{u}}^o(t)^\top (\mathbf{A}^*)^\top \mathbf{K}(\mathbf{A}^*\mathbf{u}^o(t) + \mathbf{d}^*) \quad \forall t \in \mathcal{T}(\mathbf{p}^{\mathrm{NBM}}). \tag{C.33}$$

Then, Equation (C.33) is developed as

$$\begin{aligned}
\dot{E}(t) &= \dot{\mathbf{u}}^o(t)^\top (\mathbf{A}^*)^\top (\mathbf{M}(\mathbf{A}^*)\ddot{\mathbf{u}}^o(t) + \mathbf{K}(\mathbf{A}^*\mathbf{u}^o(t) + \mathbf{d}^*)) && \text{(C.34)}\\
&= \dot{\mathbf{u}}^o(t)^\top (\mathbf{M}^*\ddot{\mathbf{u}}^o(t) + \mathbf{K}^*\mathbf{u}^o(t) + \mathbf{f}^*) && \text{(C.35)}\\
&= 0 \quad \forall t \in \mathcal{T}(\mathbf{p}^{\mathrm{NBM}}) && \text{(C.36)}
\end{aligned}$$

where the last equality is justified by Equation (5.56) and concludes the proof for conservation of energy for NBM motions within a configuration phase.

Upon change of configuration, $\mathbf{A}^*$ and $\mathbf{d}^*$ change and may therefore trigger a change in the quantity $E(t)$ according to Equation (5.63). Thus, the energy of a motion experiencing different contact phases is in fact *piecewise constant* which is also evident in numerical experiments in Sections 5.5 and 5.6.

C.4 Motions of longitudinal NSM

This is section includes figures of motions within the longitudinal NSM.

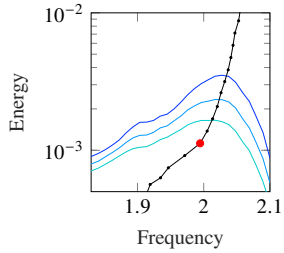

(a) FEP (Figure 5.17)

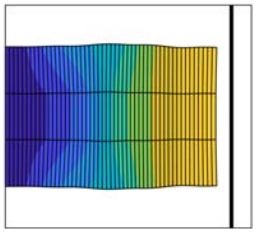

(b) $t = 0$

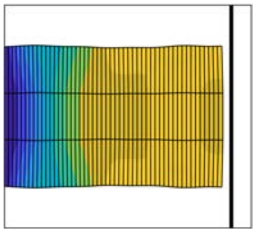

(c) $t = 0.16T$

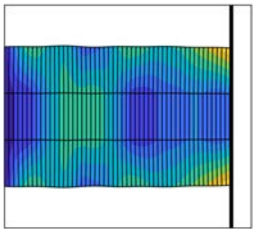

(d) $t = 0.33T$

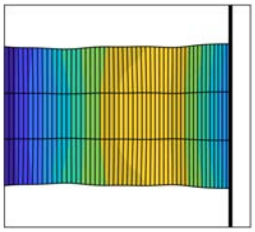

(e) $t = 0.5T$

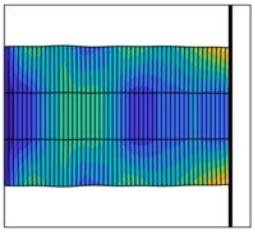

(f) $t = 0.66T$

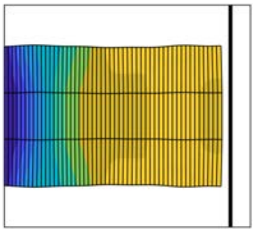

(g) $t = 0.83T$

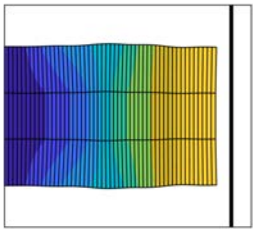

(h) $t = T$

Figure C.1: Longitudinal NSM solution at $\omega \approx 1.99$ and $E \approx 1.1 \times 10^{-3}$ marked in red in Figure C.1(a)

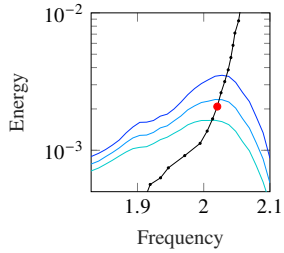

(a) FEP (Figure 5.17)

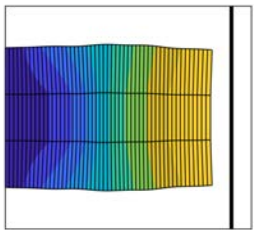

(b) $t = 0$

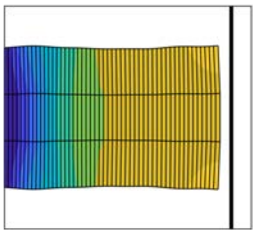

(c) $t = 0.16T$

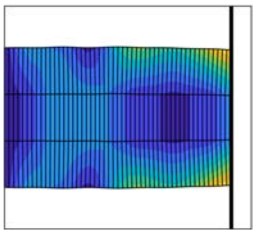

(d) $t = 0.33T$

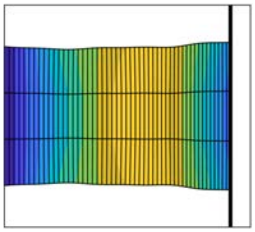

(e) $t = 0.5T$

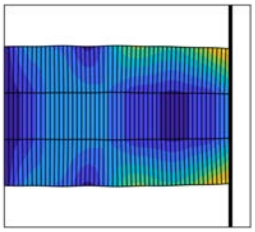

(f) $t = 0.66T$

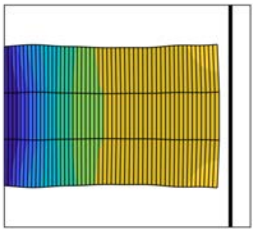

(g) $t = 0.83T$

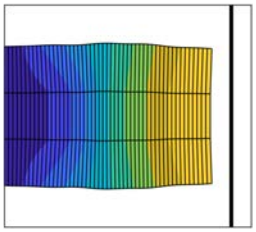

(h) $t = T$

Figure C.2: Longitudinal NSM solution at $\omega \approx 2.02$ and $E \approx 2.1 \times 10^{-3}$ marked in red in Figure C.2(a)

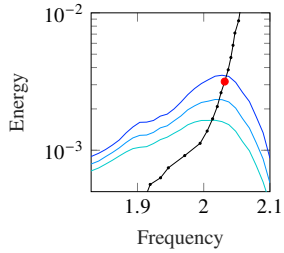

(a) FEP (Figure 5.17)

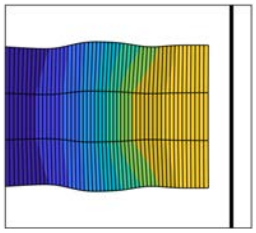

(b) $t = 0$

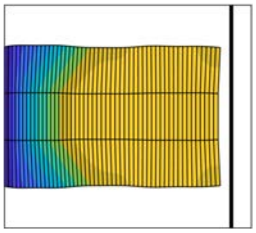

(c) $t = 0.16T$

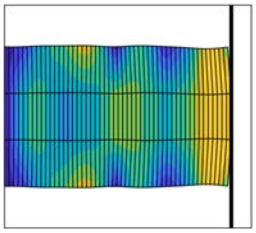

(d) $t = 0.33T$

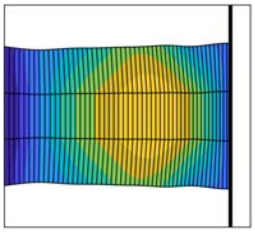

(e) $t = 0.5T$

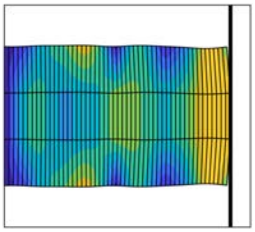

(f) $t = 0.66T$

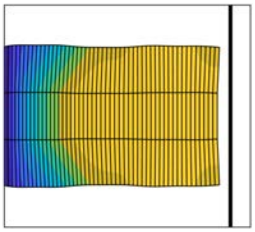

(g) $t = 0.83T$

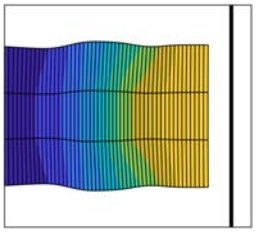

(h) $t = T$

Figure C.3: Longitudinal NSM solution at $\omega \approx 2.03$ and $E \approx 3.2 \times 10^{-3}$ marked in red in Figure C.3(a)

C.5 Motions of transversal NSM

This is section includes figures of motions within the transversal NSM.

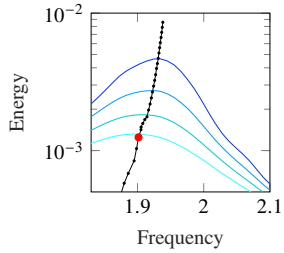

(a) FEP (Figure 5.21)

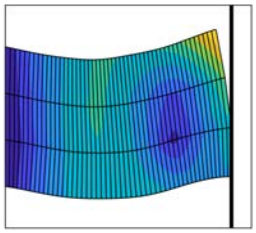

(b) $t = 0$

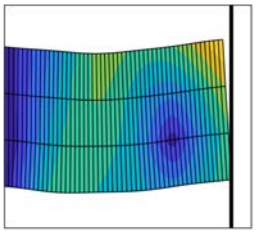

(c) $t = 0.16T$

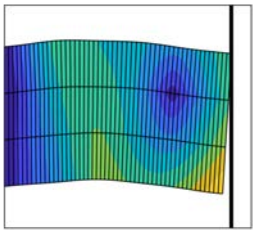

(d) $t = 0.33T$

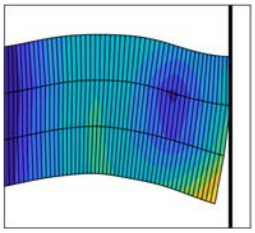

(e) $t = 0.5T$

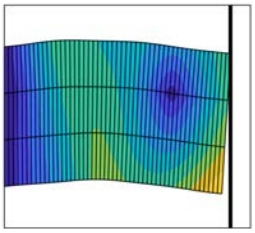

(f) $t = 0.66T$

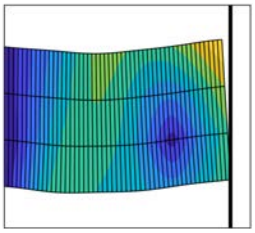

(g) $t = 0.83T$

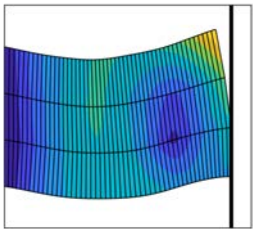

(h) $t = T$

Figure C.4: Transversal NSM solution at $\omega \approx 1.9$ and $E \approx 1.2 \times 10^{-3}$ marked in red in Figure C.4(a)

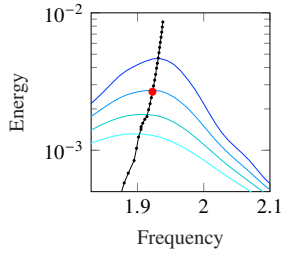

(a) FEP (Figure 5.21)

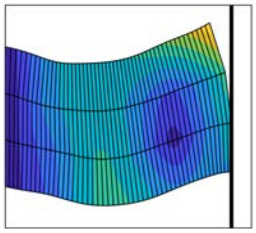

(b) $t = 0$

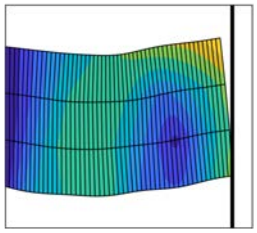

(c) $t = 0.16T$

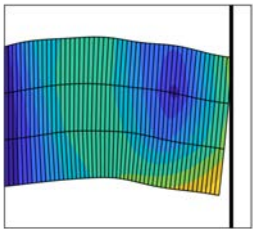

(d) $t = 0.33T$

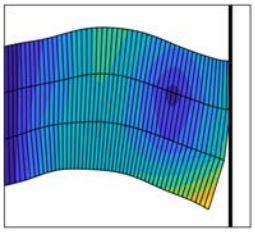

(e) $t = 0.5T$

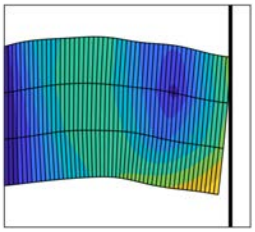

(f) $t = 0.66T$

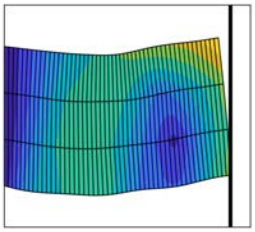

(g) $t = 0.83T$

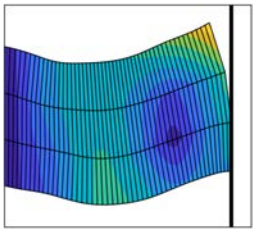

(h) $t = T$

Figure C.5: Transversal NSM solution at $\omega \approx 1.92$ and $E \approx 2.7 \times 10^{-3}$ marked in red in Figure C.5(a)

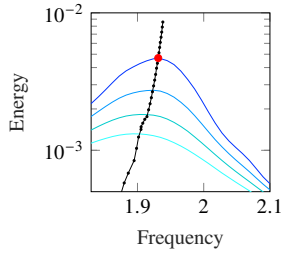

(a) FEP (Figure 5.21)

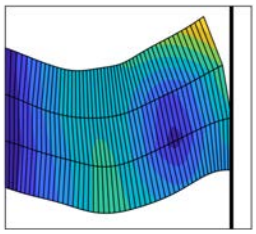

(b) $t = 0$

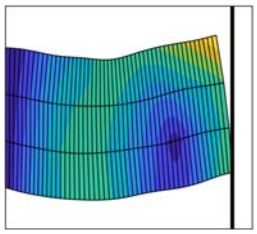

(c) $t = 0.16T$

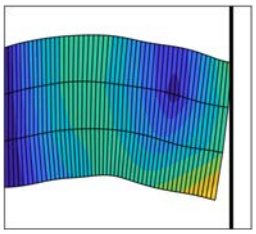

(d) $t = 0.33T$

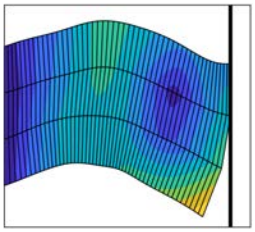

(e) $t = 0.5T$

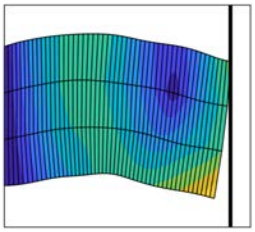

(f) $t = 0.66T$

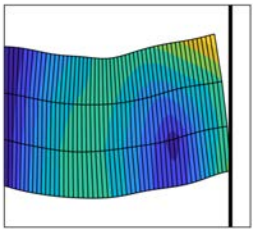

(g) $t = 0.83T$

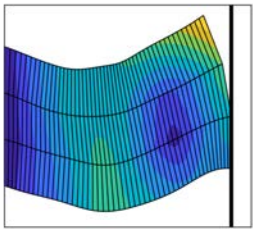

(h) $t = T$

Figure C.6: Transversal NSM solution at $\omega \approx 1.93$ and $E \approx 4.7 \times 10^{-3}$ marked in red in Figure C.6(a)

C.6 Linear modes of the investigated plate

This section includes illustrations of the first 20 linear modes of the investigated plate (defined in Definition 5.5) for purposes of context to linear mode contribution diagrams in Figures 5.16 and 5.20(b). The illustration is provided in Figure C.7.

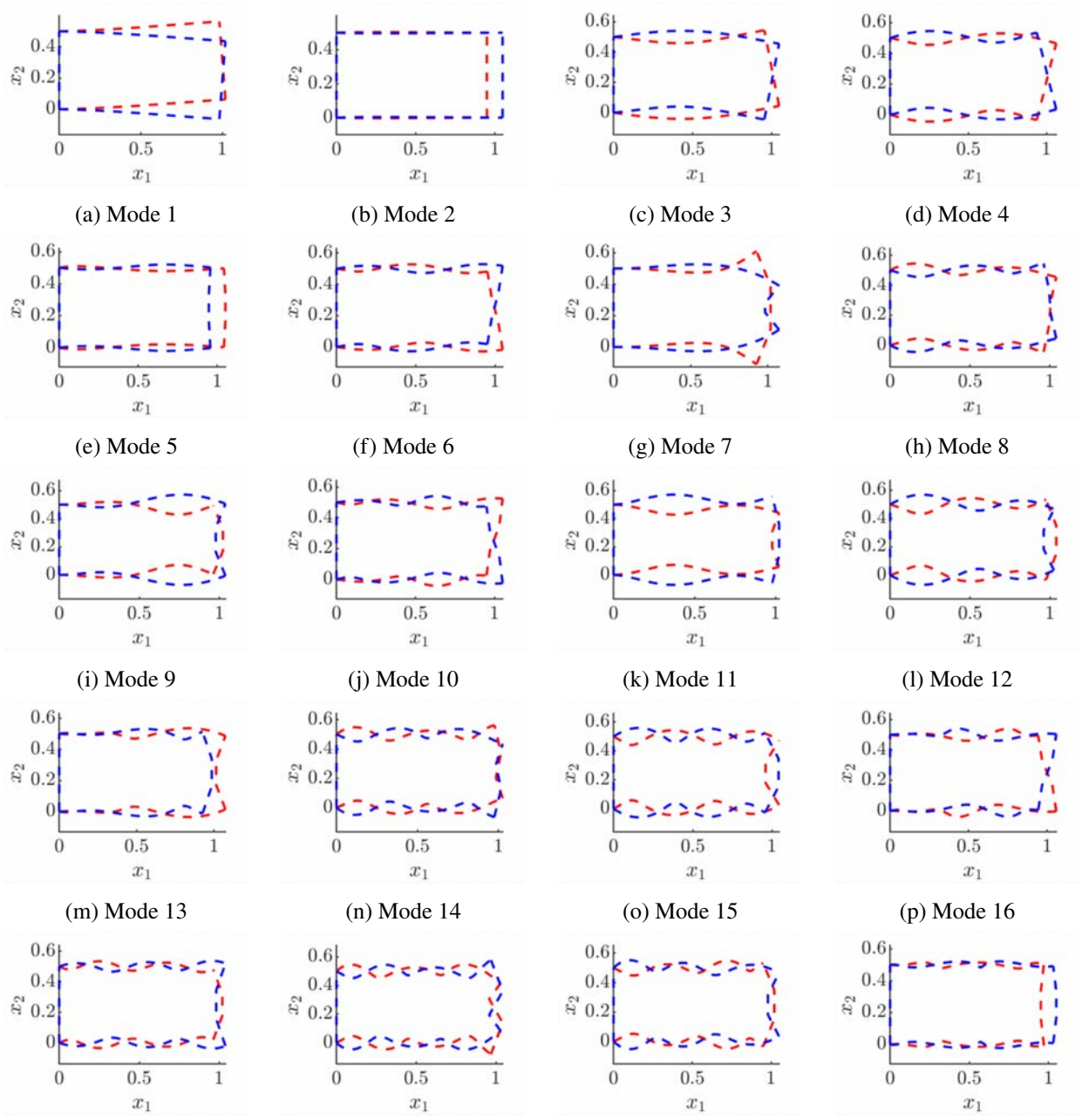

(a) Mode 1 (b) Mode 2 (c) Mode 3 (d) Mode 4

(e) Mode 5 (f) Mode 6 (g) Mode 7 (h) Mode 8

(i) Mode 9 (j) Mode 10 (k) Mode 11 (l) Mode 12

(m) Mode 13 (n) Mode 14 (o) Mode 15 (p) Mode 16

(q) Mode 17 (r) Mode 18 (s) Mode 19 (t) Mode 20

Figure C.7: Linear modes of investigated plate. Red and blue contours represent the negative amplitude of deformation and positive amplitude of deformation, respectively.